

# Direction Finding in the Presence of Complex Electromagnetic Environment



Krishna M. Pasala, PhD

Edward M. Friel, M.S.

June 1995

University of Dayton

AIR FORCE OF SCIENTIFIC RESEARCH (AFSC)  
NOTICE OF TRANSMITTAL TO DTIC  
This technical report has been reviewed and is  
approved for public release IAW AFR 190-12  
distribution is unlimited.  
Joan Boggs  
STINFO Program Manager

Approved for public release,  
distribution unlimited

19950724 041



*The University of Dayton*

DISTRIBUTION STATEMENT A

Approved for public release;  
Distribution Unlimited

DTIC QUALITY INSPECTED 5

# REPORT DOCUMENTATION PAGE

Form Approved  
OMB No. 0704-0188

Public reporting burden for this collection of information is estimated to average 1 hour per response, including the time for reviewing instructions, searching existing data sources, gathering and maintaining the data needed, and completing and reviewing the collection of information. Send comments regarding this burden estimate or any other aspect of this collection of information, including suggestions for reducing this burden, to Washington Headquarters Services, Directorate for Information Operations and Reports, 1215 Jefferson Davis Highway, Suite 1204, Arlington, VA 22202-4302, and to the Office of Management and Budget, Paperwork Reduction Project (0704-0188), Washington, DC 20503.

1. AGENCY USE ONLY (Leave blank)		2. REPORT DATE June 29, 1995	3. REPORT TYPE AND DATES COVERED Final Technical- Apr 92-15 May 95	
4. TITLE AND SUBTITLE Direction finding in the presence of complex electro-magnetic environment			5. FUNDING NUMBERS F49620-92-J-0210	
6. AUTHOR(S) Krishna M. Pasala Ph.D. Edward M. Friel M.S.				
7. PERFORMING ORGANIZATION NAME(S) AND ADDRESS(ES) University of Dayton 300 College Park Dayton, OH 45469-0226			8. PERFORMING ORGANIZATION REPORT NUMBER	
9. SPONSORING/MONITORING AGENCY NAME(S) AND ADDRESS(ES) AFOSR/NM 110 Duncan Avenue Suite B115 Bolling AFB CS 20332-001			10. SPONSORING/MONITORING AGENCY REPORT NUMBER UDR-TR-95-64	
11. SUPPLEMENTARY NOTES				
12a. DISTRIBUTION/AVAILABILITY STATEMENT Unlimited			12b. DISTRIBUTION CODE	
13. ABSTRACT (Maximum 200 words) The effects of complex electromagnetic environment on high resolution direction finding algorithms is investigated. It is demonstrated that mutually coupling adversely affects the resolution capabilities of the MUSIC algorithm. A technique utilizing the terminal impedance matrix is devised to compensate for the mutual coupling effects. Simulation studies show the efficiency of this procedure. The effect of a near field scatterer on the performance of the MUSIC algorithm is also investigated. Interference power as little as 15dB below the signal power from the near field scatterer greatly reduces the resolution capabilities of the MUSIC algorithm. A new array configuration is devised to suppress the interference. Modification of the MUSIC algorithm to account for the change in the array configuration restores the performance of the MUSIC algorithm. Simulations carried out using an electromagnetic model of the array and an edge type near field scatterer demonstrate the validity of the technique.				
14. SUBJECT TERMS			15. NUMBER OF PAGES 203	
			16. PRICE CODE	
17. SECURITY CLASSIFICATION OF REPORT Unclassification	18. SECURITY CLASSIFICATION OF THIS PAGE Unclassification	19. SECURITY CLASSIFICATION OF ABSTRACT Unclassification	20. LIMITATION OF ABSTRACT SAR	

# Direction Finding in the Presence of Complex Electromagnetic Environment

Krishna M. Pasala, PhD

Edward M. Friel, M.S.

June 1995

University of Dayton

Accession For	
NTIS CRA&I	<input checked="" type="checkbox"/>
DTIC TAB	<input type="checkbox"/>
Unannounced	<input type="checkbox"/>
Justification .....	
By .....	
Distribution /	
Availability Codes	
Dist	Avail and/or Special
A-1	

## ABSTRACT

The effects of mutual coupling on several different direction finding algorithms are investigated. This is done by comparing the spectrum estimates with the ideal, actual, and corrected signals. The ideal signal assumes no mutual coupling is present while the actual signal includes all the effects of mutual coupling. It is shown that a terminal impedance representing the mutual coupling between the terminals of the array can be derived from the method of moments model of the array. This matrix is applied to the actual signal vector to produce the corrected signal without mutual coupling. These three signals are generated for various array geometries with various antenna elements. They are used to compute the spectra with the Beamformer algorithm, Capon's algorithm, the Linear Prediction algorithm and the MUSIC algorithm. The results show that the mutual coupling has an adverse effect on the resolution capability of the super resolution algorithms and that its effects can be virtually eliminated from the spectra by pre-processing the signal with the terminal impedance matrix.

The effects of a near field scatterer on the spectrum generated from the MUSIC algorithm are also investigated. It is demonstrated that a near field scatterer significantly reduces the resolution capability of the MUSIC algorithm. This is accomplished with a linear array and near field scatterer modeled using a hybrid technique that combines the Method of Moments and the Uniform Theory of Diffraction. The effects of the scatterer are compensated for using a modified terminal impedance matrix, a new array configuration, and a modified search vector. Results are presented for various scatterers. It is shown that the terminal impedance matrix and the new array configuration can be

used to almost completely suppress the effects of a near field scatterer.

Finally, the terminal impedance matrix is applied to actual measurements to compensate for the effects of mutual coupling. The terminal impedance matrix is also applied to an array of horn elements. In this case, a new technique for calculating the terminal impedance matrix from only measurements is presented. It is then used to compensate for the effects of mutual coupling.

## TABLE OF CONTENTS

### CHAPTER

I.	Introduction .....	1
1.1	Previous Work .....	4
1.2	Overview .....	7
II.	Direction Finding in the Presence of Mutual Coupling .....	10
2.1	Ideal, Actual, and Corrected Voltages .....	11
2.2	Electromagnetic Model of the Antenna Array .....	13
2.3	Correction of the Actual Voltage Vector .....	15
2.3.1	Terminal Impedance Matrix .....	16
2.4	Antenna Elements .....	21
2.5	Antenna Arrays .....	25
2.6	Computer Simulations .....	27
2.6.1	Beamformer Algorithm .....	31
2.6.2	Capon's Algorithm .....	43
2.6.3	Linear Prediction .....	53
2.6.4	MUSIC Algorithm .....	64
2.6.5	Spiral Array .....	75
2.7	Summary and Conclusions .....	76
III.	Direction Finding in the Presence of a Near Field Scatterer .....	78
3.1	Effects of a Near Field Scatterer .....	81
3.2	Electromagnetic Model of the Array and Scatterer .....	83
3.3	Compensation for the Near Field Scatterer .....	86
3.3.1	Terminal Impedance Matrix Including the Scatterer .....	86
3.3.2	New Array Configuration .....	93
3.3.2.1	Suppression of the Interference from the Near Field Scatterer .....	95
3.3.2.2	Signal Model .....	96

3.4	Results .....	101
3.4.1	Suppression of the Interference .....	102
3.4.2	Point Scatterer .....	106
3.4.3	Distributed Scatterer .....	115
3.5	Summary and Conclusions .....	120
IV.	Mutual Coupling Compensation Applied to Measurements .....	122
4.1	Monopole Measurements .....	123
4.1.1	Antenna Arrays .....	124
4.1.2	Measurement Setup .....	126
4.1.3	Antenna Model .....	128
4.1.4	Results .....	129
4.1.4.1	Beamformer Algorithm .....	131
4.1.4.2	Capon's Algorithm .....	135
4.1.4.3	Linear Prediction .....	142
4.1.4.4	MUSIC Algorithm .....	142
4.2	Horn Array Data .....	146
4.3	Measurement Conclusions .....	154
V.	Conclusions .....	159
APPENDICES		
Appendix A	.....	162
Appendix B	.....	166
Appendix C	.....	169
Appendix D	.....	174
Appendix E	.....	181
Appendix F	.....	187
REFERENCES	.....	197

## CHAPTER I

### INTRODUCTION

It is often required to estimate the angles of arrival of incident signals. These signals may be generated by a geophysical phenomenon and received by a ground based station. They may also be signals received by an airborne platform in a hostile environment. To determine the spatial spectrum, several techniques have been developed [5,6,45,54]. These techniques frequently assume that the sensors are ideal and operate in an ideal environment. In practice, however, this is not true. There is always mutual coupling between the sensors which distorts the signals. The mutual coupling may have very drastic effects if the sensor array is designed to be operated over a large bandwidth. There may also be an object in the near field of the sensor array which scatters a portion of the incident signal toward the array. The scattered fields may effect the calculation of the spatial spectrum. This scatterer may be an airplane wing, a nearby building, or the inside of the antenna array's radome. This work quantitatively determines the effects of mutual coupling and a near field scatterer on the calculation of the spatial spectrum. Techniques are also presented to suppress these effects.

Non-parametric methods for estimating the spatial spectrum such as the Beamformer algorithm are based on the Fourier transform and make no assumptions about how the data is generated. This algorithm can be applied very efficiently with the Fast



Fourier Transform (FFT) and only requires one snapshot of data [1,2]. If, however, multiple signals are present, the angle estimates will be biased [54]. The resolution of the signals is limited by the Rayleigh Criterion since the algorithm is based on the FFT [31]. This is true regardless of the Signal to Noise Ratio (SNR). In general, the resolution of this algorithm is poor since the number of receivers is small. In this study, the number of receivers is equal to the number of antenna elements. The poor resolution of these methods led to the development of "super-resolution" algorithms such as Capon's algorithm [5], and the MUltiple Signal Classification (MUSIC) algorithm [6,45]. These algorithms are capable of yielding resolution beyond that of the Beamformer algorithm [45].

The "super-resolution" techniques require first modeling the signal and calculating the necessary parameters to estimate the spectrum. These techniques are therefore referred to as parametric methods. As already stated these techniques offer resolution greater than that of non-parametric methods for the same number of receivers. These methods are, in general, not very robust and are susceptible to modeling errors [28]. Since these techniques require calculating certain parameters first before estimating the angles of arrival, the resolution of these techniques may be worse than that of non-parametric methods if the parameters are poorly estimated [28].

The parameters may be poorly estimated for a variety of reasons. Possible sources of error are gain and phase errors on the signals due to the frequency response of the receiver, and mutual coupling between the antenna elements. The gain and phase errors have already been investigated [10-13]. This work is concerned with the effects of

mutual coupling.

The mutual coupling between the antenna elements can degrade the ability of parametric methods to resolve two signals with a small angular separation [28]. If the array is designed to resolve two closely spaced narrowband signals over a wide bandwidth, the mutual coupling effects will be severe at the low end of the frequency band. This is because the inter-element spacing at the upper frequency band must not exceed half a wavelength to prevent ambiguities caused by grating lobes in the antenna pattern. This causes the separation to be much less than half a wavelength at the low end of the frequency band. The result is strong mutual coupling which degrades the performance of the direction finding algorithm. One of the purposes of this investigation is to quantitatively determine the effects of mutual coupling and develop a procedure to compensate for these effects. Some of the work in this section has already been presented at a symposium and appeared in the literature [32,33].

The angle of arrival calculations may also be affected by the presence of a scatterer. If the scatterer is in the far field of the antenna array, the signals incident upon the array are coherent plane waves. This problem has been investigated for various array geometries [14-21]. If, however, the object is in the near field of the antenna array, the interference is in the form of spherical waves. This interference appears to be arriving at a different angles of arrival for each antenna element. This problem can arise, for example, when the object is a nearby airplane wing or the inside of the antenna array's radome.

## 1.1 Previous Work

There are many techniques that may be used to estimate the spatial spectrum. The classical technique is the beamformer algorithm which is based on the Fourier transform [1,2]. While the technique only requires one snapshot of data, its resolution capability is limited to that specified by the Rayleigh criterion [31]. The spatial spectrum may also be estimated with modern techniques such as linear prediction [3,4], Capon's "maximum likelihood" algorithm [5], MUSIC [6], and the Estimation of Signal Parameters via Rotational Invariance Technique (ESPRIT) [7,8,9]. These algorithms are computationally expensive but have resolution capabilities that exceed the Rayleigh limit [31].

The spectrum produced by super resolution techniques is affected by the number of snapshots used to form the covariance matrix and by the gain and phase of each antenna element. The gain and phase errors are introduced because each receiver has a separate amplifier with a slightly different frequency response. While these errors are small, they become significant when model based algorithms are used to estimate the angles of arrival. The effect of using a finite number of snapshots on the MUSIC algorithm is investigated in [10]. The effects of gain and phase perturbations are analyzed in [11,12]. A unified treatment of these two problems is presented in [13].

If the signals incident on the array are coherent, the procedure for determining the angles of arrival must be altered. This problem occurs when one signal is a reflection from an object in the scene. To overcome this problem a spatial smoothing technique has been developed [14 - 20] for linear arrays. However, linear arrays do not provide a full 360° coverage of the scene. To overcome this problem, the spatial smoothing

technique is extended to circular arrays [21].

Gupta and Ksienski [22] analyzed the performance of an adaptive linear array taking into account the effect of mutual couplings. They obtained a simple relationship between the open circuit voltages and the actual voltages at the terminals of the dipoles. Using this approach several authors [23], [24] studied the performance of the MUSIC [6] algorithm to determine the direction of arrival (DOA) using dipole arrays and including the effects of mutual coupling. In [23], Yeh et. al. consider both uncorrelated and coherent sources and discuss two approaches to counteract the mutual coupling effects. These modifications involve either modifying the "search vector" using the inverse of the impedance matrix or reconstructing the signal subspace by solving a generalized eigenvalue problem. Litva and Zeytinoglu [24] consider the performance of the MUSIC algorithm using a circular dipole array operating in either free space or above lossy ground. They found a significant residual bias in their DOA estimates. The modifications used in [24] to counteract the effects of mutual coupling is the same as in [23] and involves the transformation of the search vector. Steyskal and Herd [26] considered a linear array of single mode elements and formulated a coupling matrix which relates the actual and ideal voltages at the antenna terminals. They also describe an experimental technique to determine this coupling matrix and its use in beamforming. Weiss and Friedlander [27,28] modify the MUSIC algorithm to model mutual coupling effects. Their method, however, only estimates the coupling between the nearest antenna elements and requires iterating thirty times to obtain a convergent result. This iterative technique has also been shown to converge to the wrong angles of incidence in some

cases [36,37]. Swindlehurst and Kailath [29] also modify the MUSIC algorithm to account for mutual coupling but also only estimate the mutual coupling between an element and its nearest neighbor. All other coupling is assumed insignificant. Roller and Wasyliwskyj [30] modified the input signal to account for the mutual coupling in a dipole array while assuming the antenna elements to be isotropic. They also examined the effects of mismatching at the antenna terminals on direction finding. The method presented here does not alter the MUSIC algorithm, but instead seeks to correct the actual antenna voltages for the mutual coupling and then process these corrected voltages to determine the angle of arrival.

The previous work only approximated the mutual coupling effects between an antenna element and its nearest neighboring element. This coupling is the strongest, but is not the only significant coupling. The mutual coupling between all the antenna elements has an effect on the MUSIC spectrum. The results of compensating for all the mutual coupling present has also been investigated but only for the simplest case. In [38] Himed and Weiner model a dipole array with the piecewise sinusoidal Galerkin formulation of the method of moments [35]. They use one sinusoidal mode on each dipole to represent the current on the dipole. In this case, the impedance matrix from the method of moments represents the mutual coupling between every antenna element. This matrix is then successfully used to compensate for the mutual coupling effects. This procedure, however, is limited to dipole elements that are approximately a half a wavelength long. It is also only useful for dipoles that are not closely spaced together. In this case, the mutual coupling does not have a significant effect on the spectrum. If

the separation between dipole elements is small, then more than one sinusoidal mode is required to adequately represent the current on the dipole. The result is that the impedance matrix generated by the method of moments will not be the mutual coupling matrix. It is shown that the mutual coupling matrix may be extracted from the method of moments matrix. This allows an estimate of the mutual coupling matrix for other arrays such as the sleeve dipole array and spiral array [32,33].

A relatively small number of papers appear in the literature on the effects of a near field scatterer on direction finding algorithms [55-58]. The effect of a near field scatterer has been investigated in previous work. The effects of radome reflections on adaptive architectures has been addressed in [55]. The problem of radar pointing error induced by a radome is investigated in [56]. In this work a ray based technique is used to account for the scattering by a radome. The effect of boresight error has also been investigated and compared to experimental results [57]. The effects of reflections from radome and mutual coupling between antenna elements is presented in [58]. In this work it is shown that the radome reflections and mutual coupling between antenna elements degrades the ability of the MUSIC algorithm to resolve two signals.

## **1.2 Overview**

In chapter 2 the effects of mutual coupling on several different direction finding algorithms is investigated. This is done by comparing the spectrum estimates due to three different signals. The first is the ideal signal which assumes no mutual coupling is present. This represents the best possible spectrum. The actual signals are calculated from the method of moments model of the array. This signal includes all the mutual

coupling effects. It is shown that a terminal impedance representing the mutual coupling between the terminals of the array can be derived from the method of moments model of the array. This matrix is then applied to the actual signal vector to correct for the mutual coupling effects. These three signals are generated for various array geometries with various antenna elements. These signals are used to compute the spectra with the Beamformer algorithm, Capon's algorithm, the Linear Prediction algorithm and the MUSIC algorithm. The results show that the mutual coupling has an adverse effect on the resolution capability of the super resolution algorithms and that these effects can be virtually eliminated from the spectra by pre-processing the signal with the terminal impedance matrix.

In chapter 3 the effects of a near field scatterer on the spectrum generated from the MUSIC algorithm are investigated. This scatterer produces interference in the form of spherical waves that degrade the ability of the MUSIC algorithm to resolve two signals with a small angular separation. To determine the effects of a scatterer, a linear array with the near field scatterer is modeled using a hybrid technique that combines the Method of Moments and the Uniform Theory of Diffraction [34,35]. The effects of the scatterer are then compensated for using a modified terminal impedance matrix and a new array configuration. The modified terminal impedance matrix accounts for the additional mutual coupling between the array and scatterer. The new array configuration is used to suppress the spherical waves from the scatterer. To account for the new array configuration, the search vector of the MUSIC algorithm is modified. Results are presented for various scatterers. It is shown that the terminal impedance matrix and the

new array configuration can be used to virtually completely suppress the effects of a near field scatterer.

In chapter 4, the terminal impedance matrix is applied to actual measurements to compensate for the effects of mutual coupling. This is first done on a variety of monopole arrays. The terminal impedance matrix is also applied to an array of horn elements. In this case, a new technique for calculating the terminal impedance matrix from only measurements is presented. It is then used to compensate for the effects of mutual coupling.

The conclusions are presented in chapter 5 and various Appendices are included before the references are given. In chapter 5, all the work is summarized. Avenues for future investigation are also discussed. The contributions of this work are also outlined in this chapter. Appendix A presents the method of moments which is used to model the antenna arrays. Appendices B through E describe the direction finding algorithms. The last Appendix describes the hybrid method of moments - Uniform Theory of Diffraction technique for modeling the near field scatterer and the linear array.



## CHAPTER II

### DIRECTION FINDING IN THE PRESENCE OF MUTUAL COUPLING

Direction finding systems are often required to work well on narrow band signals which may occur over a wide range of frequencies. This requires that the inter-element spacing be less than half a wavelength at the highest frequency of operation to avoid the ambiguities that arise from the formation of grating lobes. Therefore, at the low end of the frequency band, the inter element spacing is electrically small leading to significant mutual coupling between the antenna elements. This mutual coupling degrades the ability of the direction finding algorithm to resolve two signals with a small angular separation.

To determine quantitatively the effects of mutual coupling, the angles of arrival are calculated with the ideal, actual, and corrected signals. The ideal signal assumes that there is no mutual coupling between the antenna elements. This yields the best possible spatial spectrum. The actual signal is the voltage that would be measured at the terminals of the antenna elements. This signal is calculated from an electromagnetic model of the antenna array and includes all the effects of mutual coupling. The corrected signal is obtained by processing the actual signal with the terminal impedance matrix which models the mutual coupling between the antenna elements. It will be shown that this removes virtually all the effects of mutual coupling in the signal. The result is that

the new spectrum is almost identical to the ideal case.

Three antenna elements are used to form the direction finding antenna arrays. The first element, the dipole, is the simplest but can only be operated over a narrow band of frequencies. Therefore, it is useful only for theoretical investigations. The second element, the sleeve dipole, is a modification of the dipole and can be operated over a one octave bandwidth. The spiral antenna is the third element and is referred to as a frequency independent antenna since it is possible to operate it over a one decade bandwidth or more.

The antenna elements are formed into linear, cross, and circular arrays for the direction finding algorithms. The linear array is useful for resolving angles of arrival over a range from  $0^\circ$  to  $180^\circ$ . The cross and circular arrays can be used over a full  $360^\circ$  angular coverage. The spiral antenna is only used in a linear array since its physical size limits its usefulness in direction finding over a large bandwidth as will be shown later.

The antenna arrays are used with several different direction finding algorithms to determine the effects of mutual coupling and the usefulness of the compensation technique described later. These techniques are the Beamformer algorithm, Capon's algorithm, the Linear Prediction algorithm, and the MUSIC algorithm. It will be shown that the direction finding capability of the algorithms is improved by compensating for the mutual coupling.

## **2.1 Ideal, Actual and Corrected Voltages**

The direction finding algorithms are examined with the ideal, actual, and corrected signals. The ideal signal assumes that there is no mutual coupling between the antenna

elements. Mathematically, the voltage at the  $M^{\text{th}}$  antenna element can be expressed as

$$V_M = e^{j\beta(x_M \cos\phi + y_M \sin\phi)} e^{j\omega t} \quad (1)$$

where  $\beta$  is the propagation constant,  $\phi$  is the angle of arrival with respect to the x - axis,  $x_M$  and  $y_M$  are the location of the  $M^{\text{th}}$  antenna elements, and  $\omega$  is the temporal frequency. This signal assumes that there are no gain or phase errors. These errors occur since the frequency response of each antenna element amplifier may be slightly different.

The actual signal at the terminals of the antenna array is calculated with the reaction integral equation. This is one of several integral equations that may be used [42]. This equation is then solved using the method of moments [40,41]. The result is a complex constant for each of the antenna terminals. The time variation is then added so that the signal at the  $M^{\text{th}}$  antenna element may be expressed as

$$V_M = A_M e^{j\psi_M} e^{j\omega t} \quad (2)$$

where  $A_M e^{j\psi_M}$  is the complex constant from the method of moments model of the antenna array. This constant is not only a function of the incident field at the antenna elements but also the mutual coupling between the array elements.

The corrected signal at the  $M^{\text{th}}$  antenna element is found by multiplying the actual signal in equation (2) by the terminal impedance matrix. The terminal impedance matrix represents the mutual coupling between the antenna elements and is derived from the moment method model of the antenna array. Mathematically, the corrected signal is

$$\begin{bmatrix} V_1 \\ V_2 \\ \vdots \\ V_M \end{bmatrix} = \begin{bmatrix} Z_{11} & Z_{12} & \cdots & Z_{1M} \\ Z_{21} & Z_{22} & \cdots & Z_{2M} \\ \vdots & \vdots & \ddots & \vdots \\ Z_{M1} & Z_{M2} & \cdots & Z_{MM} \end{bmatrix} \begin{bmatrix} A_1 e^{j\psi_1} \\ A_2 e^{j\psi_2} \\ \vdots \\ A_M e^{j\psi_M} \end{bmatrix} e^{j\omega t} \quad (3)$$

where  $V_1, V_2, \dots, V_M$  are the corrected voltages,  $Z_{ij}$  is the mutual coupling between antenna elements  $i$  and  $j$ , and  $A_1 e^{j\psi_1}$ ,  $A_2 e^{j\psi_2}$ , and  $A_M e^{j\psi_M}$  are the complex constants from equation (2).

## 2.2 Electromagnetic Model of the Antenna Array

The reaction integral equation is used to determine the current induced on an antenna illuminated by a plane wave. The current on the antenna is represented with overlapping piecewise sinusoids as shown in figure 1. The integral equation is then reduced to a system of linear equations with the method of moments as described in Appendix A. The system of equations is solved to yield the current at all points on the antenna. The voltage at the antenna terminals is computed by multiplying the current at the antenna terminals by the load impedance for the element.

Using the method of moments, the integral equation is reduced to the system of equations

$$\sum_{n=1}^N Z_{mn} I_n = V_m \quad m=1, 2, \dots, N \quad (4)$$

$$\text{where } Z_{mn} = \int_S \vec{J}_m \cdot \vec{E}_n^s ds \quad (5)$$

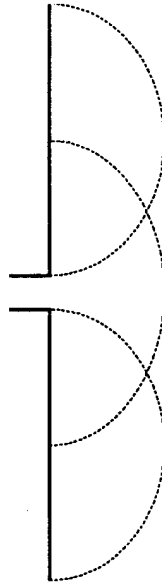


**Figure 1: Piecewise Sinusoidal Current Expansion on One Dipole**

and 
$$V_m = - \int_s \vec{J}_m \cdot \vec{E}^i ds \quad . \quad (6)$$

In these equations  $Z_{mn}$  is the mutual coupling between modes  $m$  and  $n$ ,  $I_n$  and  $I_m$  are the currents at modes  $n$  and  $m$  respectively,  $V_m$  is the excitation at mode  $m$ ,  $E^i$  is the incident electric field, and  $ds$  is the differential length along one dipole.

The number of piecewise sinusoids needed to adequately represent the current on a thin wire antenna is dependent upon the length of the antenna element. Since the dipole elements are approximately half a wavelength long at the center of the bandwidth, the current on them can be adequately represented by three piecewise sinusoidal modes. Note that from equation (5) that the impedance matrix  $Z_{mn}$  is not dependent upon the incident field. This matrix is unique to the geometry of the antenna array and the frequency of the incident signal. The frequency is important because it determines the number of

piecewise sinusoids that must be used to adequately represent the current on the antenna element. Note, in contrast, that the excitation  $V_m$  is dependent upon the incident field and therefore the angle of arrival.

After  $Z_{mn}$  and  $V_m$  are calculated, the modal current on the antenna elements is found using equation (4). The voltage at the  $n^{\text{th}}$  terminals is then calculated with

$$V_n^{Te} = I_n^{Te} \cdot Z_n \quad (7)$$

where  $I_n^{Te}$  is the modal current at the  $n^{\text{th}}$  terminals of the antenna array, and  $Z_n$  is the load impedance at the  $n^{\text{th}}$  terminals. Therefore, the voltage vector representing the actual signal that includes the effects of mutual coupling is

$$V_a = [V_1^{Te} \ V_2^{Te} \ \dots \ V_n^{Te}]^T \quad (8)$$

This voltage should not be confused with the voltage in equation (4).

### 2.3 Correction of the Actual Voltage Vector

The impedance matrix  $Z_{mn}$  and the voltage vector  $V_m$  are calculated using equations (5) and (6). The current on the antenna elements is then found using equation (4). Unfortunately, since there is mutual coupling between the antenna elements as described by  $Z_{mn}$ , the voltage  $V_m$  will be corrupted by this mutual coupling. The objective of the next section is to derive a terminal impedance matrix which describes the mutual coupling between the antenna elements in terms of the mutual coupling between the sinusoidal modes  $m$  and  $n$ . Mathematically, the objective is to reduce equation (4) which is repeated below for convenience

$$\sum_{n=1}^N Z_{mn} I_n = V_m \quad m = 1, 2, \dots, N \quad (9)$$

to

$$\sum_{l=1}^M Z_{kl}^{Te} I_l = V_k \quad k = 1, 2, \dots, M \quad (10)$$

where  $Z_{mn}$  is the mutual coupling between piecewise sinusoidal modes  $m$  and  $n$ ,  $I_n$  is the  $n^{\text{th}}$  piecewise sinusoidal current,  $V_m$  is the current at the  $m^{\text{th}}$  mode,  $Z_{kl}^{Te}$  is the mutual coupling between the  $k^{\text{th}}$  and  $l^{\text{th}}$  antenna elements,  $I_l$  is the  $l^{\text{th}}$  terminal current, and  $V_k$  is the voltage at the  $k^{\text{th}}$  antenna terminals. Note that since the current on the entire antenna structure was found using equation (4), the current  $I_l$  is already known. It therefore remains only to calculate the terminal impedance matrix  $Z_{kl}^{Te}$ .

### 2.3.1 Terminal Impedance Matrix

Let there be  $M$  antenna elements in the array with the current on each element represented by  $N_m$  modes. The size of the impedance matrix  $Z_{mn}$  is  $N \times N$  where  $N = M \times N_m$ . The objective is to reduce this matrix to  $M \times M$  matrix whose elements represent the reaction between the antenna terminals.

The mutual impedance between the terminals  $k$  and  $l$  is defined as [17]

$$Z_{kl}^{Te} = \frac{V_{kl}^{Te}}{I_l^{Te}}, \quad (11)$$

where  $V_{kl}^{Te}$  is the open circuit voltage at the  $k^{th}$  antenna terminal due to the current on the  $l^{th}$  antenna terminal. The open circuit voltage can be expressed mathematically as,

$$V_{kl}^{Te} = -\frac{1}{I_k^{Te}} \int_{k^{th} antenna} \vec{E}_{kl} \cdot \vec{I}^k dl , \quad (12)$$

where  $\vec{E}_{kl}$  is the incident field at the  $k^{th}$  antenna due to the  $l^{th}$  antenna. Noting that the current on the antenna is expanded as a finite series of piecewise sinusoidal functions, the currents on the  $l^{th}$  and  $k^{th}$  antenna elements of the array are given by,

$$I^l = \sum_{p=1+(l-1)N_m}^{lN_m} I_p^l F_p(z) \quad (13)$$

$$I^k = \sum_{m=1+(k-1)N_m}^{kN_m} I_m^k F_m(z) \quad (14)$$

where  $F_p(z)$  are the piecewise sinusoidal expansion functions [40] and  $I_p^l$  and  $I_m^k$  are the mode currents on the  $l^{th}$  and  $k^{th}$  antenna elements respectively. The electric field at the  $k^{th}$  antenna element due to the  $l^{th}$  antenna element is shown graphically in figure 2 and may be written as

$$\vec{E}_{kl} = \sum_{m=1+(k-1)N_m}^{kN_m} \vec{E}_m^l G(z-z_m) , \quad (15)$$



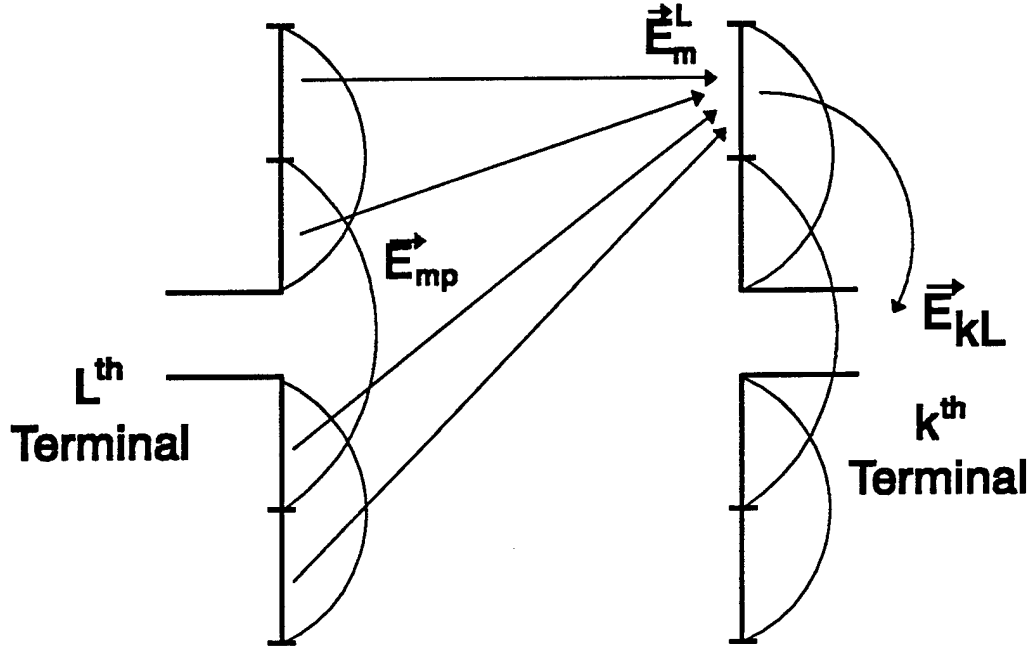


Figure 2: Geometry for the Derivation of the Terminal Impedance Matrix

where  $\vec{E}_m^l$  is the field at the  $m^{\text{th}}$  mode due to the current  $I^l$  on the  $l^{\text{th}}$  antenna element and  $G(z - z_m)$  is unity over the  $m^{\text{th}}$  mode and zero elsewhere. The electric field  $\vec{E}_{kl}$  is also shown graphically for a dipole array in figure 2. The electric field  $\vec{E}_m^l$  is the sum total of the field from all the modes on the  $l^{\text{th}}$  antenna. This field may be expressed as,

$$\vec{E}_m^l = \sum_{p=1+(l-1)N_m}^{lN_m} \vec{E}_{mp} \quad (16)$$

Substituting equation (16) into equation (15) yields,

$$\vec{E}_{kl} = \sum_{m=1+(k-1)N_m}^{kN_m} \sum_{p=1+(l-1)N_m}^{lN_m} \vec{E}_{mp} G(z-z_m) \quad (17)$$

Substituting equation (17) in equation (12) yields,

$$V_{kl}^{Te} = -\frac{1}{I_k^{Te}} \int_{k^{th} antenna} \left[ \sum_{m=1+(k-1)N_m}^{kN_m} \sum_{p=1+(l-1)N_m}^{lN_m} \vec{E}_{mp} G(z-z_m) \right] \cdot \vec{I}^k dl$$

$$V_{kl}^{Te} = -\frac{1}{I_k^{Te}} \sum_{m=1+(k-1)N_m}^{kN_m} \sum_{p=1+(l-1)N_m}^{lN_m} \int_{k^{th} antenna} \vec{E}_{mp} G(z-z_m) \cdot \vec{I}^k dl$$

$$V_{kl}^{Te} = -\frac{1}{I_k^{Te}} \sum_{m=1+(k-1)N_m}^{kN_m} \sum_{p=1+(l-1)N_m}^{lN_m} \int_{m^{th} mode} \vec{E}_{mp} \cdot \vec{I}^m dl \quad (18)$$

Note that mutual impedance between modes m and p is given by,

$$Z_{mp} = \frac{V_{mp}}{I_p} = -\frac{1}{I_p I_m} \int \vec{E}_{mp} \cdot \vec{I}^m dl \quad (19)$$

Rearranging this equation yields,

$$-\int_{m^{th} mode} \vec{E}_{mp} \cdot \vec{I}^m dl = Z_{mp} I_m I_p \quad (20)$$

Substituting equation (20) into equation (18) yields,

$$V_{kl}^{Te} = -\frac{1}{I_k^{Te}} \sum_{m=1+(k-1)N_m}^{kN_m} \sum_{p=1+(l-1)N_m}^{lN_m} -Z_{mp} I_m I_p \quad (21)$$

Therefore,

$$Z_{kl}^{Te} = \frac{V_{kl}^{Te}}{I_l^{Te}} = \frac{1}{I_k^{Te} I_l^{Te}} \sum_{m=1+(k-1)N_m}^{kN_m} \sum_{p=1+(l-1)N_m}^{lN_m} Z_{mp} I_m I_p \quad k, l = 1, 2, \dots, M. \quad (22)$$

Once the terminal impedance matrix  $Z^{Te}$  is determined, the corrected voltage matrix  $v_c$  is readily obtained using

$$v_c = Z^{Te} I^{Te}, \quad (23)$$

where,

$$I^{Te} = [I_1^{Te}, I_2^{Te}, \dots, I_M^{Te}]^T. \quad (24)$$

The actual terminal currents  $I_m^{Te}$  are obtained from equation (4) and are the same as in equation (7).

Note from equation (22) that if there is only one piecewise sinusoidal mode on each dipole, (i.e.  $N_m = 1$ ) then  $Z_{kl}^{Te} = Z_{mn}$ . In other words, if there is only one piecewise sinusoidal mode on each dipole, the terminal impedance matrix reduces to the impedance matrix in equation (4). The mutual coupling effects can then be easily compensated for since this matrix is calculated using equation (5). This is exactly the correction procedure used in [38]. Unfortunately, the current on the antenna element can only be accurately

represented with one mode for half wavelength dipoles that are reasonably far apart [35 pp. 325-327]. For longer dipoles or dipoles that are close together, the current can not be accurately estimated with one mode. Single mode representation is also not possible for the sleeve dipole or the spiral antenna.

## 2.4 Antenna elements

Three antenna elements are used to design antenna arrays that operated over a one octave bandwidth from 200 MHz to 400 MHz. The first element is the dipole with a length of half a meter. This length corresponds to half a wavelength at the center of the operating frequency band. The dipole, however, is inherently a narrow band element since its input impedance varies greatly over the bandwidth of the array as shown in figure 3. The large variation in the input impedance creates a large variation in the reflection coefficient. This means that at the edges of the operating band, large amounts of power will be reflected by the dipole. This limits the use of the dipole to narrow band applications. However, since the radiation pattern of the dipole does not change significantly over the frequency bandwidth, it is still useful for theoretical investigations.

The sleeve dipole is a dipole with two parasitic elements placed very close to it as shown in figure 4. The parasitic elements are referred to as sleeves since they reside very close to the dipole. The effect of the sleeves is to broaden the operating bandwidth of the dipole without significantly affecting its radiation pattern. Referring to figure 4, the parameters of the sleeve dipole are:  $H = 0.513$  meters,  $L = 0.2888$  meters,  $S = 0.051$  meters, and  $D = 0.029$  meters. The wire diameter of the sleeve dipole is significantly larger than that of the ordinary dipole. For the sleeve dipole the wire diameter is 0.029

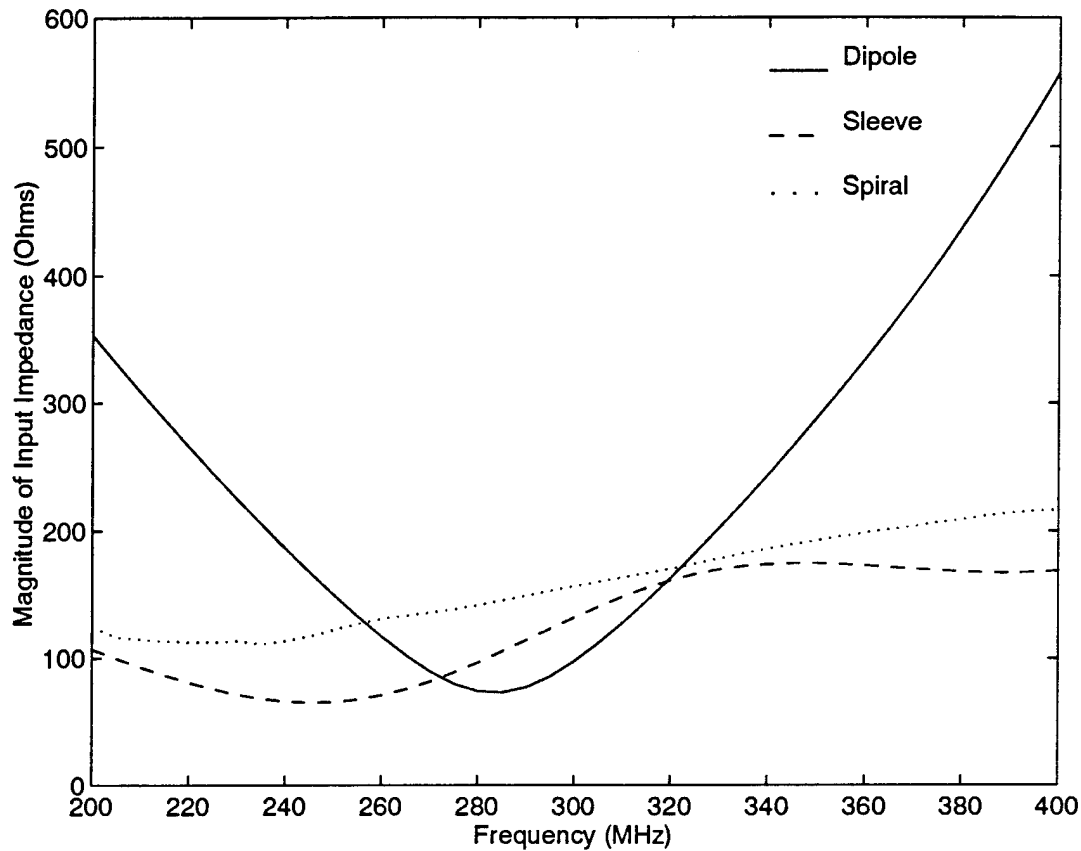


**Figure 3: Input Impedance of Dipole, Sleeve Dipole and Spiral Antennas**

meters while for the dipole described previously the wire diameter is 0.0008 meters. It is necessary to increase the diameter of the dipole to achieve the one octave bandwidth. The sleeve dipole is modeled using three piecewise sinusoids on both the dipole and the sleeves. A detailed discussion of the design of the sleeve dipole can be found in [35].

The variation of the input impedance of the sleeve dipole is shown in figure 3. Notice that the magnitude of the input impedance does not vary nearly as much as that of the dipole. Since its input impedance and radiation pattern do not vary significantly over the one octave bandwidth, the sleeve dipole is a practical broadband element.

The spiral antenna has significant size in two dimensions and is referred to as a

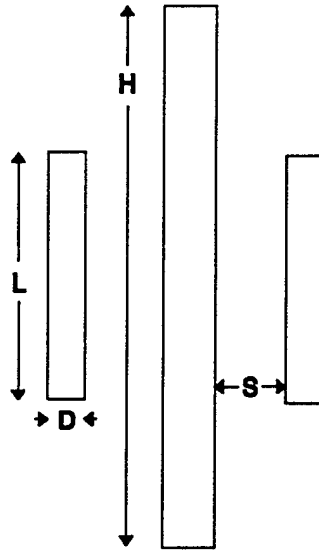


**Figure 4: Sleeve Dipole**

frequency independent antenna since it can be operated over an arbitrarily prescribed bandwidth. A spiral antenna for the operating range of 200 MHz to 400 MHz is shown in figure 5. This antenna is referred to as an archimedean spiral and its design is discussed in [43]. The antenna in figure 5 is described by the equations

$$r = a\phi_1 \quad 4.17 < \phi_1 < 31.6 \quad (25)$$

$$r = a\phi_2 \quad 1.03 < \phi_1 < 28.5 \quad (26)$$

where  $a = 0.072$  meters, and  $r$  is the radial distance from the coordinate origin to a point on the spiral.

To model the spiral antenna with the thin wire method of moments code, the spiral is simulated with 84 straight wire segments as shown in figure 6. This yielded 83 piecewise sinusoidal modes for one spiral. The input impedance of the spiral antenna in

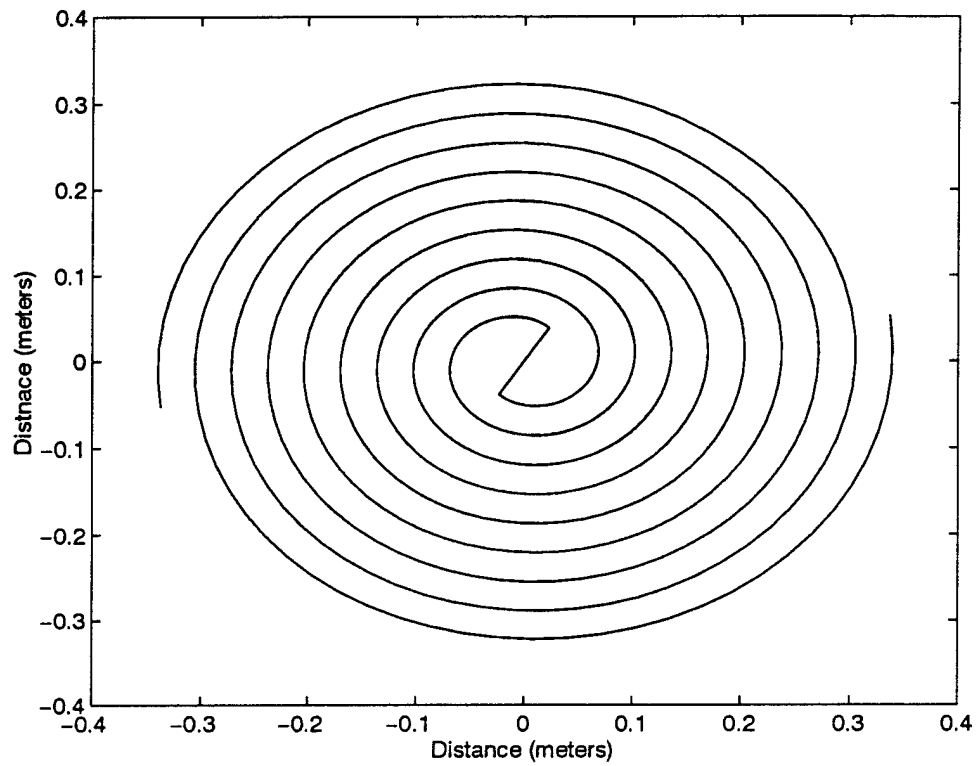


**Figure 5: 200 MHz to 400 MHz Spiral Antenna**

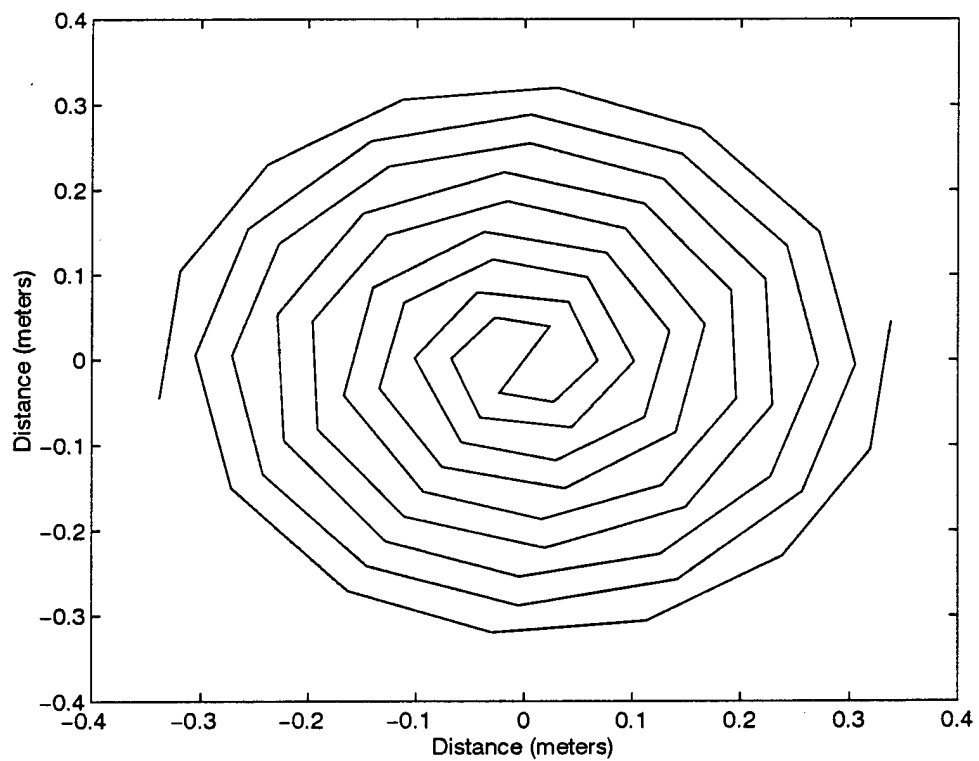


**Figure 6: Segmented Spiral Antenna for the Method of Moments**

figure 6 is shown in figure 3. Notice that the magnitude of the input impedance is very flat indicating the broadband characteristic of the antenna element.

## 2.5 Antenna Arrays

The three antenna elements described in the previous section are formed into linear, cross, and circular arrays. The linear array is useful for resolving angles of incidence over 2 quadrants in one plane while the cross and circular arrays can resolve angles over all four quadrants in one plane. In all cases the arrays are designed to resolve narrow band signals occurring over a one octave bandwidth from 200 MHz to 400 MHz. They are also each composed of nine antenna elements. This requires 27 piecewise sinusoidal modes for the dipole array, 81 modes for the sleeve dipole array, and 747 modes for the spiral array. Each of the array elements are terminated with the complex conjugate of the input impedance. The arrays are illuminated with a vertically polarized plane wave with the electric field vector parallel to the dipole and sleeve dipole elements and in the same plane as the spiral antenna.

The first array is a linear array of dipoles. As stated before, the dipoles are half a wavelength long at 300 MHz. The dipoles are separated by 0.375 meters along the x - axis. This is the largest spacing that does not produce any grating lobes anywhere within the bandwidth of the array. Grating lobes are undesirable since they yield ambiguous angles of arrival.

The linear sleeve dipole array is also arrayed along the x - axis with the dipoles oriented parallel to the z - axis. The view of the sleeve dipole array from the z - axis is shown in figure 7. The dipoles are again separated by 0.375 meters to prevent the



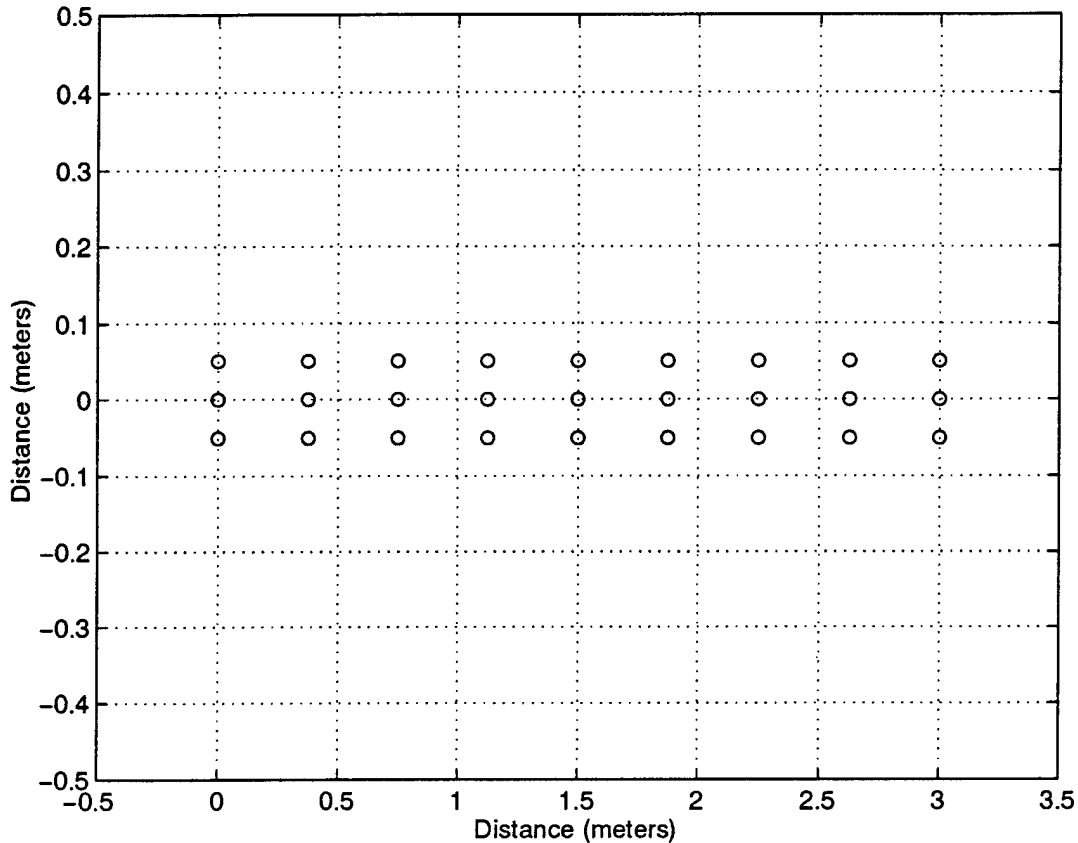


**Figure 7: Linear Sleeve Dipole Array**

formation of grating lobes. As shown in the figure, the sleeves are placed very close to the dipoles as described in section 2.4.

The cross array is capable of resolving angles of arrival over a full  $360^\circ$  [48]. This array is composed of two orthogonal equally spaced linear arrays that share a common element in the middle of each array. This array can be thought of as an unequally spaced, unequally excited linear array. Therefore, there is no clear spacing which does not produce grating lobes. It is found, however, that a spacing of 0.3 meters is sufficient to prevent ambiguous angles of arrival over the entire operating band.

The cross sleeve dipole array is shown in figure 9. This array is the same as the cross array except that it contains sleeves around each element. As shown in figure 8,

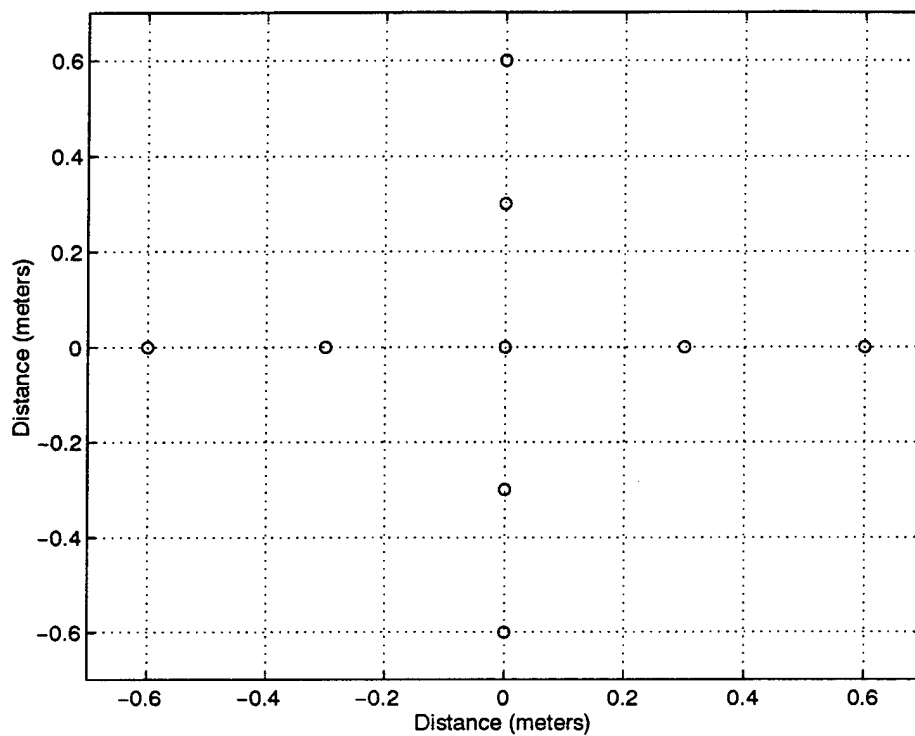
the sleeves are always parallel to the  $y$  - axis.

The circular dipole array and circular sleeve dipole array are also capable of resolving angles of arrival over a full  $360^\circ$ . These arrays are shown in figures 10 and 11. They are also modeled using an unequally spaced, unequally excited linear array [47]. It is found that ambiguous angles of arrival could be avoided with an array radius of 0.375 meters.

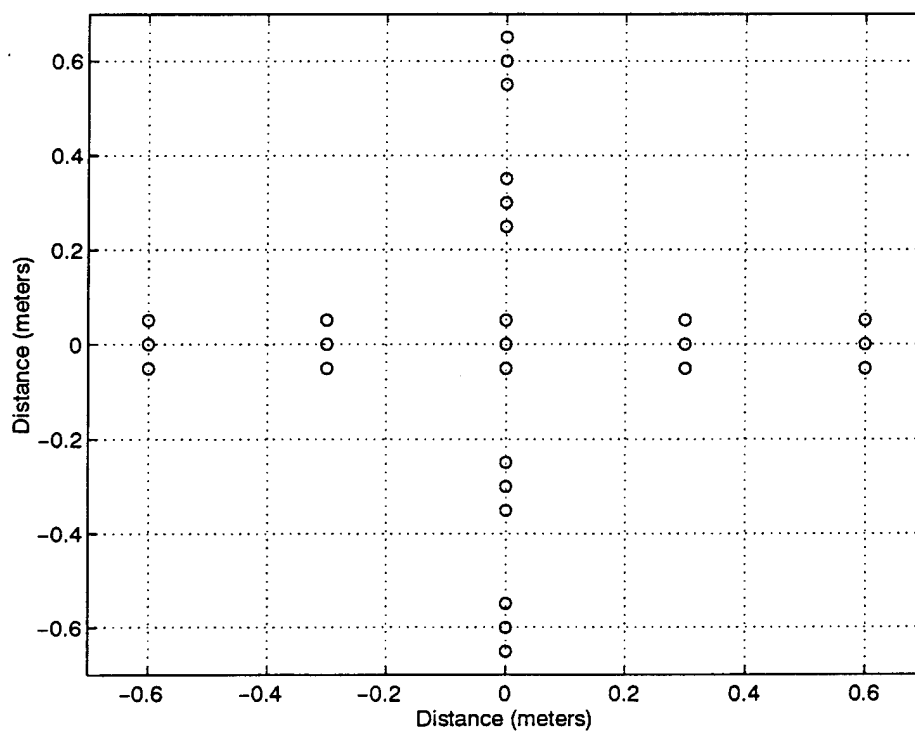
The spiral element is only used in a linear array configuration. Unfortunately, because of the significant size of the spiral, it is impossible to array the elements such that the element spacing is less than half a wavelength for all frequencies within the operating bandwidth. Therefore, grating lobes are unavoidable and produce ambiguous angles of arrival. This prevents the spiral from being used in an array to resolve angles of arrival over a frequency range of 200 MHz to 400 MHz even though the spiral can be successfully operated over this frequency bandwidth.

## 2.6 Computer Simulations

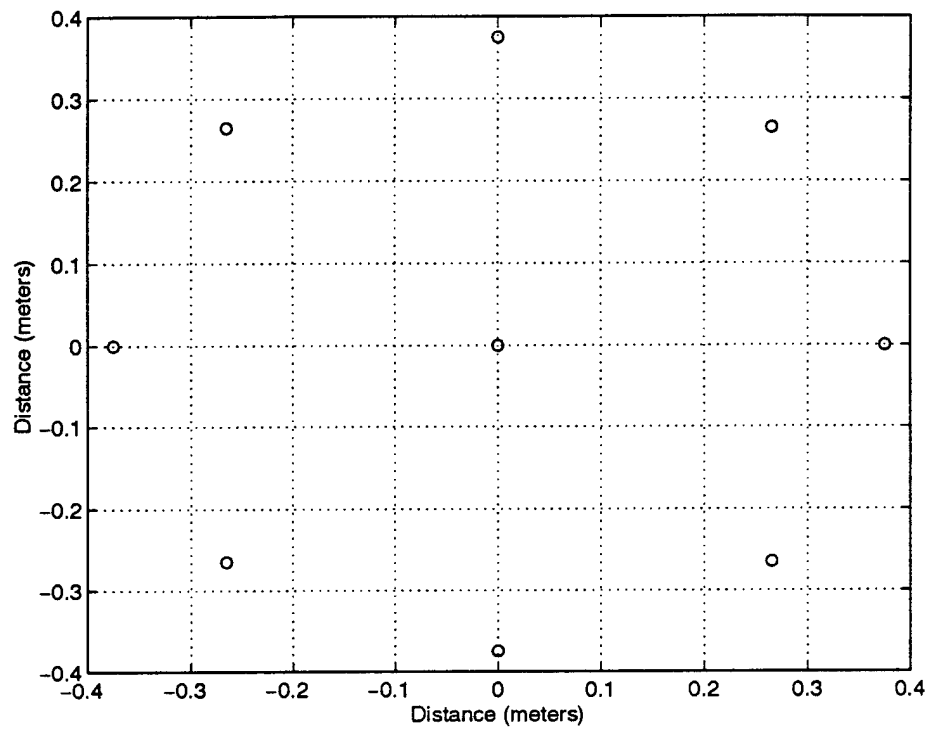
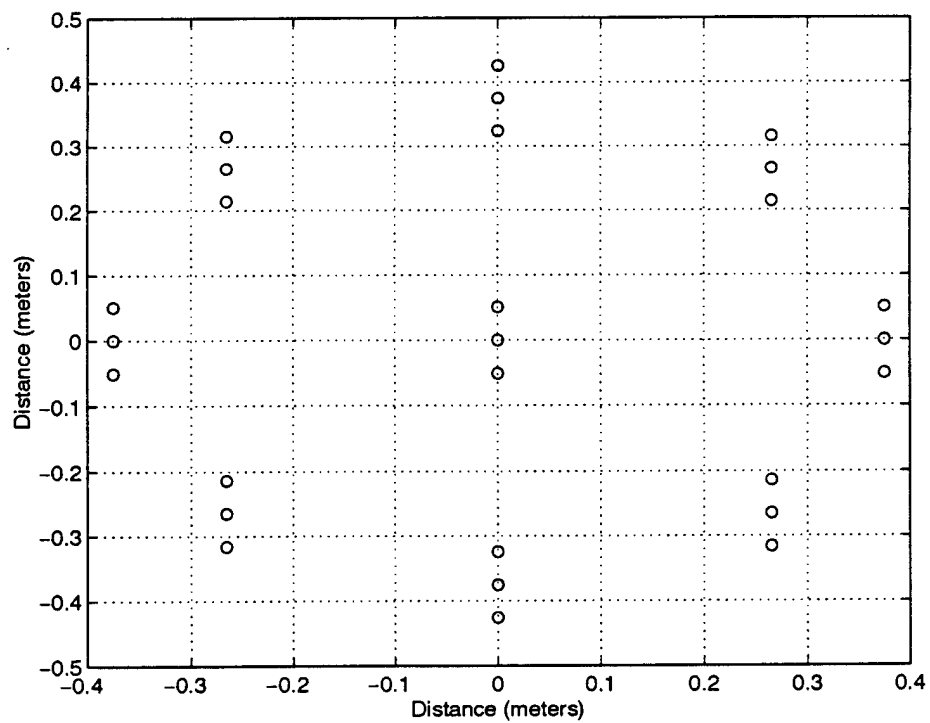
The effect of mutual coupling on direction finding algorithms is investigated by examining the spectrum of four different direction finding algorithms with three different signals. The ideal signal from equation (1) is used to determine the best possible spectrum under the given conditions. This signal assumes that there is no mutual coupling between the antenna elements. The "actual" signal from equation (8) is used to determine the effects of mutual coupling on the spatial spectrum. The corrected signal from equation (23) is used to determine the improvement in the spatial spectrum when the mutual coupling between the antenna elements is taken into account.



**Figure 8: Cross Dipole Array**



**Figure 9: Cross Sleeve Dipole Array**

**Figure 10: Circular Dipole Array****Figure 11: Circular Sleeve Dipole Array**

The ideal, actual, and corrected signals were applied to each of the arrays in section 2.5. The spectrum is calculated with the Beamformer, Capon's, linear prediction, and MUSIC algorithms to determine the effects of the correction procedure on the direction finding algorithm. These four algorithms are described in detail in appendices A through D.

The mutual coupling effects are analyzed by considering one array with  $K$  uncorrelated plane waves. This is shown graphically in figure 12 for a linear array. For the actual linear array described in section 2.5,  $d_n = 0.375 + d_{n-1}$  and  $d_1 = 0.0$  for  $n = 2, 3, \dots, M$ .

In all the simulations two non-coherent, single frequency, equal power sources in the far field of the antenna array are used to determine the effects of mutual coupling on the resolution capabilities of the algorithms. This implies that the signals are narrowband plane waves when they are incident upon the array. This also implies that the amplitude of the signal across the array is approximately constant. The sources are also assumed to be ergodic so that their statistics can be calculated with one realization of the signal. The signals are each composed of 300 snapshots of data taken at 1 GHz. This sampling frequency is well above the Nyquist rate for all frequencies within the operational bandwidth of the array. The two signals are offset by 5 MHz so that they would not be coherent which is necessary for the MUSIC algorithm. The signal to noise ratio is fixed at 10 dB where the signal power is the sum of the power in each of the two signals. The noise at each of the antenna elements is zero and Gaussian. The noise sources are uncorrelated and therefore are also independent since they are Gaussian. The

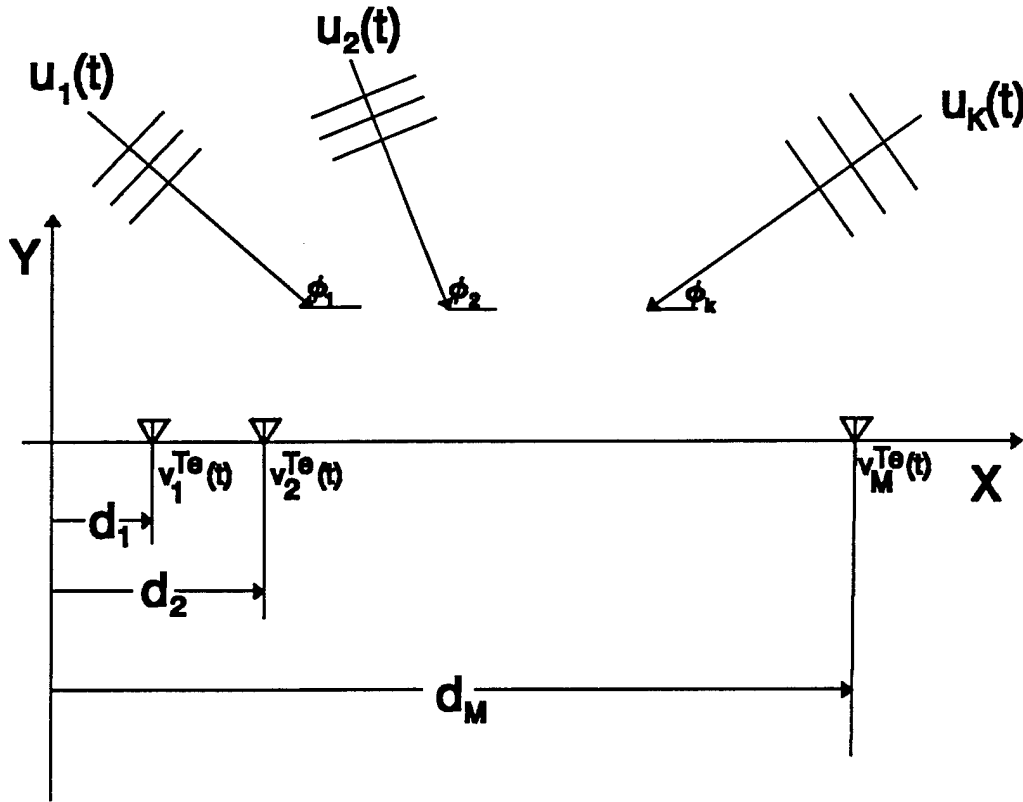


Figure 12: Geometry of Array and Sources

calculations assume that temporal filtering is done prior to the spatial filtering. Therefore, the signals in the spatial spectrum have approximately the same frequency but are not coherent. The spectra shown are a normalized average of 20 simulations computed every  $0.1^\circ$ . The covariance matrix for the two signals is estimated using the "covariance method" which produces an unbiased positive semi-definite matrix [46]. This matrix is used to compute all the spectra for each of the direction finding algorithms.

### 2.6.1 Beamformer Algorithm

The beamformer algorithm computes the spectrum by scanning the main beam of the antenna pattern. While this algorithm is very simple, its resolution capability is the

worst of the four algorithms and is limited by the Rayleigh criterion [46]. The spectrum for this algorithm is given by

$$P(\phi) = a(\phi)^H R a(\phi) \quad (27)$$

where  $R$  is the covariance matrix and  $a(\phi)$  is the search vector given by the expression

$$a(\phi) = \left[ e^{j\beta(x_1 \cos \phi + y_1 \sin \phi)} \dots e^{j\beta(x_M \cos \phi + y_M \sin \phi)} \right]^T \quad (28)$$

In equation (28)  $(x_M, y_M)$  is the location of the  $M^{\text{th}}$  antenna element and  $\phi$  is the search angle. This algorithm is robust with respect to mutual coupling. Its performance is also unaffected if the signals are coherent. The beamformer algorithm is described in detail in Appendix A.

The resolution of the algorithm is dependent upon both the angle of incidence and the frequency of operation. This can be shown by examining the beamwidth of the radiation pattern. The beamwidth between first nulls (BWFN) in the antenna pattern of a long equally spaced linear array where the length of the array is much larger than a wavelength is [35, pp. 128-129].

$$BWFN = \frac{2\lambda}{Nd} \quad (\text{near } \phi = 90^\circ) \quad (29)$$

and

$$BWFN = 2\sqrt{\frac{2\lambda}{Nd}} \quad (\text{near } \phi = 0^\circ, \text{ and } 180^\circ). \quad (30)$$

where  $\lambda$  is the wavelength,  $N$  is the number of elements in the array, and  $d$  is the spacing between elements. Notice that the beamwidth increases as the antenna is scanned away from broadside. Since the Rayleigh criterion requires that the peaks in the main beam for two signals be separated by at least a half a beamwidth, the resolution capability decreases as the antenna is scanned toward endfire. Notice also from equations (29) and (30) that the BWFN increases as the wavelength increases. Therefore, the resolution capability improves as the frequency is increased. This is clearly evident in the Beamformer spectra in figures 13 through 24.

Figures 13 and 14 show the spectra for the linear dipole array at the upper and lower frequency limits of the operational bandwidth. Notice that in both figures, the ideal and corrected spectra are virtually identical. Notice that the actual signal with mutual coupling yields angles of arrival that are actually slightly closer to the true angles of arrival than the ideal and corrected spectra. In this case, the mutual coupling causes destructive interference which has the effect of moving the signals farther apart. Notice also the resolution capability of the algorithm is clearly better at the upper frequency.

The spectra for the linear sleeve dipole array are shown in figures 15 and 16. Notice that the results are about identical to the dipole array in figures 13 and 14. This occurs because the beamformer algorithm is rather robust with regards to mutual coupling. The added mutual coupling due to the sleeves has very little effect upon the beamformer



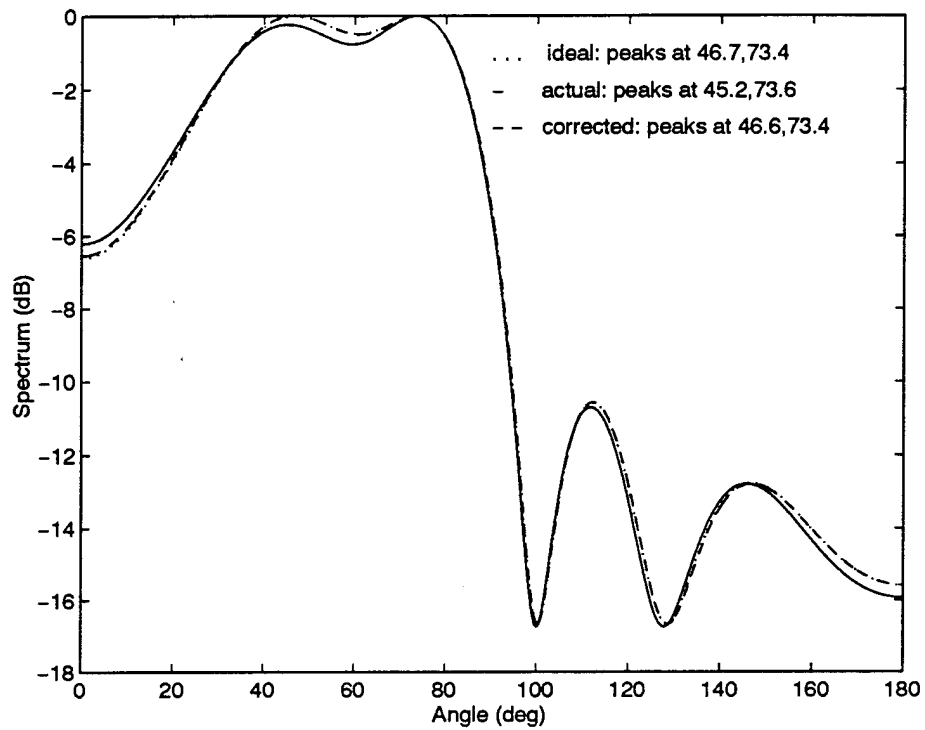


**Figure 13: Beamformer, Linear Dipole Array, Angles = 45°, 75°,  
Frequencies = 200, 205 MHz**

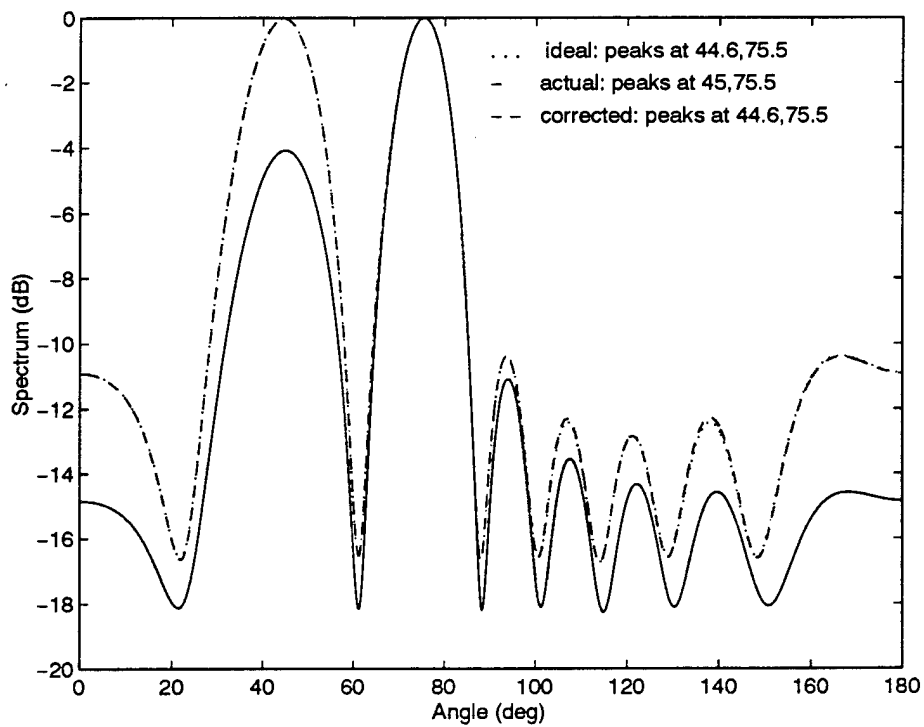


**Figure 14: Beamformer, Linear Dipole Array, Angles = 45°, 75°,  
Frequencies = 395, 400 MHz**

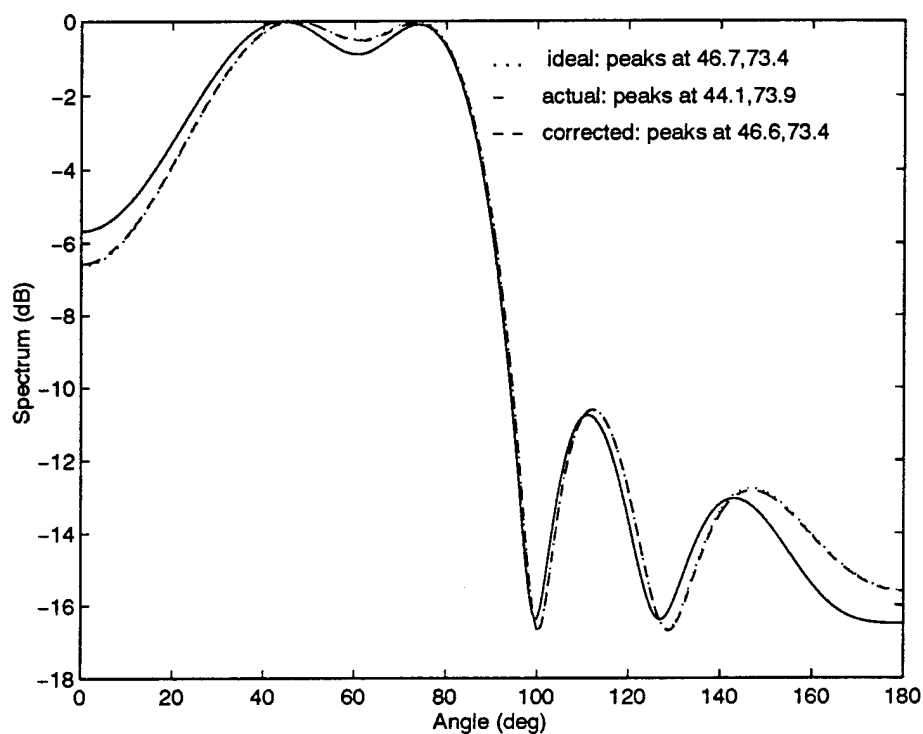


**Figure 15: Beamformer, Linear Sleeve Dipole Array, Angles = 45°, 75°,  
Frequencies = 200, 205 MHz**

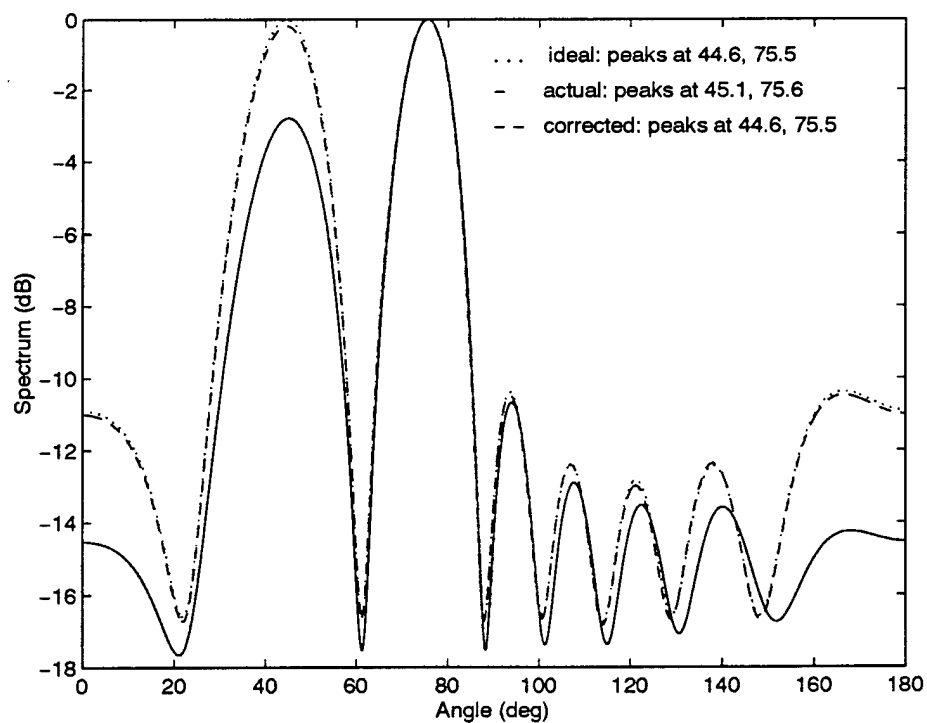


**Figure 16: Beamformer, Linear Sleeve Dipole Array, Angles = 45°, 75°,  
Frequencies = 395, 400 MHz**

spectrum.

The spectra for the cross dipole and cross sleeve dipole array are shown in figures 17 through 20. Notice that in figure 17, the mutual coupling prevents the algorithm from resolving the two signals. At the upper frequency in figure 18, the signals are clearly resolvable. Notice, however, that the angle estimates with mutual coupling present are actually slightly better than without mutual coupling. This is again due to the destructive interference of mutual coupling. The spectra for the cross sleeve dipole array in figures 19 and 20 are almost identical to the cross dipole array. Again, this is due to the fact that the added mutual coupling due to the sleeves has very little effect on the performance of the algorithm.

The spectra for the circular dipole array are shown in figures 21 and 22. Notice that in figure 21 the circular array is unable to resolve the signals with mutual coupling but is just able to resolve the signals for the ideal and corrected signals. At the upper frequency in figure 22, the signals are clearly resolvable since the resolution capability of the algorithm is better.

The results for the circular sleeve dipole array are shown in figures 23 and 24. In figure 23 the mutual coupling causes the estimated angles of arrival to be much closer to the actual angles than the ideal or corrected signals. Again, this is due to the mutual coupling effects. In figure 24 at the upper frequency, the signals are clearly resolvable with and without mutual coupling.

The results presented for the Beamformer algorithm are summarized in Table 1. Notice that in almost all cases the mutual coupling has very little effect on the spectrum.

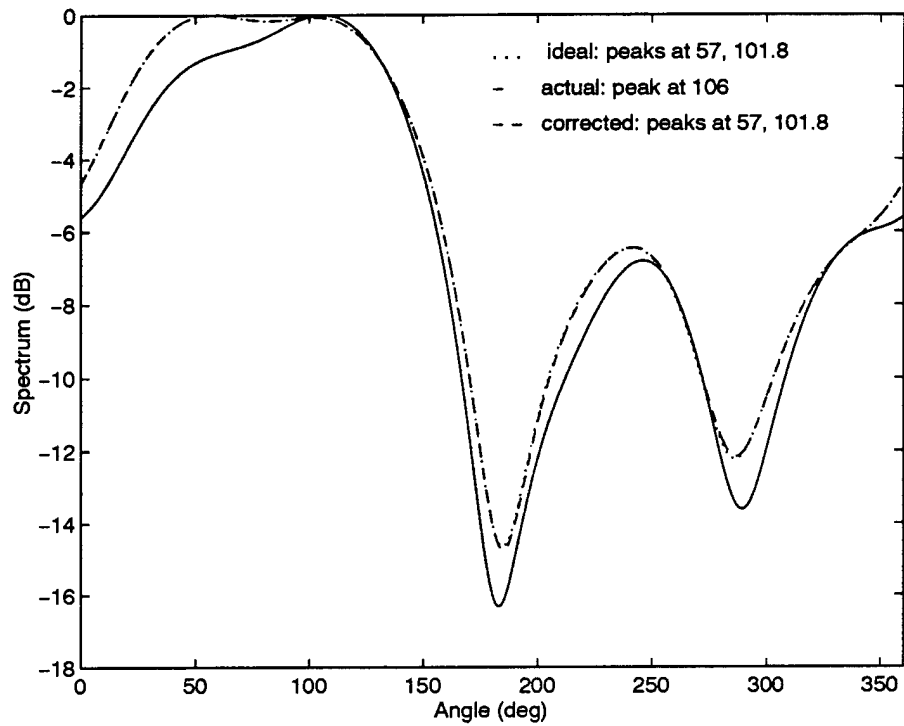


Figure 17: Beamformer, Cross Dipole Array, Angles =  $45^\circ$ ,  $110^\circ$ ,  
Frequencies = 200, 205 MHz

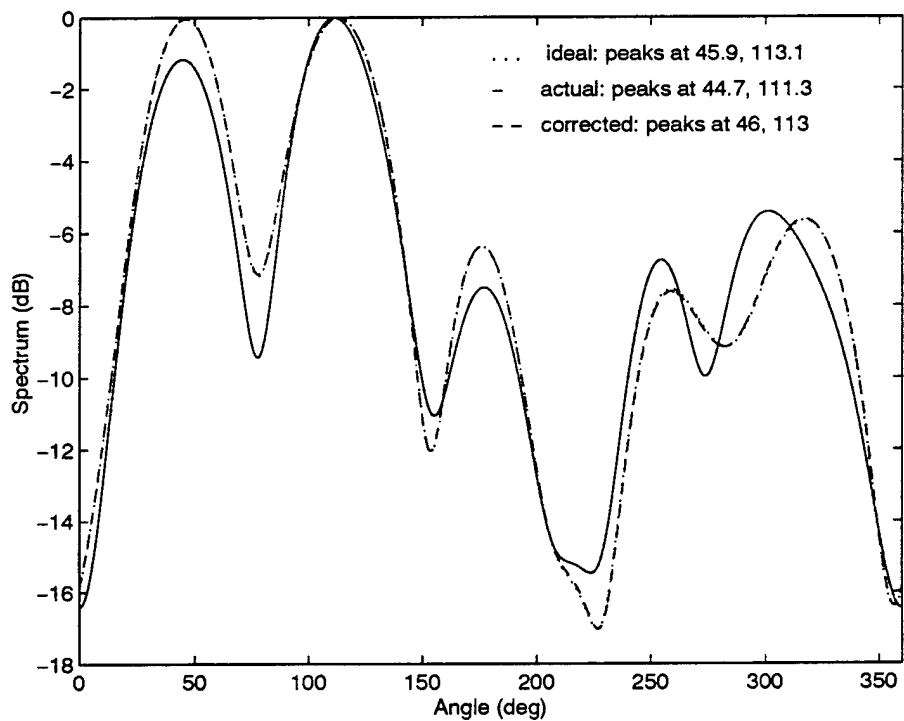
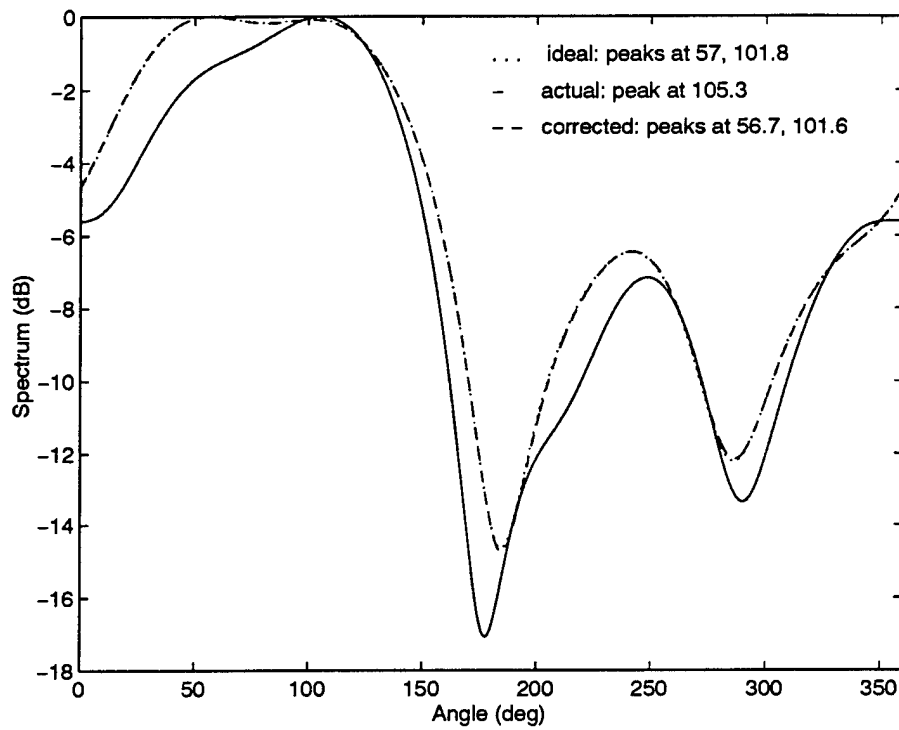
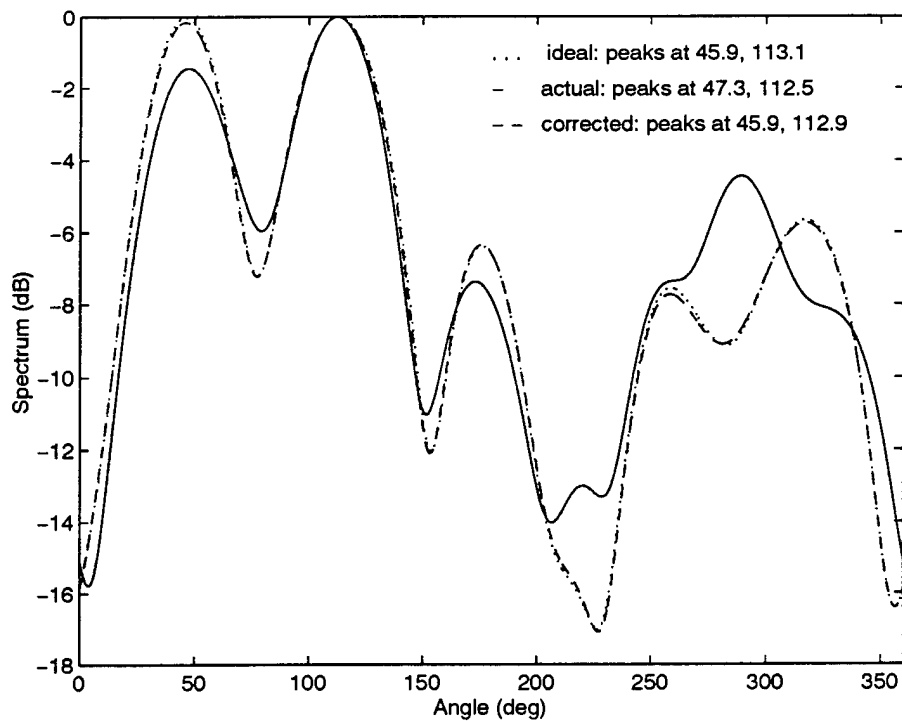


Figure 18: Beamformer, Cross Dipole Array, Angles =  $45^\circ$ ,  $110^\circ$ ,  
Frequencies = 395, 400 MHz



**Figure 19: Beamformer, Cross Sleeve Dipole Array, Angles =  $45^\circ$ ,  $110^\circ$ ,  
Frequencies = 200, 205 MHz**



**Figure 20: Beamformer, Cross Sleeve Dipole Array, Angles =  $45^\circ$ ,  $110^\circ$ ,  
Frequencies = 395, 400 MHz**

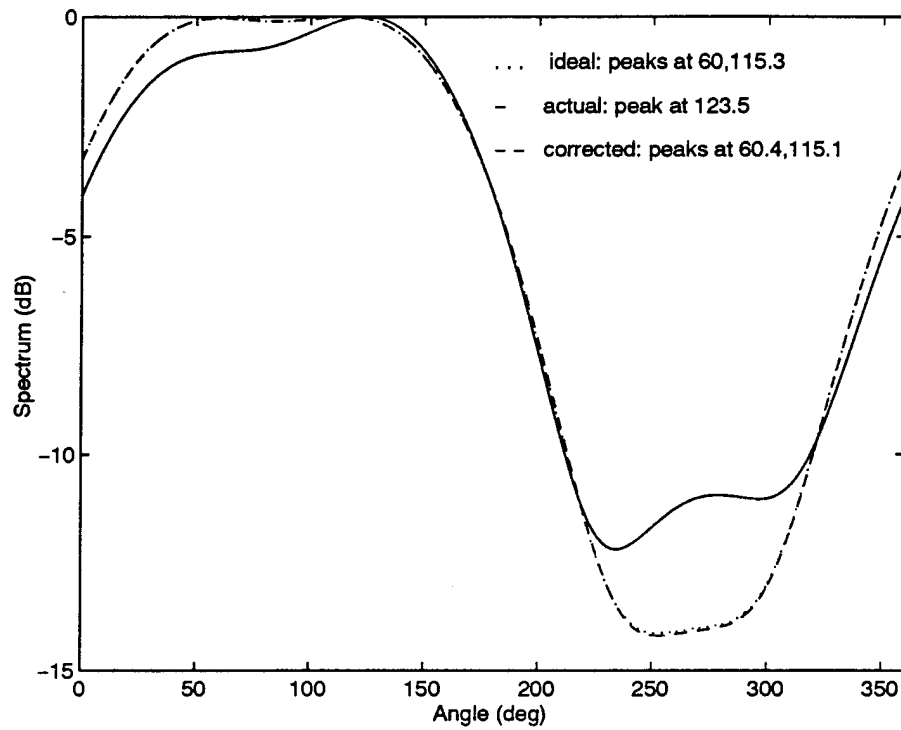


**Figure 21: Beamformer, Circular Dipole Array, Angles = 45°, 130°,  
Frequencies = 200, 205 MHz**

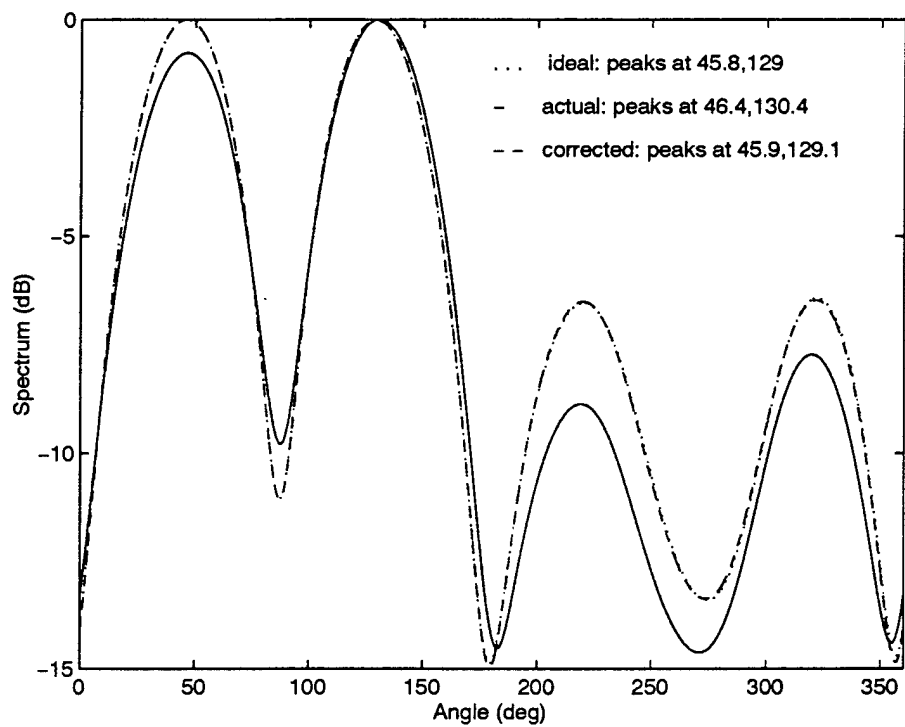


**Figure 22: Beamformer, Circular Dipole Array, Angles = 45°, 130°,  
Frequencies = 395, 400 MHz**

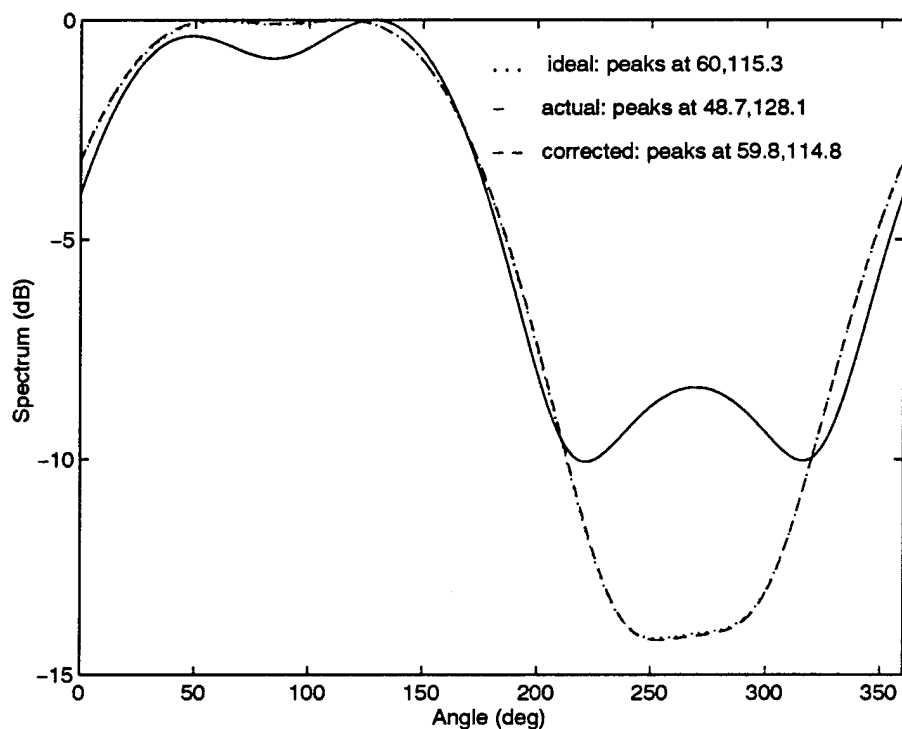


**Figure 23: Beamformer, Circular Sleeve Dipole Array, 45°, 130°, Frequencies = 200, 205 MHz**

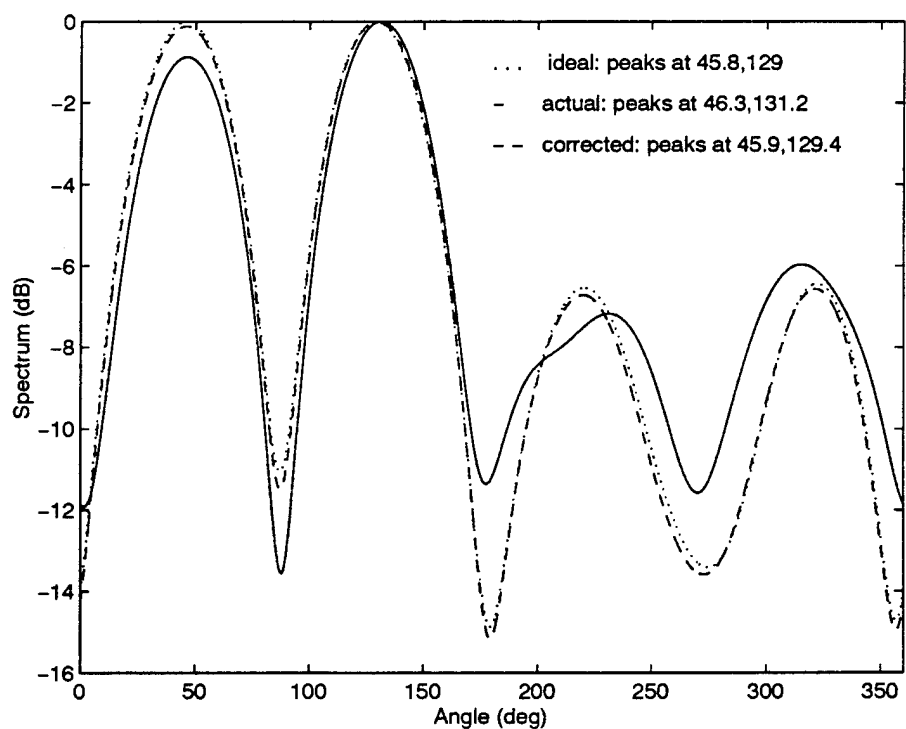


**Figure 24: Beamformer, Circular Sleeve Dipole Array, Angles = 45°, 130°, Frequencies = 395, 400 MHz**

Therefore, once this coupling is removed, the improvement in the spectrum is also very small. In some cases, as in figure 22, the actual signal with the mutual coupling actually yields angles of arrival closer to the true angles.



**Table 1: Beamformer Algorithm, SNR = 10 dB**

Array	Freq (MHz)	Angle (deg)	Ideal (deg)	Actual (deg)	Corrected (deg)
Linear Dipole	200, 205	45.0, 75.0	46.7, 73.4	45.2, 73.6	46.6, 73.4
Linear Dipole	395, 400	45.0, 75.0	44.6, 75.5	45.0, 75.5	44.6, 75.5
Linear Sleeve Dipole	200, 205	45.0, 75.0	46.7, 73.4	44.1, 73.9	46.6, 73.4
Linear Sleeve Dipole	395, 400	45.0, 75.0	44.6, 75.5	45.1, 75.6	44.6, 75.5
Cross Dipole	200, 205	45.0, 110.0	57.0, 101.8	106.0	57.0, 101.8
Cross Dipole	395, 400	45.0, 110.0	45.9, 113.1	44.7, 111.3	46.0, 113.0
Cross Sleeve Dipole	200, 205	45.0, 110.0	57.0, 101.8	105.3	56.7, 101.6
Cross Sleeve Dipole	395, 400	45.0, 110.0	45.9, 113.1	47.3, 112.5	45.9, 112.9
Circular Dipole	200, 205	45.0, 130.0	60.0, 115.3	123.5	60.4, 115.1
Circular Dipole	395, 400	45.0, 130.0	45.8, 129	46.4, 130.4	45.9, 129.1
Circular Sleeve Dipole	200, 205	45.0, 130.0	60.0, 115.3	48.7, 128.1	59.8, 114.8
Circular Sleeve Dipole	395, 400	45.0, 130.0	45.8, 129	46.3, 131.2	45.9, 129.4

### 2.6.2 Capon's Algorithm

In this section the effects of mutual coupling and the compensation procedure are investigated with Capon's algorithm. This algorithm is also referred to as the "Maximum Likelihood" method or the "Minimum Variance Distortionless Response" method because it is designed to minimize the output power subject to the constraint that the output equals unity at the observation angle [5,46]. The spectrum for this method is computed with the equation

$$P(\phi) = \frac{1}{\mathbf{a}(\phi)^H \mathbf{R}^{-1} \mathbf{a}(\phi)} \quad (31)$$

where  $\mathbf{R}^{-1}$  is the inverse of the covariance matrix and  $\mathbf{a}(\phi)$  is the search vector given in equation (28). This algorithm is described in detail in Appendix C.

Figures 25 and 26 show the spectra for Capon's algorithm at the lower and upper frequency limits of the operational bandwidth of the array. Notice from figure 25 that at the lower frequency limit, the signals can not be resolved even in the ideal case. In figure 26 it is clear that at the upper frequency limit, the signals can be resolved regardless of whether mutual coupling is considered in the analysis although the ideal and corrected spectra yield a better estimate of the actual angles of arrival.

The spectra for the linear sleeve dipole are shown in figures 27 and 28. The results are virtually the same as that of the linear dipole array in figures 25 and 26 with the exception that the actual signal in figure 28 with mutual coupling present contains a peak at  $46.7^\circ$  which is slightly farther away from the true angle of arrival than for the

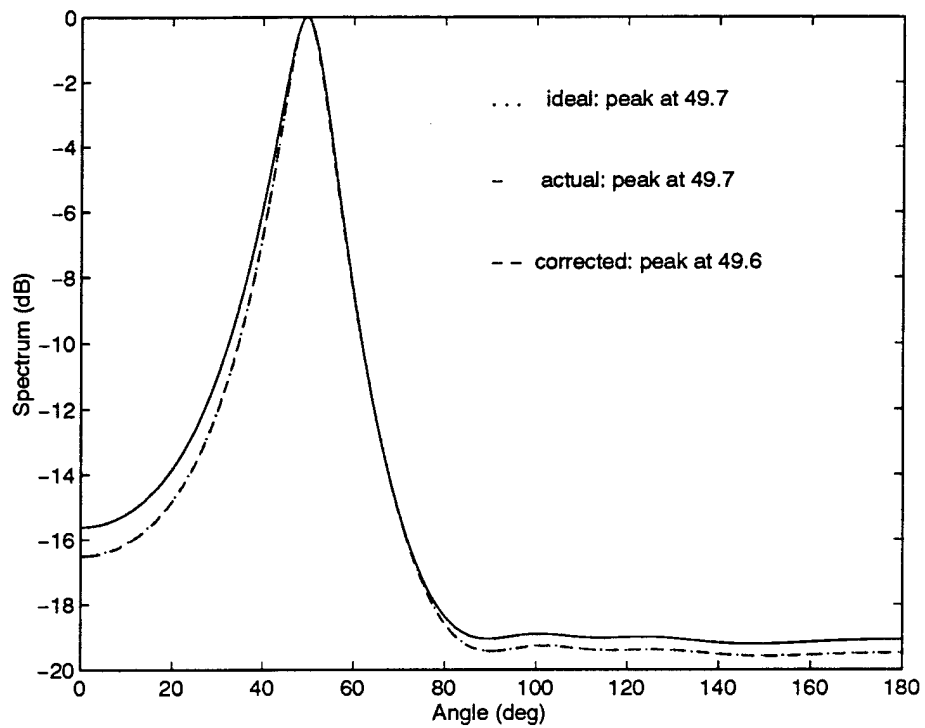


**Figure 25: Capon, Linear Dipole Array, Angles = 45°, 55°,  
Frequencies = 200, 205 MHz**

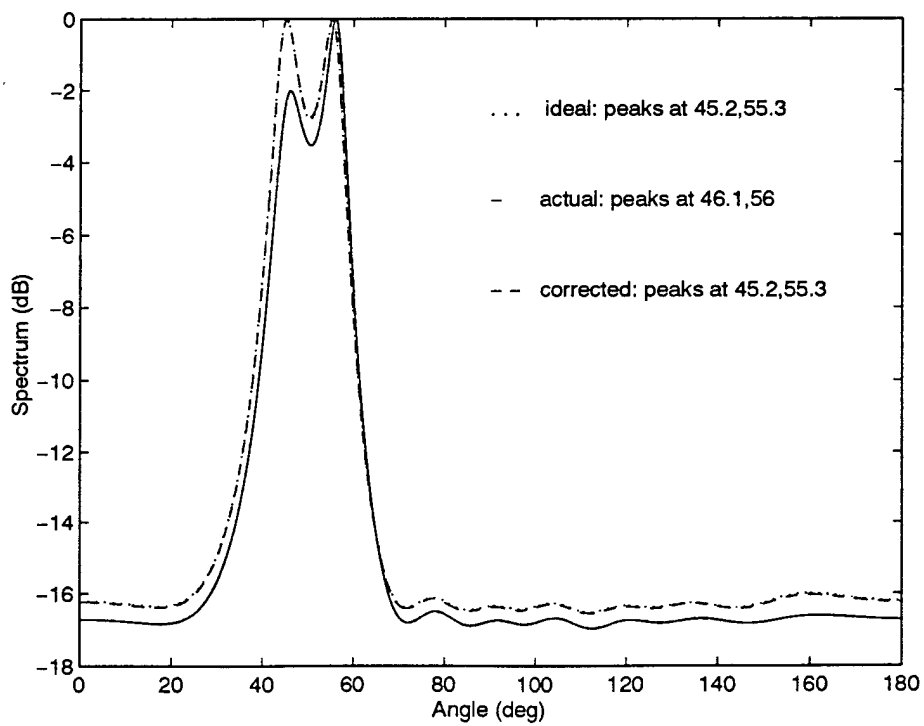


**Figure 26: Capon, Linear Dipole Array, Angles = 45°, 55°,  
Frequencies = 395, 400 MHz**

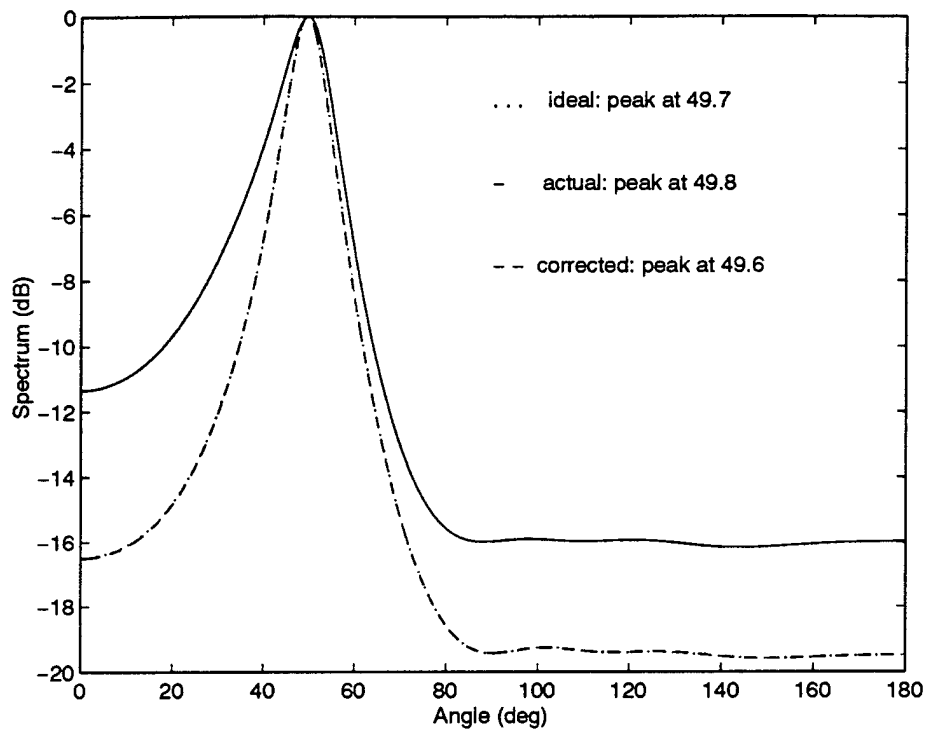


**Figure 27: Capon, Linear Sleeve Dipole Array, Angles = 45°, 55°,  
Frequencies = 200, 205 MHz**

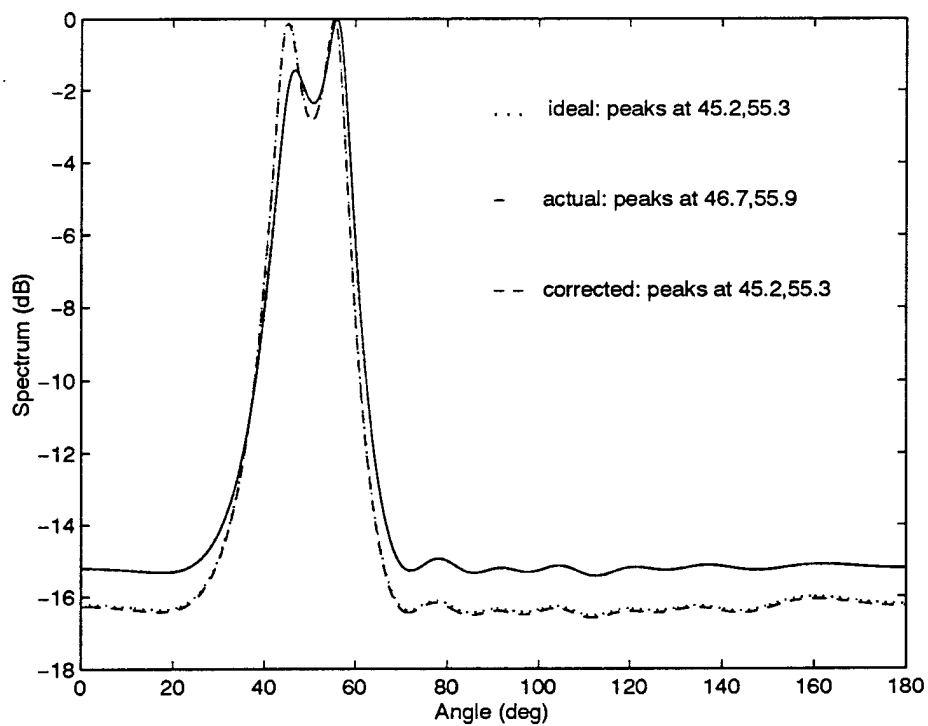


**Figure 28: Capon, Linear Sleeve Dipole Array, Angles = 45°, 55°,  
Frequencies = 395, 400 MHz**

linear dipole array in figure 26.

Figures 29 and 30 show the results for the cross dipole array. In figure 29, the signals can not be resolved even for the ideal case. At the upper frequency in figure 30 the signals can be resolved. The corrected spectrum in figure 30 yields a better estimate of the angles of arrival than the actual signal with mutual coupling.

The spectra for the cross sleeve dipole array are shown in figures 31 and 32. As before, Capon's algorithm is unable to resolve the two angles at the lower frequency limit. Figure 32 shows that the mutual coupling prevents the algorithm from resolving the two signals at the upper frequency limit. This is due to the added mutual coupling from the sleeves since the same case did yield two signals for the cross array as shown in figure 30.

Figures 33 and 34 show the spectrum for the circular dipole array. At the lower frequency limit, the signals are not resolvable as shown in figure 33. In figure 34, the signals can be separated. Notice, however, that for the circular array, the mutual coupling causes the signals to deviate away from each other instead of appears as one signal.

Figures 35 and 36 show the results for the circular sleeve dipole array. Again, at the lower frequency limit in figure 35, the signals are not resolvable. At the upper frequency, the mutual coupling due to the sleeves causes the two signals to appear as one rather than two well separated signals as in figure 34.

The results for Capon's algorithm are summarized in Table 2. Note that the calculated angles of arrival for the ideal and corrected cases are almost identical. This is because the spectra for the ideal and corrected signals in figures 25 through 36 are

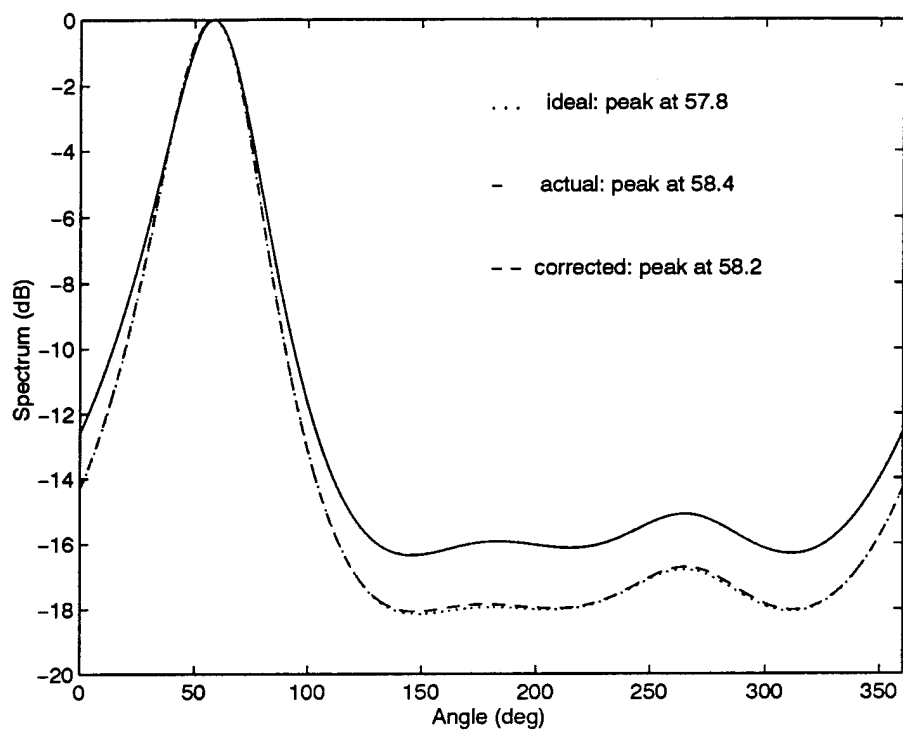


**Figure 29: Capon, Cross Dipole Array, Angles =  $45^\circ$ ,  $70^\circ$ ,  
Frequencies = 200, 205 MHz**

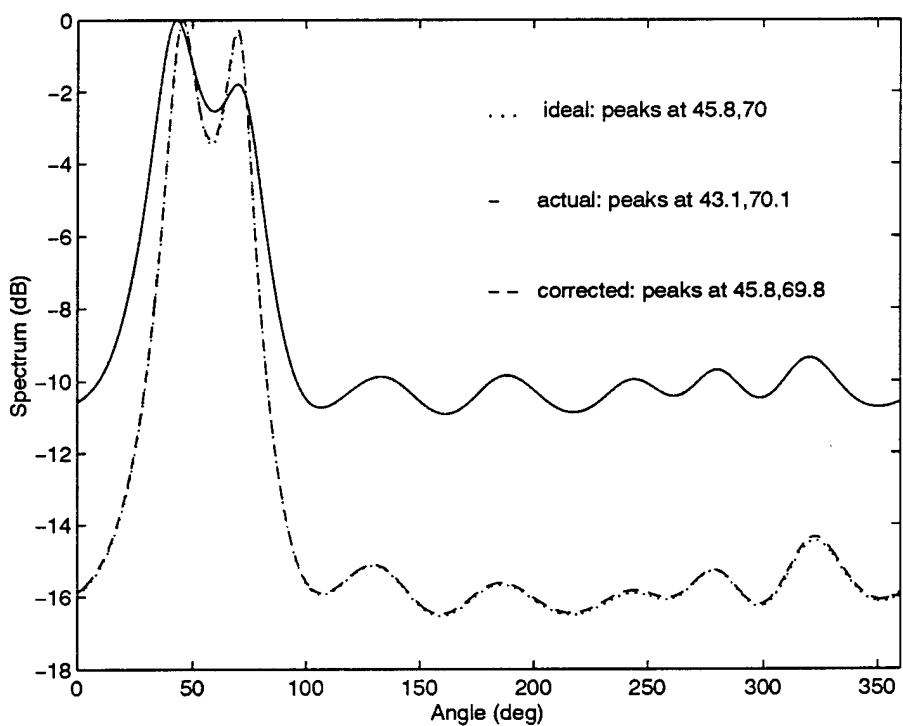


**Figure 30: Capon, Cross Dipole Array, Angles =  $45^\circ$ ,  $70^\circ$ ,  
Frequencies = 395, 400 MHz**

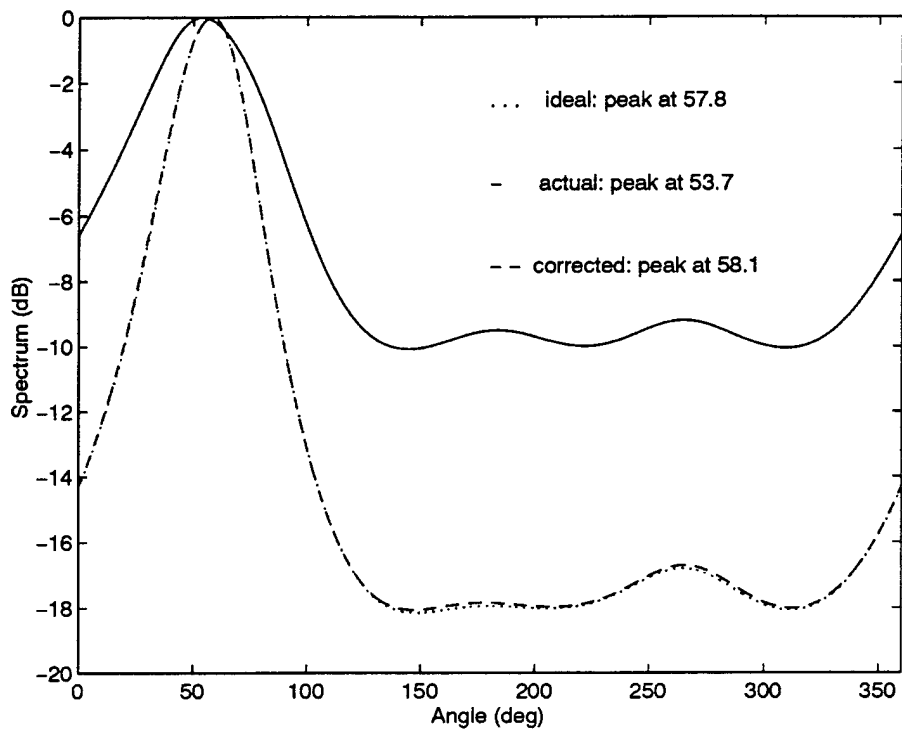


**Figure 31: Capon, Cross Sleeve Dipole Array, Angles =  $45^\circ$ ,  $70^\circ$ ,  
Frequencies = 200, 205 MHz.**

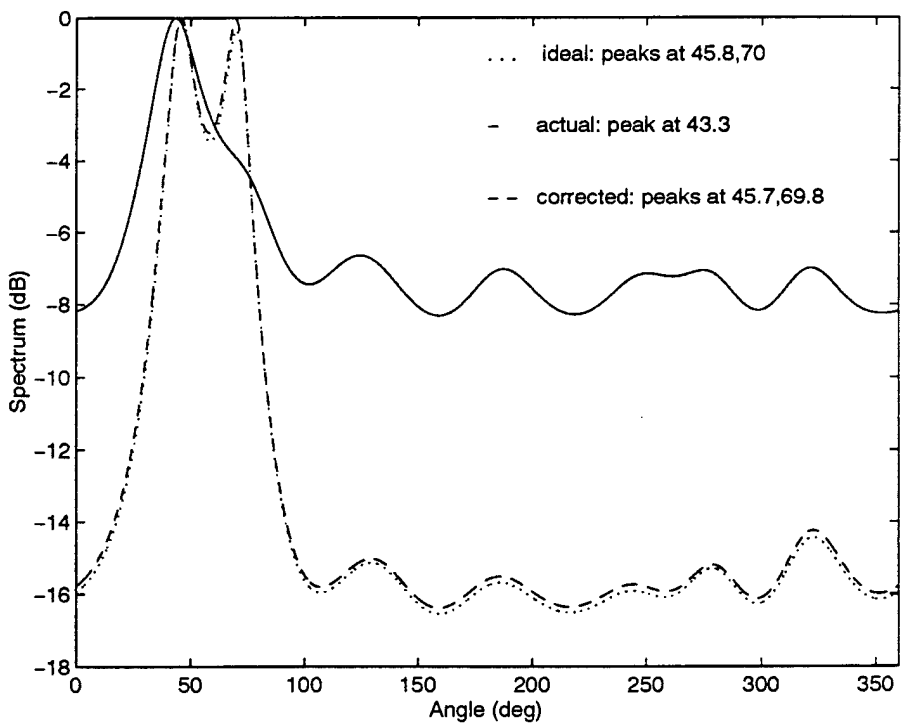


**Figure 32: Capon, Cross Sleeve Dipole Array, Angles =  $45^\circ$ ,  $70^\circ$ ,  
Frequencies = 395, 400 MHz**

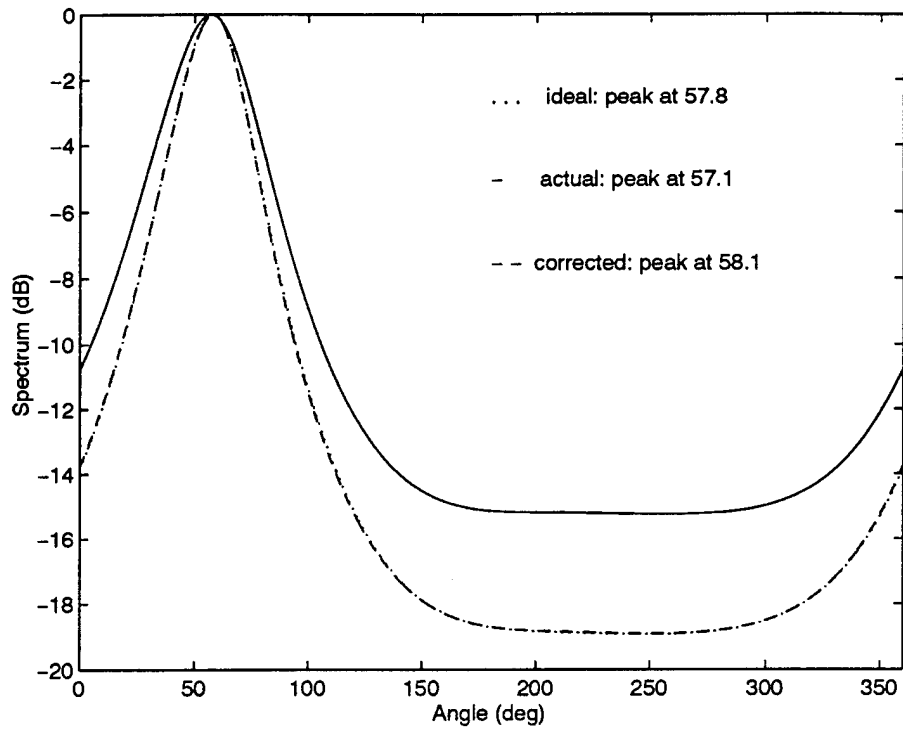


**Figure 33: Capon, Circular Dipole Array, Angles =  $45^\circ$ ,  $70^\circ$ ,  
Frequencies = 200, 205 MHz**

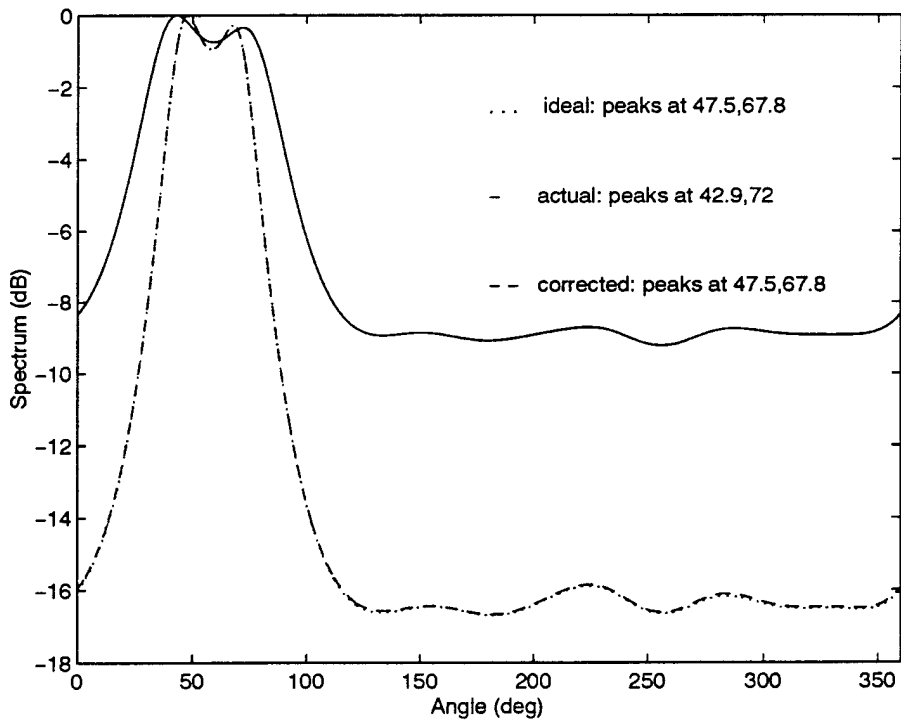


**Figure 34: Capon, Circular Dipole Array, Angles =  $45^\circ$ ,  $70^\circ$ ,  
Frequencies = 395, 400 MHz**



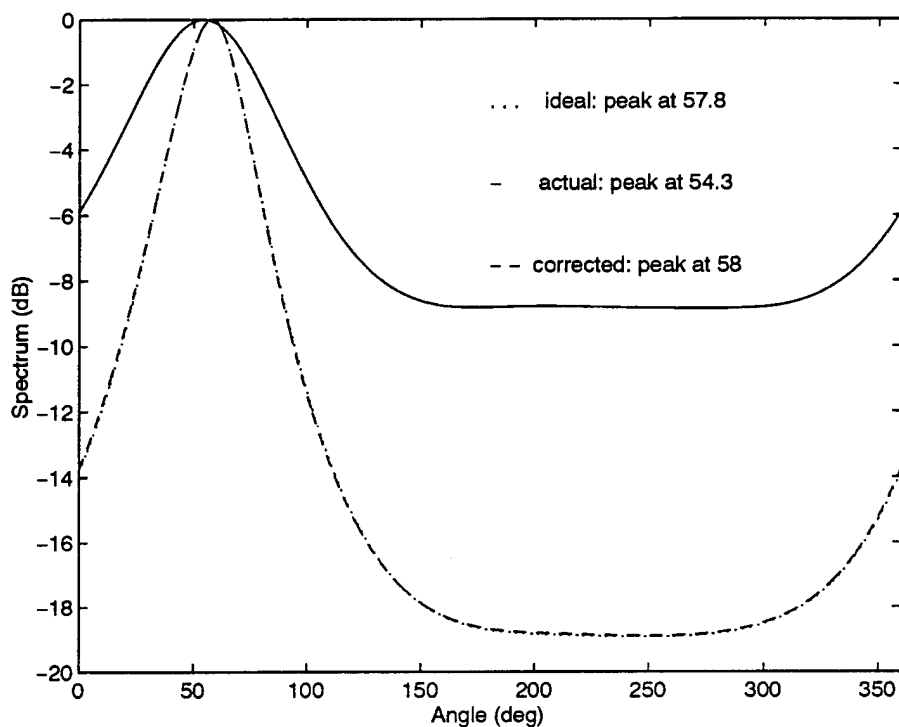


**Figure 35: Capon, Circular Sleeve Dipole Array, Angles =  $45^\circ$ ,  $70^\circ$ ,  
Frequencies = 200, 205 MHz**

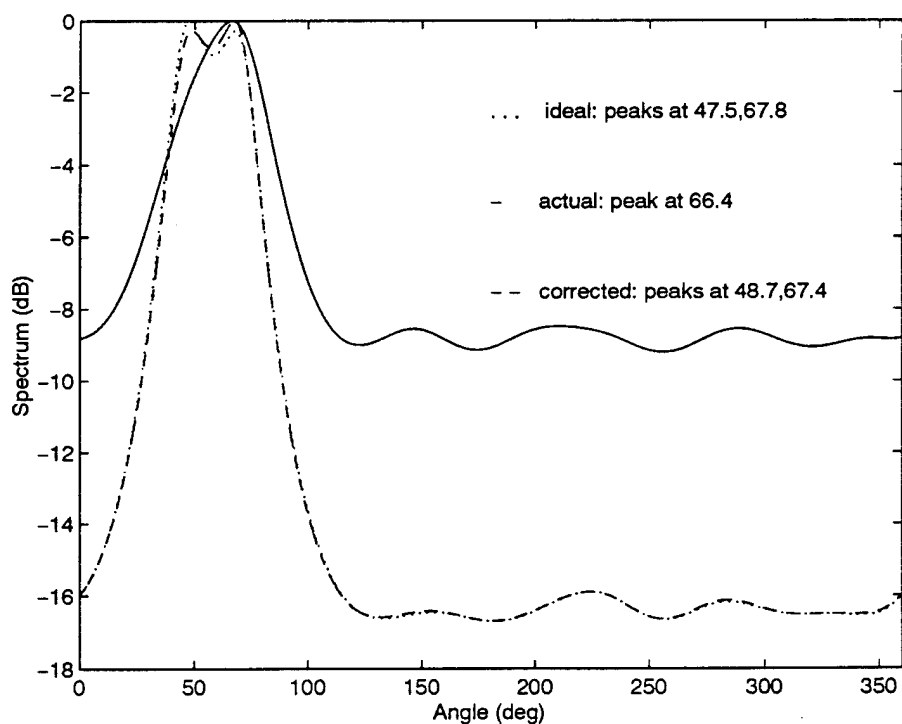


**Figure 36: Capon, Circular Sleeve Dipole Array, Angles =  $45^\circ$ ,  $70^\circ$ ,  
Frequencies = 395, 400 MHz**

almost exactly the same.

**Table 2: Capon's Algorithm, SNR = 10 dB**

Array	Freq (MHz)	Angle (deg)	Ideal (deg)	Actual (deg)	Corrected (deg)
Linear Dipole	200, 205	45.0, 55.0	49.7	49.7	49.6
Linear Dipole	395, 400	45.0, 55.0	45.2, 55.3	46.1, 56.0	45.2, 55.3
Linear Sleeve Dipole	200, 205	45.0, 55.0	49.7	49.8	49.6
Linear Sleeve Dipole	395, 400	45.0, 55.0	45.2, 55.3	46.7, 55.9	45.2, 55.3
Cross Dipole	200, 205	45.0, 70.0	57.8	58.4	58.2
Cross Dipole	395, 400	45.0, 70.0	45.8, 70.0	43.1, 70.1	45.8, 69.8
Cross Sleeve Dipole	200, 205	45.0, 70.0	57.8	53.7	58.1
Cross Sleeve Dipole	395, 400	45.0, 70.0	45.8, 70.0	43.3	45.7, 69.8
Circular Dipole	200, 205	45.0, 70.0	57.8	57.1	58.1
Circular Dipole	395, 400	45.0, 70.0	47.5, 67.8	42.9, 72.0	47.5, 67.8
Circular Sleeve Dipole	200, 205	45.0, 70.0	57.8	54.3	58.0
Circular Sleeve Dipole	395, 400	45.0, 70.0	47.5, 67.8	66.4	48.7, 67.4

### 2.6.3 Linear Prediction

The linear prediction algorithm for spectrum estimation is described in detail in Appendix D. This technique attempts to estimate the spectrum by predicting one of the antenna element's outputs as a linear combination of the other elements. The coefficients used in the linear combination are chosen so that the mean square error of the predicted element is minimized. The resulting spectrum in this case is given by the equation

$$P(\phi) = \frac{1}{\mathbf{a}(\phi)^H \mathbf{A} (\mathbf{A}^H \mathbf{A})^{-1} \mathbf{A}^H \mathbf{a}(\phi)} \quad (32)$$

$$\text{where } \mathbf{A} = \mathbf{R}^{-1} \begin{bmatrix} 1 \\ 0 \\ 0 \\ \vdots \\ 0 \end{bmatrix} \quad (33)$$

$\mathbf{R}^{-1}$  is the inverse of the covariance matrix, and  $\mathbf{a}(\phi)$  is the search vector given by equation (28).

Figures 37 and 38 show the spectra for the linear dipole array. In figure 37 the ideal signal yields a spectrum with two peaks that are approximately the same amplitude. This causes the appearance of only one peak while actually two peaks exist. The spectrum for the actual signal shows two very sharp peaks close to each other. Although these peaks could be said to correspond to the two signals, it is more likely that one peak is splitting into two peaks. This phenomenon is known as peak splitting or spectral line splitting (SLS) and is due to the estimate of the covariance matrix [49]. In particular, it is due to a biased covariance matrix and a second term in the covariance estimate which is phase dependent [49]. If the biased covariance matrix is replaced by an unbiased

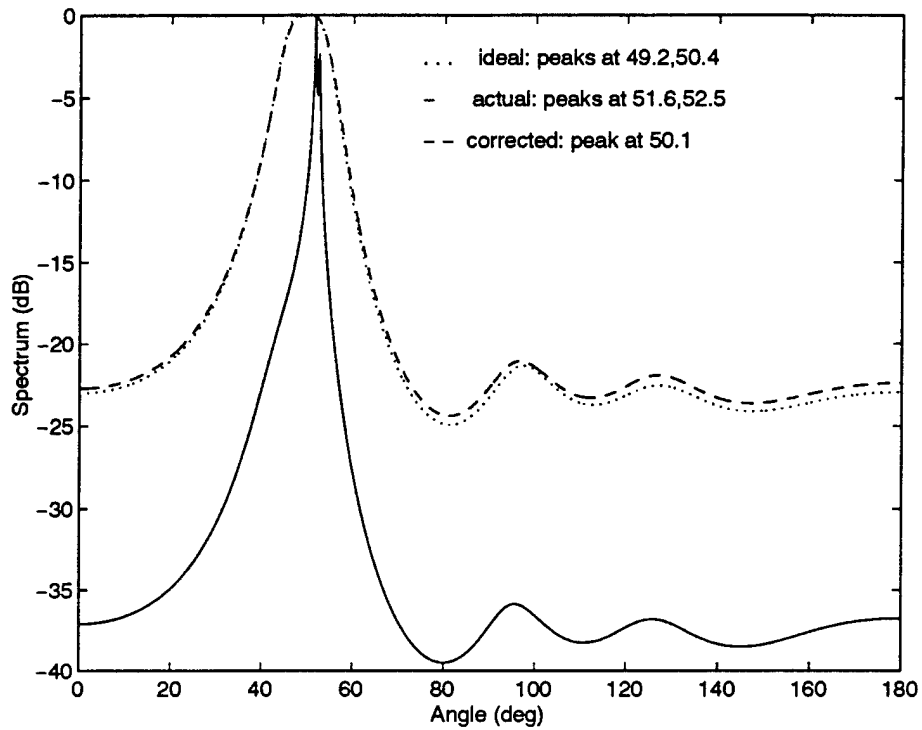


**Figure 37: Linear Prediction, Linear Dipole Array, Angles =  $45^\circ$ ,  $55^\circ$   
Frequencies = 200, 205 MHz**

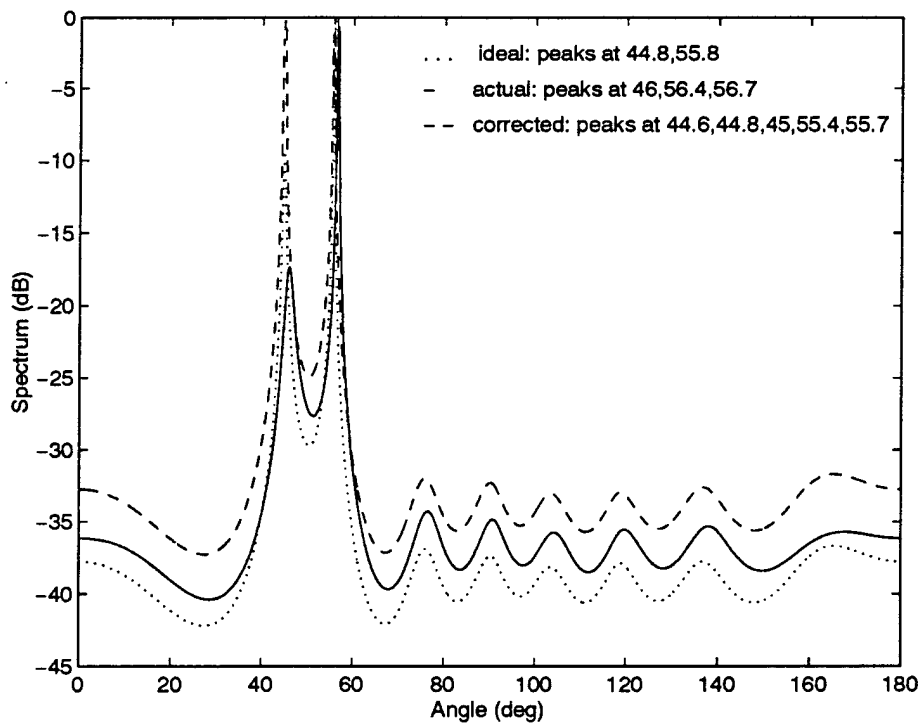


**Figure 38: Linear Prediction, Linear Dipole Array, Angles =  $45^\circ$ ,  $55^\circ$ ,  
Frequencies = 395, 400 MHz**

matrix, SLS still occurs for some initial phases [49]. Kay and Marple suggest using the Least Squares approach to remedy the problem for multiple sources [49]. However, even the least squares approach is not immune to SLS [55]. In figure 38, the ideal, actual, and corrected spectra yield angles of arrival that are very close to the true angles of arrival. Notice, however, that the actual and corrected spectra show more than two peaks. It is shown later that this peak splitting also occurs, in some cases, for the ideal spectrum.

Figures 39 and 40 show the spectra for the linear sleeve dipole array. Again, the ideal spectrum in figure 39 contains two peaks of approximately the same amplitude. This makes the two peaks appear as one. The actual and corrected spectra only show one peak approximately half way between the angles of arrival. In figure 40, all three spectra yield peaks at approximately the angles of arrival. The corrected spectrum, however, contains an extra peak due to peak splitting.

The spectra for the cross dipole array are shown in figures 41 and 42. Notice that the spectrum for the ideal signal in figure 41 suffers from peak splitting. The mutual coupling causes the spectrum from the actual signal to yield only one angle of arrival while the corrected signal yields a spectrum with two angles of arrival. At the upper frequency limit, all three spectra suffer from peak splitting. The spectra all show at least four angles of arrival when only two signals are present. Notice also that the peaks in the spectrum with mutual coupling move away from rather than toward each other as in previous cases. While the corrected spectrum shows the most peaks, all the peaks are very close to the true angles of arrival.

Figures 43 and 44 show the spectra for the cross sleeve dipole array. Note that

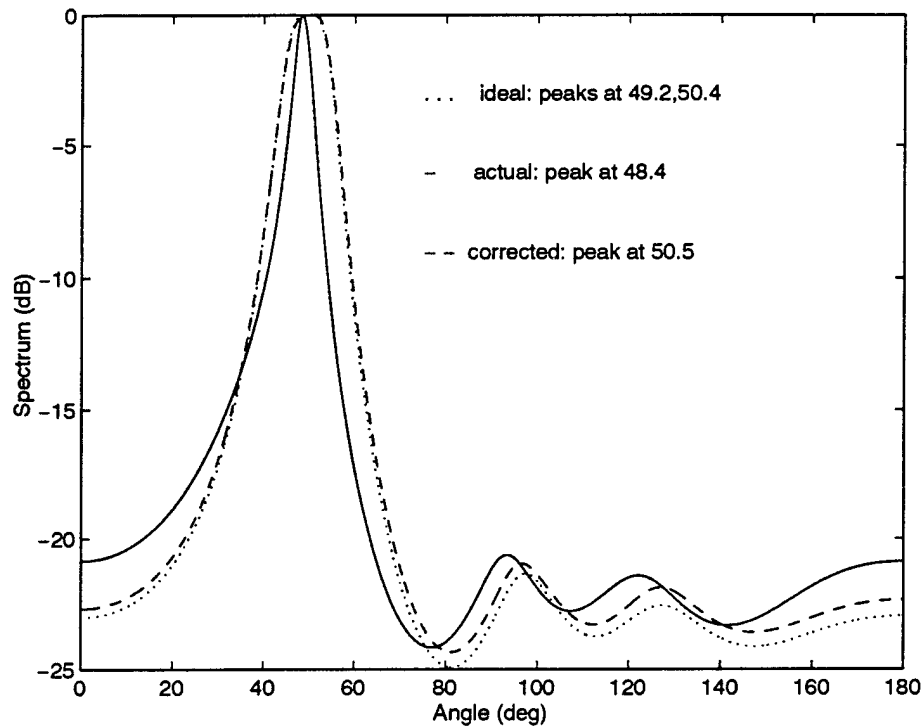


**Figure 39: Linear Prediction, Linear Sleeve Dipole Array, Angles = 45°, 55°, Frequencies = 200, 205 MHz**

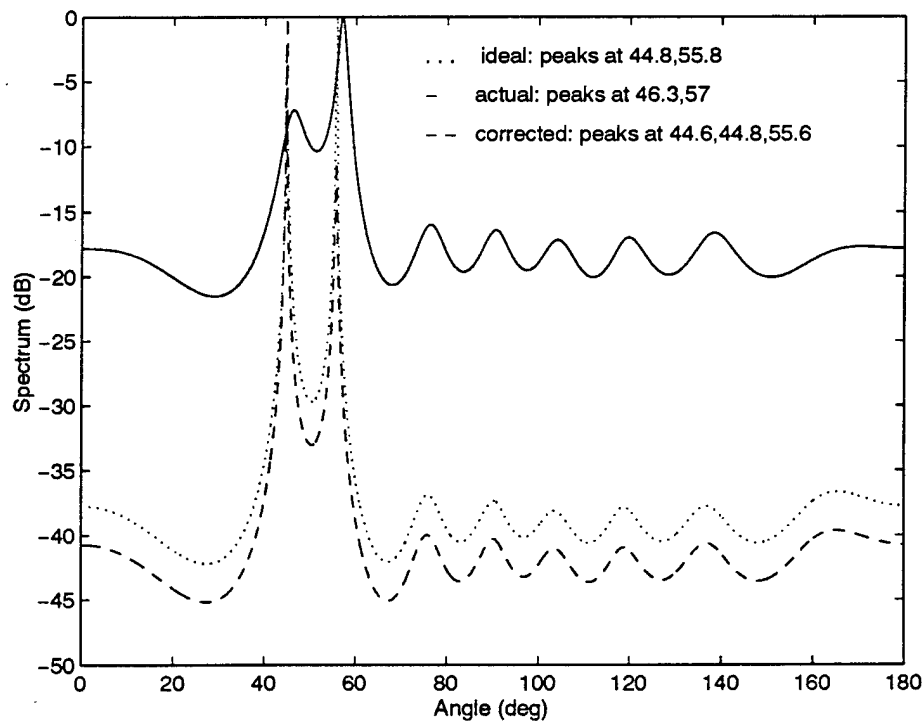


**Figure 40: Linear Prediction, Linear Sleeve Dipole Array, Angles = 45°, 55°, Frequencies = 395, 400 MHz**

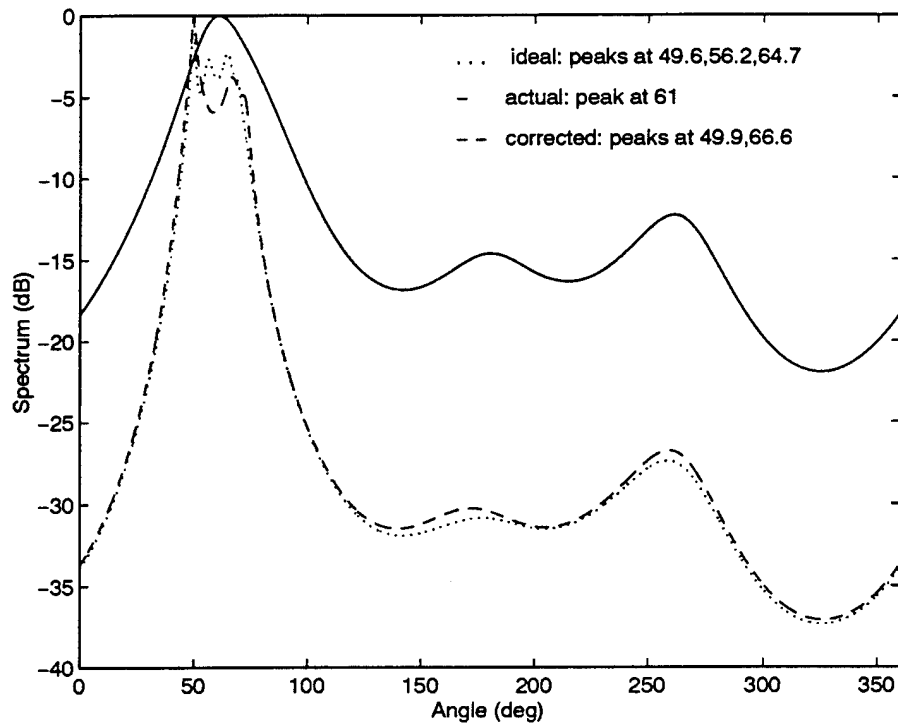


**Figure 41: Linear Prediction, Cross Dipole Array, Angles = 45°, 70°, Frequencies = 200, 205 MHz**

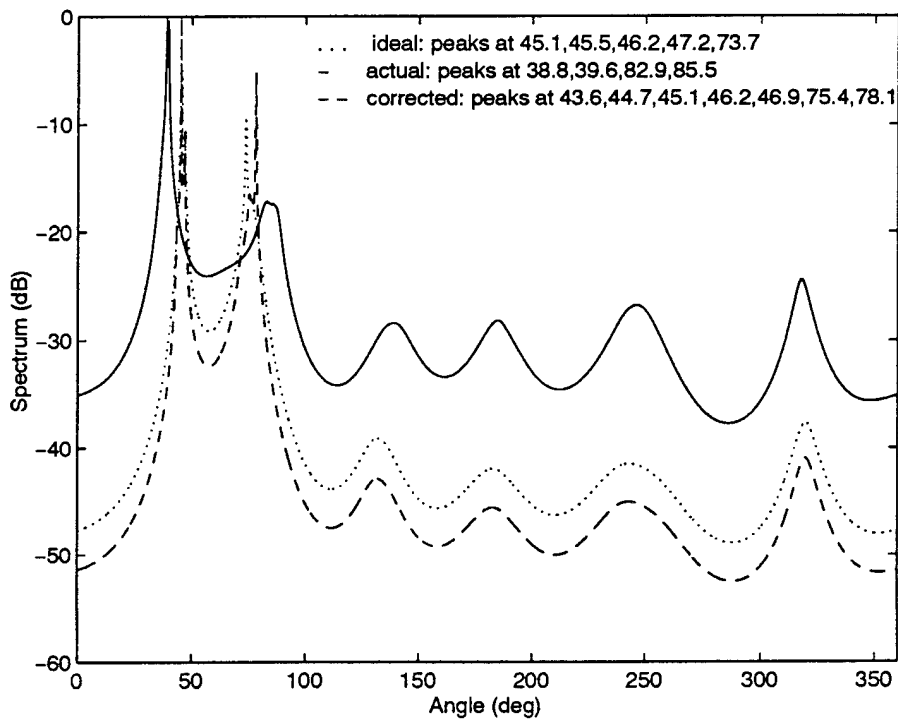


**Figure 42: Linear Prediction, Cross Dipole Array, Angles = 45°, 70° Frequencies = 395, 400 MHz**



figure 43 is very similar to figure 41 except that the estimated angle of arrival with the actual signal is much farther away from the true signals. At the upper end of the bandwidth in figure 44, all three spectra suffer severely from peak splitting.

The spectra for the circular dipole array are shown in figures 45 and 46. Notice in figure 45, that the mutual coupling causes the two signals to appear as one. In this case while both the ideal and corrected signals yield very similar spectra, they both suffer from peak splitting. Figure 46 shows the spectra at the upper frequency. Notice in this case that the corrected signal yields peaks in the spectrum that are closer to the actual angles of arrival than the ideal case. The actual signal with mutual coupling again yields a spectrum with multiple angles of arrival that are well separated from each other.

The spectra for the circular sleeve dipole array are shown in figures 47 and 48. In figure 47 the mutual coupling causes the two signals to appear as one while the ideal and corrected signals suffer from peak splitting. In figure 48, the mutual coupling again causes the signals to appear as one but in this case the angles of arrival appear far away from each other as in figure 43. Both the ideal and corrected signals yield spectra with the angles of arrival close to the true angles of arrival although both suffer from peak splitting.

The results for the linear prediction algorithm are summarized in Table 3. The mutual coupling consistently caused the spectra to yield angles of arrival much different than the true angles of arrival. Sometimes the mutual coupling causes the two signals to appear as one as in figures 47 and 48 while in other cases it caused the calculated angles of arrival to be farther apart than the true signals. In almost all cases the spectra suffered

from peak splitting which produced more angles of arrival than are actually present.

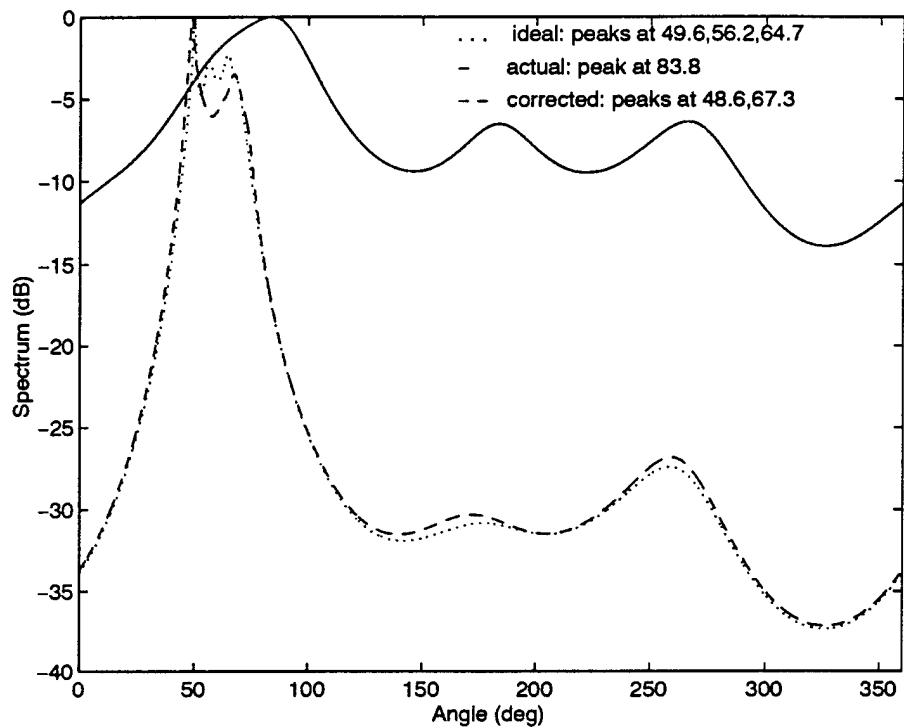


**Figure 43: Linear Prediction, Cross Sleeve Dipole Array, Angles = 45°, 70°, Frequencies = 200, 205 MHz**

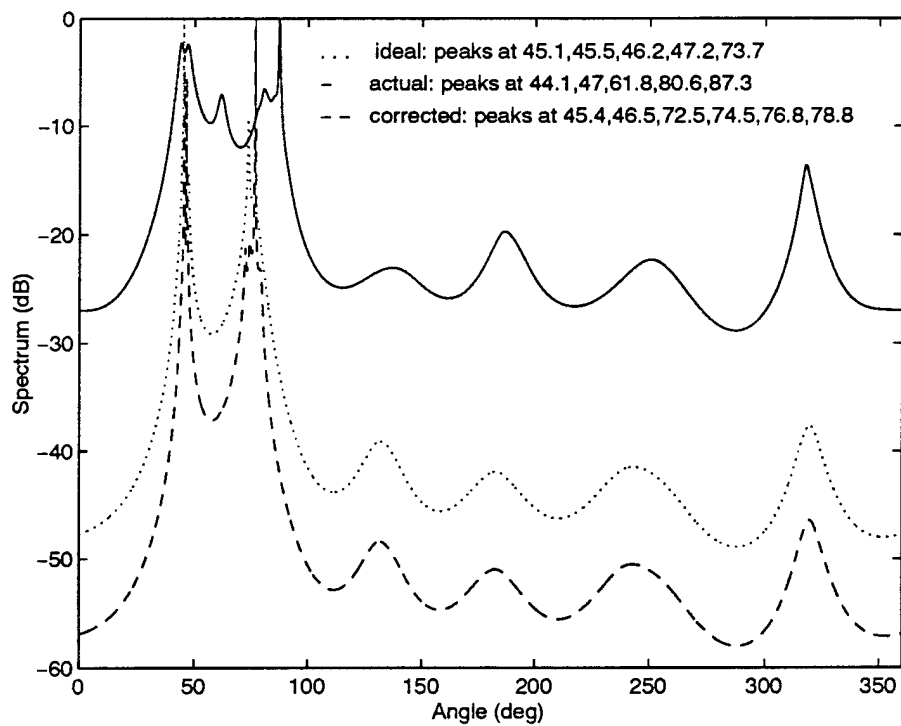


**Figure 44: Linear Prediction, Cross Sleeve Dipole Array, Angles = 45°, 70°, Frequencies = 395, 400 MHz**

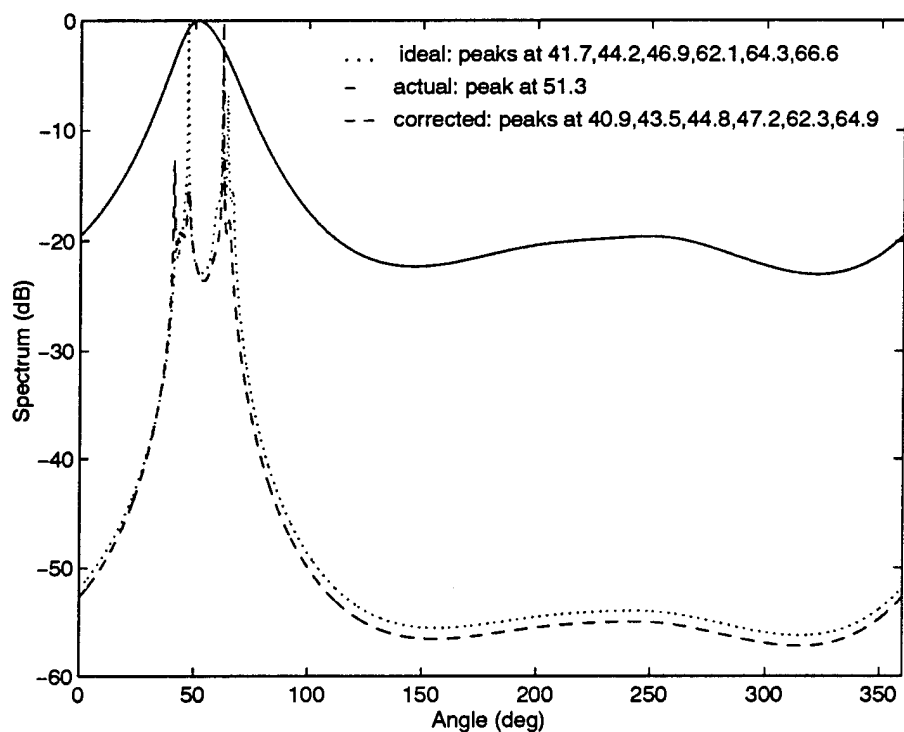


**Figure 45: Linear Prediction, Circular Dipole Array, Angles = 45°, 70°  
Frequencies = 200, 205 MHz**

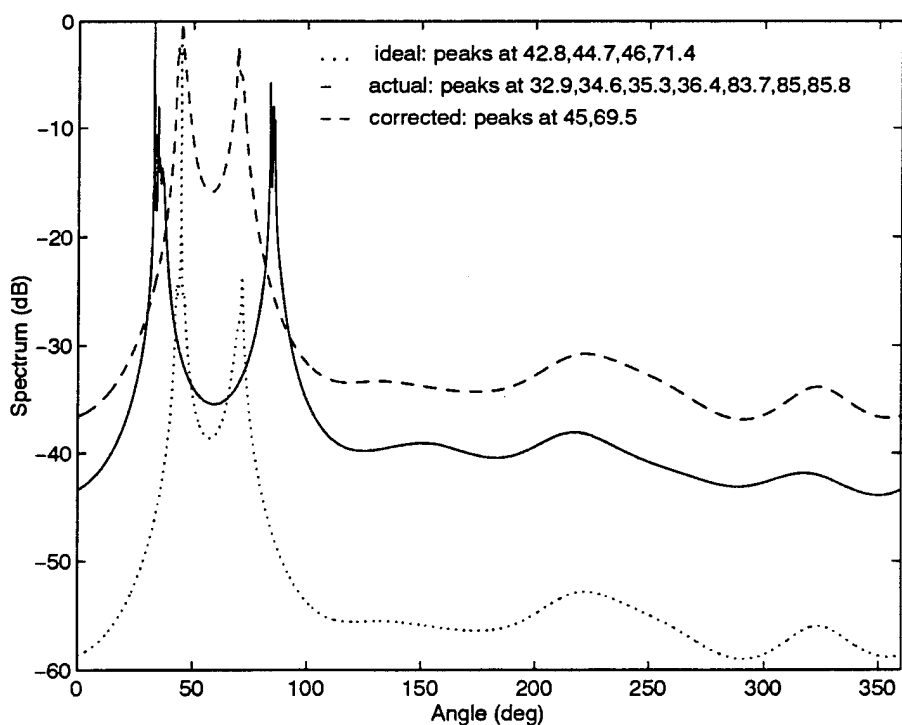


**Figure 46: Linear Prediction, Circular Dipole Array, Angles = 45°, 70°  
Frequencies = 395, 400 MHz**

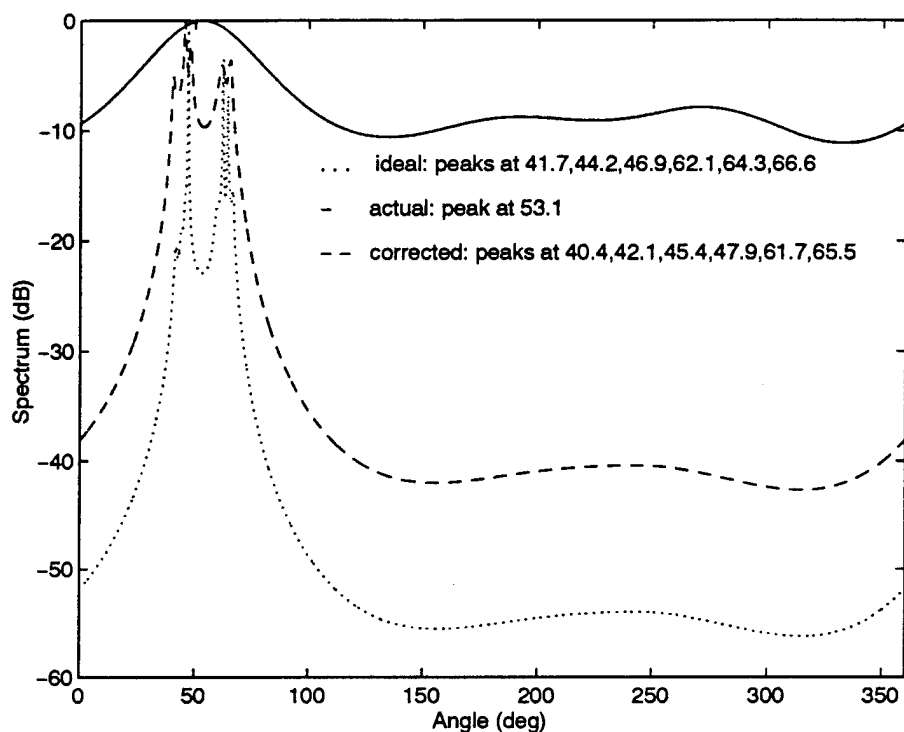


**Figure 47: Linear Prediction, Circular Sleeve Dipole Array,  
Angles = 45°, 70°, Frequencies = 200, 205 MHz**

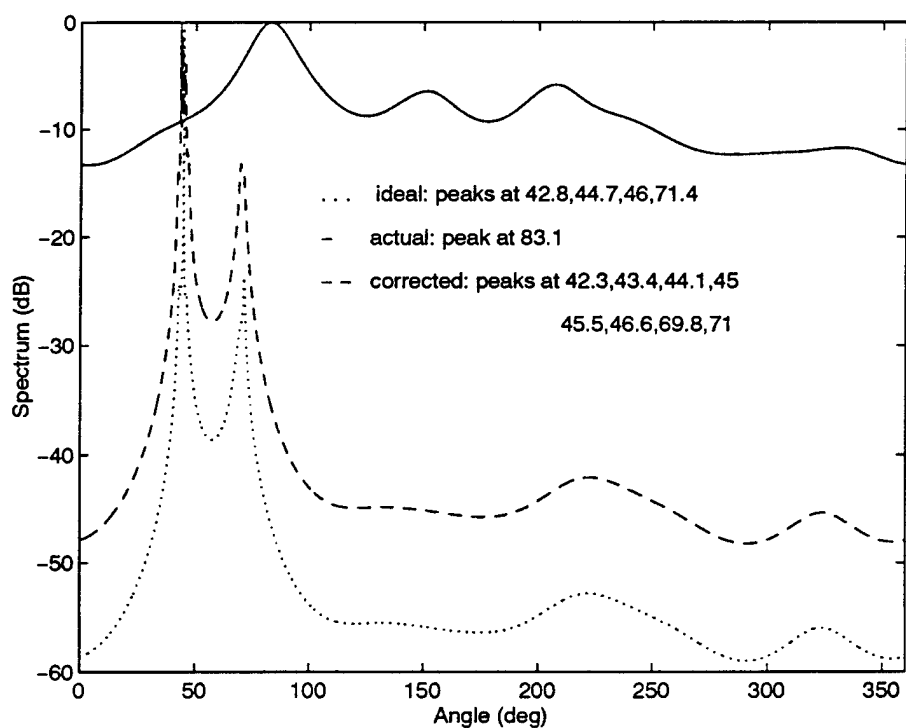


**Figure 48: Linear Prediction, Circular Sleeve Dipole Array,  
Angles = 45°, 70°, Frequencies = 395, 400 MHz**

**Table 3: Linear Prediction Algorithm, SNR = 10 dB**

Array	Freq (MHz)	Angle (deg)	Ideal (deg)	Actual (deg)	Corrected (deg)
Linear Dipole	200, 205	45.0, 55.0	49.2, 50.4	51.6, 52.5	50.1
Linear Dipole	395, 400	45.0, 55.0	44.8, 55.8	46.0, 56.4, 56.7	44.6, 44.8, 45.0, 55.4, 55.7
Linear Sleeve Dipole	200, 205	45.0, 55.0	49.2, 50.4	48.4	50.5
Linear Sleeve Dipole	395, 400	45.0, 55.0	44.8, 55.8	46.3, 57.0	44.6, 44.8, 55.6
Cross Dipole	200, 205	45.0, 70.0	49.6, 56.2 64.7	61.0	49.9, 66.6
Cross Dipole	395, 400	45.0, 70.0	45.1, 45.5, 46.2, 47.2, 73.7	38.8, 39.6, 82.9, 85.5	43.6, 44.7, 45.1, 46.2, 46.9, 75.4, 78.1
Cross Sleeve Dipole	200, 205	45.0, 70.0	49.6, 56.2, 64.7	83.8	48.6, 67.3
Cross Sleeve Dipole	395, 400	45.0, 70.0	45.1, 45.5, 46.2, 47.2, 73.7	44.1, 47.0, 61.8, 80.6, 87.3	45.4, 46.5, 72.5, 74.5, 76.8, 78.8
Circular Dipole	200, 205	45.0, 70.0	41.7, 44.2, 46.9, 62.1, 64.3, 66.6	51.3	40.9, 43.5, 44.8, 47.2, 62.3, 64.9
Circular Dipole	395, 400	45.0, 70.0	42.8, 44.7, 46.0, 71.4	32.9, 34.6, 35.3, 36.4, 83.7, 85.0, 85.8	45.0, 69.5
Circular Sleeve Dipole	200, 205	45.0, 70.0	41.7, 44.2, 46.9, 62.1, 64.3, 66.6	53.1	40.4, 42.1, 45.4, 47.9, 61.7, 65.5
Circular Sleeve Dipole	395, 400	45.0, 70.0	42.8, 44.7 46.0, 71.4	83.1	42.3, 43.4, 44.1, 45.0, 45.5, 46.6, 69.8, 71.0

### 2.6.4 MUSIC Algorithm

The Multiple Signal Classification (MUSIC) algorithm has the best resolution capability of the four algorithms. This spectrum is computed by first decomposing the covariance matrix into its eigenvalues and eigenvectors. Provided the signal to noise ratio is large enough, it is possible by examining the eigenvalues to determine which eigenvectors correspond to the signal and noise and which to only the noise. The noise only eigenvalues are then used to determine the noise subspace. The spectrum is then computed by searching for the angles of arrival that are orthogonal to the noise subspace. The resulting pseudospectrum is given by,

$$P(\phi) = \frac{1}{\sum_{i=k+1}^M |\beta_i^H a(\phi)|^2} \quad (34)$$

where  $M$  is the number of eigenvectors,  $k$  is the number of sources,  $\beta_i$  is the  $i^{\text{th}}$  noise eigenvector, and  $a(\phi)$  is defined in equation (28). This algorithm is described in detail in Appendix E.

Figures 49 and 50 show the MUSIC spectra for the dipole array with one signal at  $45^\circ$  and the other at  $55^\circ$ . These figures show that the resolution capability of the algorithm improves as the frequency increases. Notice that in both figures virtually all the mutual coupling is eliminated and the resolution of the algorithm is restored to that of the ideal case. The same conditions are used for Capon's algorithm in figures 25 through 36. Comparing figures 25 and 49 it is clear that the MUSIC algorithm has better

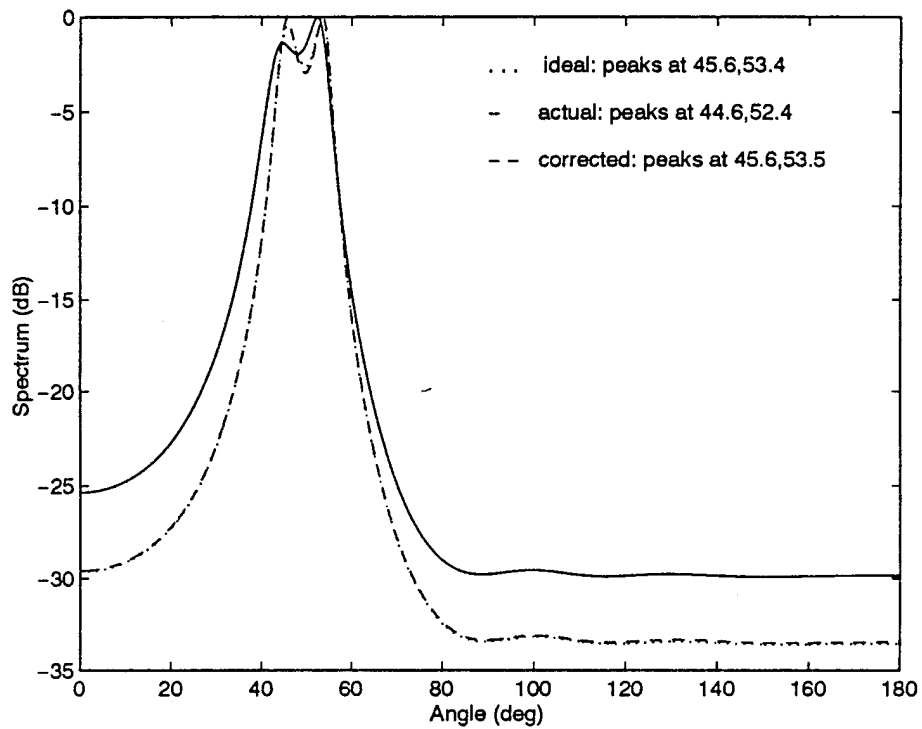


**Figure 49: MUSIC, Linear Dipole Array, Angles =  $45^\circ$ ,  $55^\circ$ ,  
Frequencies = 200, 205 MHz**

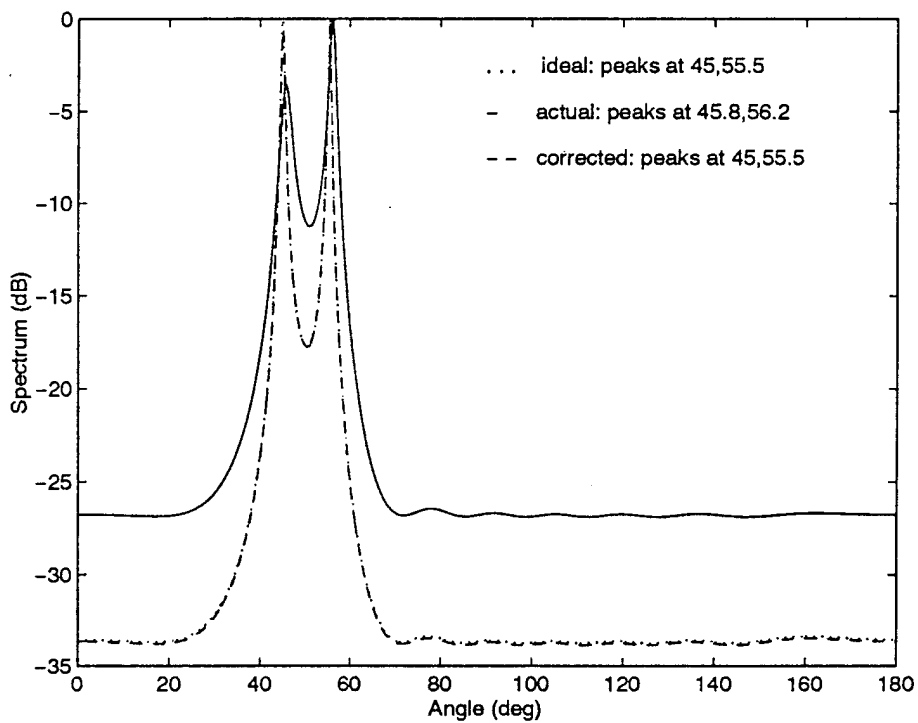


**Figure 50: MUSIC, Linear Dipole Array, Angles =  $45^\circ$ ,  $55^\circ$ ,  
Frequencies = 395, 400 MHz**



resolution capability than Capon's algorithm. Notice that even with the mutual coupling present, the MUSIC algorithm is able to resolve the two signals while Capon's algorithm fails to separate the signals for the ideal case. At the upper frequency limit, both Capon's algorithm and the MUSIC algorithm can resolve the two signals as shown in figures 26 and 50. The angular estimates are approximately the same but the MUSIC algorithm yields a sharper spectrum.

Figures 51 and 52 show the results for the sleeve dipole array. In figure 51 the mutual coupling prevents the resolution of the two signals. In this case it is the mutual coupling between the dipoles and sleeves that prevent the separation of the two signals. This is clearly the case since in the absence of the sleeves the two signals could be resolved as shown in figure 49. As shown in figures 51 and 52, the mutual coupling effects are eliminated with the corrected signal. Comparing figures 51 and 52 with figures 27 and 28 it is again clear that the MUSIC algorithm performs better than Capon's algorithm. Notice that at the lower frequency limit, Capon's algorithm can not resolve the two signals even in the ideal case while the MUSIC algorithm can resolve them with the corrected signal.

The spectra for the cross dipole array are shown in figures 53 and 54 for plane waves at  $45^\circ$  and  $70^\circ$ . At the low end of the bandwidth in figure 53, the mutual coupling clearly prevents the signals from being resolved. This coupling is accounted for and removed by the corrected signal as shown by the spectrum. At the upper frequency limit, the resolution capability of the algorithm is improved as shown in figure 54.

Figures 55 and 56 show the spectra for the cross sleeve dipole array. As with the

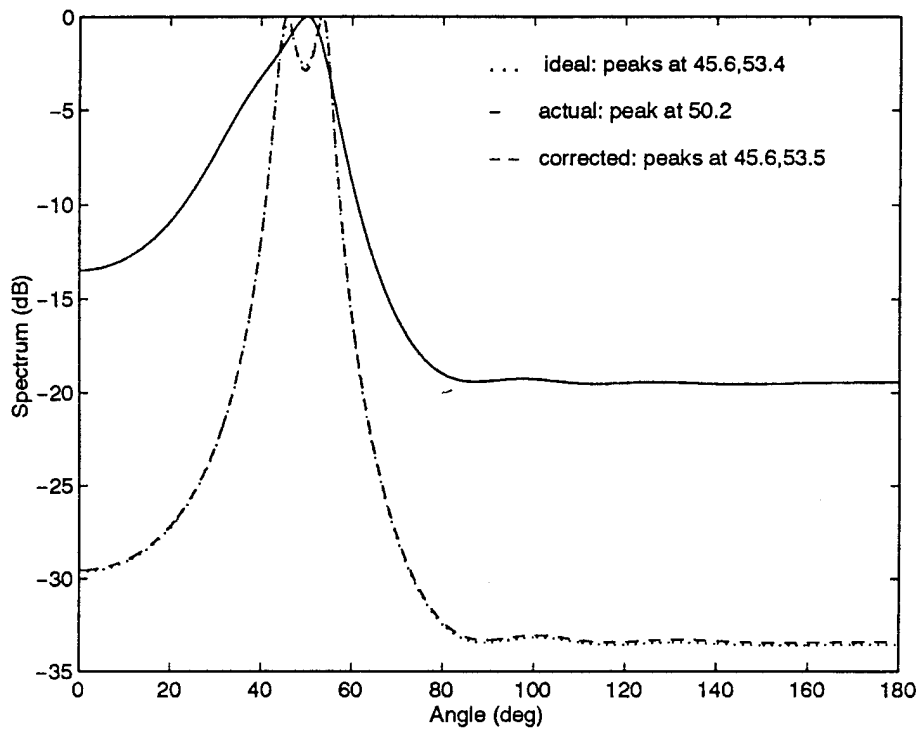


Figure 51: MUSIC, Linear Sleeve Dipole Array, Angles =  $45^\circ$ ,  $55^\circ$ ,  
Frequencies = 200, 205 MHz

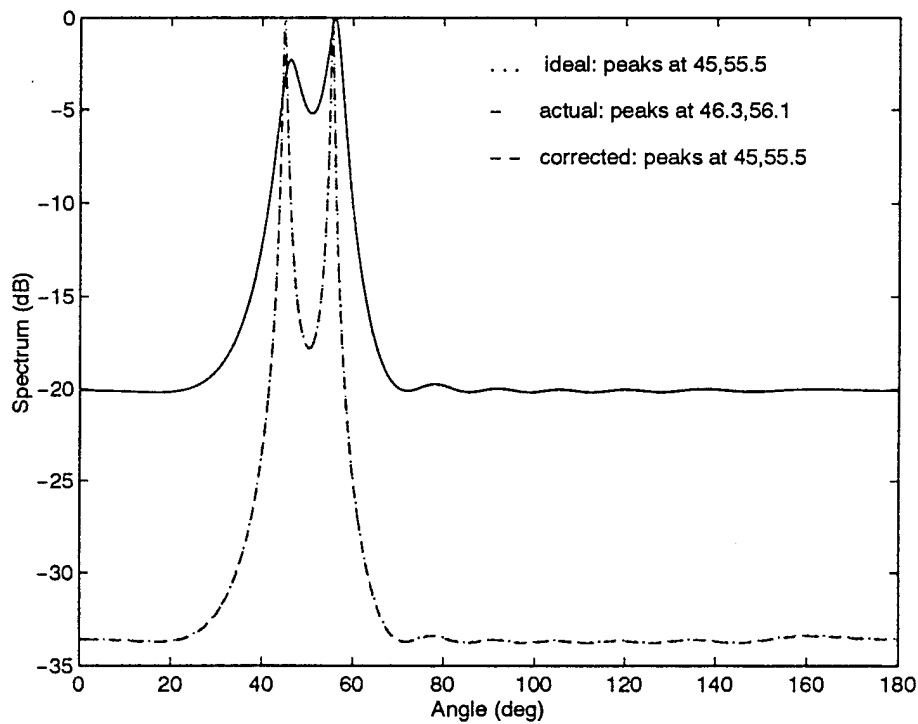
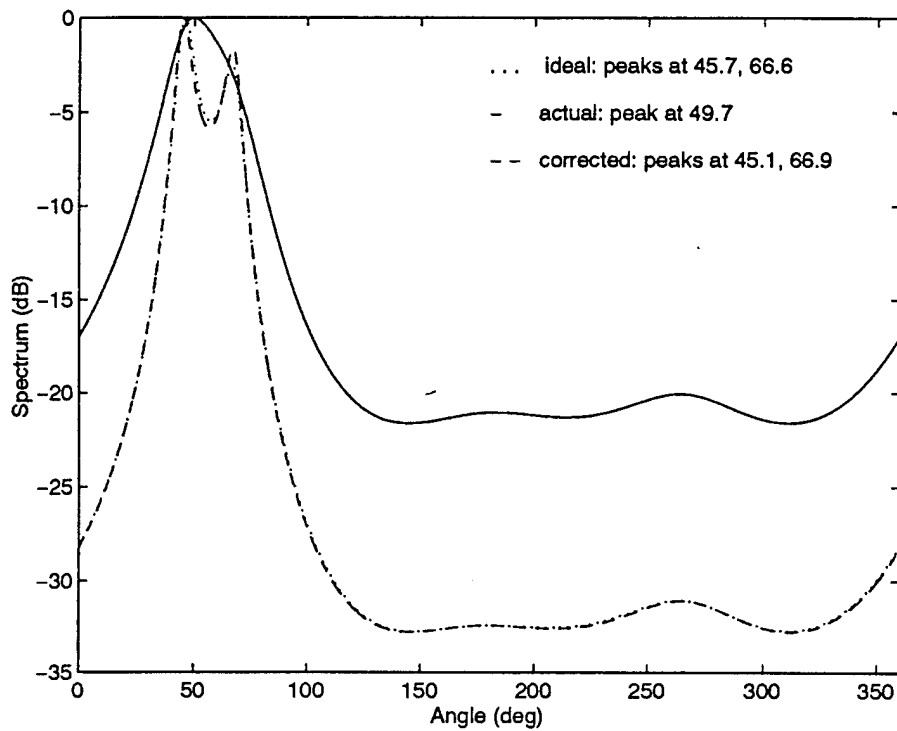
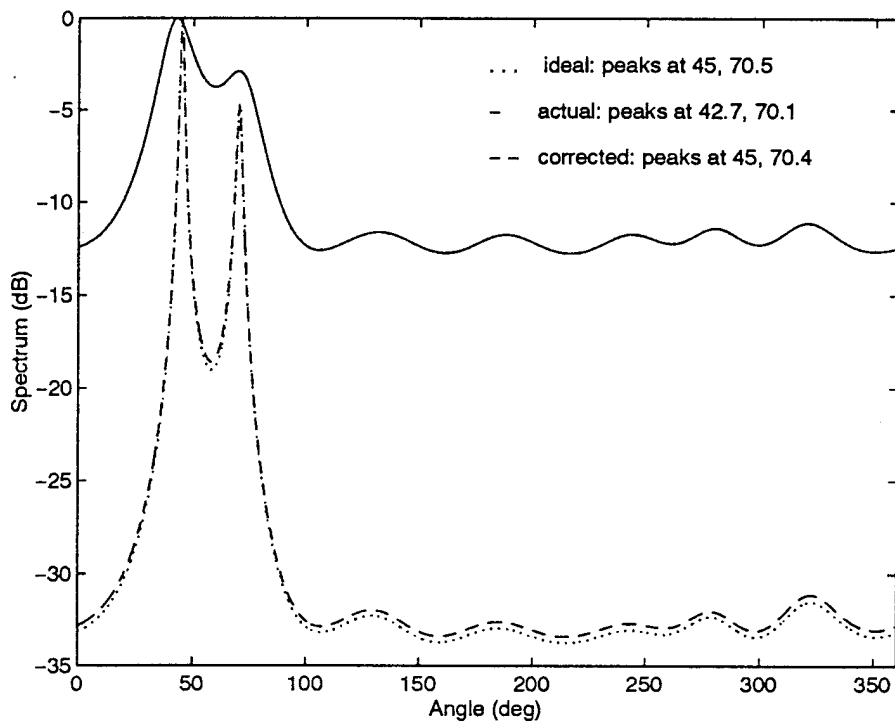


Figure 52: MUSIC, Linear Sleeve Dipole Array, Angles =  $45^\circ$ ,  $55^\circ$ ,  
Frequencies = 395, 400 MHz



**Figure 53: MUSIC, Cross Dipole Array, Angles =  $45^\circ$ ,  $70^\circ$ ,  
Frequencies = 200, 205 MHz**



**Figure 54: MUSIC, Cross Dipole Array, Angles =  $45^\circ$ ,  $70^\circ$ ,  
Frequencies = 395, 400 MHz**

cross dipole array in figure 53, the signals are not resolvable when mutual coupling is present. Figure 56 at the upper frequency limit is very similar to figure 32.

The spectra for the circular dipole array are shown in figures 57 and 58 for incident plane waves at  $45^\circ$  and  $70^\circ$ . Notice that at the low end of the frequency band, the mutual coupling makes the signals unresolvable. Once the effects of mutual coupling are removed, the signals can be resolved as shown by the corrected spectrum. At the upper frequency limit, the mutual coupling does not prevent the resolution of the two signals as shown in figure 58. Notice, however, that the mutual coupling does cause the signals to appear more than  $4^\circ$  away from the true angles of arrival. When the mutual coupling is taken into account, the spectrum is as good as the ideal case. Comparing figures 57 and 58 with 33 and 34, it is clear that the MUSIC algorithm performs better than Capon's algorithm. Notice from figures 57 and 33 that once the mutual coupling effects are mitigated, the MUSIC algorithm can resolve the two signals while Capon's algorithm fails to resolve them.

The spectra for the circular sleeve dipole array are shown in figures 59 and 60. At the lower frequency limit in figure 59, the mutual coupling prevents the resolution of the two signals. The effects of the mutual coupling are removed by the terminal impedance matrix as shown by the spectrum for the corrected signal. Figure 60 shows the spectra at the upper end of the operational bandwidth of the array. Notice that the mutual coupling effects prevent the resolution of the two signals. Comparing this figure with figure 58 shows that the added mutual coupling due to the sleeves prevents the MUSIC algorithm from resolving the two signals.

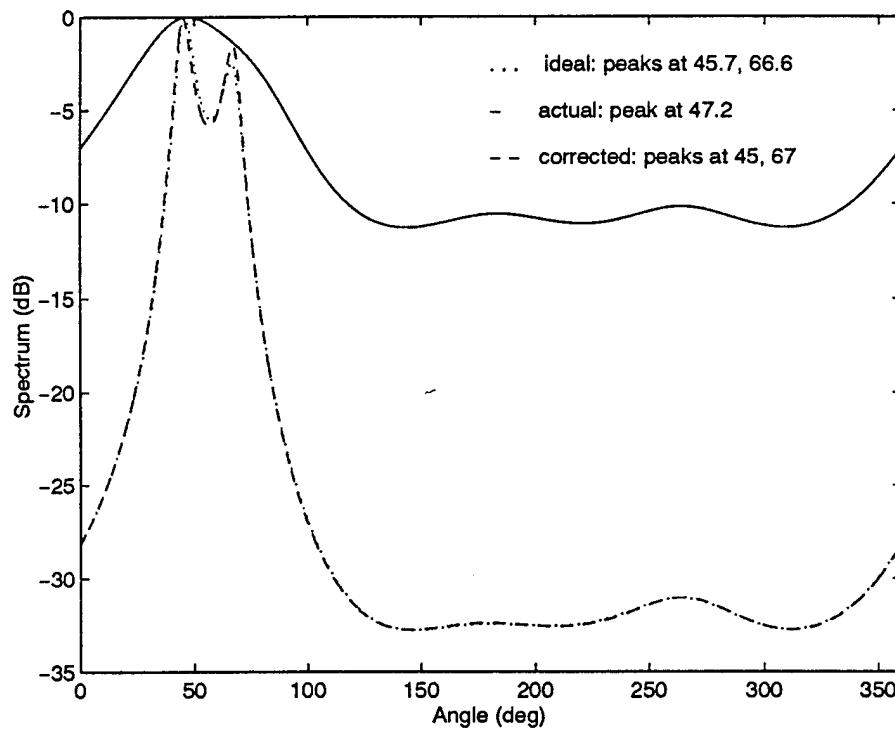


Figure 55: MUSIC, Cross Sleeve Dipole Array, Angles =  $45^\circ$ ,  $70^\circ$ ,  
Frequencies = 200, 205 MHz

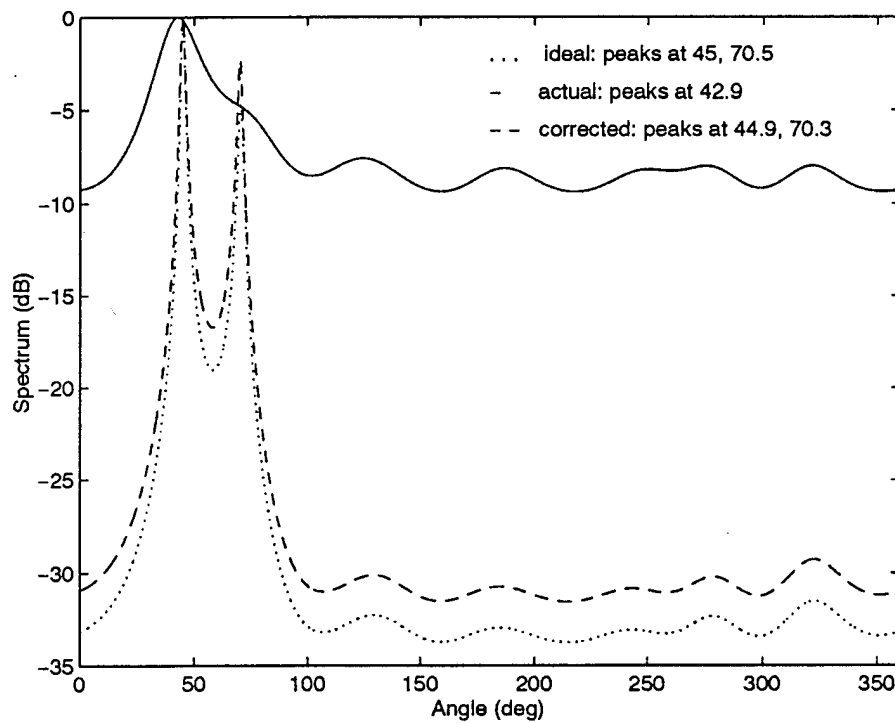


Figure 56: MUSIC, Cross Sleeve Dipole Array, Angles =  $45^\circ$ ,  $70^\circ$ ,  
Frequencies = 395, 400 MHz

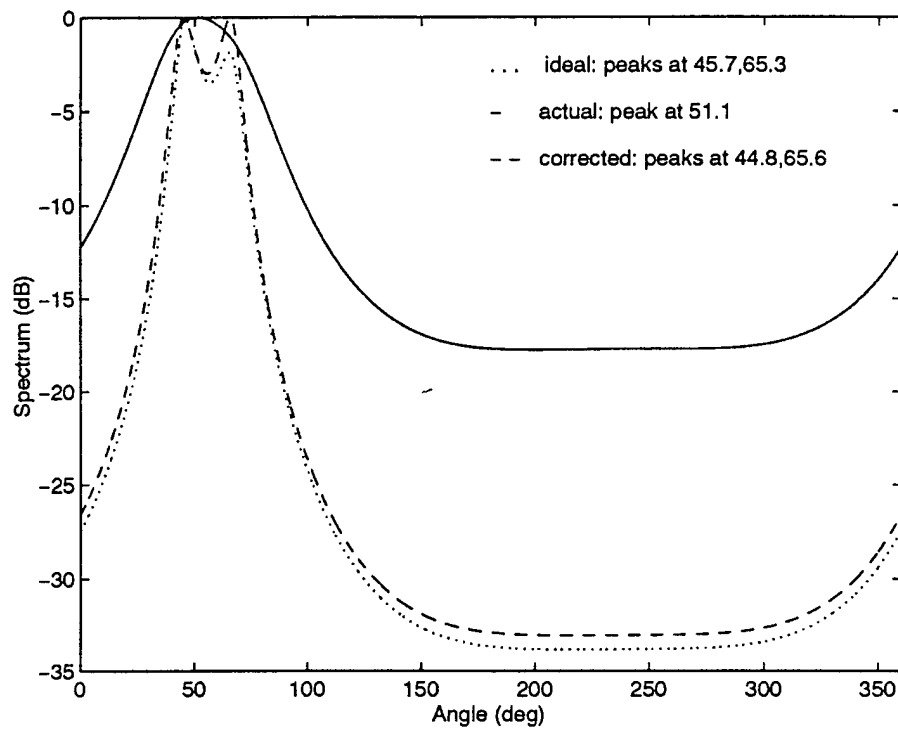


Figure 57: MUSIC, Circular Dipole Array, Angles =  $45^\circ$ ,  $70^\circ$ ,  
Frequencies = 200, 205 MHz

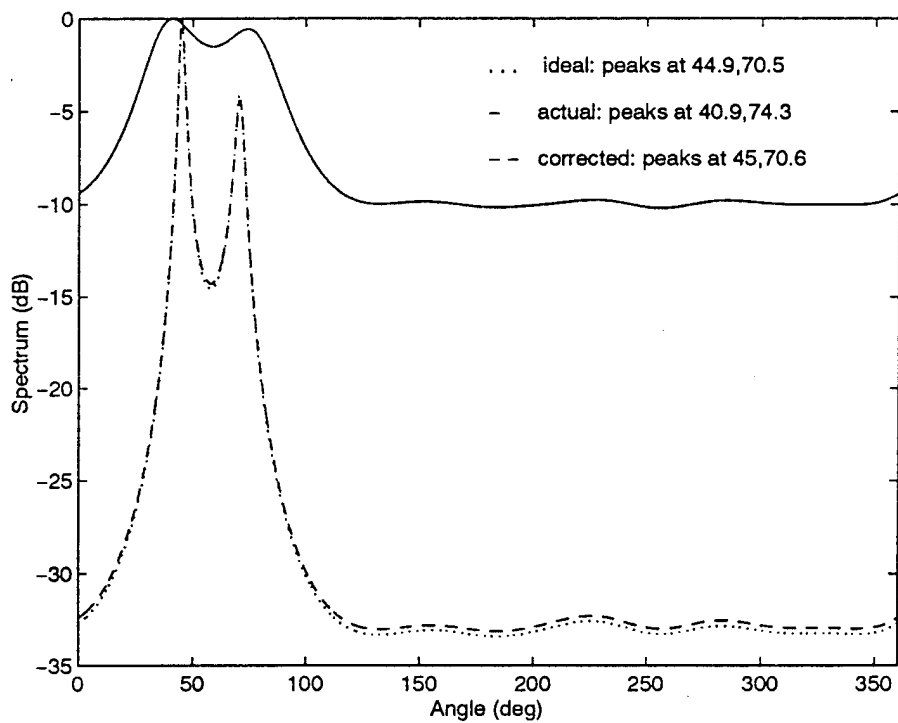


Figure 58: MUSIC, Circular Dipole Array, Angles =  $45^\circ$ ,  $70^\circ$ ,  
Frequencies = 395, 400 MHz.

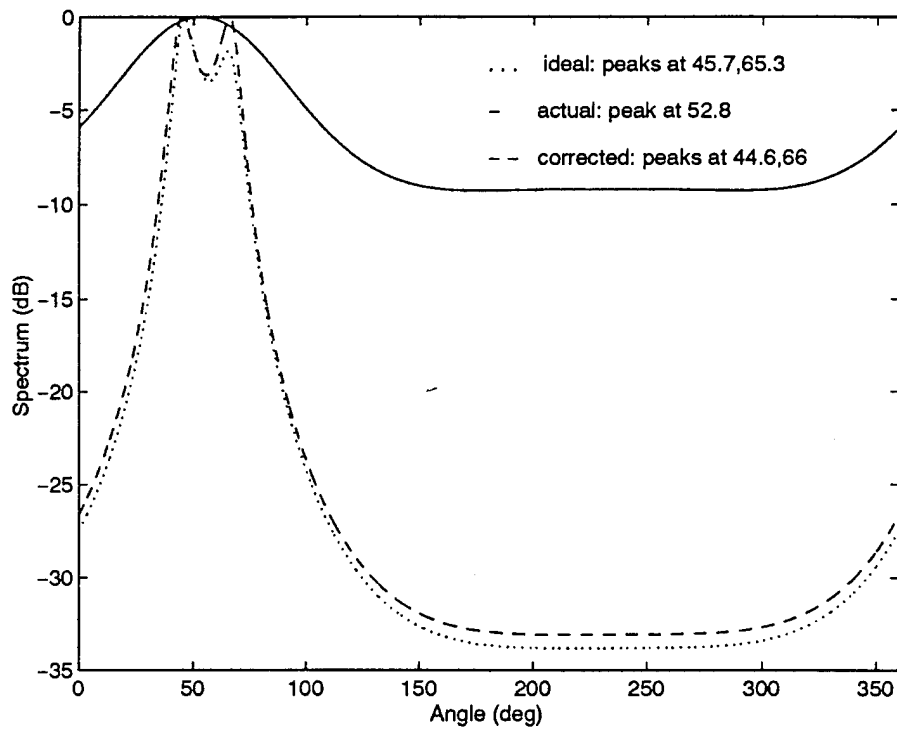


Figure 59: MUSIC, Circular Sleeve Dipole Array, Angles =  $45^\circ$ ,  $70^\circ$ ,  
Frequencies = 200, 205 MHz

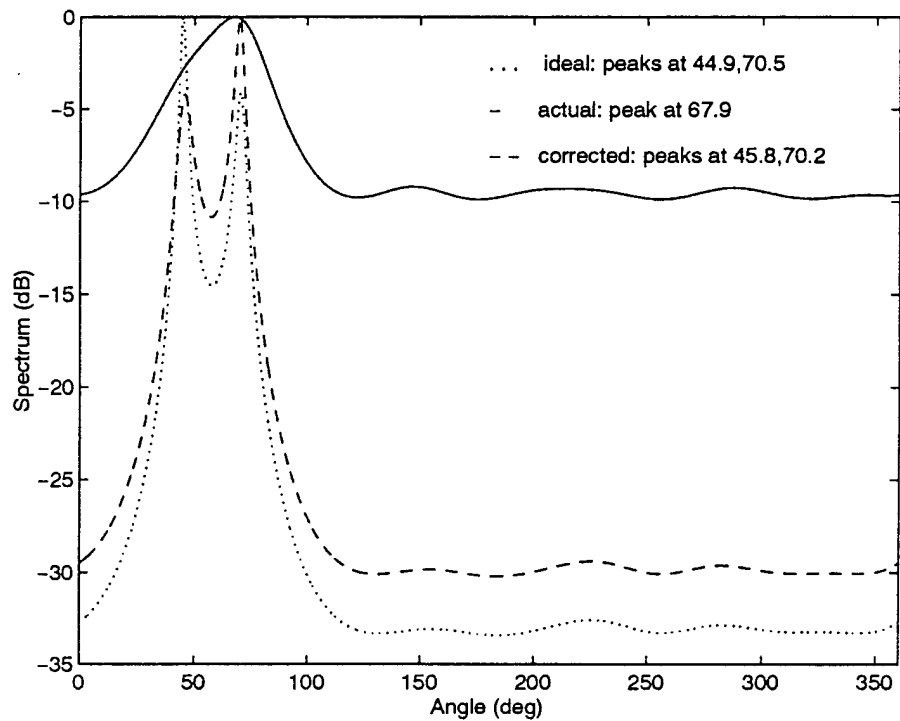


Figure 60: MUSIC, Circular Sleeve Dipole Array, Angles =  $45^\circ$ ,  $70^\circ$ ,  
Frequencies = 395, 400 MHz

The results for the MUSIC algorithm are summarized in Table 4. This algorithm, as stated before has the best resolution capability of the four techniques. In many cases, the mutual coupling caused the two signals to appear as one. In every case presented, the two signals could be resolved with the corrected signal. The angles of arrival for the corrected signal are also seen to be approximately the same as in the ideal case.



Table 4: MUSIC Algorithm, SNR = 10 dB

Array	Freq (MHz)	Angle (deg)	Ideal (deg)	Actual (deg)	Corrected (deg)
Linear Dipole	200, 205	45.0, 55.0	45.6, 53.4	44.6, 52.4	45.6, 53.5
Linear Dipole	395, 400	45.0, 55.0	45.0, 55.5	45.8, 56.2	45.0, 55.5
Linear Sleeve Dipole	200, 205	45.0, 55.0	45.6, 53.4	50.2	45.6, 53.5
Linear Sleeve Dipole	395, 400	45.0, 55.0	45.0, 55.5	46.3, 56.1	45.0, 55.5
Cross Dipole	200, 205	45.0, 70.0	45.7, 66.6	49.7	45.1, 66.9
Cross Dipole	395, 400	45.0, 70.0	45.0, 70.5	42.7, 70.1	45.0, 70.4
Cross Sleeve Dipole	200, 205	45.0, 70.0	45.7, 66.6	47.2	45.0, 67.0
Cross Sleeve Dipole	395, 400	45.0, 70.0	45.0, 70.5	42.9	44.9, 70.3
Circular Dipole	200, 205	45.0, 70.0	45.7, 65.3	51.1	44.8, 65.6
Circular Dipole	395, 400	45.0, 70.0	44.9, 70.5	40.9, 74.3	45.0, 70.6
Circular Sleeve Dipole	200, 205	45.0, 70.0	45.7, 65.3	52.8	44.6, 66.0
Circular Sleeve Dipole	395, 400	45.0, 70.0	44.9, 70.5	67.9	45.8, 70.2

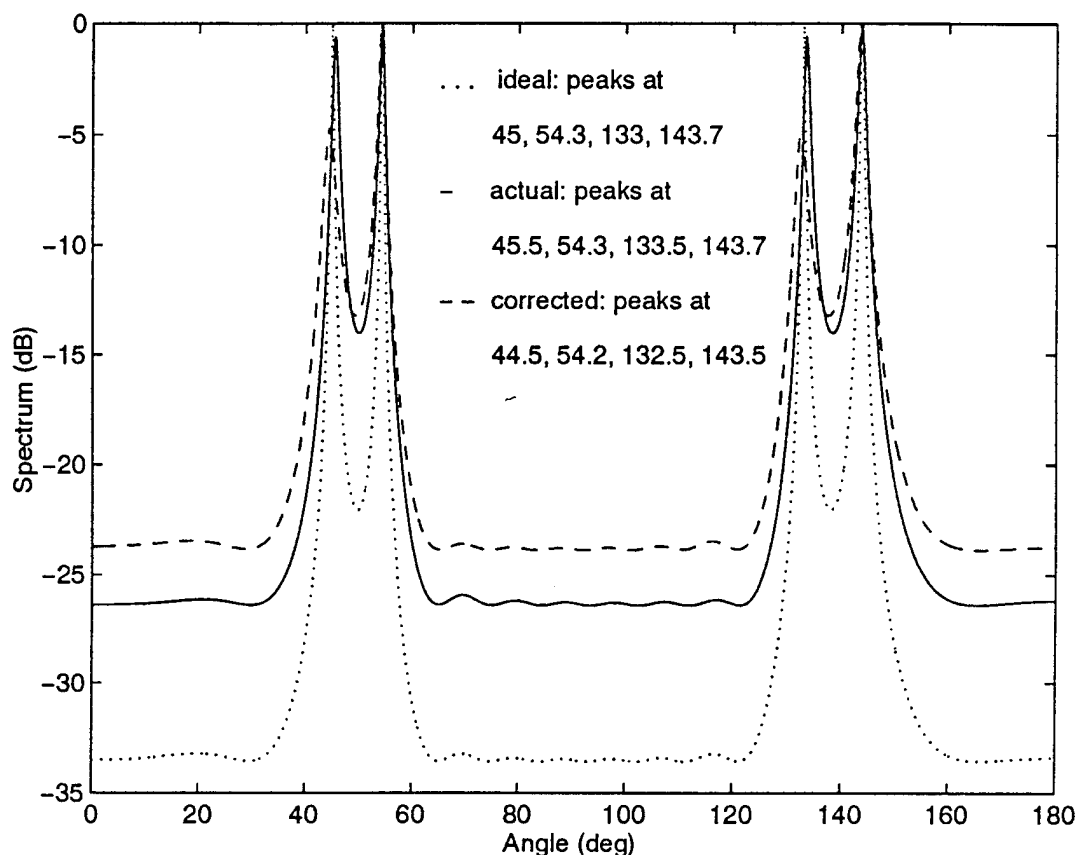


Figure 61: MUSIC, Linear Spiral Array, Angles = 45, 55,  
Frequencies = 300, 305 MHz

### 2.6.5 Spiral Array

Unlike the dipole and the sleeve dipole antenna, the spiral antenna has significant size. It has a radius of about 0.24 wavelengths at the lowest frequency of operation. As a result, the minimum possible spacing is 0.48 wavelengths at the lowest frequency of operation which at the highest frequency of operation equals 0.96 wavelengths. While the larger spacing makes the antenna array less susceptible to mutual coupling effects, ambiguities in the angle determination become unavoidable due to the formation of grating lobes. Figure 61 shows the simulation results for a nine element spiral array where the frequency is 300 MHz and the angles of arrival are  $45^\circ$  and  $55^\circ$ . The spectrum

shows two peaks due to the actual signals and two peaks from the grating lobes. The large physical size of the spiral element make it impractical for use in wideband direction finding arrays.

## 2.7 Summary and Conclusions

Direction finding systems are used to resolve narrow band signals that can occur over a large bandwidth. This requirement yields antenna arrays with strong mutual coupling effects especially at the lower end of the operating bandwidth. As shown, this mutual coupling degrades the ability of the direction finding algorithm to resolve two signals with a small angular separation.

The results of mutual coupling compensation for the Beamformer algorithm are shown in figures 13 through 24. This algorithm is simple to apply and robust with respect to noise and mutual coupling. Unfortunately, its resolution capability is the worst of the four algorithms. It is seen in figures 13 through 24 that the mutual coupling had very little effect on the ability of the algorithm to locate the peaks in the spectrum. In all cases the spectrum from the corrected signal is almost identical to that of the ideal signal. In general, because the Beamformer algorithm is robust with respect mutual coupling, the compensation for mutual coupling is not worth the effort.

The spectra for the ideal and corrected signals for Capon's algorithm are also almost identical. In this case, however, the compensation for mutual coupling is very beneficial. In particular, figures 32 and 36 show that without mutual coupling compensation, the two signals could not be resolved but with compensation the calculated angles of arrival are approximately as good as the ideal case.

The spectra for the linear prediction algorithm also show that mutual coupling hinders the ability of the algorithm to resolve two signals. This is clearly shown in figures 41, 43, 47, and 48. In all of these cases the resolution capability of the algorithm is restored by compensating for the mutual coupling. The spectra from the linear prediction algorithm manifest a phenomenon known as peak splitting which prevents a clear picture of the two signals [49].

The spectra for the MUSIC algorithm are shown in figures 49 through 60. This algorithm yields the best resolution of the four algorithms but requires estimating the number of sources. As with the other algorithms, sometimes the mutual coupling caused the two signals to appear as one and sometimes it caused the calculated angles of arrival to be farther apart. However, the compensation technique successfully restored the performance of the MUSIC algorithm.

The MUSIC spectrum is also calculated for the spiral antenna array. It is shown in figure 61 that the large spacing of the spirals caused grating lobes in the antenna pattern which manifested themselves as ambiguous angles of arrival in the spatial spectrum. Therefore, although the spiral is a broadband element, it can not be used in a broadband array for direction finding.

### **CHAPTER III**

## **DIRECTION FINDING IN THE PRESENCE OF A NEAR FIELD SCATTERER**

The previous chapter demonstrates that the resolution capability of the MUSIC algorithm is adversely affected by the presence of mutual coupling. It also shows that the mutual coupling effects can be compensated for by pre-processing the actual signal with the terminal impedance matrix. The result is that the corrected spectrum is approximately the same as the ideal spectrum which assumes that no mutual coupling is present.

In this chapter, the effects of an object in the near field of an antenna array on the MUSIC algorithm are investigated. As shown in figure 62, the scatterer produces spherical waves which hinder the ability of the MUSIC algorithm to resolve two incident plane waves with a small angular separation. This near field object may be a building, an airplane wing, or the inside of the antenna array's radome as shown in figure 63. Also presented is a technique which overcomes the adverse effects on the MUSIC algorithm of the near field scatterer.

Section 3.1 demonstrates the adverse effects of the interference from a near field scatterer. In this section a typical array with far field signals and near field interfering signals is investigated. It is shown that even when the interfering signals are relatively

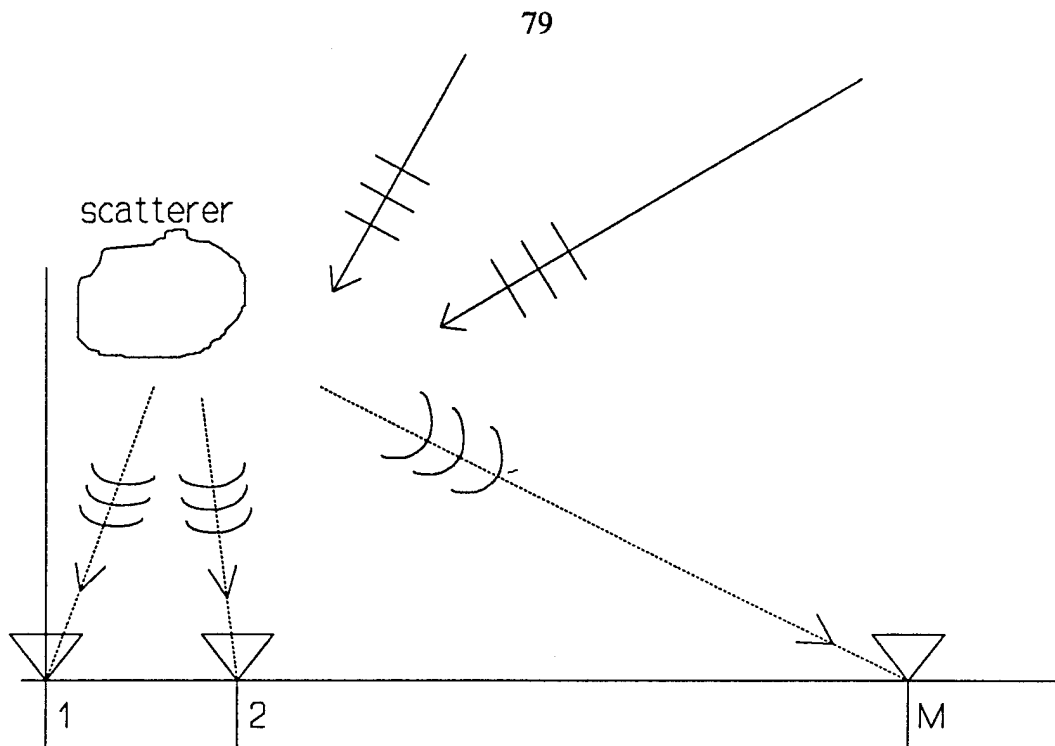


Figure 62: Geometry of the Array, Sources, and Scatterer

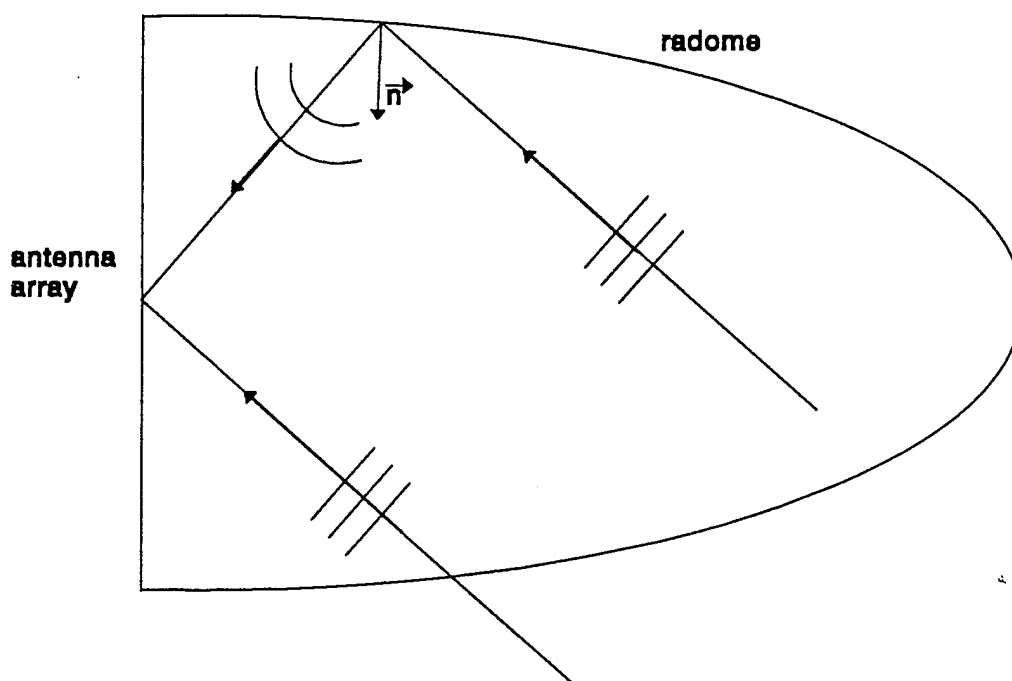


Figure 63: Near Field Scattering by the Inside of a Radome

weak compared to the desired signals, the resolution capability of the MUSIC algorithm is greatly reduced.

In section 3.2 the linear dipole array and near field scatterer are modeled quantitatively. This is accomplished by using a hybrid technique that combines the method of moments with the Uniform Theory of Diffraction (UTD) [34,35]. This technique produces a second impedance matrix which is added to the original moment method impedance matrix. It also yields a second excitation vector which is added to the original excitation vector. The new system of equations is obtained by combining these techniques to yield the current on the antenna due to both the incident fields and the near field scatterer.

Section 3.3 presents a new procedure to compensate for the near field scatterer. This technique consists of modifying the array configuration and terminal impedance matrix. The modified array configuration is used to suppress the fields incident on the array from the scatterer. This modification changes the search vector used in the MUSIC algorithm. The terminal impedance matrix is modified to account for the additional coupling through the scatterer. These two modifications permit an almost perfect cancellation of the fields from the nearby scatterer.

The results of the simulations for synthetic interfering signals, a point scatterer, and a distributed scatterer are presented in section 3.4. The simulations are first performed on an ideal antenna array with incident plane waves and synthetic interference sources modeled as point sources. This case shows that the new antenna array configuration can adequately suppress the interfering spherical waves. In section 3.4.2

a point scatterer with a specified RCS is used to determine the effectiveness of the new terminal impedance matrix with the new antenna array configuration. It is found that the scatterer can be successfully suppressed. In the final case a finite length edge is used as the scatterer. The simulations show that the interference can be adequately suppressed with the new terminal impedance matrix and antenna configuration if all the scattered energy can be considered as having a common phase center. The results in section 3.4 show that the modified terminal impedance matrix and the new array configuration with the new search vector can successfully suppress the effects of a near field scatterer.

### 3.1 Effects of a Near Field Scatterer

Figure 64 presents a typical scene where spherical waves adversely effect the resolution capability of the MUSIC algorithm. In this case, the nine element linear array of chapter 2 is used to resolve incident plane waves. Two plane waves at 300 MHz and 305 MHz are incident at  $45^\circ$  and  $55^\circ$  relative to the array axis. Two spherical waves, representing interference from a nearby scatterer are also incident upon the array as shown in figure 64. Figure 64 shows the typical interference from a near field scatterer that can degrade the resolution capability of the MUSIC algorithm.

Figure 65 shows the spectrum for the problem in figure 64 for several different signal to interference (S/I) ratios. The plane waves are the desired signals and the spherical waves are the interfering signals. As in chapter 2, the spectrum is a normalized average of 20 simulations. The ideal spectrum which shows the result of the MUSIC algorithm when no spherical waves are present is also included in figure 65. Notice that as the S/I ratio decreases, the two peaks begin to merge. Notice also that when the S/I



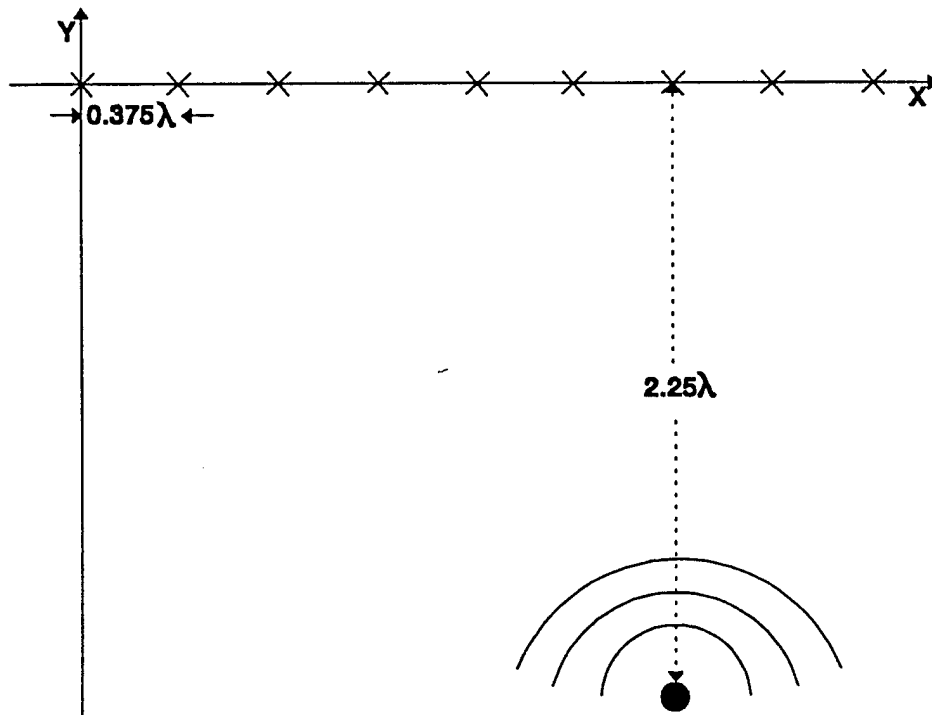


Figure 64: Plane Waves and Spherical Waves Incident Upon an Array

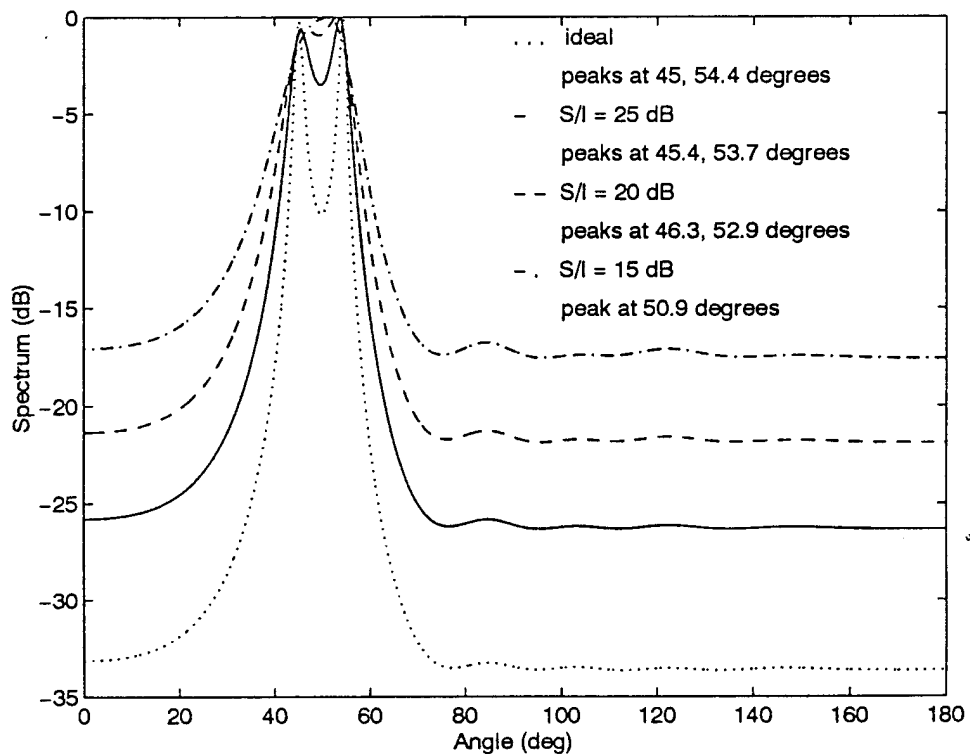


Figure 65: Effect of Spherical Waves on the MUSIC Spectrum

ratio is 15 dB, the two peaks can no longer be separated. Figure 65 shows that even when the power in the plane waves is much greater than that in the spherical waves, the resolution of the MUSIC algorithm is significantly affected.

### 3.2 Electromagnetic Model of the Array and Scatterer

As in chapter 2, the reaction integral equation is used to determine the current induced on an antenna array illuminated by a plane wave. This equation is reduced to a system of linear equations with the method of moments described in Appendix A. The scatterer is incorporated into the model by using a hybrid technique that combines the Method of Moments with the Uniform Theory of Diffraction [34,35]. This creates a new system of equations which are then solved to yield the current on the antenna array. The terminal voltages are computed by multiplying the current at the antenna terminals by the load impedance.

Using the method of moments as described in Appendix A, the integral equation for the antenna array becomes the system of equations

$$\sum_{n=1}^N Z_{mn} I_n = V_m \quad m = 1, 2, \dots, N \quad (35)$$

$$Z_{mn} = \int_s \vec{J}_m \cdot \vec{E}_n^s ds \quad (36)$$

$$V_m = - \int_s \vec{J}_m \cdot \vec{E}^i ds \quad (37)$$

where  $Z_{mn}$  is the mutual coupling between modes "m" and "n",  $I_n$  and  $I_m$  are the currents at modes "n" and "m" respectively,  $V_m$  is the excitation at mode "m",  $E^i$  is the incident field and  $ds$  is the differential length along the dipole.

The presence of the scatterer can be accounted for in the MoM model of the antenna array by modifying each of the integrals [34, 35 pp. 500-510]. In particular, equations (36) and (37) become

$$Z'_{mn} = \int_s \vec{J}_m \cdot (\vec{E}_n^s + a \vec{E}_n^s) ds \quad (38)$$

$$V'_m = - \int_s \vec{J}_m \cdot (\vec{E}^i + b \vec{E}^i) ds \quad (39)$$

where  $Z'_{mn}$  is the new impedance matrix,  $V'_m$  is the new excitation vector,  $(a E_n^s)$  is the field from the  $n^{\text{th}}$  mode scattered by the object and  $(b E^i)$  is the incident field scattered by the object. The system of equations is now

$$\sum_{n=1}^N Z'_{mn} I'_n = V'_m \quad m = 1, 2, \dots, N \quad (40)$$

where  $I'_n$  is the new  $n^{\text{th}}$  mode of current on the antenna. Equations (38) and (39) can be expanded to yield

$$Z'_{mn} = \int_s \vec{J}_m \cdot \vec{E}_n^s ds + \int_s \vec{J}_m \cdot a \vec{E}_n^s ds \quad (41)$$

$$V_m' = \int_s \vec{J}_m \cdot \vec{E}^i ds + \int_s \vec{J}_m \cdot b \vec{E}^i ds \quad (42)$$

The new impedance matrix and excitation vector can now be represented as

$$Z_{mn}' = Z_{mn} + Z_{mn}^g \quad (43)$$

$$\text{and} \quad V_m' = V_m + V_m^g \quad (44)$$

$$\text{where} \quad Z_{mn}^g = \int_s \vec{J}_m \cdot a \vec{E}_n^s ds \quad (45)$$

$$\text{and} \quad V_m^g = \int_s \vec{J}_m \cdot b \vec{E}^i ds \quad (46)$$

Note that the terms "a" and "b" in equations (44) and (45) can not be pulled out of the integrals since they are, in general, dependent upon modes "m" and "n."

Substituting equations (43) and (44) into equation (40) yields

$$\sum_{n=1}^N (Z_{mn} + Z_{mn}^g) I_n' = (V_m + V_m^g) \quad m=1, 2, \dots, N \quad (47)$$

Note that  $Z_{mn}$  and  $V_m$  have already been calculated from the method of moments model of the antenna array. The terms  $Z_{mn}^g$  and  $V_m^g$  are calculated using equations (45) and

(46). The equations for calculating these terms for an edge type of scatterer in the near field of the antenna array are derived in Appendix F.

### 3.3 Compensation for the Near Field Scatterer

The presence of an object in the vicinity of the antenna array affects both the method of moments impedance matrix and the excitation vector as shown in equation (47). To eliminate the degradation effects of the near field scatterer, both of these factors must be corrected. The added mutual coupling due to  $Z_{mn}^s$  is compensated for by a terminal impedance matrix similar to equation (22). The vector  $V_m^s$  must also be suppressed to restore the resolution capability of the MUSIC algorithm. This is accomplished by combining the output voltages of the antenna elements to null the contributions from the interfering scatterer. Mathematically, the objective is to reduce equation (47) to

$$\sum_{l=1}^M Z_{kl}^{Te} I_l = V_k \quad k = 1, 2, \dots, M \quad (48)$$

where  $Z_{kl}^{Te}$  is the modified terminal impedance matrix that accounts for the presence of the scatterer,  $I_l$  is the  $l^{\text{th}}$  terminal current on the antenna, and  $V_k$  is the voltage at the  $k^{\text{th}}$  antenna terminals. Note that the current at the antenna terminals is already known since the current at all points on the antenna array was found from equation (47). Therefore, it only remains to calculate the matrix  $Z_{kl}^{Te}$  and suppress the vector  $V_m^s$ .

#### 3.3.1 Terminal Impedance Matrix Including the Scatterer

The derivation of the terminal impedance matrix that includes the effect of the

scatterer is very similar to the derivation of the terminal impedance matrix without the scatterer. This new matrix consists of two terms. The first term accounts for the direct mutual coupling between the antenna elements. The second term models the mutual coupling between antenna elements through the scatterer. The new terminal impedance matrix is the sum of these two terms.

As in chapter 2, let there be  $M$  antenna elements in the array with the current on each element represented by  $N_m$  modes. The size of the moment method impedance matrix,  $Z_{mn}$ , is  $N \times N$  where  $N = M \times N_m$ . This matrix will be reduced to a  $M \times M$  matrix whose elements represent the mutual coupling between the antenna terminals.

As before, the overall mutual impedance between terminals  $k$  and  $l$  is defined as

$$Z_{kl}^{Te} = \frac{V_{kl}^{Te}}{I_l^{Te}} \quad (49)$$

where  $V_{kl}^{Te}$  is the open circuit voltage at the  $k^{\text{th}}$  antenna terminal due to the current on the  $l^{\text{th}}$  antenna. The open circuit voltage which is also the same as in section 2.3.1, is given by the expression

$$V_{kl}^{Te} = -\frac{1}{I_k^{Te}} \int_{k^{\text{th}} \text{ antenna}} \vec{E}_{kl} \cdot \vec{l}^k dl \quad (50)$$

where  $E_{kl}$ , as shown in figure 66, is the electric field at the  $k^{\text{th}}$  antenna element due to the  $l^{\text{th}}$  antenna. The presence of the scatterer changes  $E_{kl}$  to

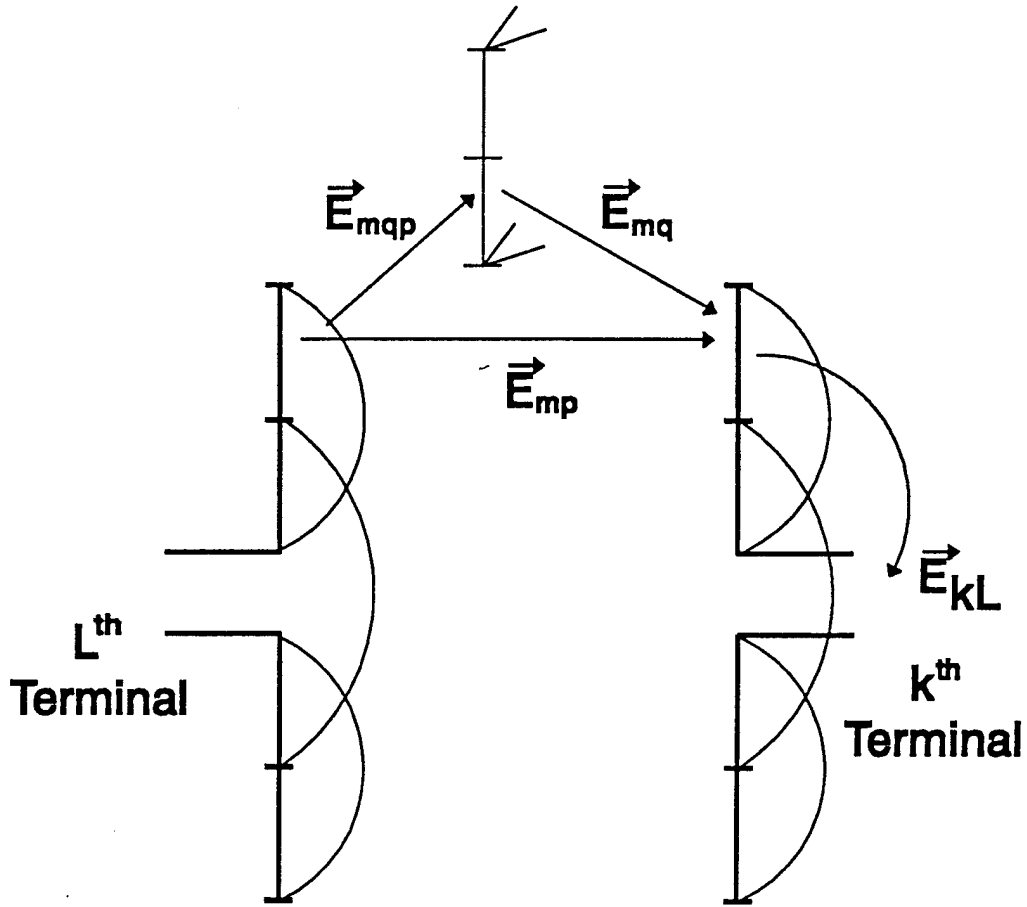


Figure 66: Geometry for the Terminal Impedance Matrix with Scatterer

$$\vec{E}_{kl} = \sum_{m=1+(k-1)N_m}^{kN_m} [\vec{E}_m^l + \vec{E}_m^w D_{mqp} A_{mqp} e^{-j\beta s_{mq}}] G(z-z_m) \quad (51)$$

where

$E_m^l$  = the electric field at the  $m^{\text{th}}$  mode from the  $l^{\text{th}}$  element

$E_m^w$  = the electric field at the  $m^{\text{th}}$  mode scattered by the wedge

$D_{mqp}$  = the diffraction coefficient from p to q to m

$A_{mqp}$  = the spreading factor from p to q to m

$S_{mq}$  = the distance from the  $q^{\text{th}}$  segment to the  $m^{\text{th}}$  mode

and  $G(z-z_m)$  = the gate function. The electric field  $E_m^1$  which is the sum of the electric field from all the  $p^{\text{th}}$  modes on the  $l^{\text{th}}$  antenna element is

$$\vec{E}_m^1 = \sum_{p=1+(l-1)N_s}^{lN_s} \vec{E}_{mp} \quad (52)$$

The electric field due to the wedge,  $E_m^w$ , is the sum of the electric field due to each of the segments comprising the wedge

$$\vec{E}_m^w = \sum_{q=1}^{N_s} \vec{E}_{mq} \quad (53)$$

where  $N_s$  is the number of wedge segments. The electric field,  $E_{mq}$ , is the sum of all the fields from the  $p$  modes on the  $l^{\text{th}}$  antenna element diffracted by the  $q^{\text{th}}$  segment toward the  $m^{\text{th}}$  mode on the  $k^{\text{th}}$  element.

$$\vec{E}_{mq} = \sum_{p=1+(l-1)N_s}^{lN_s} \vec{E}_{mqp} \quad (54)$$

Substituting equation (54) into (53) yields

$$\vec{E}_m^w = \sum_{q=1}^{N_s} \sum_{p=1+(l-1)N_s}^{lN_s} \vec{E}_{mqp} \quad (55)$$



Substituting equations (52), and (55) into (51) yields

$$\vec{E}_{kl} = \sum_{m=1+(k-1)N_m}^{kN_m} \sum_{p=1+(l-1)N_m}^{lN_m} \left[ \vec{E}_{mp} + \sum_{q=1}^{N_s} \vec{E}_{mqp} D_{mqp} A_{mqp} e^{-j\beta s_{mq}} \right] G(z-z_m) \quad (56)$$

Let

$$\vec{E}_{mp}(q) = \vec{E}_{mqp} D_{mqp} A_{mqp} e^{-j\beta s_{mq}} \quad (57)$$

The electric field  $E_{kl}$  now becomes

$$\vec{E}_{kl} = \sum_{m=1+(k-1)N_m}^{kN_m} \sum_{p=1+(l-1)N_m}^{lN_m} \left[ \vec{E}_{mp} + \sum_{q=1}^{N_s} \vec{E}_{mp}(q) \right] G(z-z_m) \quad (58)$$

Substituting (58) into (50) yields

$$V_{kl}^{Te} = -\frac{1}{I_k^{Te}} \int_{k^{th} antenna} \left[ \sum_{m=1+(k-1)N_m}^{kN_m} \sum_{p=1+(l-1)N_m}^{lN_m} \left[ \vec{E}_{mp} + \sum_{q=1}^{N_s} \vec{E}_{mp}(q) \right] G(z-z_m) \right] \cdot \vec{I}^k dl \quad (59)$$

The discrete summations can be taken outside the integral. This yields

$$V_{kl}^{Te} = -\frac{1}{I_k^{Te}} \sum_{m=1+(k-1)N_m}^{kN_m} \sum_{p=1+(l-1)N_m}^{lN_m} \int_{k^{th} antenna} \left[ \vec{E}_{mp} + \sum_{q=1}^{N_s} \vec{E}_{mp}(q) \right] G(z-z_m) \cdot \vec{I}^k dl$$

(60)

Since the gate function is non-zero only over the  $m^{\text{th}}$  mode, the terminal voltage becomes

$$V_{kl}^{Te} = -\frac{1}{I_k^{Te}} \sum_{m=1+(k-1)N_s}^{kN_s} \sum_{p=1+(l-1)N_s}^{lN_s} \int_{m^{\text{th mode}}} \left[ \vec{E}_{mp} + \sum_{q=1}^{N_s} \vec{E}_{mp}(q) \right] \cdot \vec{I}^m dl \quad (61)$$

Expanding this equation yields

$$V_{kl}^{Te} = -\frac{1}{I_k^{Te}} \sum_{m=1+(k-1)N_s}^{kN_s} \sum_{p=1+(l-1)N_s}^{lN_s} \left[ \int_{m^{\text{th mode}}} \vec{E}_{mp} \cdot \vec{I}^m dl + \sum_{q=1}^{N_s} \int_{m^{\text{th mode}}} \vec{E}_{mp}(q) \cdot \vec{I}^m dl \right] \quad (62)$$

The voltage between the  $m^{\text{th}}$  and  $p^{\text{th}}$  modes is

$$V_{mp} = -\frac{1}{I_m^{Te}} \int_{m^{\text{th mode}}} \vec{E}_{mp} \cdot \vec{I}^m dl \quad (63)$$

Similarly, the voltage between the  $m^{\text{th}}$  and  $p^{\text{th}}$  modes due to the electric field scattered by the  $q^{\text{th}}$  segment of the wedge is

$$V_{mqp} = -\frac{1}{I_m^{Te}} \int_{m^{\text{th mode}}} \vec{E}_{mp}(q) \cdot \vec{I}^m dl \quad (64)$$

For both voltages in equations (63) and (64), the mutual coupling between the  $m^{\text{th}}$  and  $p^{\text{th}}$  modes is

$$Z_{mp} = \frac{V_{mp}}{I_p} \quad (65)$$

$$Z_{mqp} = \frac{V_{mqp}}{I_p} \quad (66)$$

Substituting equations (63) and (64) into equations (65) and (66) respectively yields

$$Z_{mp} = -\frac{1}{I_m I_p} \int_{m^{th} mode} \vec{E}_{mp} \cdot \vec{I}^m dl \quad (67)$$

$$Z_{mqp} = -\frac{1}{I_m I_p} \int_{m^{th} mode} \vec{E}_{mp}(q) \cdot \vec{I}^m dl \quad (68)$$

Rearranging equations (67) and (68) produces

$$\int_{m^{th} mode} \vec{E}_{mp} \cdot \vec{I}^m dl = -Z_{mp} I_m I_p \quad (69)$$

$$\int_{m^{th} mode} \vec{E}_{mp}(q) \cdot \vec{I}^m dl = -Z_{mqp} I_m I_p \quad (70)$$

Next, equations (69) and (70) are substituted into equation (62) to yield

$$V_{kl}^{Te} = -\frac{1}{I_k^{Te}} \sum_{m=1+(k-1)N_m}^{kN_m} \sum_{p=1+(l-1)N_m}^{lN_m} \left[ -Z_{mp} I_m I_p + \sum_{q=1}^{N_s} -Z_{mqp} I_m I_p \right] \quad (71)$$

Since the mutual coupling between the  $k^{\text{th}}$  and  $l^{\text{th}}$  elements is

$$Z_{kl}^{Te} = \frac{V_{kl}^{Te}}{I_l^{Te}}, \quad (72)$$

The terminal impedance matrix with the edge present is

$$Z_{kl}^{Te} = \frac{1}{I_k^{Te} I_l^{Te}} \sum_{m=1+(k-1)N_m}^{kN_m} \sum_{p=1+(l-1)N_m}^{lN_m} \left[ Z_{mp} + \sum_{q=1}^{N_s} Z_{mqp} \right] I_m I_p \quad (73)$$

Note that if no scatterer is present,  $N_s$  is zero and the terminal impedance matrix reduces to equation (22).

### 3.3.2 New Array Configuration

The array is configured to suppress the interference from the scatterer. This is done by combining the original elements in pairs to obtain effectively new elements as shown in figure 67. Each of the pairs of elements has a degree of freedom in the form of a weight that can be chosen appropriately. This weight is chosen to greatly reduce the signal from the interference appearing at the outputs of the new elements. Note also that the elements are reused in the sense that each new element shares at least one of the

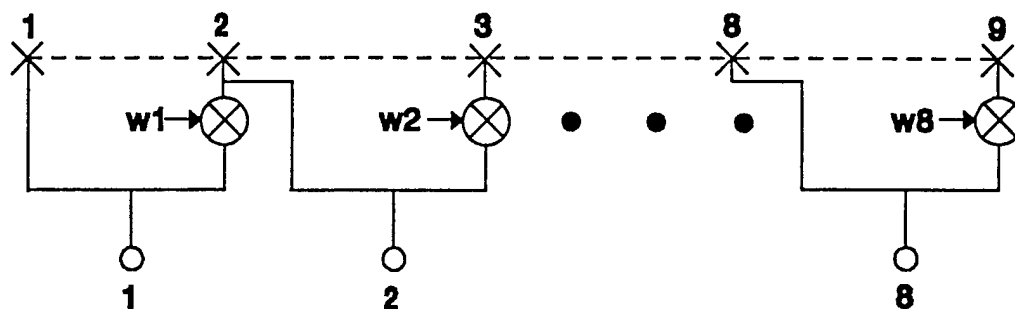


Figure 67: Configuration for Near Field Scatterer Nulling

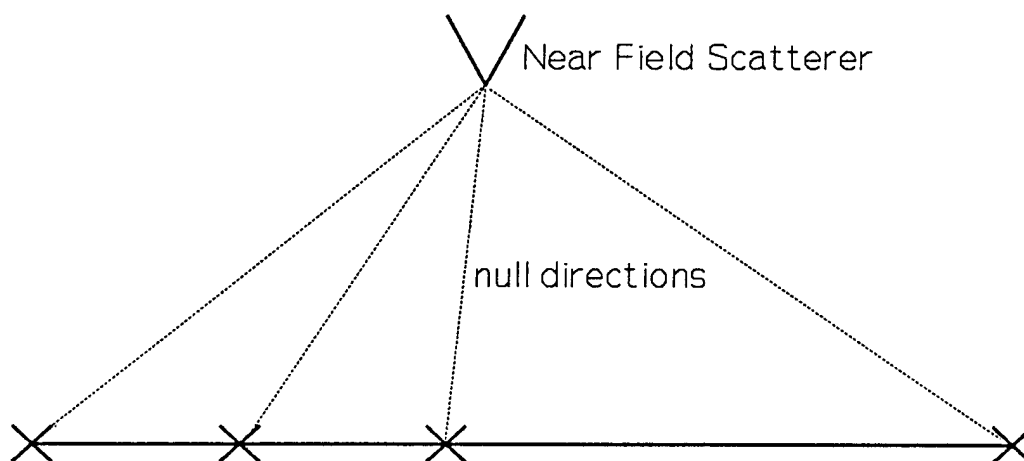


Figure 68: Array of Elements with Nulls in the Direction of the Near Field Scatterer

original elements with another one of the new elements. For example, the output of the original element number 2 is part of the outputs of both the new elements 1 and 2. This causes the noise signals at the outputs of the new elements to be correlated. The noise sources are decorrelated by applying the Mahalanobis transformation which leads to a modification of the search vector in equation (28). This array configuration is used to suppress the interference from a near field scatterer.

### 3.3.2.1 Suppression of the Interference from the Near Field Scatterer

Figure 68 shows the antenna elements and the near field scatterer. As indicated in the figure, each of the new composite antenna elements does not receive a signal from the scatterer. To achieve this interference nulling the original isotropic elements are combined in pairs as shown in figure 67. Each pair of elements is combined with a complex weight to form a new antenna element. To determine the weights, consider the first two isotropic elements and the first weight. The interference signal at the output of the new element is the sum of two spherical waves. Setting this output to zero yields

$$A_1 \frac{e^{-j\beta r_1}}{r_1} + w_1 A_2 \frac{e^{-j\beta r_2}}{r_2} = 0 \quad (74)$$

where  $A_1$  = the amplitude of the spherical wave incident upon element 1

$A_2$  = the amplitude of the spherical wave incident upon element 2

$r_1$  = the distance from the scatterer to element 1

$r_2$  = the distance from the scatterer to element 2

$\beta$  = the phase propagation constant.

Solving equation (74) for  $w_1$  yields

$$w_1 = -\frac{A_1 r_2}{A_2 r_1} e^{-j\beta(r_1 - r_2)} \quad (75)$$

Assuming that the amplitudes  $A_1$  and  $A_2$  are the same and produces

$$w_1 = -\frac{r_2}{r_1} e^{-j\beta(r_1-r_2)} . \quad (76)$$

For the wedge scatterer the amplitudes  $A_1$  and  $A_2$  are a function of the diffraction coefficient. This coefficient is in turn a function of the observation angle of the scatterer. Since the observation angle changes from element to element, the amplitudes also change from element to element. However, since the distance between adjacent elements is usually small compared to the distance between the elements and the scatterer, the change in the observation angle is small. Therefore the change in the diffraction coefficient and the amplitude of the spherical wave is small. The result is that the ratio of the amplitudes can be considered unity.

In general, the weight for the  $i^{\text{th}}$  element pair is

$$w_i = -\frac{r_{i+1}}{r_i} e^{-j\beta(r_i-r_{i+1})} \quad (77)$$

where  $r_i$  is the distance from the scatterer to the  $i^{\text{th}}$  antenna element. These weights are computed by knowing only the location of the scatterer.

### 3.3.2.2 Signal Model

The next step is to determine the effect of the new array configuration on the MUSIC algorithm. To do this, consider the incoming signals without the interference. The signal at the new composite  $i^{\text{th}}$  antenna element due to only the incident plane waves

is

$$x_i(t) = \sum_{k=1}^K u_k(t) [e^{+j\beta d_i \cos(\phi_k)} + w_i e^{+j\beta d_{i+1} \cos(\phi_k)}] + n_i(t) + w_i n_{i+1}(t) \quad (78)$$

where  $u_k(t)$  = the  $k^{\text{th}}$  narrow band plane wave

$\beta$  = the phase propagation constant

$d_i$  = the distance from the origin to the  $i^{\text{th}}$  antenna element

$\phi_k$  = the incident angle of the  $k^{\text{th}}$  signal

$n_i(t)$  = the noise at the  $i^{\text{th}}$  antenna element

$w_i$  = the  $i^{\text{th}}$  complex weight

and  $K$  = the number of sources present.

For two signals equation (78) becomes

$$x(t) = \begin{bmatrix} e^{+j\beta d_1 \cos(\phi_1)} + w_1 e^{+j\beta d_2 \cos(\phi_1)} & e^{+j\beta d_1 \cos(\phi_2)} + w_1 e^{+j\beta d_2 \cos(\phi_2)} \\ \vdots & \vdots \\ e^{+j\beta d_8 \cos(\phi_1)} + w_8 e^{+j\beta d_9 \cos(\phi_1)} & e^{+j\beta d_8 \cos(\phi_2)} + w_8 e^{+j\beta d_9 \cos(\phi_2)} \end{bmatrix} \begin{bmatrix} u_1(t) \\ u_2(t) \end{bmatrix} + n_a(t) + n_b(t) \quad (79)$$

where

$$n_a(t) = [n_1(t) \ n_2(t) \ \dots \ n_8(t)]^T \quad (80)$$

$$n_b(t) = [w_1 n_2(t) \ w_2 n_3(t) \ \dots \ w_8 n_9(t)]^T \quad (81)$$



In matrix notation equation (79) becomes

$$\vec{x} = A\vec{u} + \vec{n}_a + \vec{n}_b \quad (82)$$

where

$$A = \begin{bmatrix} e^{+j\beta d_1 \cos(\phi_1)} + w_1 e^{+j\beta d_2 \cos(\phi_1)} & e^{+j\beta d_1 \cos(\phi_2)} + w_1 e^{+j\beta d_2 \cos(\phi_2)} \\ \vdots & \vdots \\ e^{+j\beta d_8 \cos(\phi_1)} + w_8 e^{+j\beta d_9 \cos(\phi_1)} & e^{+j\beta d_8 \cos(\phi_2)} + w_8 e^{+j\beta d_9 \cos(\phi_2)} \end{bmatrix} \quad (83)$$

The covariance matrix is given by

$$R_x = E[\vec{x}\vec{x}^H] = E[(A\vec{u} + \vec{n}_a + \vec{n}_b)(A\vec{u} + \vec{n}_a + \vec{n}_b)^H] \quad (84)$$

where  $E[\cdot]$  denotes mathematical expectation. Since the noise sources are zero mean, independent and uncorrelated with the incident signals and each other, equation (84) reduces to

$$R_x = AR_u A^H + E[\vec{n}_a \vec{n}_a^H] + E[\vec{n}_a \vec{n}_b^H] + E[\vec{n}_b \vec{n}_a^H] + E[\vec{n}_b \vec{n}_b^H] \quad (85)$$

where

$$R_u = E[\vec{u}\vec{u}^H] \quad (86)$$

Using equation (80) and (81), the expectations in equation (85) become

$$E[\bar{n}_a \bar{n}_a^H] = \begin{bmatrix} \sigma^2 & 0 & \dots & 0 \\ 0 & \sigma^2 & \dots & 0 \\ \vdots & \vdots & \ddots & \vdots \\ 0 & 0 & \dots & \sigma^2 \end{bmatrix} \quad (87)$$

$$E[\bar{n}_b \bar{n}_b^H] = \begin{bmatrix} |w_1|^2 \sigma^2 & 0 & \dots & 0 \\ 0 & |w_2|^2 \sigma^2 & \dots & 0 \\ \vdots & \vdots & \ddots & \vdots \\ 0 & 0 & \dots & |w_8|^2 \sigma^2 \end{bmatrix} \quad (88)$$

$$E[\bar{n}_a \bar{n}_b^H] = \begin{bmatrix} 0 & 0 & 0 & \dots & 0 \\ w_1^* \sigma^2 & 0 & 0 & \dots & 0 \\ 0 & w_2^* \sigma^2 & 0 & \dots & 0 \\ \vdots & \vdots & \vdots & \ddots & \vdots \\ 0 & 0 & 0 & w_8^* \sigma^2 & 0 \end{bmatrix} \quad (89)$$

$$E[\bar{n}_b \bar{n}_a^H] = \begin{bmatrix} 0 & w_1 \sigma^2 & 0 & \dots & 0 \\ 0 & 0 & w_2 \sigma^2 & \dots & 0 \\ 0 & 0 & 0 & \dots & 0 \\ \vdots & \vdots & \vdots & \ddots & \vdots \\ 0 & 0 & 0 & 0 & w_8 \sigma^2 \end{bmatrix} \quad (90)$$

Note that  $E[\bar{n}_a \bar{n}_b^H]$  is the Hermitian of  $E[\bar{n}_b \bar{n}_a^H]$ . Substituting equations (87), (88),

(89), and (90) into equation (85) yields

$$R_x = A R_u A^H + \sigma^2 \Sigma_\eta \quad (91)$$

where

$$\Sigma_{\eta} = \begin{bmatrix} 1 + |w_1|^2 & w_1 & 0 & \dots & 0 \\ w_1^* & 1 + |w_2|^2 & w_2 & \dots & 0 \\ 0 & w_2^* & 1 + |w_3|^2 & \dots & 0 \\ \vdots & \vdots & \vdots & \ddots & w_7 \\ 0 & 0 & 0 & w_7^* & 1 + |w_8|^2 \end{bmatrix} \quad (92)$$

Equation (91) can be cast in a form suitable for the MUSIC algorithm by first applying the Mahalanobis transformation which is,

$$\bar{y} = \Sigma_{\eta}^{-1/2} \bar{x} \quad (93)$$

Applying this transformation to equation (84) yields

$$R_y = \Sigma_{\eta}^{-1/2} A R_u A^H \Sigma_{\eta}^{-H/2} + \sigma^2 I \quad (94)$$

where  $I$  is the identity matrix. Setting

$$B = \Sigma_{\eta}^{-1/2} A \quad (95)$$

yields

$$R_y = B R_u B^H + \sigma^2 I \quad (96)$$

Comparing this to equation (185) in Appendix E, shows that the MUSIC algorithm can now be applied in the usual manner but with the search vector being

$$a(\phi) = \Sigma_{\eta}^{-1/2} \begin{bmatrix} e^{+j\beta d_1 \cos(\phi)} + w_1 e^{+j\beta d_2 \cos(\phi)} \\ \vdots \\ e^{+j\beta d_8 \cos(\phi)} + w_8 e^{+j\beta d_9 \cos(\phi)} \end{bmatrix} \quad (97)$$

This will suppress the interference that arrives at the antenna elements due to the scatterer without significantly affecting the resolution of the MUSIC algorithm.

### 3.4 Results

The MUSIC algorithm with the array configuration in figure 67 and the search vector in equation (97) is investigated for three different cases. In the first case no mutual coupling is present between the array elements or the elements and the source of the interfering signals. Therefore, equation (73) is not needed and the ability of the array configuration in figure 67 with the search vector in equation (97) to suppress interfering signals can be investigated. In the second case, a point scatterer is used to generate the interfering signals. In this case there exists mutual coupling between the array elements and the scatterer. Therefore it is necessary to use equation (73) along with the new array configuration and search vector in equation (97) to suppress the interfering signals. In the third scenario, the point scatterer is replaced by a distributed scatterer. The interference no longer emanates from a single point. In this case equations (73) and (97) are used to suppress the interference where it is assumed that all the interference can be considered as arriving from a single point. This is a valid assumption in some cases but not in all cases. These cases show the usefulness of the new array configuration along with the new search vector in suppressing the scattering from a near field object.

In this chapter all the simulations are performed on the nine element linear dipole

array of chapter 2. This array is designed to resolve angles of arrival over one octave from 200 MHz to 400 MHz. The incident signals are plane waves at frequencies in the center of the operating band at 300 MHz and 305 MHz. The spectra shown are the normalized average of 20 simulations computed every  $0.1^\circ$ . In all simulations, the SNR is fixed at 10 dB. The simulated data is composed of 300 snapshots as in chapter 2.

### 3.4.1 Suppression of the Interference

The antenna element configuration with the search vector as given in equation (97) is used to resolve plane waves when interference from a near field scatterer is present. The spherical waves emanate from point sources located at the given position and with the same frequency as the incident plane waves. Point sources are used since, unlike a scatterer, they are uncoupled to the antenna array. Therefore, the usefulness of the element configuration in figure 67 can be investigated without being concerned about the effects of mutual coupling.

The simulations are performed with two plane waves and two point sources. The point sources are located as shown in figure 64. Mathematically, the incident signals are

$$s_1 = \left( A_1 e^{-j(n-1)\beta_1 d \cos(\phi_1)} + A_2 \frac{e^{-j\beta_1 r_n}}{r_n} \right) e^{-j2\pi k \frac{f_1}{f_s}} \quad (98)$$

$$s_2 = \left( A_1 e^{-j(n-1)\beta_2 d \cos(\phi_2)} + A_2 \frac{e^{-j\beta_2 r_n}}{r_n} \right) e^{-j2\pi k \frac{f_2}{f_s}} \quad (99)$$

where  $A_1$  is the amplitude of the plane waves,  $n$  is the antenna element index,  $d$  is the separation between elements,  $\phi_1$  and  $\phi_2$  are the angles of arrival of the incident plane waves with respect to the axis of the array,  $A_2$  is the amplitude of the spherical waves,  $r_n$  is the distance from the  $n^{\text{th}}$  antenna element to the point sources,  $k$  is the snapshot number, and  $f_s$  is the sampling frequency.

The simulations are performed for various signal to interference (S/I) ratios. The desired signals are the plane waves and the interfering signals are the spherical waves. In the first case, the plane wave and spherical wave amplitudes are chosen such that the S/I ratio is 5 dB. In the second and third cases, the S/I ratio is 0 dB and -5 dB respectively. The third case does not represent a realistic near field scatterer since the spherical waves are stronger than the plane waves. These simulations show the usefulness of the antenna element configuration in figure 67 of suppressing spherical waves.

Figure 69 shows the effect of the spherical waves when the S/I ratio is +5 dB. The spectrum labeled "Plane Waves Only" shows the ideal spectrum without the interference. This spectrum is calculated with the search vector in equation (28) and represents the best possible spectrum under the given conditions. The spectrum labeled "Plane and Spherical Waves" shows the MUSIC spectrum with the search vector in equation (28) and the incident signals in equations (98), and (99). Notice that the presence of the spherical waves prevents the resolution of the desired signals. The spectrum labeled "Compensated" shows the output of the MUSIC algorithm with the search vector calculated using equations (77), (92), and (97). Notice that the spectrum is almost identical to the ideal case. Figure 69 shows that when the S/I ratio is 5 dB, the

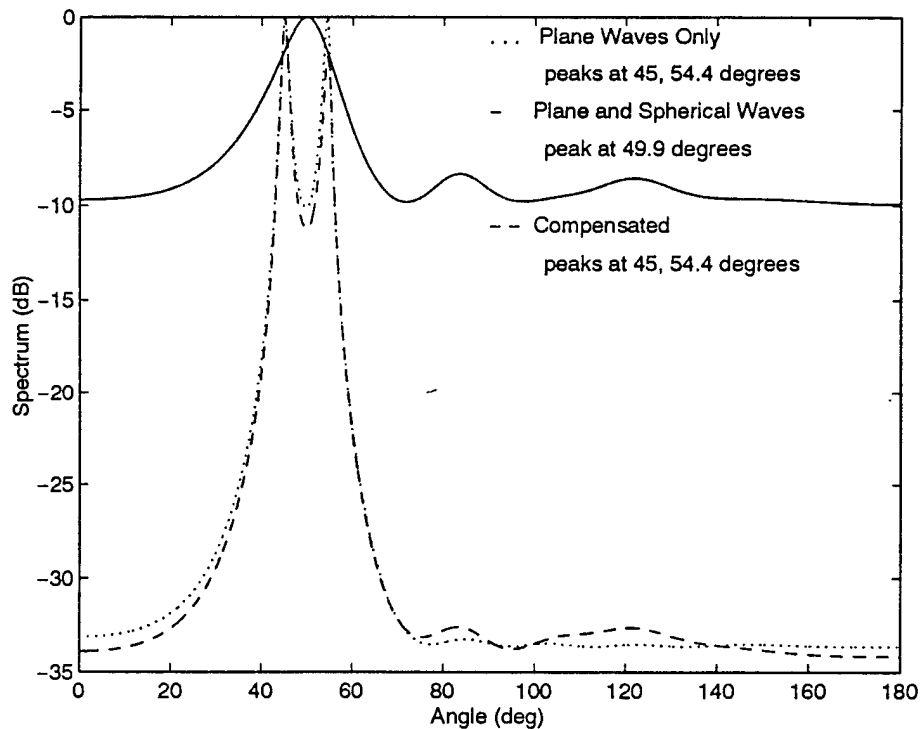


**Figure 69: Compensation for Point Sources, S/I = 5 dB**

resolution of the MUSIC algorithm can be restored with the modified search vector.

Figure 70 shows the effect of the interference when the S/I ratio is 0 dB. In this case, the interfering spherical waves are as strong as the incident plane waves. In figure 70, the ideal spectrum is repeated for reference. The "Plane and Spherical Waves" spectrum show that again the MUSIC algorithm can not resolve the two plane waves with the search vector in equation (28). This is to be expected since figure 69 shows that even with weaker spherical waves, the plane waves can not be resolved. The compensated spectrum shows that with the search vector in equation (97), it is possible to restore, almost completely, the resolution capability of the algorithm. Figure 70 shows that even when the interference is as strong as the desired signal, it can be completely suppressed with the array configuration in figure 67.

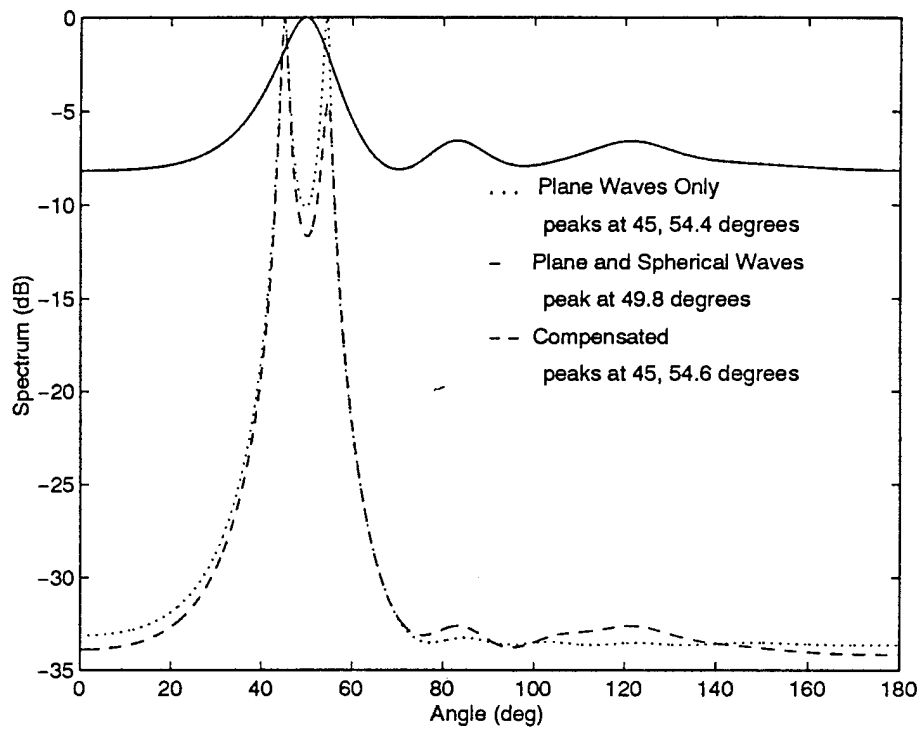


Figure 70: Compensation for Point Sources,  $S/I = 0$  dB

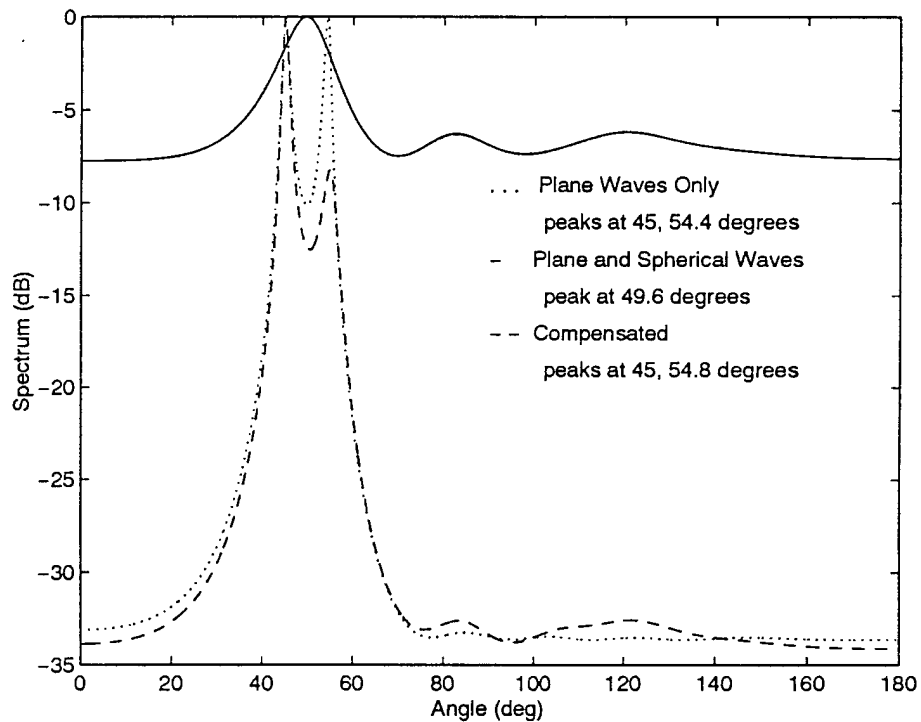


Figure 71: Compensation for Point Sources,  $S/I = -5$  dB



Figure 71 shows the effect of the spherical waves when the S/I ratio is -5 dB. In this case, the interfering spherical waves are stronger than the incident plane waves. Again, in figure 71, the ideal spectrum is included as a reference of the best possible result. The "Plane and Spherical Waves" spectrum shows the MUSIC algorithm can not resolve the plane waves using the search vector in equation (28). The compensated spectrum shows the spherical waves can be suppressed with the search vector in equation (97). Again, the interference is almost completely suppressed by the array configuration in figure 67. Figure 71 shows that even when the spherical waves are stronger than the plane waves, they can be suppressed to the extent that the MUSIC algorithm can resolve the two plane waves.

Figures 69, 70, and 71 show the results of using the antenna element configuration in figure 67 to suppress the interference from a near field scatterer. In all three cases the interference adversely affects the resolution capability of the MUSIC algorithm. The resolution of the MUSIC algorithm, however, is restored by using the new antenna element configuration and the new search vector. The resolution of the algorithm is restored even when the interference is stronger than the incident signals.

### 3.4.2 Point Scatterer

The antenna element configuration and the terminal impedance matrix are used in this section to suppress the effect of a near field point scatterer. The scatterer is represented as a point so that all the energy scattered by the object can be considered to be arriving from a single point. Unlike the point sources in the previous chapter, however, the point scatterer is coupled to the antenna array. Therefore, it is necessary to

use the terminal impedance matrix along with the new antenna array configuration in figure 67 to compensate for the effects of the near field scatterer. Since the scatterer is small enough to be considered a point, the terminal impedance matrix in equation (73) is calculated with  $N_s = 1$ . In this section, the new array configuration, search vector and terminal impedance matrix are used to suppress the interference from a point scatterer.

The simulations in this section are performed on the linear array in figure 64. In this figure, the source of the spherical waves is replaced with a point scatterer. The scatterer produces spherical waves at the same frequency as the incident plane waves. This interference hinders the ability of the MUSIC algorithm to resolve the two plane waves. Note that the point scatterer produces signals very similar to the point sources in the previous section in the sense that they appear to be coming from the same point and have the same frequency as the incident plane waves. The linear array in figure 64 is used to determine the effects of a point scatterer on the resolution capability of the MUSIC algorithm.

The nine element linear dipole array is designed as described in chapter 2. This array can resolve plane waves over a one octave bandwidth from 200 to 400 MHz. The incident signals are uniform plane waves at 300 and 305 MHz with angles of arrival at  $45^\circ$  and  $60^\circ$ . The usual angle of arrival of  $55^\circ$  is replaced with  $60^\circ$  so that in the absence of a scatterer, the MUSIC algorithm can resolve the signals with mutual coupling present. These parameters are used for the nine element dipole array to determine the ability of the array configuration in figure 67 and the terminal impedance matrix in suppressing the effects of a point scatterer.

The Radar Cross Section (RCS) of the point scatterer is varied to determine the ability of the new array configuration to suppress a near field scatterer. The RCS is defined by the equation [50]

$$\sigma = \lim_{r \rightarrow \infty} 4\pi r^2 \frac{|\vec{E}^s|^2}{|\vec{E}^i|} \quad (100)$$

where  $\sigma$  is the RCS,  $E^i$  is the electric field incident upon the scatterer, and  $E^s$  is the electric field scattered by the object. The RCS is typically expressed in decibels and is a measure of how much energy is scattered by the object. The RCS of the point scatterer is varied from -5 to 5 dBsm to determine the ability of the terminal impedance matrix and the new array configuration in suppressing the interference from a point scatterer.

Figure 72 shows the MUSIC spectrum for the nine element linear dipole array of chapter 2 and a near field scatterer with an RCS of -5 dBsm. The ideal curve shows the spectrum without mutual coupling and without the scatterer present. This is the best possible spectrum achievable with the MUSIC algorithm under the given conditions. The solid curve in figure 72 is calculated with equation (35) and shows the effects of only mutual coupling without the scatterer present. The third spectrum is calculated with equation (47) and shows the effects of the near field scatterer. Notice that the scatterer almost prevents the signals from being resolved. Figure 72 shows the effects of an uncompensated near field point scatterer with a RCS of -5 dBsm.

Figure 73 shows the results of compensating for the near field scatterer. The ideal

curve is the same as that in figure 72 and is included as a reference. The solid curve shows the result of compensating for the mutual coupling including the scatterer but not compensating for the interference from the scatterer with the new array configuration and search vector. This corresponds to the equation

$$\sum_{l=1}^M Z_H^{Te} I_l' = V_k + V_k^s \quad k = 1, 2, \dots, M \quad (101)$$

where  $Z_H^{Te}$  is given in equation (73). Notice that the solid curve yields a good estimate of the actual spectrum. This is because the signal from the scatterer is very small with a RCS of -5 dBsm. The dashed curve corresponds to correcting for  $V_k^s$  but not mutual coupling. In this case, the spherical waves from the scatterer are suppressed with the array configuration in figure 67 but no compensation is made for the mutual coupling effects. In this case the effect on the spectrum is more significant since the mutual coupling between the antenna elements is stronger than the signal from the scatterer. The final spectrum in figure 73 corresponds to correcting for both mutual coupling and the spherical waves from the scatterer using figure 67 and equations (73) and (97). This case corresponds to equation (48). Notice that the new spectrum is very close to the ideal spectrum. Figure 73 shows that compensating for only the mutual coupling produces a reasonably good estimate of the spectrum but compensating for both the mutual coupling and the interfering signals from the scatterer yields a spectrum almost as good as the ideal case.

Figure 74 shows the effect of a point scatterer with a RCS of 0 dBsm on the

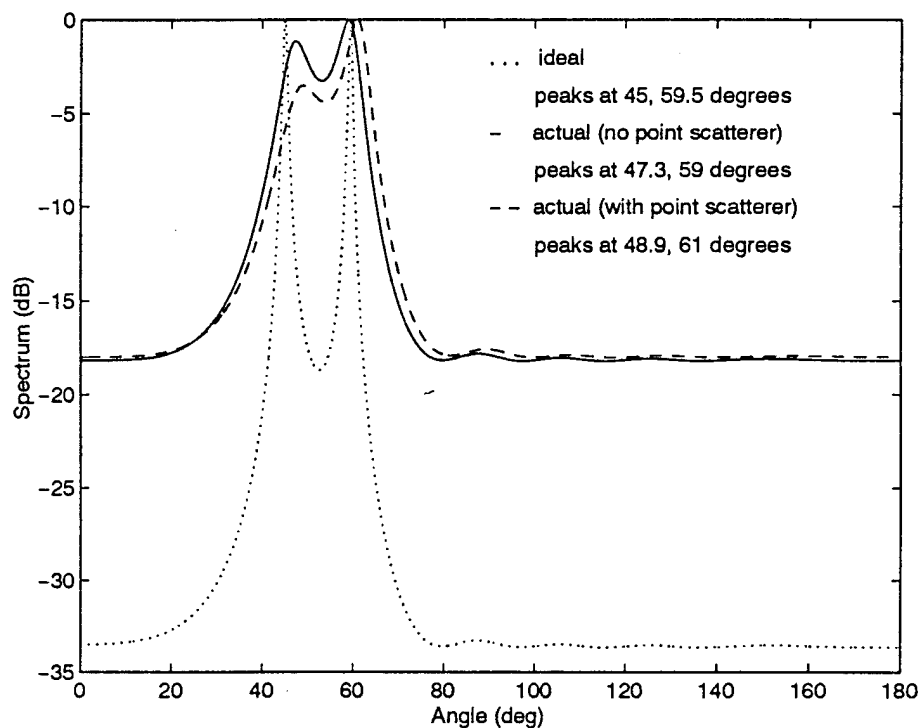


**Figure 72: MUSIC, Actual Spectrums, RCS = -5 dBsm,  
Angles = 45°, 60°, Frequencies = 300, 305 MHz**

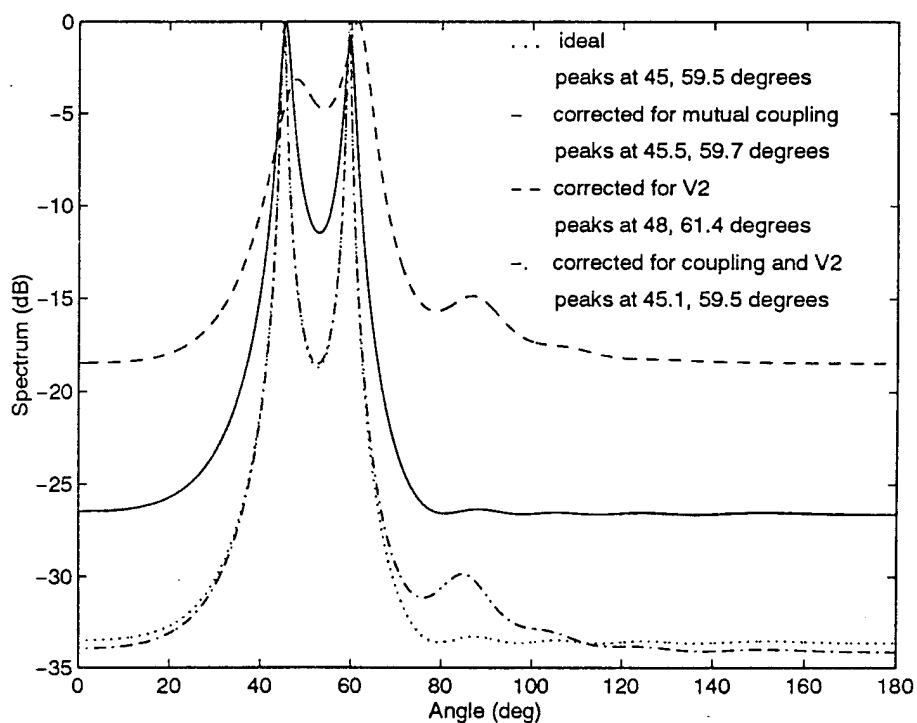


**Figure 73: MUSIC, Corrected Spectrums, RCS = -5 dBsm,  
Angles = 45°, 60°, Frequencies = 300, 305 MHz**

MUSIC spectrum. As in figure 72, the ideal curve shows the spectrum without mutual coupling and without the scatterer present. The solid curve shows the effect of mutual coupling without the scatterer present. The dashed curve shows the spectrum with mutual coupling and the 0 dBsm point scatterer. This spectrum is very similar to the corresponding spectrum in figure 72. Notice, however, that the signals are closer to being unresolvable. Figure 74 shows the effect of a 0 dBsm point scatterer in the MUSIC spectrum.

In figure 75 the point scatterer is compensated for as in figure 73. Notice that the spectra in figure 75 are very similar to those in figure 73. In this case, the solid curve which represents compensating for only mutual coupling has a minimum value greater than that of the corresponding spectrum in figure 73. This occurs since the object scatters more energy to the array since the RCS is larger. The final spectrum shows that compensating for both the mutual coupling and the interference from the scatterer produces a spectrum almost as good as the ideal case. This spectrum is practically the same as the compensated spectrum in figure 73.

Figures 76 and 77 for a point scatterer of 5 dBsm correspond to figures 72 and 73. The effect of the scatterer in figure 76 almost prevents the two signals from being resolved. This spectrum yields the worst estimate of the angles of arrival compared to the corresponding spectra in figures 72 and 74. Figure 77 shows the result of compensating for the effects of the scatterer. Notice that the spectrum from correcting for only mutual coupling is worse than in figures 73 and 75. This is due to the fact that the RCS of the scatterer is the largest of the three cases. Notice that even with the large

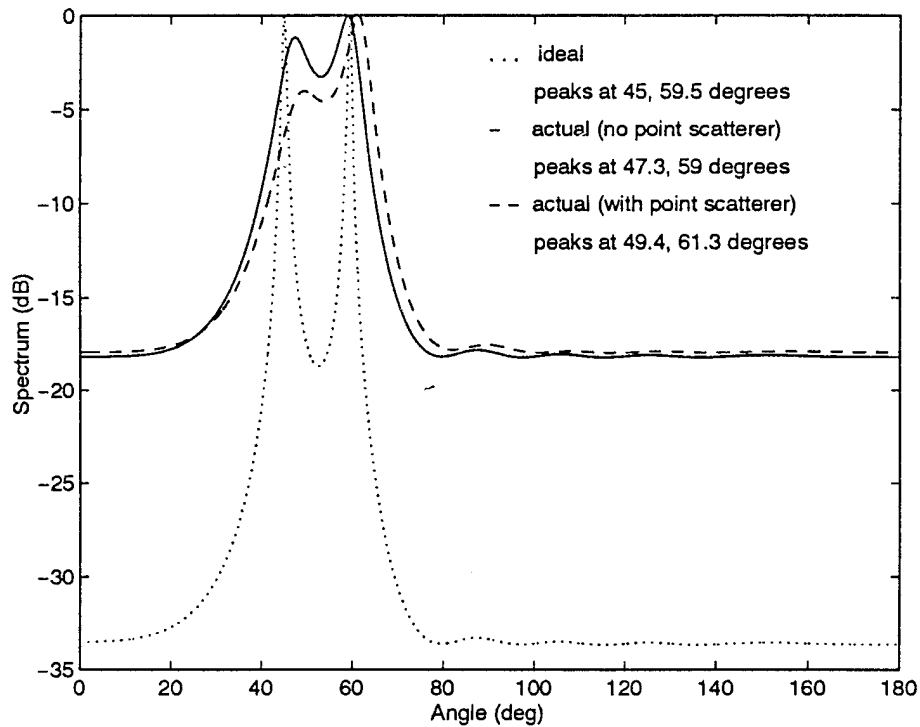


**Figure 74: MUSIC, Actual Spectrums, RCS = 0 dBsm,  
Angles = 45°, 60°, Frequencies = 300, 305 MHz**

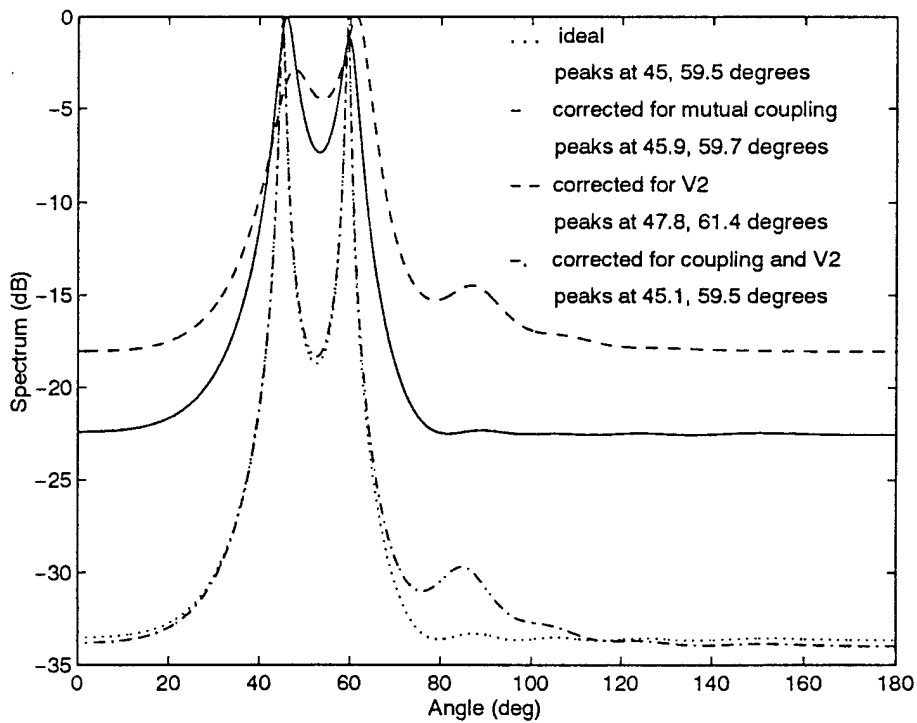


**Figure 75: MUSIC, Corrected Spectrums, RCS = 0 dBsm,  
Angles = 45°, 60°, Frequencies = 300, 305 MHz**

RCS, the final spectrum yields an estimate of the angles of arrival almost as good as the ideal case. Figures 76 and 77 show the result of a point scatterer of 5 dBsm.

The mutual coupling is shown to be significant in figures 72 through 77. The mutual coupling between two objects is inversely proportional to the distance between them. Since the antenna elements are separated by  $0.375\lambda$  the coupling between them is significant. The coupling between the near field object and the antenna array is less significant because the distance between them, in general, is greater. The coupling is also less significant since the object does not scatterer all the energy from the array back toward the array. The mutual coupling between the scatterer and the array is less significant than the coupling between the elements themselves. Mathematically, this means that

$$Z_{mp} > \sum_{q=1}^{N_s} Z_{mqp} \quad \text{for every } m \text{ and } p. \quad (102)$$

In other words, equation (22) is approximately the same as equation (73). Note that in this section the near field object is a point scatterer and therefore  $N_s = 1$ .

The significance of compensating for the mutual coupling between the scatterer and the array is investigated in figure 78. In this case a point scatterer with a RCS of 5 dBsm is placed  $0.5\lambda$  from the array. The results for this case are shown in figure 79. The ideal spectrum shows the result when no mutual coupling or scatterer is present. This is the best possible spectrum under the given conditions. The spectrum labeled "actual" shows the expected result when mutual coupling and the scatterer are present.



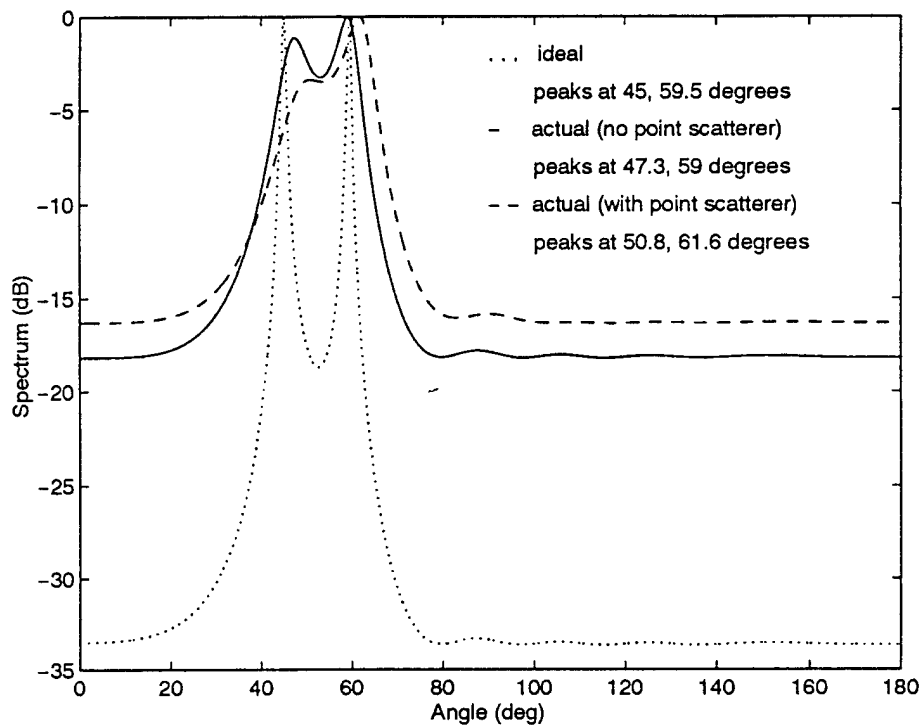


**Figure 76: MUSIC, Actual Spectrums, RCS = 5 dBsm,  
Angles = 45°, 60°, Frequencies = 300, 305 MHz**

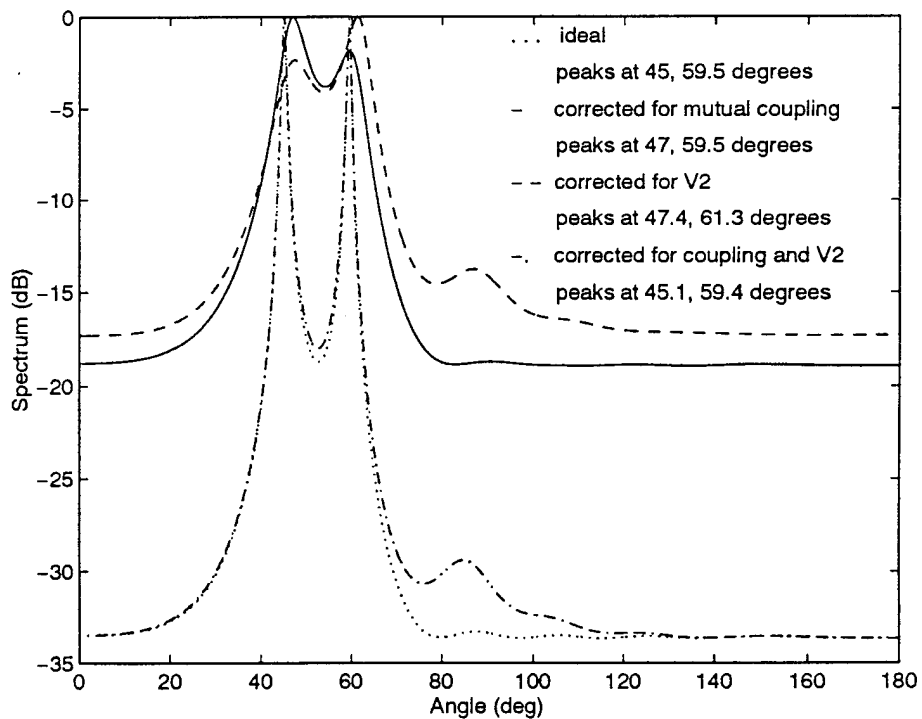


**Figure 77: MUSIC, Corrected Spectrums, RCS = 5 dBsm,  
Angles = 45°, 60°, Frequencies = 300, 305 MHz**

No compensation is performed for either the mutual coupling or the interference from the scatterer. The spectrum labeled "corrected for antenna coupling" shows the result when the new array configuration and search vector are used but the terminal impedance matrix is calculated with equation (22). This assumes that

$$\sum_{q=1}^{N_s} Z_{mqp} \quad (103)$$

is negligible compared to  $Z_{mp}$  for all  $m$  and  $p$ . This spectrum yields a very accurate estimate of the angles of arrival even though a strong scatterer with a RCS of 5 dBsm is near the array. The final spectrum labeled "corrected for all coupling" shows the result of using the new array configuration and equation (73) instead of equation (22). Note that the spectrum is not significantly improved. Figures 78 and 79 show that only a small improvement results when the coupling between the scatterer and the antenna array is compensated.

### 3.4.3 Distributed Scatterer

Sections 3.4.1 and 3.4.2 show the results when all the interference arrives from a single point. In section 3.4.1, point sources are used to generate the interference. In this case, the array configuration in figure 67 along with the modified search vector in equation (97) is used to suppress the interference and restore the resolution capability of the MUSIC algorithm. In section 3.4.2, the point sources are replaced with a point scatterer. In this case, the interference is very similar to the previous case but there is now mutual coupling between the scatterer and the array. This coupling is accurately

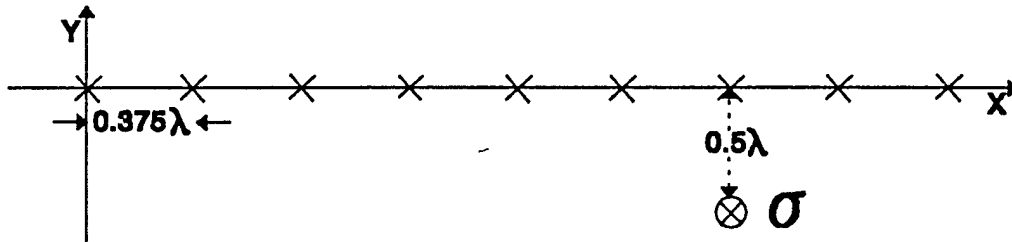


Figure 78: Array with Nearby Scatterer

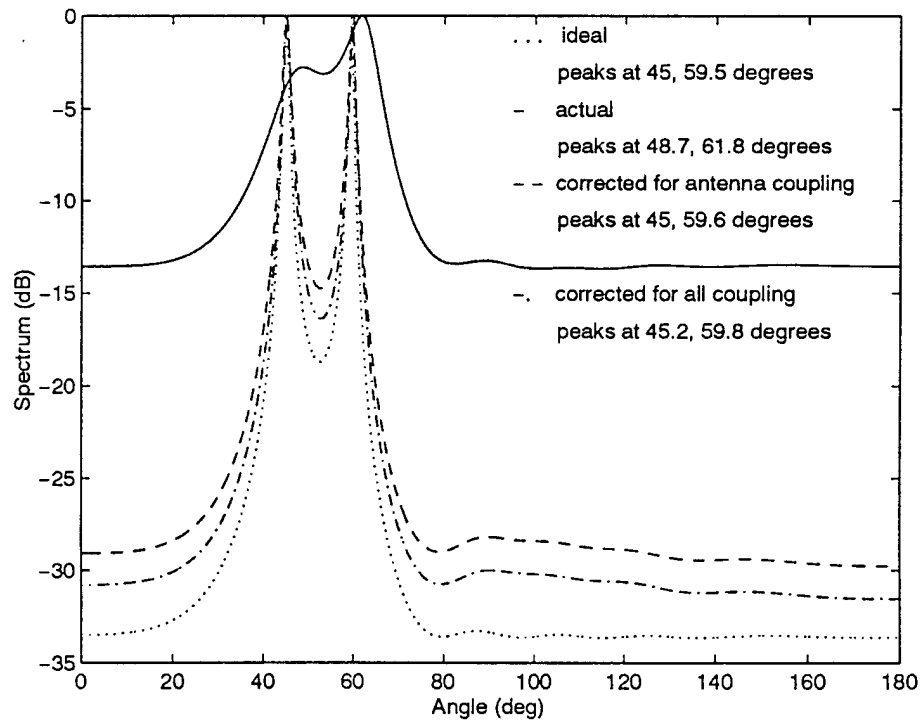


Figure 79: Compensation for a Strong Near Field Scatterer

suppressed with equation (73). The previous two sections demonstrate that the interference can be adequately suppressed when it arrives from a single point.

In this section, the scattered energy arrives from a finite size object. However, all the energy can be considered as having one phase center. As shown in figure 80, the scatterer is a  $90^\circ$  wedge with a length of 10 meters. The mutual coupling between the wedge and scatterer is suppressed using equation (73). For the wedge scatterer, the energy arriving at the array from the scatterer can be considered as emanating from the endpoints of the wedge which are  $10\lambda$  apart. However, since the length of the wedge lies in the plane of the electric field vector, the energy can be considered as arriving from the midpoint of the wedge which lies in the xy plane. Therefore, the weights for the array configuration in figure 67 are chosen assuming that the wedge is a point scatterer at the location shown in figure 80.

The results for the uncompensated distributed scatterer are shown in figure 81. The ideal spectrum assumes that no mutual coupling or scatterer is present. The solid curve shows the spectrum with mutual coupling but without the scatterer. This is the expected spectrum when no scatterer is present and no compensation is made for mutual coupling. The final spectrum in figure 81 shows the expected spectrum when the scatterer is present and no compensation is attempted. Notice that the spectrum is slightly worse due to the presence of the scatterer. Figure 81 shows that adding the scatterer causes a slight change in the actual spectrum which is much worse than the ideal spectrum.

Figure 82 shows the result of compensating for the distributed scatterer. As usual,

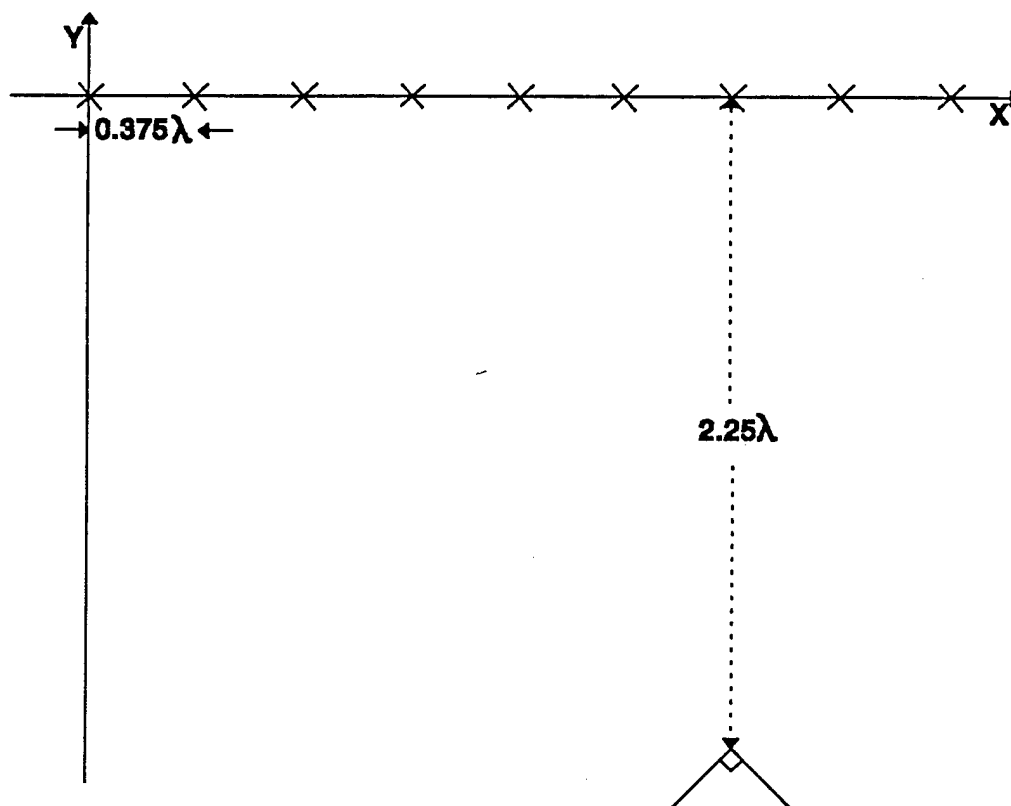


**Figure 80: Distributed Near Field Scatterer**

the ideal spectrum is included as a reference. The solid curve represents compensating for mutual coupling with equation (73). In this case  $N_s$  is much greater than one since the scatterer has significant size. The spectrum labeled "corrected for V2" shows the effect of correcting for the interference from the scatterer but not the mutual coupling between the scatterer and the array or between the array elements themselves. Notice that in this case only one signal is apparent in the spectrum. The final spectrum represents compensating for all the mutual coupling and the interference from the scatterer. Notice that the spectrum is almost as good as the ideal case. Figure 82 shows that the resolution capability of the MUSIC algorithm can be restored for a large scatterer if all the scattered

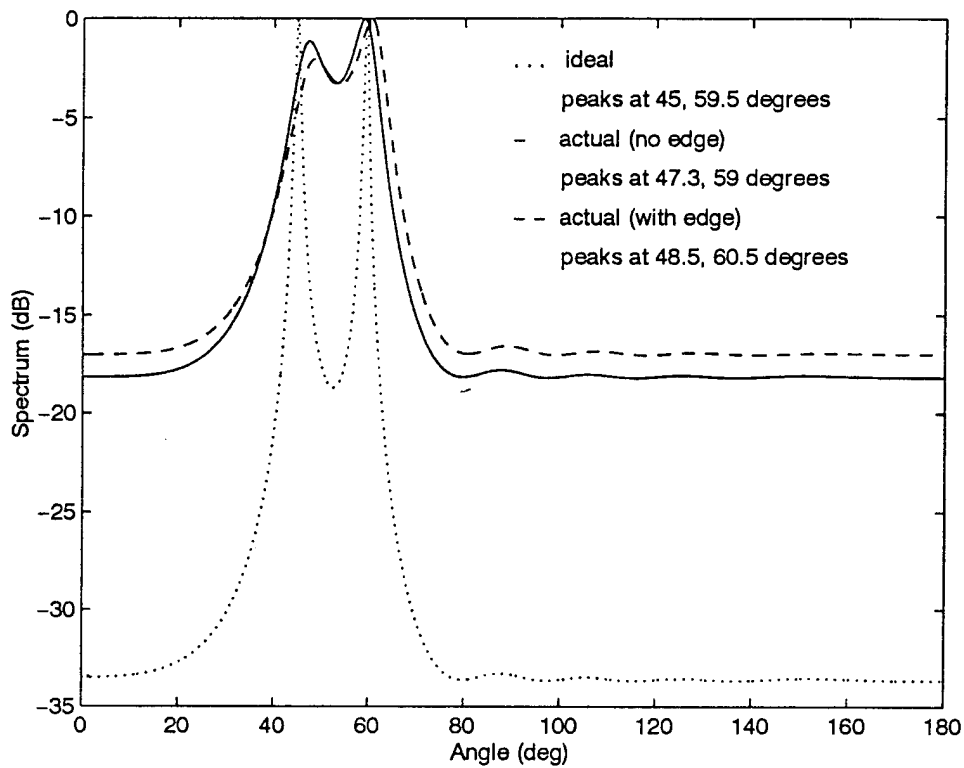


Figure 81: Effects of Mutual Coupling and a Nearby Edge

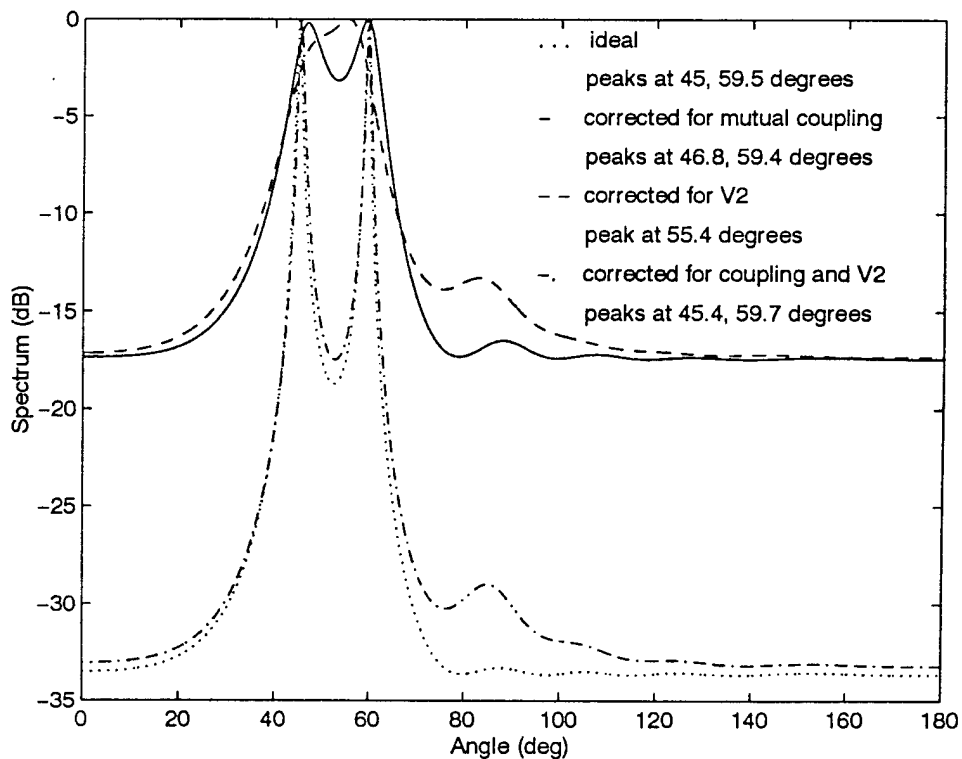


Figure 82: Correction for a Nearby Edge

energy can be considered as arriving from one point on the scatterer.

### 3.5 Summary and Conclusions

The effects of a near field scatterer on the MUSIC algorithm are investigated in this chapter. This object may be a nearby building or the inside of an antenna array's radome. This object scatters energy toward the array and degrades the ability of the algorithm to resolve two signals with a small angular separation. It is shown that the effect of a near field scatterer can be suppressed by the method presented here.

The presence of a near field scatterer is modeled with a hybrid technique that combines the method of moments with the Uniform Theory of Diffraction. The method of moments is used to model the array while diffraction theory is used to model the scatterer. This hybrid technique produces a second moment method impedance matrix and a second excitation vector. These terms alter the original system of equations to produce the currents on the array due to both the incident signals and the scattered fields.

The effect of a near field scatterer is compensated for by a new terminal impedance matrix and a new array configuration. The new matrix models both the mutual coupling directly between the antenna terminals and the coupling between the elements due to the field from one element scattered by the object to one of the elements. The new antenna element configuration combines the elements in pairs with a complex weight. The weight for each pair is chosen such that a null is placed at the point of the scatterer. This produces correlated noise which is decorrelated using the Mahalanobis transformation. The MUSIC algorithm is then applied with an altered 1 search vector to account for this transformation. The new terminal impedance matrix and

array configuration successfully suppress the effects of a near field scatterer.

The suppression of near field interference is first investigated with uncoupled nearby point sources. Since these sources are uncoupled, no mutual coupling exists between them and the array. No mutual coupling is also assumed between the elements. This allows an investigation of the ability of the new array configuration and search vector in suppressing the effects of near field interference. It is shown that the interference can be suppressed and the resolution of the algorithm can be restored even when the interference is stronger than the original signal.

In the next case, the point sources are changed to a point scatterer. In this case there is mutual coupling between the scatterer and the array along with interference from the scatterer. The new terminal impedance matrix is used to compensate for the mutual coupling and the new array configuration is used to suppress the interference. The results show that even when the scatterer has a large RCS, its effects can be adequately suppressed.

In the final case, the scatterer is changed to a finite length wedge. In this case, the interference arrives from all parts of the wedge. However, the interference can be suppressed using the new array configuration since all the energy can be considered as having one phase center. The simulations show that the effects of a finite length near field scatterer can be suppressed using the technique in this chapter if all the energy has a common phase center.



## CHAPTER IV

### MUTUAL COUPLING COMPENSATION

### APPLIED TO MEASUREMENTS

Chapter 2 shows that the mutual coupling between antenna elements adversely effects the ability of the direction finding algorithm to resolve two signals with a small angular separation. The mutual coupling effects are effectively eliminated by using the terminal impedance matrix which models the mutual coupling between the antenna elements. The new spectrum is approximately the same as the ideal spectrum which assumes no mutual coupling is present.

In this chapter the terminal impedance matrix is applied to actual measurements rather than a simulated signal. This is done with two sets of measurements. The first set consists of time domain data taken with various monopole arrays. These measurements are obtained from a colleague in Germany [52]. The second set of measurements consists of steady state frequency domain data for a horn array. In this case the magnitude and phase at the terminals of each horn is given for a particular frequency. These measurements are obtained from WL/AARM-3 at Wright-Patterson Air Force Base. For the horn measurements, the terminal impedance matrix is calculated in a different manner since the technique in chapter 2 is derived for thin wire antennas.

Neither of the two sets of experimental data used here is obtained specifically to

illustrate the problems of strong mutual coupling in an antenna array. For the monopole array data the inter-element spacing is  $0.34\lambda$  or larger. For the horn array data, the element spacing is half a wavelength. Therefore, the mutual coupling is not very strong. Also, it would have been best to measure the mutual coupling matrix with the actual setup and use this matrix for compensation purposes. Unfortunately, this data is not available. The mutual coupling matrix is obtained from an electromagnetic model of the antenna array. With this model, it is difficult or impossible to account for the realistic effects of a curved lossy earth. For the horn array data, a new technique is derived to extract the mutual coupling matrix from the data. The horn array is not modeled numerically. The resulting mutual coupling matrix is shown to be sensitive to the angle of arrival. This should not be the case since, as shown in Appendix A, the mutual coupling matrix is only dependent upon the geometry of the array and the frequency of operation. However, even with these difficulties, it is still illustrative to process the measurements.

#### 4.1 Monopole Measurements

In chapter 2, the simulations are performed on arrays designed to resolve narrowband signals that can occur over a bandwidth of one octave. To prevent the formation of grating lobes which leads to ambiguous angles of arrival, the arrays are designed to have an inter-element spacing of  $\lambda/2$  at the highest frequency of operation. This leads to strong mutual coupling at the low end of the operational bandwidth.

In this chapter the monopole arrays are not specifically designed to resolve narrowband signals over a wide bandwidth. Therefore the mutual coupling effects are not nearly as significant as in chapter 2. This can be determined by examining the spacing

in wavelengths of the three arrays operated at their respective frequencies. For the linear array, the spacing is  $0.4\lambda$ . In chapter 2 the spacing varies from  $0.25\lambda$  to  $0.5\lambda$ . For the cross array the spacing in this chapter is  $0.453\lambda$ . In chapter 2 the separation between adjacent elements in the cross array varies from  $0.2\lambda$  to  $0.4\lambda$ . For the circular array in this chapter, the separation between adjacent elements is  $0.347\lambda$ . In chapter 2, this spacing varies from  $0.19\lambda$  to  $0.382\lambda$ . In chapter 2 the separation between elements is much smaller since the arrays are designed to operate over one octave. This leads to significant mutual coupling effects which hinder the ability of the direction finding algorithm to resolve two signals with a small angular separation. In this chapter, the arrays are not designed for this purpose and therefore the mutual coupling effects are less significant.

In this section, the terminal impedance matrix from chapter 2 is used to compensate for the mutual coupling effects in the monopole measurements. These measurements are made with linear, cross and circular arrays as in chapter 2. The antenna arrays are modeled with the method of moments to determine the effects of mutual coupling. The terminal impedance matrix from the moment method model of the antenna array is then used to compensate for the mutual coupling effects in the measurements.

#### **4.1.1. Antenna Arrays**

The measurements are made with linear, cross, and circular monopole arrays. At the frequencies of interest, the earth can be considered to be a perfect conductor and therefore the monopoles can be considered to be dipoles. Each monopole is 2 meters

long which corresponds to between 0.18 and 0.40 wavelengths at the frequencies of interest. The diameter of the monopole is 2.5 mm with a dielectric coating of "glass fibre reinforced plastic" which extends the outer diameter of the monopole to 7.55 mm [51]. Each monopole is connected to a high input impedance amplifier. These elements are used in linear, cross, and circular arrays to determine the effects of mutual coupling on the direction finding algorithms described in Appendices B through E.

The monopoles are formed into a linear array as described in chapter 2. For this array, the incident signals are from two independent transmitters located approximately 200 meters from the array with a frequency of 60 MHz [51]. Since the transmitters are independent, the signals are uncorrelated although they are at the same nominal frequency. The inter-element spacing is 2 meters which corresponds to 0.4 wavelengths at 60 MHz. This spacing prevents the formation of grating lobes which lead to ambiguous angles of arrival. Three sets of data are used to determine the resolution capability of the algorithms for actual measurements. In all cases, the signals are at 60 MHz with angles of incidence at  $64^\circ$  and  $78^\circ$ .

The measurements are also made with a cross array. The shortest distance between elements in the cross array is 5.0 meters. The signals are also from independent transmitters located 200 meters away from the array but with frequencies of 27.185 MHz [51]. With this frequency and spacing, grating lobes begin to appear in the antenna pattern which lead to ambiguous angles of arrival. Only one set of data is available for the cross array.

The final set of measurements are made with a circular array. In this case the

transmitters are 60 meters away from the array. The radius of the array is 5.0 meters and the frequency is again 27.185 MHz [51]. At this frequency, no grating lobes appear in the antenna pattern, and therefore no ambiguous angles of arrival appear in the spectrum. For this array, two sets of data are available.

#### 4.1.2 Measurement Setup

The system in figure 83 is used to produce the in-phase and quadrature components of the incident signal at baseband [52]. In this block diagram, the signal is first received by a monopole antenna element connected to a high input impedance amplifier. This signal is then mixed with a variable local oscillator. The frequency of this oscillator is adjusted to produce a replica of the signal at 40 MHz. This signal is then filtered to restrict the bandwidth of the signal to 9 kHz. This new signal is then mixed with a second local oscillator at a fixed frequency of 39.9375 MHz. This produces a replica of the original signal at 62.5 kHz. This signal is then sampled at 83.3 kHz to produce the digital signal. The 9 kHz bandpass filter prevents information from being lost by sampling less than the Nyquist rate. Next, this signal is multiplied with a complex exponential at 62.5 kHz to produce the quadrature components of the signal at baseband. This set up is used behind each monopole element to produce the signals used in the direction finding algorithms.

Mathematically, the signal at the  $i^{\text{th}}$  antenna element is

$$x_i(t) = A_i(t) \cos(\omega t + \phi_i(t)) \quad (104)$$

The amplitude is different from element to element due to mutual coupling in the array

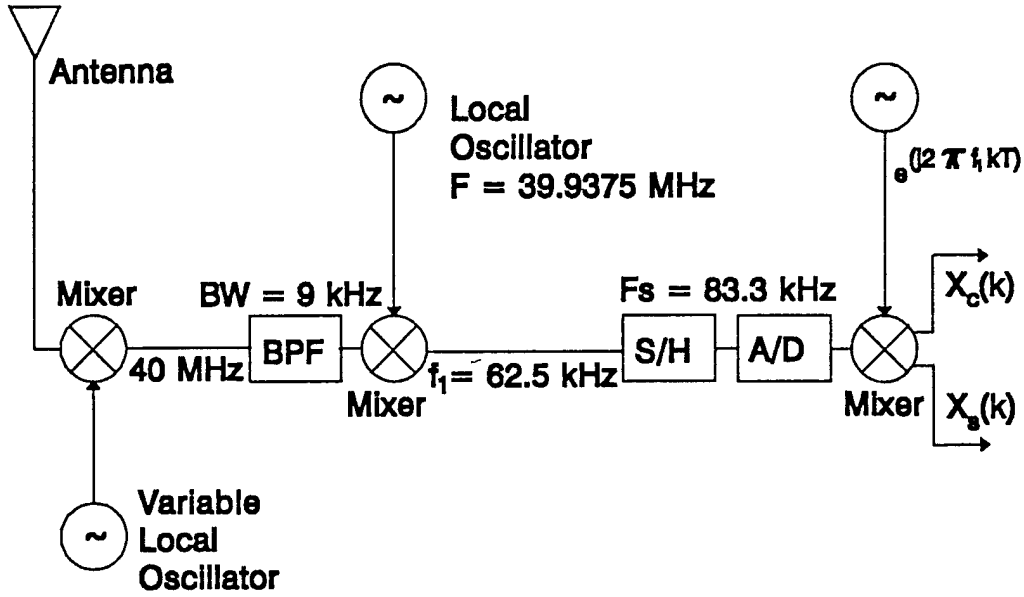


Figure 83: Receiver for Each Monopole Element

although it changes very little with respect to time. The phase at each element is different because of the physical separation between the elements. The amplitude and phase terms may vary slightly with time due to noise and modulation on the signal. This signal emerges from the analog to digital converter as

$$x_i(k) = A_i(k) \cos\left(\frac{3\pi k}{2} + \phi_i(k)\right) . \quad (105)$$

Note that although the signal is undersampled, no information will be lost since the bandwidth of the signal has been restricted to 9 kHz. This signal can be expressed as a sum of complex exponentials as

$$x_i(k) = \frac{A_i(k)}{2} \left[ e^{+j\left(\frac{3\pi k}{2} + \phi_i(k)\right)} + e^{-j\left(\frac{3\pi k}{2} + \phi_i(k)\right)} \right] . \quad (106)$$

After multiplying by the complex exponential and simplifying, the output of the multiplier in figure 83 is

$$x_i(k) = \frac{A_i(k)}{2} [e^{j((3\pi k) + \phi_i(k))} + e^{-j\phi_i(k)}] . \quad (107)$$

For even  $k$ , the output  $x_i(k)$  reduces to the in-phase component

$$x_c(k) = A_i(k) \cos(\phi_i(k)) . \quad (108)$$

For odd  $k$ , the output becomes the quadrature component

$$x_s(k) = -A_i(k) \sin(\phi_i(k)) . \quad (109)$$

The final signal used in the direction finding algorithms is

$$y(k) = x_c(k) + jx_s(k) . \quad (110)$$

Notice that for no amplitude or phase modulation, the in-phase and quadrature components are constant for all time.

#### 4.1.3 Antenna Model

The monopole arrays are modeled with the method of moments as described in Appendix A. At the frequencies of interest, the earth can be considered approximately a perfect conductor [44]. Therefore, the monopoles are modeled as dipoles as in chapter 2. Since each monopole is 2 meters long, each dipole is 4 meters long. Three piecewise sinusoidal modes are used to represent the current on the dipole as in chapter 2. Each element contained a dielectric coating of "glass fibre reinforced plastic" [51]. The

dielectric constant of this coating affects the calculation of the moment method impedance matrix. Unfortunately, the dielectric constant of the coating is not known. However, it is found that the dielectric constant of the coating did not effect the impedance matrix much since the elements are terminated with a high input impedance. Therefore the dielectric constant is estimated as  $\epsilon_r = 2.6 + j0.0$  since this is the dielectric constant of glass reinforced polystyrene [50]. The load impedance of the monopole is calculated using the circuit diagram of the amplifier. The input impedance of the dipole is then twice that of the monopole [35]. This model does not account for the gain and phase errors introduced by the amplifier. These errors occur since each amplifier has a slightly different frequency response. The change in frequency response between amplifiers, although small, can significantly affect the spectrum of model based spectrum estimators. The moment method model of the antenna array calculates the predicted signal at the terminals of the monopoles with mutual coupling but without the gain and phase errors introduced by the amplifiers.

The terminal impedance matrix for the antenna array is calculated using equation (22). This matrix is then applied to the measurements to eliminate the mutual coupling effects from the spectrum. This matrix is, of course, susceptible to any errors in the modeling of the monopole arrays.

#### 4.1.4 Results

In this section the terminal impedance matrix is used to compensate for the mutual coupling effects. In each of the figures, four spectra are shown. The first is the ideal spectrum which represents the best possible spectrum. In this case, no mutual coupling



is present and there are no gain or phase errors present in the signal. Next, the simulated spectrum for the data is shown. This spectrum is calculated from the moment method model of the antenna array. This spectrum includes the effects of mutual coupling but not any gain or phase errors. The third spectrum in the figures is from the actual measurements. The final spectrum is the result of processing the measurements with the terminal impedance matrix from the moment method model of the array. These four spectra are calculated for each set of measurements with each of the direction finding algorithms in chapter 2.

In all the spectra, two sources are used to determine the effects of mutual coupling on the resolution capability of the direction finding algorithms. The signals arrive from two independent sources at approximately the same frequency and therefore are uncorrelated. For the ideal and simulated spectra, the sources are separated by 500 KHz so that they will be uncorrelated. The spectra in these two cases are an average of twenty simulations. In all cases the spectra are computed every  $0.1^\circ$ .

For each of the direction finding algorithms, the covariance matrix is calculated using the "covariance method" as in chapter 2 [46]. For all except the cross array data, 16 snapshots of the quadrature components are available. For the cross array, 32 snapshots of data are available. The small number of snapshots may lead to an inaccurate estimate of the covariance matrix which may effect the direction finding algorithm.

For each set of data, the SNR is calculated. The SNR is calculated by first computing the power in the measured data. This represents the signal plus noise power. Next the covariance matrix is decomposed into its eigenvalues and eigenvectors. The

eigenvalues not associated with the signal are approximately equal to the noise power. The mean value of these eigenvalues is used to estimate the noise power. The signal power is then calculated by subtracting the noise power from the signal plus noise power calculated previously.

#### **4.1.4.1 Beamformer Algorithm**

The beamformer algorithm calculates the spectrum by scanning the main beam of the antenna array. This algorithm is computationally inexpensive although its resolution is limited by the Rayleigh criterion [46]. This algorithm is applied to each of the sets of data for the linear, cross, and circular arrays. The results are shown in figures 84 through 7.

The results for the first set of linear array data are shown in figure 84. The ideal spectrum assumes no mutual coupling or other sources of error are present. The simulated spectrum shows the result of using the moment method model of the array which includes the effects of mutual coupling. Notice that both peaks for this spectrum are shifted toward larger angles of incidence. The spectrum from the actual measurements shows that the peaks are closer to the actual signals than both the ideal and simulated spectra, and that the peaks are close to being unresolvable. The compensated spectrum shows the results of applying the terminal impedance matrix to the measurements. Notice that this yields the best estimate of the actual signals although the peaks are still very close to being unresolvable. Figure 84 shows that the estimate of the angles of arrival is improved for the first set of data by applying the terminal impedance matrix before processing the data.

The results of the second set of data for the linear array are shown in figure 85. The ideal spectrum and simulated spectrum show the same angles of arrival as in figure 84 because the only difference is a slightly smaller SNR. The spectrum for the measurements, however, clearly shows only peak in the spectrum. In this case, the two signals are unresolvable. After applying the terminal impedance matrix to the measurements, the compensated spectrum shows that the two signals are still unresolvable. Figure 85 shows that both the measurements and the corrected spectra can not resolve the two signals although the parameters are almost identical to the those of figure 84.

The spectra for the third data set are shown in figure 86. Again, the ideal and simulated spectra are approximately the same as those in figures 84 and 85 since the only difference is a slightly larger SNR. For this data set, however, the measurements clearly show two signals in the spectrum. Notice, however, that the angle estimates are not as good as those in figure 84. After applying the terminal impedance matrix to the measurements, the compensated spectrum shows that the estimated angles of arrival are now slightly farther away from the true angles of incidence. Figure 86 shows that using the terminal impedance matrix to account for mutual coupling causes a slightly worse estimate of the angles of arrival.

The results for the cross array with the Beamformer algorithm are shown in figure 87. The ideal and simulated spectra show that the mutual coupling has very little effect on the spectrum. The spectra for the measurements and compensated data are also almost identical. In all cases, the spectra are unable to resolve the two signals because the

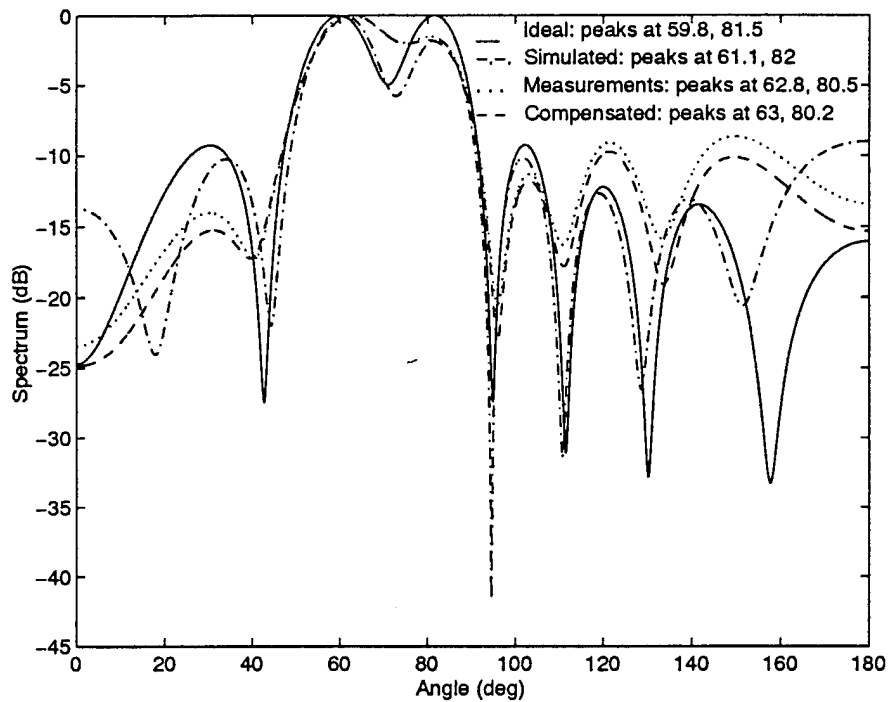


**Figure 84: Beamformer, Linear Array, Angles = 64°, 78°,  
Frequency = 60 MHz, SNR = 41.9 dB**

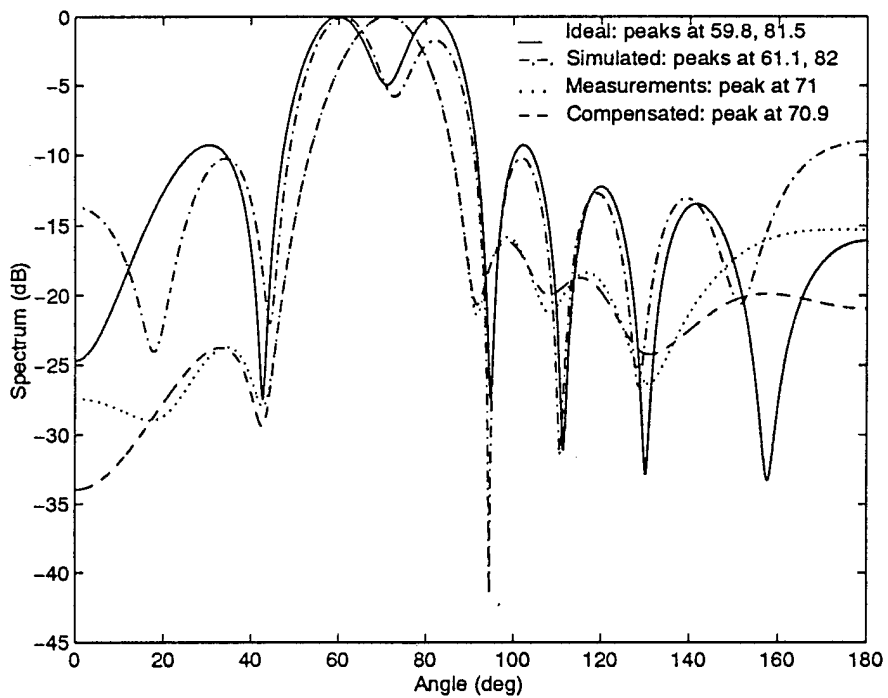


**Figure 85: Beamformer, Linear Array, Angles = 64°, 78°,  
Frequency = 60 MHz, SNR = 41.5 dB**

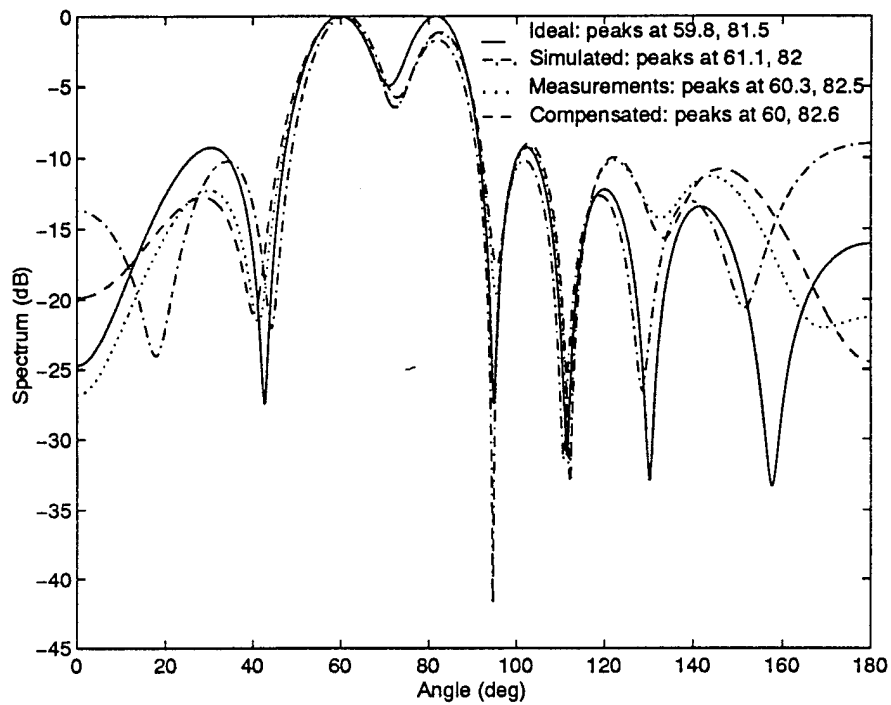


Figure 86: Beamformer, Linear Array, Angles =  $64^\circ$ ,  $78^\circ$ ,  
Frequency = 60 MHz, SNR = 42.6 dB

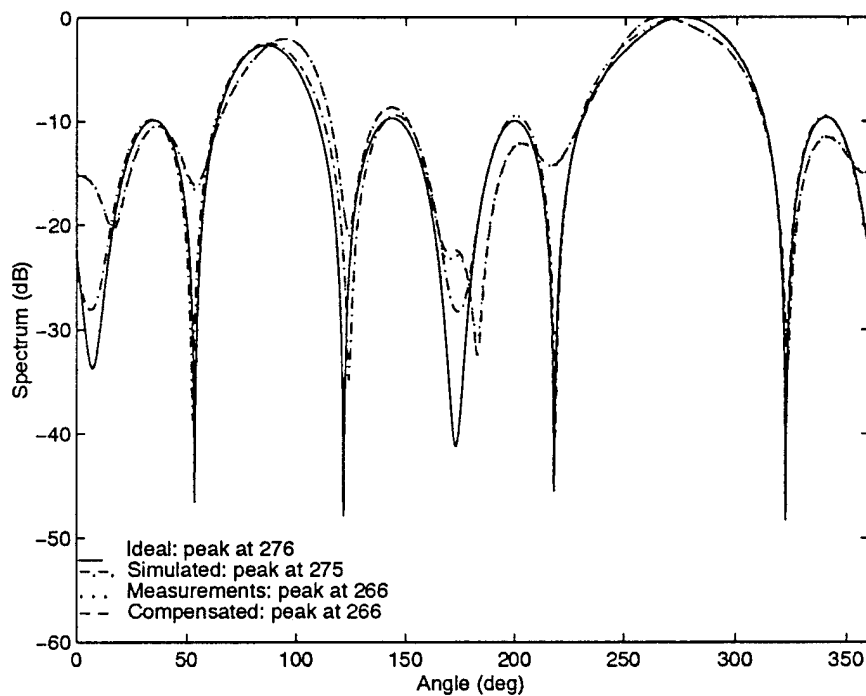


Figure 87: Beamformer, Cross Array, Angles =  $263^\circ$ ,  $289^\circ$ ,  
Frequency = 27.185 MHz, SNR = 42.3 dB

signals do not meet the Rayleigh criterion. Notice that aside from the main lobe centered around  $270^\circ$  there is also a lobe around  $90^\circ$ . This occurs because a grating lobe is present in the antenna pattern. Figure 87 shows that the beamformer algorithm is unable to resolve the signals for the cross array and that compensating for mutual coupling has almost no effect on the spectrum.

The spectra for the two sets of circular array data are shown in figures 88 and figure 89. In both figures, all four spectra only show one angle of arrival. In figure 88 and 89 the ideal and simulated spectra are almost completely identical. This is also true for the measurements and compensated spectra. Figures 88 and 89 show that compensating for mutual coupling has almost no effect on the spectrum for circular arrays with a large SNR.

#### **4.1.4.2 Capon's Algorithm**

Capon's algorithm is discussed in Appendix C. The spectrum in this case is computed by minimizing the output power subject to the constraint that the output equals unity at the observation angle [5,46]. This algorithm is applied to the linear, cross, and circular array sets of data. The ability of the terminal impedance matrix to compensate and improve the spectrum of the actual measurements is investigated in the next 3 sections.

The spectra with Capon's algorithm for the first set of linear array data are shown in figure 90. Notice that the ideal spectrum is very smooth and yields a very accurate estimate of the angles of arrival. The simulated spectrum which includes the effects of mutual coupling also yields a smooth spectrum with an accurate estimate of the angles

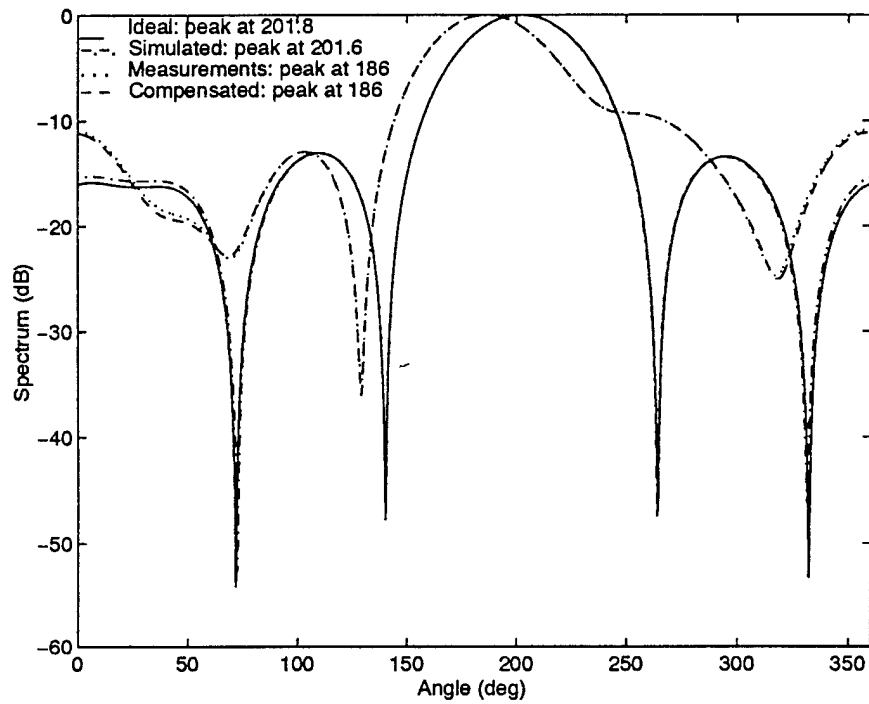


Figure 88: Beamformer, Circular Array, Angles =  $184^\circ$ ,  $220^\circ$ ,  
Frequency = 27.185 MHz, SNR = 63.4 dB

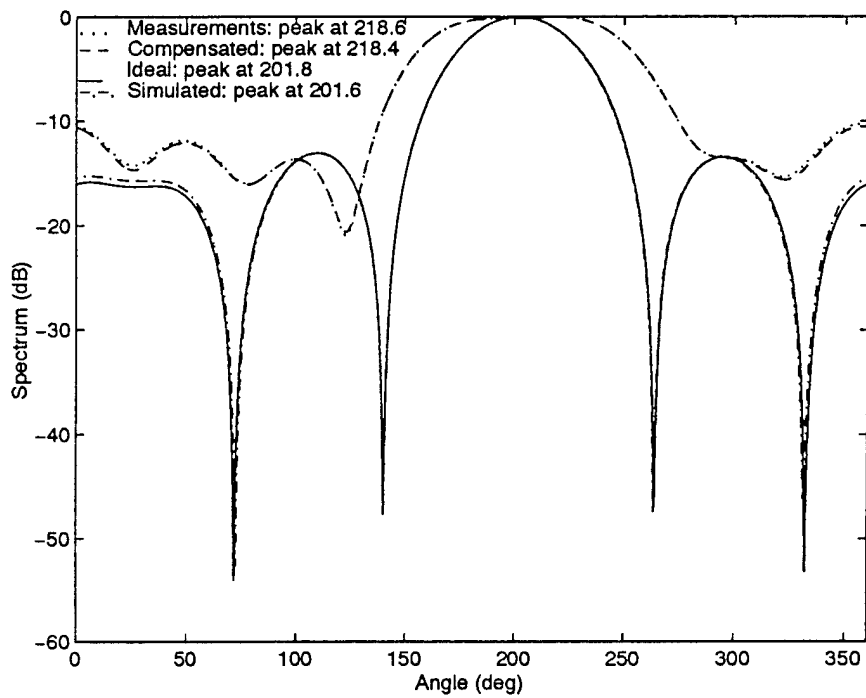


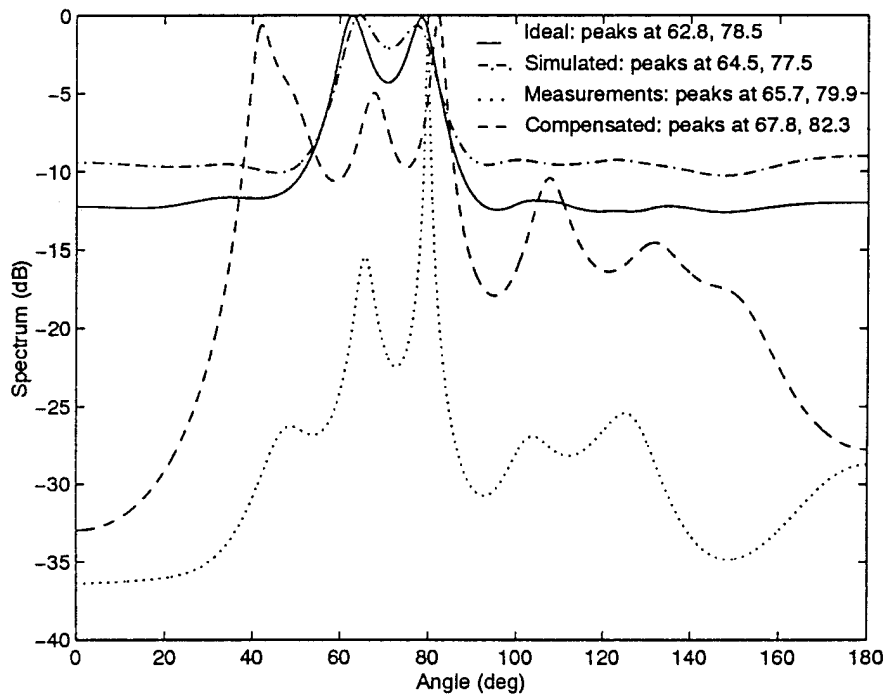
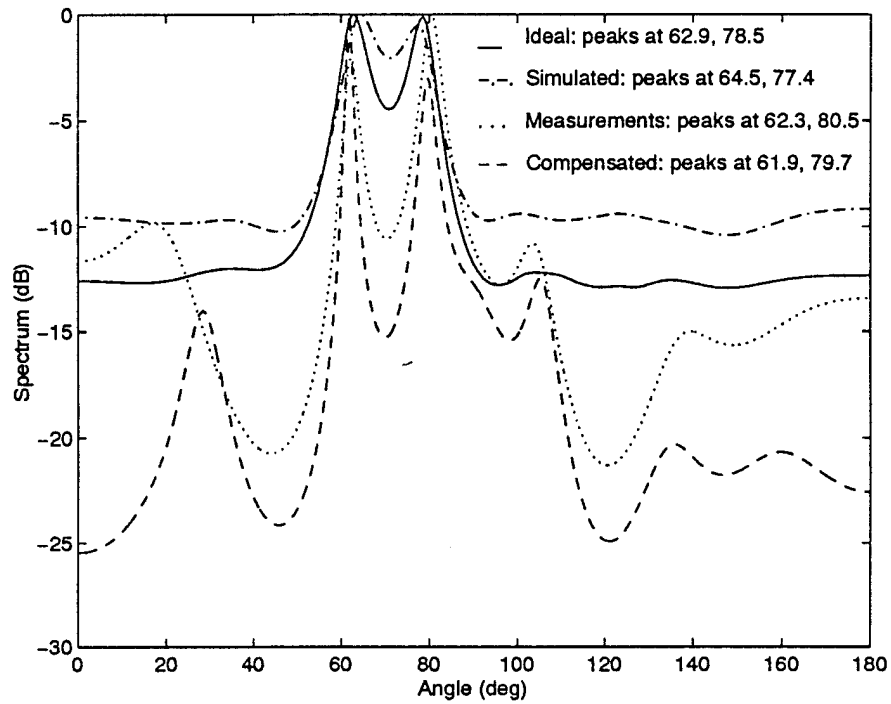
Figure 89: Beamformer, Circular Array, Angles =  $184^\circ$ ,  $220^\circ$ ,  
Frequency = 27.185 MHz, SNR = 57.4 dB

of arrival. The measurements, however, yield a spectrum with many spurious peaks along with a good estimate of the actual angles of arrival. These spurious peaks do not disappear when the mutual coupling effects are compensated for as shown by the fourth spectrum. This indicates that either the terminal impedance matrix used for this array does not accurately model the mutual coupling or that there are other sources of error. The other possible sources of error are gain and phase errors which arise in practical situations since each antenna element has an amplifier with a slightly different frequency response. Figure 90 shows that while the ideal and simulated spectra yield relatively accurate spectra, the measurements and compensated spectra show spurious peaks along with the angles of arrival.

Figure 91 shows the spectra from Capon's algorithm for the second set of linear array data. The ideal and simulated spectra are almost exactly the same as in figure 90 since the SNR is only slightly smaller. The measurements show a reasonably accurate estimate of the angles of arrival along with other smaller spurious peaks. The compensated spectrum, however, has a peak in the spectrum away from the actual angles of arrival that is stronger than one of the signals. In this case, the compensated spectrum is worse than the measurements. Figure 91 shows that spectrum becomes a less accurate estimate of the actual spectrum when the effects of mutual coupling are compensated.

The spectrum from Capon's algorithm for the third set of linear array data is shown in figure 92. The ideal and simulated spectra are almost the same as the in figures 90 and 91 since only the SNR is slightly different. For this set of data, both the measurements and the compensated spectra yield very poor estimates of the actual





spectrum. Both of these spectra contain several strong spurious peaks away from the actual angles of arrival. In this case, the compensated spectrum is almost the same as the measurements except shifted in magnitude.

The results for the cross array with Capon's algorithm are shown in figure 93. The ideal and simulated spectra show two peaks close to the actual angles of arrival. The peaks from the simulated data are actually slightly closer to the actual signals than those of the ideal signal. In both cases, an ambiguous angle of arrival begins to emerge in the spectrum at approximately  $100^\circ$ . This peak arises due to a grating lobe in the antenna pattern. The measurements also indicate two signals near the actual angles of arrival. These peaks, however, are not as close to the actual angles of arrival as the ideal and simulated data. The compensated spectrum shows that the change in the spectrum is insignificant when the terminal impedance matrix is used to compensate for the mutual coupling present. Figure 93 shows that the Capon's algorithm can clearly resolve the two signals and that compensating for the mutual coupling effects has virtually no effect on the spectrum.

The spectra from Capon's algorithm for the first and second sets of circular array data are shown in figures 94 and 95. In both figures the ideal and simulated spectra yield very smooth and accurate estimates of the angles of arrival. The measurements yield accurate estimates of the angles of arrival but also strong spurious peaks at other angles of arrival. Using the terminal impedance matrix to compensate for the mutual coupling produces almost no change in the spectra in both figures. Figures 94 and 95 show that the measurements produce spurious peaks which are unchanged when the signal is pre-

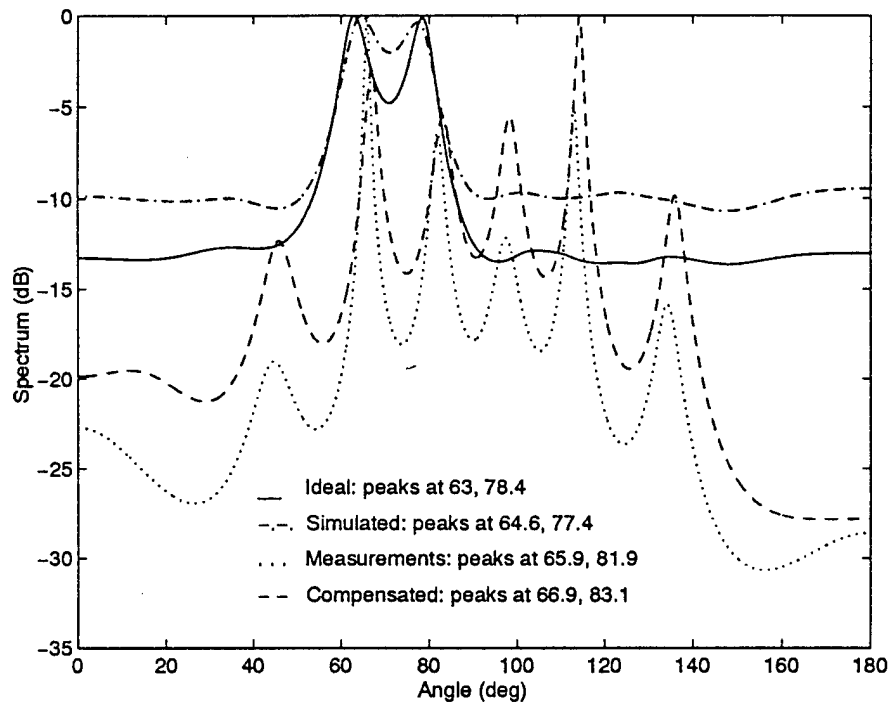


Figure 92: Capon, Linear Array, Angles =  $64^\circ$ ,  $78^\circ$ ,  
Frequency = 60 MHz, SNR = 42.6 dB

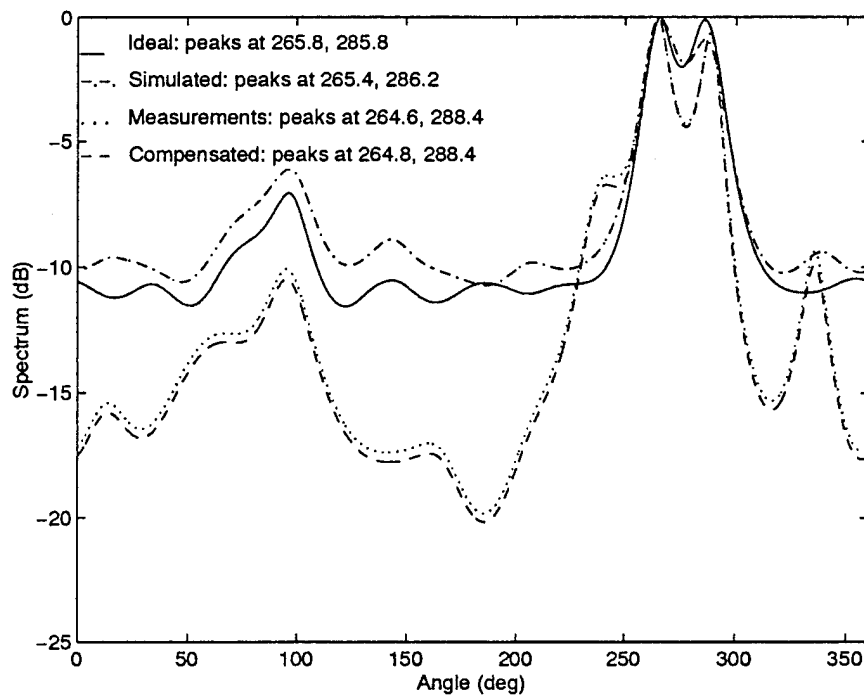


Figure 93: Capon, Cross Array, Angles =  $263^\circ$ ,  $289^\circ$ ,  
Frequency = 27.185 MHz, SNR = 42.3 dB

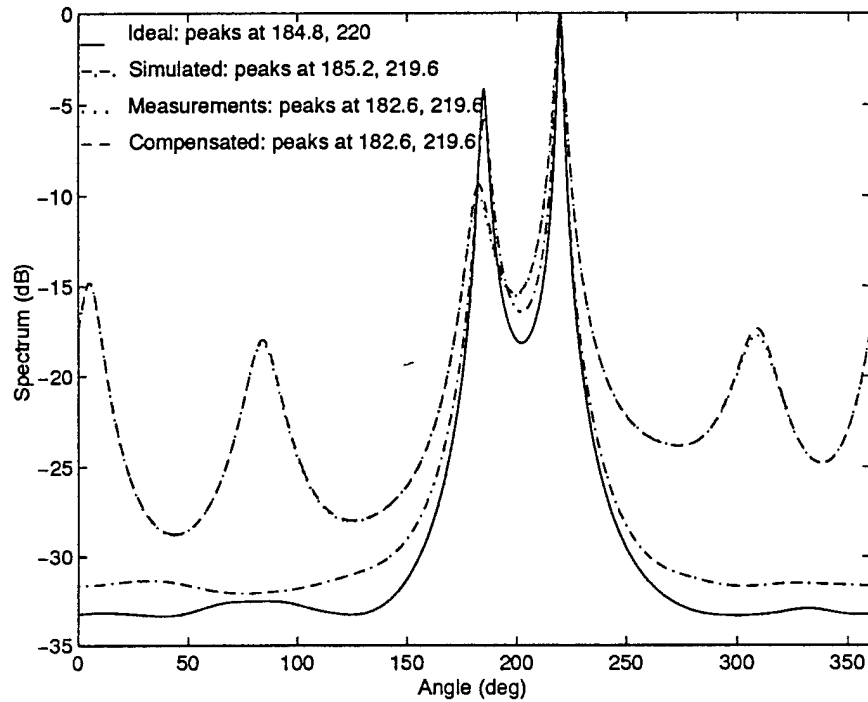


Figure 94: Capon, Circular Array, Angles =  $184^\circ$ ,  $220^\circ$ ,  
Frequency = 27.185 MHz, SNR = 63.4 dB

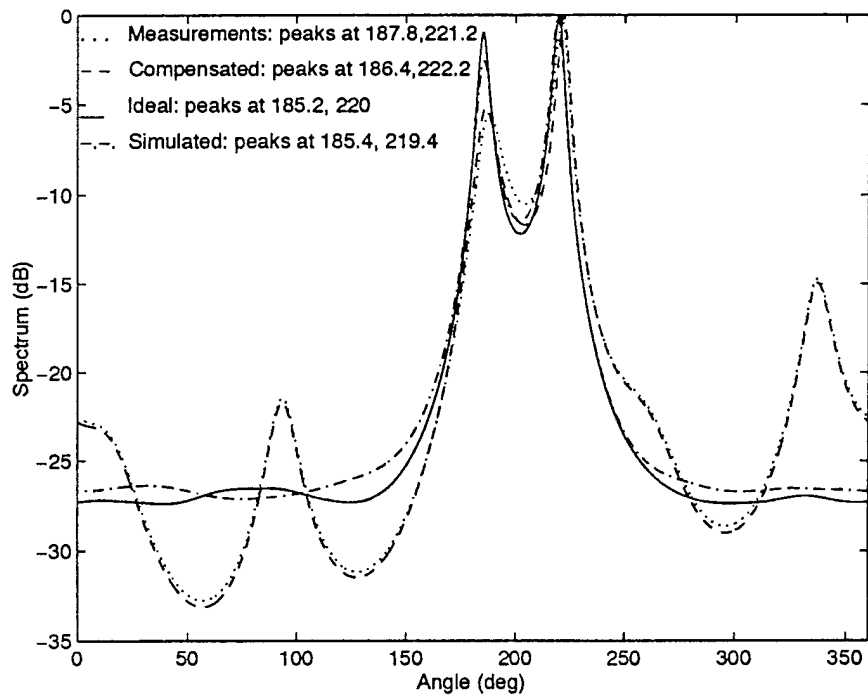


Figure 95: Capon, Circular Array, Angles =  $184^\circ$ ,  $220^\circ$ ,  
Frequency = 27.185 MHz, SNR = 57.4 dB

processed with the terminal impedance matrix.

#### **4.1.4.3 Linear Prediction**

In this chapter, the linear prediction algorithm is not applied to the data. As stated earlier, only 16 snapshots of data are available for the linear and circular arrays, and 32 snapshots for the cross array. It is found that since the covariance matrix is 9 by 9, the covariance matrix estimate is not very accurate. This leads to an inaccurate calculation of the model parameters and therefore a poor estimate of the spatial spectrum. It is interesting to note that while the covariance matrix is not sufficient for the linear prediction algorithm, it is sufficient for Capon's algorithm. However, the angle estimates in Capon's algorithm may improve if more snapshots are used to estimate the covariance matrix.

#### **4.1.4.4 MUSIC algorithm**

The MUltiple Signal Classification algorithm, as discussed earlier, computes the spectrum by searching for angles of arrival that are orthogonal to the noise subspace. This algorithm is shown in chapter 2 to yield the best spectrum of the four techniques considered here. It is applied to the measurement data in the following 3 sections.

The MUSIC spectra for the first set of linear array data is shown in figure 96. The ideal spectrum which is calculated assuming no mutual coupling or other sources of error are present is very smooth with a very accurate estimate of the angles of arrival. The simulated spectrum from the method of moments model of the array also yields a very smooth spectrum and a very accurate estimate of the angles of arrival. The spectrum from the measurements is very similar to the spectrum from the simulated data. The

compensated spectrum shows that once the mutual coupling effects are accounted for with the terminal impedance matrix, the new spectrum is only slightly better than the original data. Notice, however, that all of these spectra are very smooth compared to those in figures 90 through 95. Figure 96 shows that MUSIC spectrum from the first set of linear array data is very smooth with very accurate estimates of the angles of arrival. The angle estimates, however, are only slightly improved by the compensating for the mutual coupling effects with the terminal impedance matrix.

The MUSIC spectra for the second set of linear array data are shown in figure 97. The ideal and simulated spectra are approximately the same as in figure 96 since only the SNR is slightly different. The MUSIC spectrum for the measurements also yields a very smooth spectrum with accurate estimates of the angles of arrival. The compensated spectrum shows that removing the effects of mutual coupling improves both estimates of the angles of arrival. Figure 97 shows that compensating for the mutual coupling effects improves the MUSIC spectrum for the second set of linear array data.

The spectra for the third set of linear array data is shown in figure 98. The ideal and simulated spectra are again the same as in figures 96 and 97 since the SNR is almost the same. The measurements again yield a smooth accurate estimate of the angles of arrival. The compensation for mutual coupling, however, does not improve the spectrum as in the previous cases. Figure 98 shows the compensated spectrum is virtually the same as the spectrum for the measurements.

The spectra for the cross array with the MUSIC algorithm are shown in figure 99. The ideal spectrum clearly indicates the two angles of arrival. It also indicates a spurious

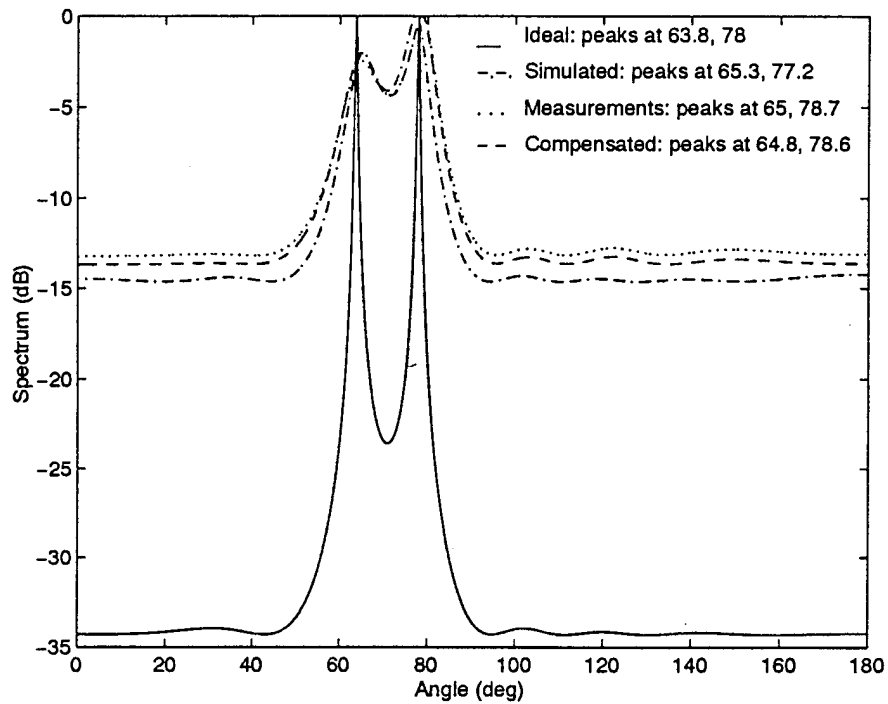


**Figure 96: MUSIC, Linear Array, Angles = 64°, 78°,  
Frequency = 60 MHz, SNR = 41.9 dB**

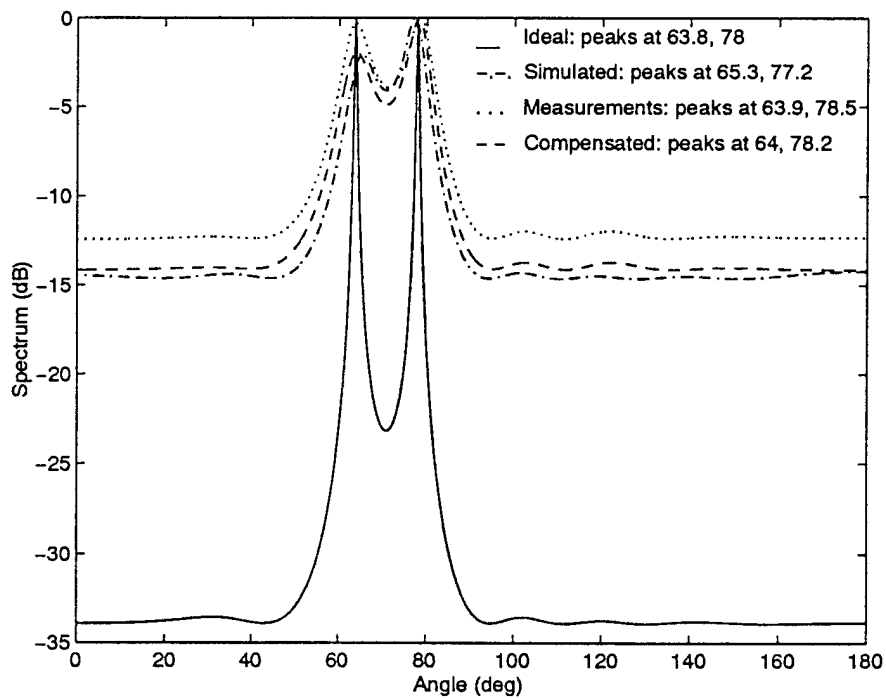


**Figure 97: MUSIC, Linear Array, Angles = 64°, 78°,  
Frequency = 60 MHz, SNR = 41.5 dB**

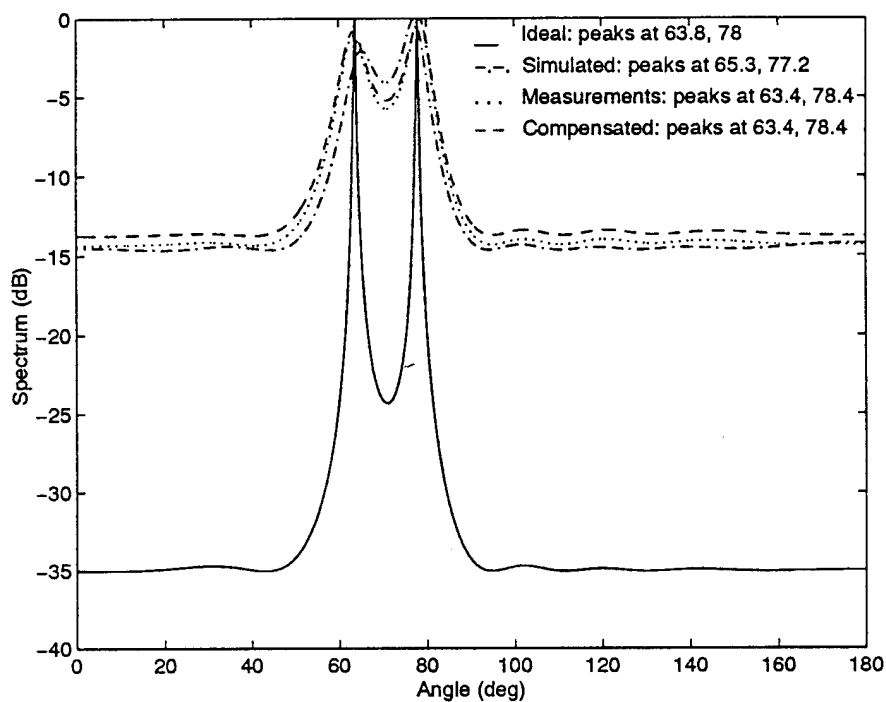


**Figure 98: MUSIC, Linear Array, Angles =  $64^\circ$ ,  $78^\circ$ ,  
Frequency = 60 MHz, SNR = 42.6 dB**

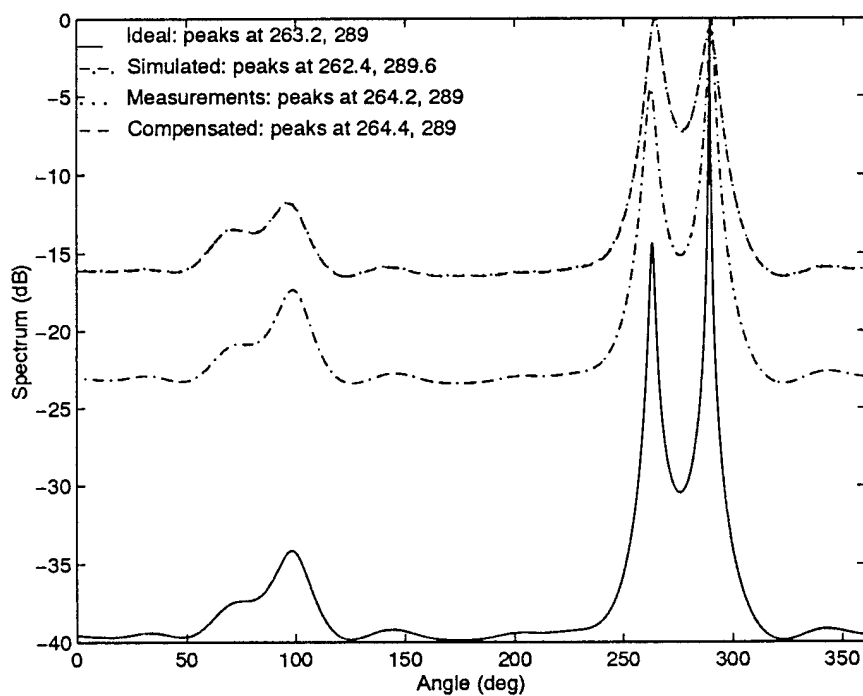


**Figure 99: MUSIC, Cross Array, Angles =  $263^\circ$ ,  $289^\circ$ ,  
Frequency = 27.185 MHz, SNR = 42.3 dB**



peak due to the grating lobe in the antenna pattern. The simulated spectrum which includes the effects of mutual coupling is the middle spectrum in figure 99. Notice that it also yields a very accurate estimate of the angles of arrival. The measurement and compensated spectra have a minimum value of -15 dB. These two spectra are almost identical. Figure 99 shows that MUSIC algorithm can clearly resolve the two signals and that compensating for the mutual coupling in the cross array has very little effect on the spectrum.

The spectra for the two circular array sets of data are shown in figures 100 and 101. The ideal signal yields a smooth spectrum with peaks very close to the actual angles of arrival. The simulated signal also yields a smooth spectrum with peaks close to the actual angles of arrival. The measurements produce a very clean spectrum with accurate estimates of the angles of arrival. In both figures, however, the minimum value in the spectra are much larger than that of the simulated signal. This is in contrast to the linear array where the floor of the simulated spectrum is approximately the same as that of the measurements. In both figures 100 and 101 the compensated spectrum yields a slightly better estimate of the angles of arrival than from only the measurements. Figures 100 and 101 show that the angle of arrival estimates are improved by using the terminal impedance matrix to compensate for the mutual coupling effects.

#### **4.2 Horn Array Data**

The terminal impedance matrix can be calculated from the method of moments model of a thin wire antenna array as shown in section 2.3.1. A numerical model for the horn array is very complex, however, and is not presented here. Instead, a new method

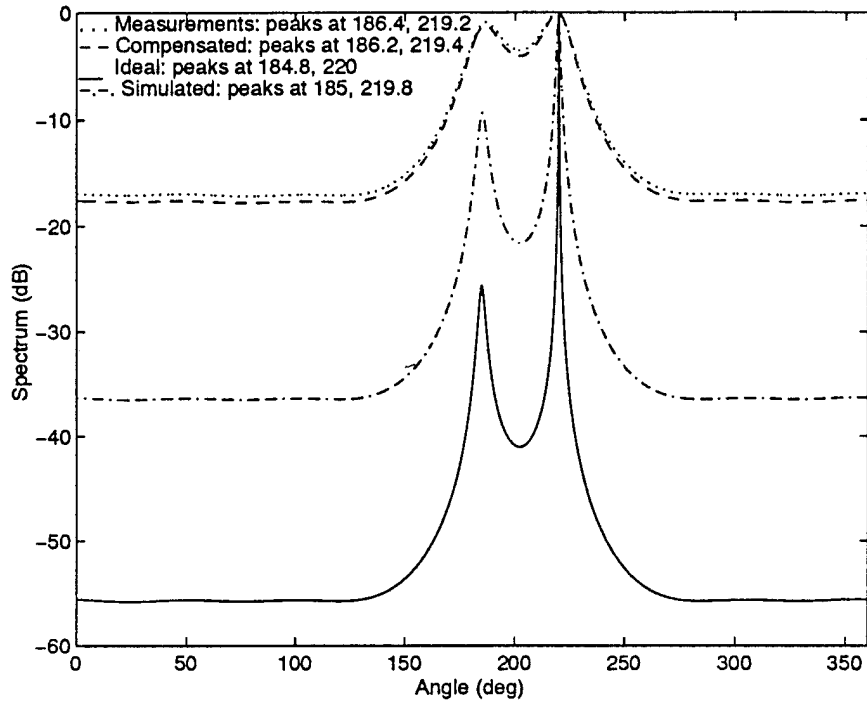


**Figure 100: MUSIC, Circular Array, Angles = 184°, 220°,  
Frequency = 27.185 MHz, SNR = 63.4 dB**

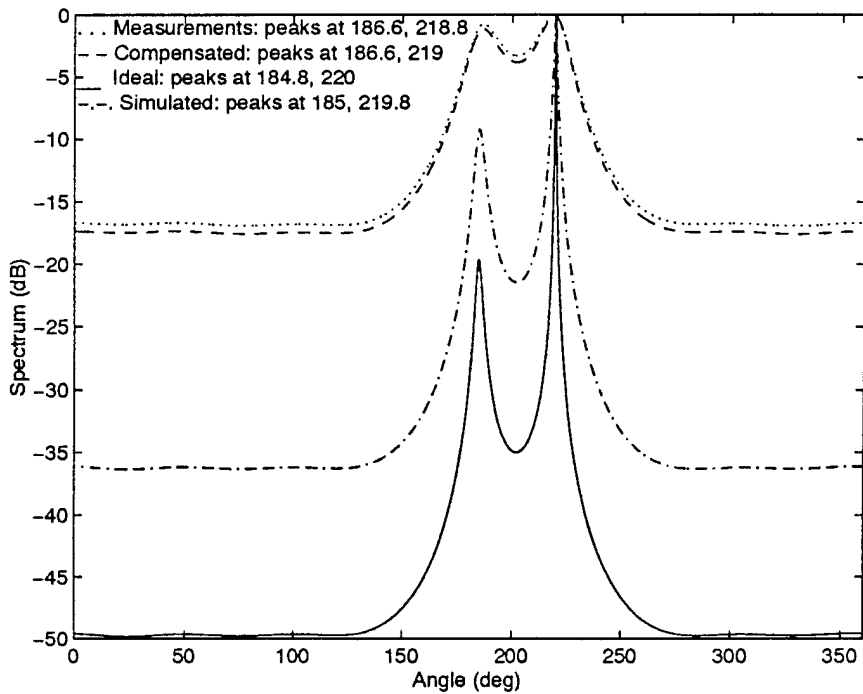


**Figure 101: MUSIC, Circular Array, Angles = 184°, 220°,  
Frequency = 27.185 MHz, SNR = 57.4 dB**

is presented to calculate the terminal impedance matrix directly from the measurements.

For convenience, this new method is derived for a four element linear array. It is applicable, however, to a linear array of any size. The voltage at the output of a four element array is given by

$$\begin{bmatrix} V_1 \\ V_2 \\ V_3 \\ V_4 \end{bmatrix} = \begin{bmatrix} Z_{11} & Z_{12} & Z_{13} & Z_{14} \\ Z_{21} & Z_{22} & Z_{23} & Z_{24} \\ Z_{31} & Z_{32} & Z_{33} & Z_{34} \\ Z_{41} & Z_{42} & Z_{43} & Z_{44} \end{bmatrix} \begin{bmatrix} I_1 \\ I_2 \\ I_3 \\ I_4 \end{bmatrix} \quad (111)$$

where  $V_1$ ,  $V_2$ ,  $V_3$ , and  $V_4$  are the output voltages calculated using the known angle of arrival,  $I_1$ ,  $I_2$ ,  $I_3$ , and  $I_4$  are the measured currents, and  $Z_{ij}$  is the mutual coupling between the  $i^{\text{th}}$  and  $j^{\text{th}}$  antenna elements [35]. The voltage at the  $i^{\text{th}}$  antenna element is

$$V_i = -Ae^{j2\pi d_i \cos \phi} \quad (112)$$

where  $d_i$  is the distance from the coordinate origin to the  $i^{\text{th}}$  antenna element, and  $\phi$  is the known angle of incidence. Since the array is linear and the elements are equally spaced, the impedance matrix is Toeplitz [35]. Therefore, of the sixteen elements in the impedance matrix, only four of them are unique. This permits equation (111) to be simplified to

$$\begin{bmatrix} V_1 \\ V_2 \\ V_3 \\ V_4 \end{bmatrix} = \begin{bmatrix} Z_{11} & Z_{12} & Z_{13} & Z_{14} \\ Z_{12} & Z_{11} & Z_{12} & Z_{13} \\ Z_{13} & Z_{12} & Z_{11} & Z_{12} \\ Z_{14} & Z_{13} & Z_{12} & Z_{11} \end{bmatrix} \begin{bmatrix} I_1 \\ I_2 \\ I_3 \\ I_4 \end{bmatrix} \quad (113)$$

This equation can be rearranged to yield

$$\begin{bmatrix} V_1 \\ V_2 \\ V_3 \\ V_4 \end{bmatrix} = \begin{bmatrix} I_1 & I_2 & I_3 & I_4 \\ I_2 & I_1 + I_3 & I_4 & 0 \\ I_3 & I_2 + I_4 & I_1 & 0 \\ I_4 & I_3 & I_2 & I_1 \end{bmatrix} \begin{bmatrix} Z_{11} \\ Z_{12} \\ Z_{13} \\ Z_{14} \end{bmatrix}. \quad (114)$$

Solving this equation for the impedance elements yields

$$\begin{bmatrix} Z_{11} \\ Z_{12} \\ Z_{13} \\ Z_{14} \end{bmatrix} = \begin{bmatrix} I_1 & I_2 & I_3 & I_4 \\ I_2 & I_1 + I_3 & I_4 & 0 \\ I_3 & I_2 + I_4 & I_1 & 0 \\ I_4 & I_3 & I_2 & I_1 \end{bmatrix}^{-1} \begin{bmatrix} V_1 \\ V_2 \\ V_3 \\ V_4 \end{bmatrix}. \quad (115)$$

The voltages are known to within a constant since the angle of arrival is known. The currents are known since they are measured at the terminals of the antenna. If all the current values  $I_1$  through  $I_4$  are unique, the matrix in equation (114) will have a non-zero determinant. This is the case for all angles of incidence except broadside. The resultant system is then solved for the impedance elements  $Z_{11}$ ,  $Z_{12}$ ,  $Z_{13}$ , and  $Z_{14}$  using equation (115). The terminal impedance matrix is then determined to within a constant by using equation (113). The matrix is only accurate to within a constant since the amplitude,  $A$ , in equation (112) is unknown. This matrix is then used to compensate for the mutual coupling effects. The complex constant will be insignificant since the spectrum from the MUSIC algorithm is normalized.

The results for one angle of arrival are shown in figures 102 and 103. The ideal spectrum in figure 102 assumes that there is no mutual coupling between the horn elements and that there are no gain or phase errors in the signals. The actual spectrum is calculated from the unprocessed horn measurements. The corrected spectrum is

obtained by first pre-processing the measurements with the terminal impedance matrix. This matrix is derived using equations (112) and (115). The results are clearly demonstrated in figure 103. The ideal spectrum yields an unbiased estimate of the angle of arrival with a very sharp peak. The actual spectrum yields a biased estimate of the angle of arrival and has a slightly broader peak. This may be the result of gain and phase errors. The corrected spectrum is obtained by first pre-processing the data with the terminal impedance matrix before computing the MUSIC spectrum. In this case the peak is broader but the spectrum yields an unbiased estimate of the angle of arrival.

Figures 104 and 105 show the result of using a different angle of arrival to calculate the impedance matrix. In these figures the ideal and actual spectra are the same as in figures 102 and 103. The impedance matrix is calculated using the measurement data for  $65.3^\circ$  instead of  $44.7^\circ$ . The corrected spectra in figures 104 and 105 show the result of applying this matrix to the measurement data. In this case, the improvement in the spectrum is much less than in figures 102 and 103. The corrected spectrum in figures 104 and 105 is not as good as the spectra in figures 102 and 103 since the terminal impedance matrix is different.

The terminal impedance calculation changes for different angles of incidence. Figures 106 and 107 show the magnitude and phase of the unique terminal impedance elements for  $44.7^\circ$  and  $65.3^\circ$ . In these figures the x-axis represents the impedance element. For example, 4 on the x-axis represents the impedance element  $Z_{14}$  and 9 represents the element  $Z_{19}$ . Notice in figure 106 that the magnitudes of the elements are different for each angle of incidence. In figure 107 the phase of each element is varies

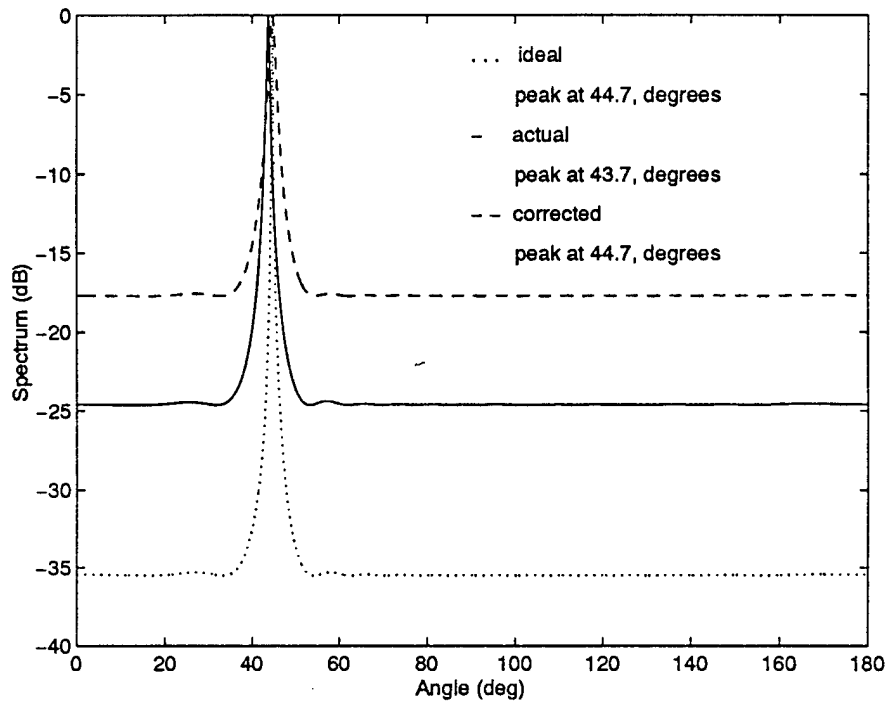


**Figure 102: MUSIC Spectrum from the 16 Element Horn Array,  
Angle = 44.7°, Frequency = 9.8 GHz**

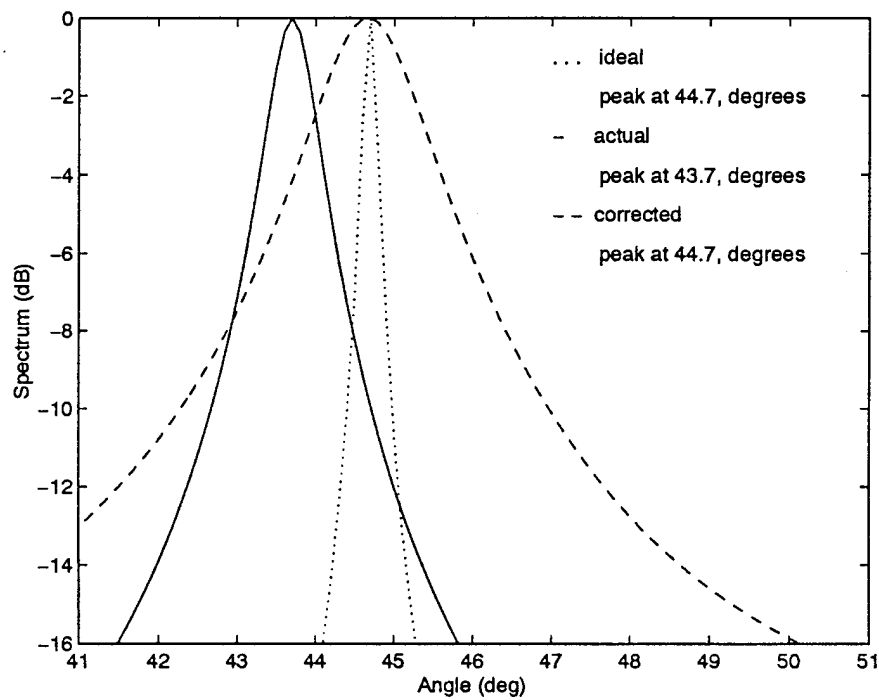


**Figure 103: MUSIC Spectrum from the Horn Measurements  
Showing Peaks, Angle = 44.7°, Frequency = 9.8 GHz**

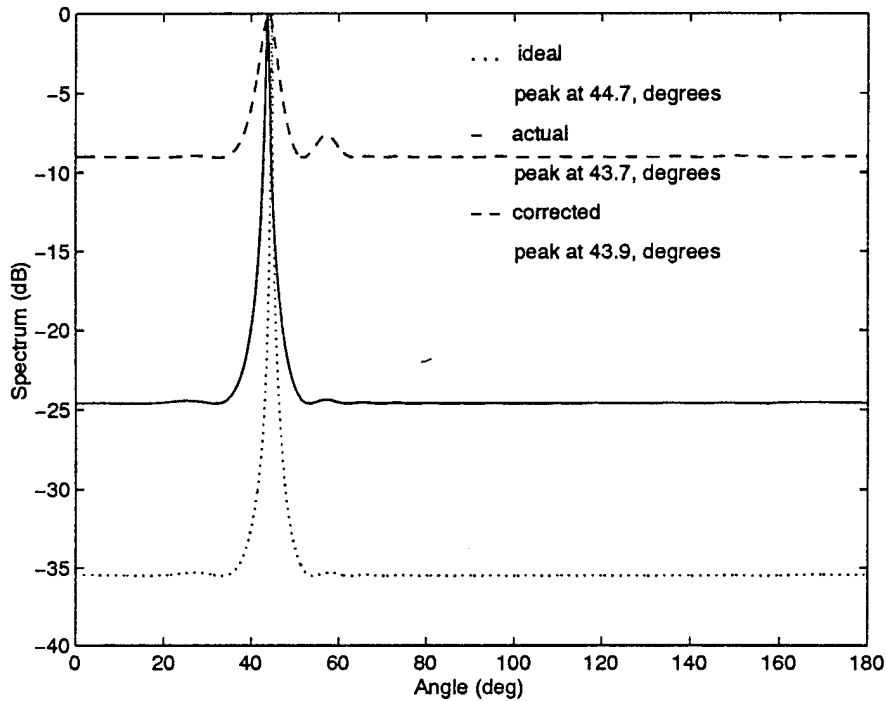


Figure 104: MUSIC Spectrum Using Different Impedance Matrix from a Different Angle of Arrival

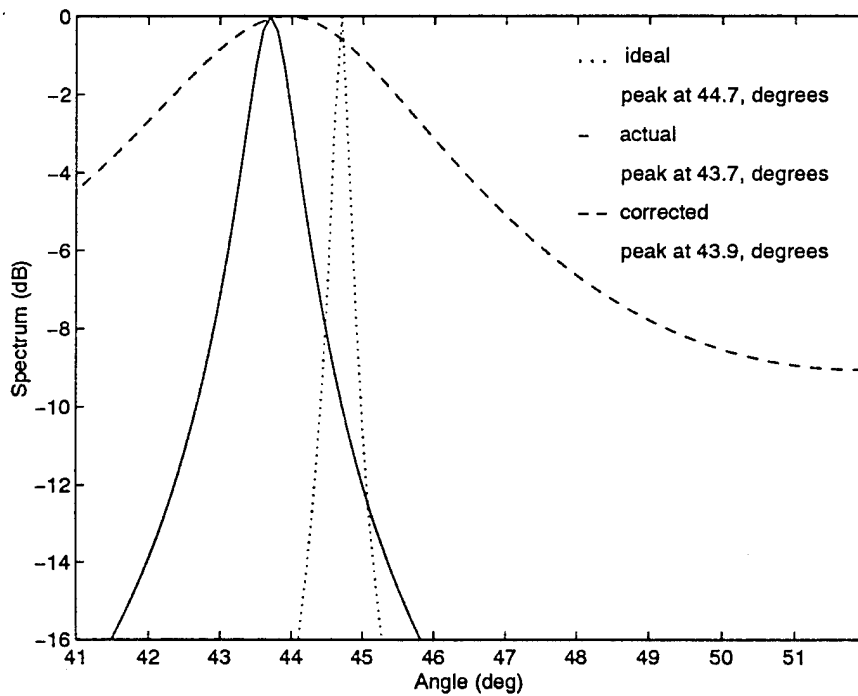


Figure 105: MUSIC Spectrum Showing Peaks

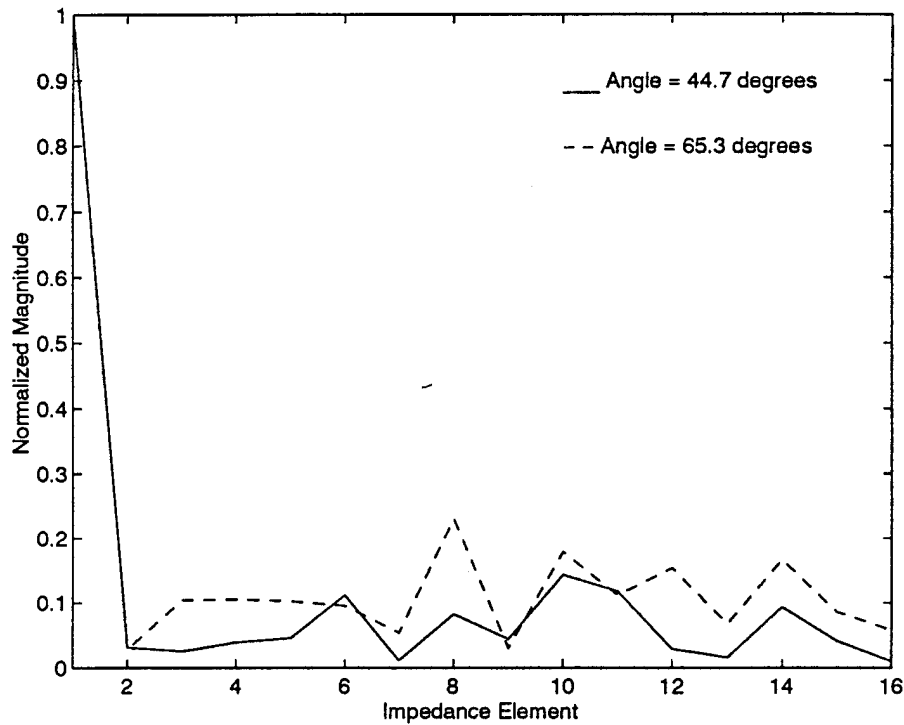


Figure 106: Normalized Magnitude of Impedance Elements

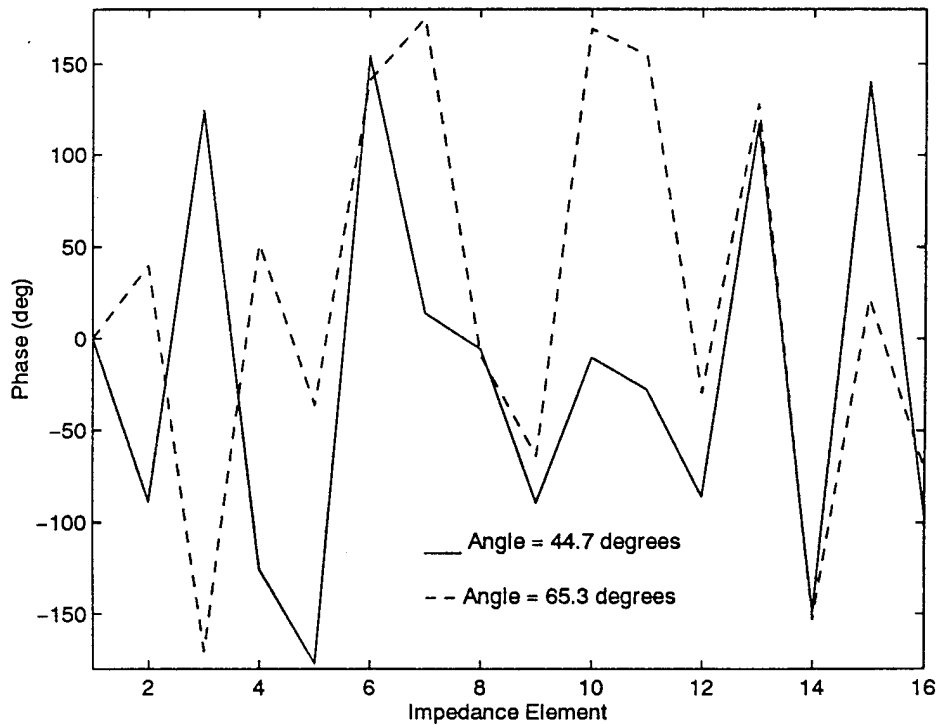


Figure 107: Phase of Impedance Elements



greatly depending upon the angle of incidence. The impedance matrix, however, is invariant with respect to the angle of incidence as shown in Appendix A. Figures 106 and 25 show that the impedance elements calculated using equations (112), and (115) are different for different angles of incidence.

The variation in impedance values may be due to measurement noise. This noise causes the current values  $I_1, I_2, \dots, I_{16}$  to depart from the values expected by the displacement in position. This variation in current causes a variation in the impedance matrix. From the discussion of the method of moments in Appendix A and chapter 2, the impedance elements do not change due to angle of incidence. They are solely dependent upon the geometry of the antenna and frequency of operation.

### 4.3 Measurement Conclusions

In this section, the terminal impedance matrix is applied to two sets of measurements. The first set of measurements is obtained from a colleague in Germany. These measurements consisted of time domain data from various monopole arrays. The second set of data is obtained from WL/AARM-3 at Wright-Patterson Air Force Base. This data consists of the magnitude and phase of the voltages at one frequency at the terminals of a 16 element horn array. These sets of measurements are used to investigate the ability of the terminal impedance matrix to compensate actual measurements.

The spectra for the monopole measurements are compared to the spectra generated by pre-processing the measurements with the terminal impedance matrix to remove the mutual coupling effects. For the beamformer algorithm it is shown that sometimes the pre-processing improved the angle estimates, sometimes no change is apparent, and

sometimes the angle estimates actually became worse than without pre-processing. In particular, when the signals are close to being unresolvable as in figure 84, correcting for mutual coupling improves the angle estimates. If the signals are already clearly distinguishable, correcting for mutual coupling actually makes the angle estimates worse as shown in figure 86. This is exactly the same phenomenon that occurred for the simulations as can be seen by comparing figure 86 with figure 96 of section 2.6.1. In particular, compare figures 84 and 4 with 12 and 14. For Capon's algorithm, the spectrum from the measurements and compensated spectrum always shows spurious peaks. Compensating for the mutual coupling effects does not improve the spectrum and sometimes makes it worse. The linear prediction algorithm could not be applied since the limited number of snapshots prevented an accurate estimate of the covariance matrix. The MUSIC algorithm performed better than the other three algorithms. The spectra did not show any spurious peaks except in the case of the cross array and that is due to a grating lobe in the antenna pattern. In all cases the spectra clearly shows the two signals. In all but one case, compensating for the mutual coupling effects improved the angle estimates. In the one case that did not show improvement, the estimates did not become worse after compensating for mutual coupling. The spectra in this section show that the MUSIC algorithm performs better than all the other direction finding algorithms on actual measurements with improvement or no change when the terminal impedance matrix is used to compensate for the mutual coupling effects.

The compensation of the mutual coupling effects in the measurements may be affected by the antenna model. In particular, the earth is not exactly a ground plane and

therefore, the monopoles may not be considered to be dipoles. The dielectric constant of the coatings on the monopoles is also only approximate. This parameter effects the calculation of the moment method impedance matrix and therefore the terminal impedance matrix. A more accurate model of the antenna array may yield a better compensated spectrum.

The compensation of the measurements may be affected by gain and phase errors. These errors arise since each amplifier has a slightly different frequency response. Although they are schematically the same, the frequency response may be different due to the components in the amplifier. The gain and phase errors may have as much effect on the spectrum as mutual coupling. Therefore, the spectra may be completely compensated for in terms of mutual coupling but the gain and phase errors prevent any significant improvement in the spectra.

The lack of improvement of the spectrum with the terminal impedance matrix may also be due to the limited number of snapshots. For all the measurements except the cross array, only 16 snapshots are available. For the cross array, 32 snapshots are available. Since the number of snapshots is small, the estimate of the covariance matrix is not as accurate as in chapter 2 where 300 snapshots are used. This is not a factor with the beamformer algorithm since the covariance matrix is not required and the algorithm can be successfully applied even with one snapshot. In the case of Capon's algorithm, this may be a significant factor since the matrix is inverted which may enhance the errors caused by the poor estimate of the covariance matrix. The limited number of snapshots prevents the linear prediction algorithm from yielding a suitable spectrum. The small

number of snapshots does not seem to effect the MUSIC algorithm, however. The MUSIC algorithm performed extremely well on all the measurements.

The variation in the signal over time may also be the reason the spectra are not improved much with the terminal impedance matrix. The magnitude and phase of the signal at one element in the array is shown in figures 108 and 109. Note that the amplitude and phase varies as a function of time. Although this variation is small, it may be significant when calculating the spectra.

The horn array is not a thin wire array and therefore the equation for the terminal impedance matrix in section 2.3.1 can not be used. Therefore, the terminal impedance matrix is estimated in a new manner using the known angle of incidence and the currents at the terminals of the array. Figures 102 and 103 show that the estimate of the angle of arrival is improved by using the terminal impedance matrix calculated as described in this section. Unfortunately, the calculation of the terminal impedance matrix from the data varies as a function of angle. From Appendix A, however, we know that the impedance matrix is invariant with respect to the angle of arrival. Therefore, the variation in the terminal impedance matrix must be due to some other factor such as measurement noise. Since the impedance matrix calculation varies significantly with angle of incidence, it is not practical to use it to compensate for the mutual coupling effects.

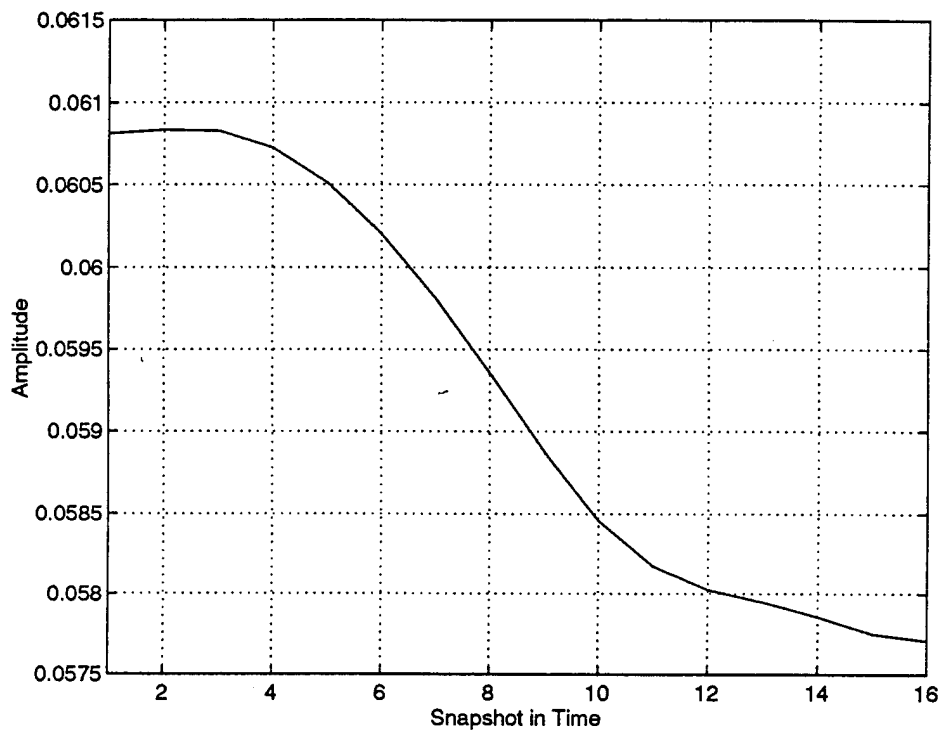


Figure 108: Amplitude Variation of Monopole Signal

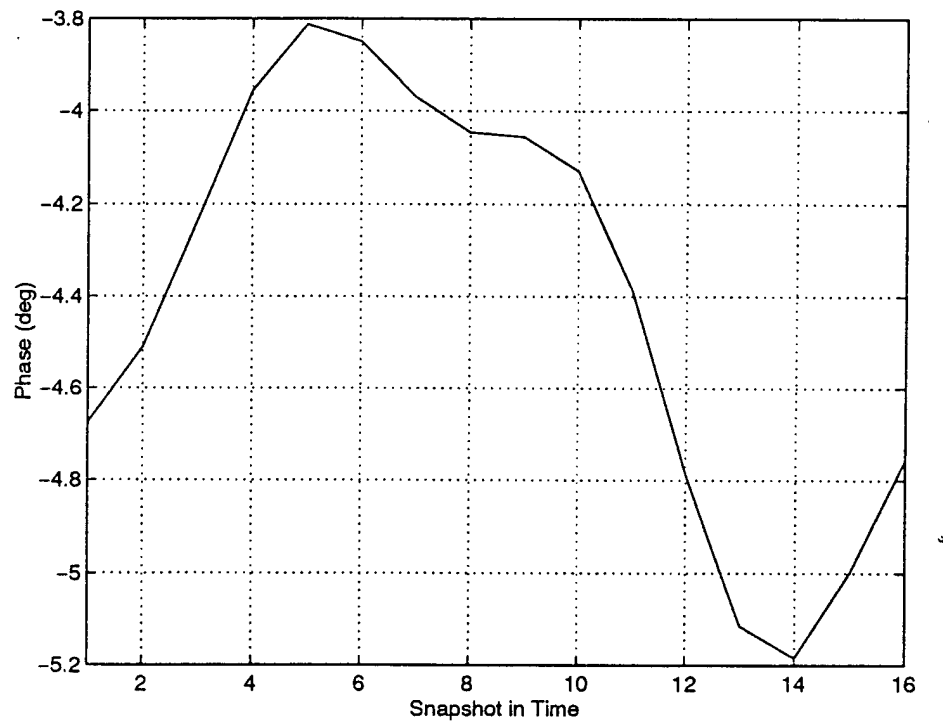


Figure 109: Phase Variation of Monopole Signal

## CHAPTER V

### CONCLUSIONS

Super-resolution algorithms are very susceptible to mutual coupling effects. In addition, there may be an object in the near field of the antenna array that scatters energy toward the array and hinders the resolution of the signals. In this work, the effects of mutual coupling and a near field scatterer are examined quantitatively. Techniques are also presented to compensate for these effects and restore the performance of the super-resolution algorithms.

In chapter 2 the effects of mutual coupling on several different direction finding algorithms is investigated. This is done by comparing the spectrum estimates due to three different signals. The first is the ideal signal which assumes no mutual coupling is present. This represents the best possible spectrum. The actual signals are calculated from the method of moments model of the array. This signal includes all the mutual coupling effects. It is shown that a terminal impedance matrix representing the mutual coupling between the terminals of the array can be derived from the method of moments model of the array. This matrix is then applied to the actual signal vector to correct for the mutual coupling effects. These three signals are generated for various array geometries with various antenna elements. These signals are used to compute the spectra with the Beamformer algorithm, Capon's algorithm, the Linear Prediction algorithm and

the MUSIC algorithm. The results show that the mutual coupling has an adverse effect on the resolution capability of the super resolution algorithms and that these effects can be virtually eliminated from the spectra by pre-processing the signal with the terminal impedance matrix.

In chapter 3 the effects of a near field scatterer on the spectrum generated from the MUSIC algorithm are investigated. This scatterer produces interference in the form of spherical waves that degrade the ability of the MUSIC algorithm to resolve two signals with a small angular separation. To determine the effects of a scatterer, a linear array with the near field scatterer is modeled using a hybrid technique that combines the Method of Moments and the Uniform Theory of Diffraction [34,35]. The effects of the scatterer are then compensated for using a modified terminal impedance matrix and a new array configuration. The modified terminal impedance matrix accounts for the additional mutual coupling between the array and scatterer. The new array configuration is used to suppress the spherical waves from the scatterer. To account for the new array configuration, the search vector of the MUSIC algorithm is modified. Results are presented for various scatterers. It is shown that the terminal impedance matrix and the new array configuration can be used to virtually completely suppress the effects of a near field scatterer.

In chapter 4, the terminal impedance matrix is applied to actual measurements to compensate for the effects of mutual coupling. This is first done on a variety of monopole arrays. The terminal impedance matrix is also applied to an array of horn elements. In this case, a new technique for calculating the terminal impedance matrix

from only measurements is presented. It is then used to compensate for the effects of mutual coupling.

In this report, it is demonstrated that the electromagnetic environment in which the array operates has significant adverse effects on the signal processing algorithms. However, by knowing the electromagnetic environment, modifications can be made to restore the performance of these algorithms. In this work, two factors are investigated. First, it is shown that the mutual coupling between the antenna elements is significant for super-resolution algorithms and that its effects can be virtually eliminated by using a terminal impedance matrix derived from the method of moments model of the array. Second, it is shown that the effects of a near field scatterer can be suppressed by modifying the array configuration and the signal processing algorithm.



## APPENDIX A

### METHOD OF MOMENTS

The reaction integral equation is one of several integral equation formulations [42] that may be used to determine the current induced in an antenna illuminated by a plane wave. This equation is reduced to a system of linear equations using the method of moments. The Galerkin formulation is used where both the expansion and testing functions are piecewise sinusoids [40,41]. This technique yields a relatively small system of equations for thin wire antennas. The solution of the system of equations yields the current on the antenna array. The voltages at the antenna terminals are found by multiplying the current at the antenna terminals by the antenna load impedance for each element.

The reaction integral equation for an arbitrary scatterer is shown below

$$\int_s (\vec{J}_m \cdot \vec{E}^s - \vec{M}_m \cdot \vec{H}^s) ds = - \int_s (\vec{J}_m \cdot \vec{E}^i - \vec{M}_m \cdot \vec{H}^i) ds \quad m=1, 2, \dots, N \quad (116)$$

where  $J_m$  and  $M_m$  are the  $m^{\text{th}}$  testing functions,  $E^s$  and  $H^s$  are the scattered fields, and  $E^i$  and  $H^i$  are the incident fields. Since the wire is non-magnetic, the equivalent magnetic current is zero and the reaction integral reduces to

$$\int_s \vec{J}_m \cdot \vec{E}^s ds = - \int_s \vec{J}_m \cdot \vec{E}^i ds \quad (117)$$

The scattered field is now expressed as arising from a series of piecewise sinusoidal current modes as shown in figure 110 [35]. This yields

$$\int_s \vec{J}_m \cdot \left[ \sum_{n=1}^N I_n \vec{E}_n^s \right] ds = - \int_s \vec{J}_m \cdot \vec{E}^i ds \quad (118)$$

In this expression  $E_n^s$  is the field from the  $n^{\text{th}}$  piecewise sinusoidal mode and  $I_n$  is the  $n^{\text{th}}$  complex current. The testing functions,  $J_m$ , are also piecewise sinusoids which produces the efficient Galerkin formulation. In general, for the  $m^{\text{th}}$  mode of the expansion equation (118) becomes

$$\sum_{n=1}^N I_n \int_s \vec{J}_m \cdot \vec{E}_n^s ds = - \int_s \vec{J}_m \cdot \vec{E}^i ds \quad m = 1, 2, 3, \dots, N \quad (119)$$

This can be expressed as [35]

$$\sum_{n=1}^N Z_{mn} I_n = V_m \quad m=1, 2, \dots, N \quad (120)$$

$$Z_{mn} = \int_s \vec{J}_m \cdot \vec{E}_n^s ds \quad V_m = - \int_s \vec{J}_m \cdot \vec{E}^i ds \quad (121)$$

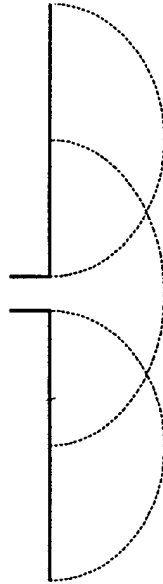


**Figure 110: Piecewise Sinusoidal Current Expansion on One Dipole**

where  $Z_{mn}$  is the mutual coupling between modes  $m$  and  $n$ ,  $I_n$  and  $I_m$  are the currents at modes  $n$  and  $m$  respectively,  $V_m$  is the excitation at mode  $m$ ,  $E^i$  is the incident electric field, and  $ds$  is the differential length along one dipole.

The number of piecewise sinusoids needed to adequately represent the current on a thin wire antenna is dependent upon the length of the antenna element. Since the dipole elements are approximately half a wavelength long at the center of the bandwidth, the current on them can be adequately represented by three piecewise sinusoidal modes. Note that from equation (121) that the impedance matrix  $Z_{mn}$  is not dependent upon the incident field. This matrix is unique to the geometry of the antenna array and the frequency of the incident signal. Note that in contrast, the excitation  $V_m$  is dependent upon the incident field and therefore the angle of arrival.

After  $Z_{mn}$  and  $V_m$  are calculated, the modal current on the antenna elements is found using equation (120). The voltage at the  $n^{\text{th}}$  terminals is then calculated with

$$V_n^{Te} = I_n^{Te} \cdot Z_n \quad (122)$$

where  $I_n^{Te}$  is the modal current at the  $n^{\text{th}}$  terminals of the antenna array, and  $Z_n$  is the load impedance at the  $n^{\text{th}}$  terminals. Therefore, the voltage vector representing the actual signal that includes the effects of mutual coupling is

$$V_a = [V_1^{Te} \ V_2^{Te} \ \dots \ V_n^{Te}]^T \quad (123)$$

This voltage should not be confused with the voltage in equation (120).

## APPENDIX B

### THE BEAMFORMER ALGORITHM

The beamformer algorithm is a simple and computationally inexpensive technique for calculating the spectrum [54]. This algorithm is analogous to the Discrete Fourier Transform (DFT) and therefore its resolution is limited to that specified by the Rayleigh criterion [54].

To derive the Beamformer algorithm, let there be one source illuminating an M element antenna array. The time variation is assumed to be  $e^{j\omega t}$ . Mathematically, the signal at the  $n^{\text{th}}$  antenna element is

$$u_n = A e^{+j\beta (x_n \cos\phi + y_n \sin\phi)} \quad (124)$$

where  $A$  = the amplitude of the incident signal

$\beta$  = the phase propagation constant

$(x_n, y_n)$  = the location of the  $n^{\text{th}}$  antenna element

$\phi$  = the angle of arrival with respect to the x-axis.

The output at each of the antenna terminals of the array is multiplied by a complex weight and added up to yield

$$y = w_1^* u_1 + w_2^* u_2 + \dots + w_M^* u_M = \vec{w}^H \vec{u} \quad (125)$$

where the weights are shown as complex conjugates for convenience. The weights have the form

$$w_n^* = B_n e^{-j\beta (x_n \cos\phi' + y_n \sin\phi')} \quad (126)$$

The output of the beamformer algorithm is equal to the expected value of  $y$  squared. In other words

$$P(\phi) = E[|\vec{y}|^2] = E[\vec{y}\vec{y}^H] = E[(\vec{w}^H \vec{u})(\vec{u}\vec{w}^H)^H] \quad (127)$$

$$P(\phi) = E[\vec{w}^H \vec{u} \vec{u}^H \vec{w}] = \vec{w}^H R_u \vec{w} \quad (128)$$

where

$$R_u = E[\vec{u} \vec{u}^H] \quad (129)$$

is the covariance matrix. Substituting equations (126) and (124) into equation (125) shows the output  $y$  will be a maximum when  $\phi = \phi'$ .

From an antenna point view, the beamformer algorithm corresponds to scanning the main beam of the antenna pattern. The peak in the spectrum corresponds to the main beam being pointed in the direction of the incoming signal. This value, however, will be biased for multiple signals [54]. The smaller peaks in the spectrum correspond to a sidelobe of the antenna array being pointed in the direction of the signal. The sidelobes, and therefore the spurious peaks, can be made smaller by judiciously choosing the value of  $B_n$  [35, pp. 145-154]. This, however, widens the main beam and therefore decreases

the resolution capability of the algorithm. This can be thought of spatial windowing and is analogous to the windowing of temporal signals. From a signal processing point of view, equation (125) corresponds to a Finite Impulse Response (FIR) filter with complex weights.

## APPENDIX C

### CAPON'S ALGORITHM

Capon's algorithm estimates the spectrum by minimizing the output power subject to the constraint that the output equals unity at the current observation angle [5,46]. This technique first designs a causal Finite Impulse Response (FIR) filter with the center frequency at the observation angle  $\phi'$ . This filter is designed by requiring the average output power to be a minimum subject to the condition that the output equals unity at the current observation angle  $\phi'$ . The spectrum is generated by observing the average output power as the observation angle is varied.

Let impulse response of the filter for the look angle  $\phi'$  be

$$\vec{h}_{\phi'} = [h_{\phi'}(1) \ h_{\phi'}(2) \ \dots \ h_{\phi'}(M)]^T \quad (130)$$

where M is the length of the filter. This filter contains one tap for each antenna element.

The data used in the filter is given by the vector

$$\vec{x} = [x(n) \ x(n-1) \ \dots \ x(n-(M-1))]^T \quad (131)$$

In equation (131) each entry in the vector contains all the snapshots in time from one particular antenna element. Note that this data is spatially reversed in the sense that the highest numbered antenna entry is the first element in the vector and the first antenna



element is the last entry in the vector. In the temporal case, this organization of the data is called time reversal. The response of the FIR filter due to the data is

$$y(n) = \sum_{k=1}^M h_{\phi'}(k) x(n-k) = \vec{h}_{\phi'}^T \vec{x} \quad (132)$$

The output power of the filter is

$$P = E[|\vec{y}|^2] = E[\vec{y} \vec{y}^H] = E[(\vec{h}_{\phi'}^T \vec{x})(\vec{h}_{\phi'}^T \vec{x})^H] \quad (133)$$

$$P = E[\vec{h}_{\phi'}^T \vec{x} \vec{x}^H \vec{h}_{\phi'}^*] = \vec{h}_{\phi'}^T \hat{R}_x \vec{h}_{\phi'}^* \quad (134)$$

where  $\hat{R}_x$  is the correlation matrix for the time reversed data. However, using the fact that

$$\hat{R}_x = R_x^T = R_x^* \quad (135)$$

equation (134) becomes

$$P = \vec{h}_{\phi'}^T R_x^* \vec{h}_{\phi'}^* \quad (136)$$

Since the power is a real number,  $P = P^*$ . Therefore, taking the complex conjugate of both sides of equation (136) yields

$$P = \vec{h}_{\phi'}^H R_x \vec{h}_{\phi'} \quad (137)$$

The system transfer function is

$$H_{\phi'}(e^{j\phi'}) = \sum_{k=1}^M h_{\phi'}(k) e^{-j\beta(x_k \cos \phi' + y_k \sin \phi')} = \vec{w}_{\phi'}^H \vec{h}_{\phi'} \quad (138)$$

$$\text{where } \vec{w}_{\phi'} = [e^{+j\beta(x_1 \cos \phi' + y_1 \sin \phi')} \dots e^{+j\beta(x_M \cos \phi' + y_M \sin \phi')}]^T \quad (139)$$

The constraint that the output power of the filter be unity is expressed mathematically as

$$\vec{w}_{\phi'}^H \vec{h}_{\phi'} = 1 \quad (140)$$

Therefore, the problem is to minimize

$$P = \vec{h}_{\phi'}^H R_x \vec{h}_{\phi'} \quad (141)$$

subject to constraint of equation (140). This problem can be solved by first forming the Lagrangian

$$L = \vec{h}_{\phi'}^H R_x \vec{h}_{\phi'} + \mu (1 - \vec{w}_{\phi'}^H \vec{h}_{\phi'}) + \mu^* (1 - \vec{h}_{\phi'}^H \vec{w}_{\phi'}) \quad (142)$$

where  $\mu$  is the Lagrange multiplier. The minimization problem is solved by setting the complex gradient to zero. This yields

$$\nabla \vec{h}_{\phi'}^*(L) = R_x \vec{h}_{\phi'} + 0 + \mu^* (-\vec{w}_{\phi'}) = 0 \quad (143)$$

Rearranging equation (143) and multiplying both sides by  $R_x^{-1}$  yields

$$\vec{h}_{\phi'} = \mu^* R_x^{-1} \vec{w}_{\phi'} \quad (144)$$

This is one of the two equations needed. Multiplying both sides by  $\vec{w}_{\phi'}^H$  yields

$$\vec{w}_{\phi'}^H \vec{h}_{\phi'} = \mu^* \vec{w}_{\phi'}^H R_x^{-1} \vec{w}_{\phi'} \quad (145)$$

Using the constraint in equation (140) produces

$$1 = \mu^* \vec{w}_{\phi'}^H R_x^{-1} \vec{w}_{\phi'} \quad (146)$$

This is the second of the two equations. Solving for  $\mu^*$  and substituting in equation (144) yields

$$\vec{h}_{\phi'} = \frac{R_x^{-1} \vec{w}_{\phi'}}{\vec{w}_{\phi'}^H R_x^{-1} \vec{w}_{\phi'}} \quad (147)$$

Substituting this equation into equation (134) for the output power yields

$$P = \frac{\vec{w}_{\phi'}^H R_x^{-1} R_x R_x^{-1} \vec{w}_{\phi'}}{(\vec{w}_{\phi'}^H R_x^{-1} \vec{w}_{\phi'})^2} = \frac{\vec{w}_{\phi'}^H R_x^{-1} \vec{w}_{\phi'}}{(\vec{w}_{\phi'}^H R_x^{-1} \vec{w}_{\phi'})^2} \quad (148)$$

$$P = \frac{1}{(\vec{w}_{\phi'}^H R_x^{-1} \vec{w}_{\phi'})} \quad (149)$$

This is the response of the optimized filter tuned to the look angle  $\phi'$ . The response of the filter for any angle  $\phi$  is a spectrum estimate of  $x(n)$  and is given by

$$P(\phi) = \frac{1}{(a(\phi)^H R_x^{-1} a(\phi))} \quad (150)$$

$$a(\phi) = [e^{+j\beta(x_1 \cos \phi + y_1 \sin \phi)} \dots e^{+j\beta(x_M \cos \phi + y_M \sin \phi)}]^T \quad (151)$$

where  $a(\phi)$  is the search vector.

## APPENDIX D

### LINEAR PREDICTION ALGORITHM

The linear prediction algorithm produces an estimate of the spectrum by minimizing the mean square error between the actual value of one of the antenna elements and the value predicted by a linear combination of the remaining elements [45,46]. The predicted error is the difference between the predicted value and the actual value. This error is minimized using a Finite Impulse Response (FIR) filter [46]. This error is also white noise provided that the order of the filter is large enough. Next, the system is inverted such that the white noise source drives the filter and produces the input sequence. This new filter is an all pole Infinite Impulse Response (IIR) filter. The filter coefficients are then calculated subject to the constraint that the variance of the predicted error is minimized. The result is an Autoregressive model of the system. This algorithm produces a spectrum estimate with a resolution better than that of Capon's algorithm.

The mean square error between the actual value of one antenna element and its predicted value is minimized to calculate the spectrum. The actual element chosen is rather arbitrary in estimating the spatial spectrum [53]. For the linear array the element farthest away from the origin is used. For the cross array, the element with the most negative position on the x-axis is used. The circular array uses the element located at  $\phi = 225^\circ$ . The choice of an element may be important in a particular case, but on the

average any element is as good as any other element in calculating the spatial spectrum [53].

The first step in calculating the spectrum using the linear prediction algorithm is to predict one of the antenna element's output as a linear combination of the other elements. This can be expressed as

$$\hat{x}(n) = -a_1 x(n-1) - a_2 x(n-2) - \dots - a_p x(n-p) \quad (152)$$

$$\hat{x}(n) = -\sum_{k=1}^P a_k x(n-k) \quad (153)$$

where  $\hat{x}(n)$  is the predicted value and the number of antenna elements is  $M = P + 1$

1. The error between the predicted and actual value is

$$\epsilon(n) = x(n) - \hat{x}(n) \quad (154)$$

Combining equations (153) and (154) yields

$$\epsilon(n) = \sum_{k=0}^P a_k x(n-k) \quad (155)$$

where  $a_0 = 1$ . The mean square error is

$$\sigma_\epsilon^2 = E[|x(n) - \hat{x}(n)|^2] \quad (156)$$

$$\sigma_{\epsilon}^2 = E[\epsilon(n) \epsilon^*(n)] \quad (157)$$

The objective is to find the weights  $a_1, a_2, \dots, a_p$  that minimize  $\sigma_{\epsilon}^2$ .

The output  $\epsilon(n)$  is the result of the prediction error filter. Let the transfer function of this filter be

$$A(z) = 1 + a_1 z^{-1} + a_2 z^{-2} + \dots + a_p z^{-p} . \quad (158)$$

The output  $\epsilon(n)$  will be approximately white noise provided that  $P$  is large. Next, the prediction error filter is inverted such that the white noise drives a filter with the transfer function

$$H(z) = \frac{1}{A(z)} \quad (159)$$

and produces the output  $x(n)$ . This yields the Autoregressive (AR) model. Mathematically, the spectrum is

$$|X(z)|^2 = |H(z)|^2 \sigma_w^2 = \frac{\sigma_w^2}{|A(z)|^2} = \frac{\sigma_w^2}{|1 + a_1 z^{-1} + a_2 z^{-2} + \dots + a_p z^{-p}|^2} \quad (160)$$

where  $\sigma_w^2 = \sigma_{\epsilon}^2$ . Equation (160) can be expressed as

$$x(n) + a_1 x(n-1) + a_2 x(n-2) + \dots + a_p x(n-p) = w(n) \quad (161)$$

where  $w(n)$  is the white noise sequence with variance  $\sigma_w^2$ . Substituting equation (161) into

$$E[x(n) x^*(n-l)] \quad (162)$$

yields the system of equations

$$\begin{aligned} R_x(0) + a_1 R_x(-1) + \dots + a_p R_x(-p) &= R_{wx}(0) \\ R_x(1) + a_1 R_x(0) + \dots + a_p R_x(p-1) &= R_{wx}(1) \\ &\vdots \\ R_x(p) + a_1 R_x(p-1) + \dots + a_p R_x(0) &= R_{wx}(p) \end{aligned} \quad (163)$$

From system theory, however,

$$R_{xw}(l) = h(l) * R_w(l) = h(l) * \sigma_w^2 \delta(l) = \sigma_w^2 h(l) \quad (164)$$

but

$$R_{wx}(l) = R_{xw}^*(-l) \quad (165)$$

Therefore,

$$R_{wx}(l) = \sigma_w^2 h^*(-l) \quad (166)$$

However, since the filter is causal,

$$h(-l) = 0 \quad l > 0 \quad (167)$$

Using the Initial Value Theorem to find  $h(0)$  yields



$$h(0) = \lim_{z \rightarrow \infty} \frac{1}{1 + a_1 z^{-1} + a_2 z^{-2} + \dots + a_p z^{-p}} = 1 \quad (168)$$

Therefore,

$$R_{wx}(0) = \sigma_w^2 \quad (169)$$

and from equation (167)

$$R_{wx}(l) = 0 \quad l > 0 \quad (170)$$

Equation (163) becomes

$$\begin{bmatrix} R_x(0) & R_x(-1) & \dots & R_x(-p) \\ R_x(1) & R_x(0) & \dots & R_x(p-1) \\ \vdots & \vdots & \ddots & \vdots \\ R_x(p) & R_x(p-1) & \dots & R_x(0) \end{bmatrix} \begin{bmatrix} 1 \\ a_1 \\ \vdots \\ a_p \end{bmatrix} = \begin{bmatrix} \sigma_w^2 \\ 0 \\ \vdots \\ 0 \end{bmatrix} \quad (171)$$

but

$$R_x(-l) = R_x^*(l) \quad (172)$$

This produces

$$\begin{bmatrix} R_x(0) & R_x^*(1) & \dots & R_x^*(p) \\ R_x(1) & R_x(0) & \dots & R_x^*(1-p) \\ \vdots & \vdots & \ddots & \vdots \\ R_x(p) & R_x(p-1) & \dots & R_x(0) \end{bmatrix} \begin{bmatrix} 1 \\ a_1 \\ \vdots \\ a_p \end{bmatrix} = \begin{bmatrix} \sigma_w^2 \\ 0 \\ \vdots \\ 0 \end{bmatrix} \quad (173)$$

Note that the matrix is the usual covariance matrix. Therefore

$$R \begin{bmatrix} 1 \\ a_1 \\ \vdots \\ a_p \end{bmatrix} = \begin{bmatrix} \sigma_w^2 \\ 0 \\ \vdots \\ 0 \end{bmatrix} \quad (174)$$

If the covariance matrix in equation (173) is estimated using a procedure that produces a Toeplitz matrix, the coefficients can be quickly calculated using the Levinson-Durbin algorithm [46,55]. However, since the speed of the calculation was not important, the coefficients are found by inverting the covariance matrix. Note that the variance  $\sigma_w^2$  is unimportant since only the location of the peaks is of interest. Therefore,

$$A = \begin{bmatrix} 1 \\ a_1 \\ \vdots \\ a_p \end{bmatrix} = R^{-1} \begin{bmatrix} 1 \\ 0 \\ \vdots \\ 0 \end{bmatrix}. \quad (175)$$

Recall from equation (160) that the spectrum estimate is given by the equation

$$|X(z)|^2 = \frac{\sigma_w^2}{|1 + a_1 z^{-1} + a_2 z^{-2} + \dots + a_p z^{-p}|^2}. \quad (176)$$

This can be expressed as

$$P(\phi) = \frac{1}{|a(\phi)^H A|^2}. \quad (177)$$

or

$$P(\phi) = \frac{1}{\mathbf{a}(\phi)^H \mathbf{A} \mathbf{A}^H \mathbf{a}(\phi)} \quad (178)$$

where

$$\mathbf{a}(\phi) = [e^{+j\beta(x_1 \cos(\phi) + y_1 \sin(\phi))} \dots e^{+j\beta(x_M \cos(\phi) + y_M \sin(\phi))}]^T \quad (179)$$

## APPENDIX E

### MULTIPLE SIGNAL CLASSIFICATION ALGORITHM

The Multiple Signal Classification (MUSIC) algorithm is theoretically capable of resolving two arbitrarily close signals [6,45]. This spectrum is computed by first decomposing the covariance matrix into its eigenvalues and eigenvectors. Provided that the signal to noise ratio is large enough, it is possible, by examining the eigenvalues and eigenvectors, to determine which eigenvectors correspond to the signal and noise and which to the only the noise. The noise only eigenvectors are then used to determine the noise subspace. The pseudo spectrum is calculated by searching for the angles of arrival that are orthogonal to the noise subspace. The result is a very accurate estimation of the locations of the sources. The spectrum calculated is not a true spectrum since size of the peaks do not correspond to the power in the signals.

To derive the MUSIC algorithm let there be K uncorrelated sources illuminating an M element array. The time variation in the following analysis is suppressed and is assumed to be  $e^{j\omega t}$ . Mathematically, the signal at the  $i^{\text{th}}$  antenna element is

$$x_i(t) = \sum_{k=1}^K u_k(t) e^{+j\beta(x_n \cos\phi + y_n \sin\phi)} + n_i(t) \quad i=1, 2, \dots, M \quad (180)$$

where

$u_k(t)$  = the  $k^{\text{th}}$  narrow band plane wave

$\beta$  = the phase propagation constant

$(x_n, y_n)$  = the location of the  $n^{\text{th}}$  antenna element

$\phi$  = the angle of arrival with respect to the x-axis

$n_i(t)$  = the noise at the  $i^{\text{th}}$  antenna element

For two signals, equation (180) reduces to

$$\vec{X}(t) = \begin{bmatrix} e^{+j\beta(x_1 \cos\phi_1 + y_1 \sin\phi_1)} & e^{+j\beta(x_1 \cos\phi_2 + y_1 \sin\phi_2)} \\ \vdots & \vdots \\ e^{+j\beta(x_M \cos\phi_1 + y_M \sin\phi_1)} & e^{+j\beta(x_M \cos\phi_2 + y_M \sin\phi_2)} \end{bmatrix} \begin{bmatrix} u_1(t) \\ u_2(t) \end{bmatrix} + \begin{bmatrix} n_1(t) \\ n_2(t) \end{bmatrix} \quad (181)$$

In matrix notation, equation (181) becomes

$$\vec{X} = A\vec{u} + \vec{n} \quad (182)$$

where

$$A = \begin{bmatrix} e^{+j\beta(x_1 \cos\phi_1 + y_1 \sin\phi_1)} & e^{+j\beta(x_1 \cos\phi_2 + y_1 \sin\phi_2)} \\ \vdots & \vdots \\ e^{+j\beta(x_M \cos\phi_1 + y_M \sin\phi_1)} & e^{+j\beta(x_M \cos\phi_2 + y_M \sin\phi_2)} \end{bmatrix} \quad (183)$$

The covariance matrix is given by,

$$R_x = E[\vec{X}\vec{X}^H] = E[(A\vec{u} + \vec{n})(A\vec{u} + \vec{n})^H] \quad (184)$$

Since the signals and noise are zero mean and uncorrelated with each other, equation (184) reduces to

$$R_x = AR_u A^H + \sigma^2 I \quad (185)$$

where  $R_u = E[\bar{X}\bar{X}^H]$ ,  $\sigma^2$  is the noise variance, and  $I$  is the identity matrix. Note that

the matrix  $R_u$  is of rank  $K$  since all the sources are independent. Next, let

$$R_a = AR_u A^H \quad (186)$$

Since  $A$  and  $R_u$  are of rank  $K$ ,  $R_a$  is also of rank  $K$  even though its size is  $M \times M$ . Therefore,  $R_a$  has  $K$  non-zero eigenvalues and  $(M-K)$  zero eigenvalues. The eigenvector equation for  $R_a$  is

$$R_a \beta_i = \mu_i \beta_i \quad (187)$$

where  $\mu_i$  and  $\beta_i$  are the eigenvalues and eigenvectors respectively of  $R_a$ . The eigenvalue  $\mu_i$  is non-zero for  $i = 1, 2, \dots, K$  and zero for  $i = K+1, K+2, \dots, M$ .

Now consider the expansion  $R_x \beta_i$  for  $i = 1, 2, \dots, M$ . Using equations (185)

yields

$$R_x \beta_i = (AR_u A^H + \sigma^2 I) \beta_i \quad (188)$$

$$R_x \beta_i = AR_u A^H \beta_i + \sigma^2 \beta_i \quad (189)$$

Substituting equation (186) into equation (189) produces

$$R_x \beta_i = R_a \beta_i + \sigma^2 \beta_i \quad (190)$$

Using equation (187) in equation (190) yields

$$R_x \beta_i = \mu_i \beta_i + \sigma^2 \beta_i \quad (191)$$

$$R_x \beta_i = (\mu_i + \sigma^2) \beta_i \quad (192)$$

For  $i = K+1, K+2, \dots, M$ ,  $\mu_i = 0$  and equation (192) reduces to

$$R_x \beta_i = \sigma^2 \beta_i \quad i = K+1, K+2, \dots, M \quad (193)$$

Equating equations (189) and (193) and simplifying yields

$$AR_u A^H \beta_i = 0 \quad i = K+1, K+2, \dots, M. \quad (194)$$

Since  $AR_u$  is of rank  $K$  and  $A^H \beta_i$  is a  $K \times 1$  vector

$$A^H \beta_i = 0 \quad i = K+1, K+2, \dots, M. \quad (195)$$

Using equation (183), equation (195) can be rewritten as

$$\beta_i^H \bar{a}(\phi_k) = 0 \quad k = 1, 2, \dots, K, \text{ and } i = K+1, K+2, \dots, M. \quad (196)$$

$$\text{where } \vec{a}(\phi_k) = [e^{+j\beta(x_1 \cos \phi_k + y_1 \sin \phi_k)} + \dots + e^{+j\beta(x_M \cos \phi_k + y_M \sin \phi_k)}]^T \quad (197)$$

Equation (196) states that each of the noise eigenvectors are orthogonal to the vector  $\vec{a}(\phi_k)$  where  $\phi_k$  is one of the  $k^{\text{th}}$  actual angles of arrival. The MUSIC pseudo spectrum is generated by searching for all the angles that are orthogonal to all the noise vectors  $\vec{\beta}_i^H$ .

Mathematically, this is given by the expression

$$P(\phi) = \frac{1}{\sum_{i=K+1}^M |\vec{\beta}_i^H \vec{a}(\phi)|^2} \quad (198)$$

where

$$\vec{a}(\phi) = [e^{+j\beta(x_1 \cos \phi + y_1 \sin \phi)} + \dots + e^{+j\beta(x_M \cos \phi + y_M \sin \phi)}]^T \quad (199)$$

The vector  $\vec{a}(\phi)$  is referred to as the search vector or the direction vector. It should be noted that if  $K$  is greater than  $M$  then there are no noise vectors to form the noise subspace. In this case, the MUSIC algorithm fails.

Equation (199) yields the ideal spectrum without any mutual coupling effects. To determine the effects of mutual coupling, the output voltage from the method of moments code is used instead of the ideal voltage. Mathematically, this means that equation (182) becomes



$$\vec{X} = \vec{V}_a + \vec{n} \quad (200)$$

where  $\vec{V}_a$  is the actual voltage at the antenna terminals. This voltage is given by equation (8). The corrected spectrum that compensates for the mutual coupling effects is computed with

$$\vec{X} = \vec{V}_c + \vec{n} \quad (201)$$

where  $\vec{V}_c$  is the corrected voltage given by equation (23).

## APPENDIX F

### IMPEDANCE MATRIX AND EXCITATION VECTOR FOR THE EDGE

A hybrid technique is used to combine the method of moments with the Uniform Theory of Diffraction [34,35]. This technique adds a matrix and a vector to the existing moment method matrix and vector. The second matrix represents the mutual coupling between the antenna elements and the scatterer. The second vector models the incident field scattered by the object toward the array. The matrix is a function only of the geometry of the antenna and scatterer while the second vector is also a function of the angle of arrival of the incident field. This hybrid technique permits the moment method to incorporate the effects of a nearby scatterer.

As shown in chapter 3, the effects of a nearby scatterer can be modeled with the equation

$$\sum_{n=1}^N (Z_{mn} + Z_{mn}^g) I_n' = (V_m + V_m^g) \quad m = 1, 2, \dots, N \quad (202)$$

where  $Z_{mn}$  and  $V_m$  are calculated from an existing MoM code [41]. The calculation of  $Z_{mn}^g$  and  $V_m^g$  is done using the hybrid technique that combines the moment method and

Uniform Theory of Diffraction [34,35]. The geometry used to determine  $Z_{mn}^g$  and  $V_m^g$

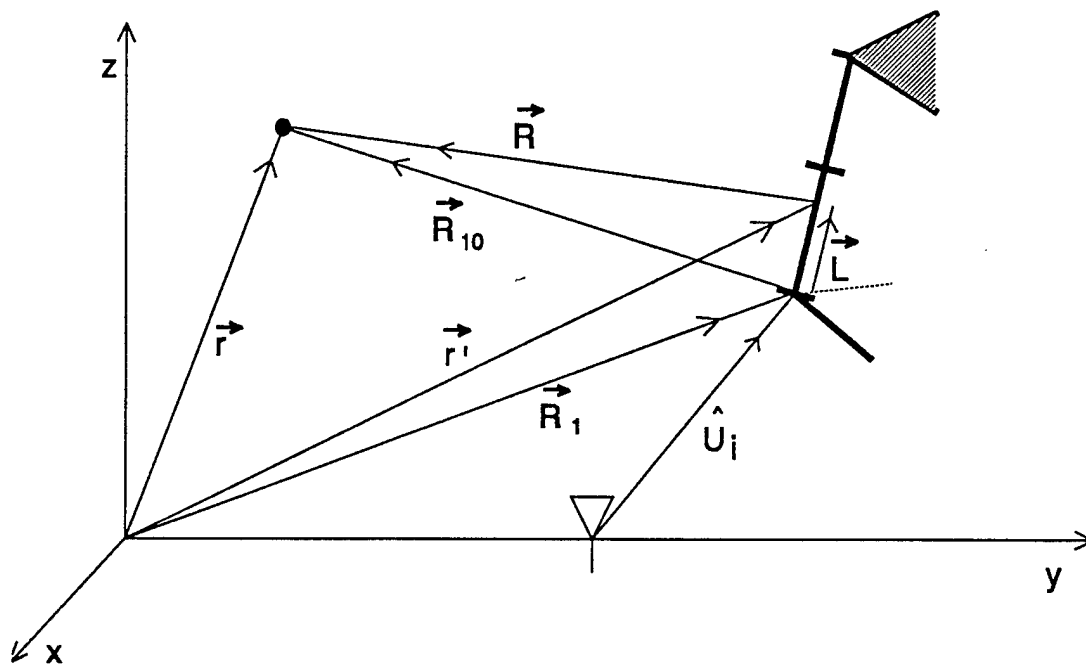


Figure 111: Geometry for Determining  $Z_{mn}^g$  and  $V_m^g$

for a near field edge is shown in figure 111

where  $\vec{r}'$  = vector from the origin to a point on the segment of the edge.

$\vec{r}$  = vector from the origin to the observation point

$\vec{R}_1$  = vector from origin to one end of a segment

$\vec{r}'$  = vector along the direction of the edge

$\vec{R}_{10}$  = vector from one end of a segment on the edge to the observation point

$\vec{R}$  = vector from the point on the edge to the observation point

$\hat{u}_i$  = unit vector in the direction of radiation from the antenna element.

The observation point shown is arbitrary but is actually on the dipole array for this particular problem. Equivalent currents and UTD are used to calculate the field scattered

by the edge. Since the observation point is, in general, in the near field of the edge, the edge is broken up into segments such that the observation point is in the far field of each segment. The far field radiation integral is then used to compute the field scattered by the edge. For the impedance matrix  $Z_{mn}^s$  the direction of propagation is from one mode on one of the antenna elements and the observation point is on any one of the elements. For the vector  $V_m^s$ , the incident field is used instead of  $E_n^s$  and the direction of arrival is used for  $\hat{u}_i$ .

To assist in the calculation of the field scattered by the edge, the vector  $V$  is defined as

$$\vec{V}(\vec{I}) = \frac{1}{4\pi} \int_{\ell} \frac{\vec{I}(\ell') e^{-j\beta R}}{R} d\ell' \quad (203)$$

where  $R$  is shown in figure 111,  $\beta$  is the propagation constant,  $I$  is the equivalent electric or magnetic current on the edge, and the integration is along the length,  $\ell$ , of the edge. Using this vector, the magnetic and electric vector potentials are respectively

$$\vec{A} = \mu \vec{V}(\vec{I}^e) \quad (204)$$

$$\vec{F} = \epsilon \vec{V}(\vec{I}^m) \quad (205)$$

where  $I^e$  and  $I^m$  are the equivalent electric and magnetic current on the edge. To find the scattered field, the usual far field approximations are used. From figure 111, the distance

in the denominator of (203) may be approximated by  $R_{10}$ . For the phase,

$$\vec{R} = (\vec{r} - \vec{r}') = \vec{r} - (\vec{R}_1 + \vec{\ell}') = (\vec{r} - \vec{R}_1) - \vec{\ell}' \quad (206)$$

but

$$\vec{R}_{10} = \vec{r} - \vec{R}_1 \quad (207)$$

Therefore,

$$\vec{R} = \vec{R}_{10} - \vec{\ell}' \quad (208)$$

The magnitude of  $R$  is

$$|\vec{R}| = [(\vec{R}_{10} - \vec{\ell}') \cdot (\vec{R}_{10} - \vec{\ell}')]^{\frac{1}{2}} = [R_{10}^2 - 2\vec{R}_{10} \cdot \vec{\ell}' + \ell'^2]^{\frac{1}{2}} \quad (209)$$

Using the Binomial expansion, the magnitude of  $R$  is

$$|\vec{R}| \approx R_{10} - \hat{R}_{10} \cdot \vec{\ell}' \quad (210)$$

Using this in (203), the vector potential becomes,

$$\vec{V}(\vec{r}) = \frac{e^{-j\beta R_{10}}}{4\pi R_{10}} \int \vec{I}(\ell') e^{+j\beta \hat{R}_{10} \cdot \vec{\ell}'} d\ell' \quad (211)$$

The equivalent electric current is given by the expression [50]

$$\vec{I}^e(\ell') = -\frac{\sqrt{8\pi\beta}}{\eta\beta} e^{-j\frac{\pi}{4}} (\vec{E}_i(\ell_o) \cdot \hat{\ell}) D_s e^{-j\beta \hat{\ell} \cdot \hat{a}_i} \hat{\ell} \quad (212)$$

where  $\eta$  is the intrinsic impedance of free space,  $D_s$  is the soft or parallel diffraction coefficient of the edge,  $\vec{E}_i(\ell_o)$  is the incident electric field at  $\ell'$  on the edge and  $\hat{a}_i$  and  $\ell'$  are defined in figure 111. Substituting this expression into (211) yields,

$$\vec{V}(\vec{I}^e) = \frac{e^{-j\beta R_{10}}}{4\pi R_{10}} \left( -\frac{\sqrt{8\pi\beta}}{\eta\beta} \right) e^{-j\frac{\pi}{4}} (\vec{E}_i(\ell_o) \cdot \hat{\ell}) D_s \hat{\ell} \int_{\ell'} e^{j\beta \hat{\ell} \cdot (R_{10} - \hat{a}_i)} d\ell' \quad (213)$$

After performing the integration and substituting into (204) the magnetic vector potential becomes,

$$\vec{A} = \frac{-\mu\sqrt{8\pi\beta}e^{-j\beta R_{10}}}{\eta\beta 4\pi R_{10}} e^{-j\frac{\pi}{4}} (\vec{E}_i(\ell_o) \cdot \hat{\ell}) D_s \hat{\ell} e^{-j(\beta_e \frac{\Delta\ell}{2})} (\Delta\ell) \frac{\sin(\beta_e \frac{\Delta\ell}{2})}{(\beta_e \frac{\Delta\ell}{2})} \quad (214)$$

where

$$\beta_e = \beta \hat{\ell} \cdot (\hat{R}_{10} - \hat{a}_i) \quad (215)$$

Similarly, the equivalent magnetic current is

$$\vec{I}^m(\ell_o) = -\frac{\eta\sqrt{8\pi\beta}}{\beta} e^{-j\frac{\pi}{4}} (\vec{H}_i(\ell_o) \cdot \hat{\ell}) D_h e^{-j\beta \hat{\ell} \cdot \hat{a}_i} \hat{\ell} \quad (216)$$

where  $\vec{H}_i(\ell_0)$  is the incident magnetic field on the edge, and  $D_h$  is the hard or perpendicular diffraction coefficient. Combining (216), (211), and (205) yields

$$\vec{F} = \frac{-\epsilon\eta\sqrt{8\pi\beta}e^{-j\beta R_{10}}}{\beta 4\pi R_{10}} e^{-j\frac{\pi}{4}} (\vec{H}_i(\ell_0) \cdot \hat{\ell}) D_h \hat{\ell} e^{j(\beta_e \frac{\Delta\ell}{2})} (\Delta\ell) \frac{\sin(\beta_e \frac{\Delta\ell}{2})}{(\beta_e \frac{\Delta\ell}{2})} \quad (217)$$

The far field due to equivalent electric current on the edge is

$$\vec{E}_A = -j\omega [\vec{A} - (\vec{A} \cdot \hat{R}) \hat{R}] \quad \vec{H}_A = \frac{1}{\eta} [\hat{R} \times \vec{E}_A] \quad (218)$$

where the radial component of  $\vec{E}_A$  has been subtracted out to yield the far field.

Similarly the far field due to the equivalent magnetic current is

$$\vec{H}_F = -j\omega [\vec{F} - (\vec{F} \cdot \hat{R}) \hat{R}] \quad \vec{E}_F = \eta [\vec{H}_F \times \hat{R}] \quad (219)$$

Since only the electric field affects the wire, the scattered field at the antenna is

$$\vec{E}_{scat} = -j\omega \vec{A} + j\omega (\vec{A} \cdot \hat{R}) \hat{R} - j\omega \eta (\vec{F} \times \hat{R}) \quad (220)$$

Since the observation point is in the far field,  $\hat{R} = \hat{R}_{10}$ . This substitution is made

because  $\hat{R}$  varies along the segment of the edge while  $\hat{R}_{10}$  is constant for each segment. Therefore, the electric field scattered by the edge is

$$\vec{E}_{scat} = -j\omega \vec{A} + j\omega (\vec{A} \cdot \hat{R}_{10}) \hat{R}_{10} - j\omega \eta (\vec{F} \times \hat{R}_{10}) \quad (221)$$

where  $\vec{A}$  is given by (214) and  $\vec{F}$  by (217). This expression is used to compute both

$Z_{mn}^s$  and  $V_m^s$ . For  $Z_{mn}^s$ ,  $\vec{E}_1(\ell'_o)$  in (214) and  $\vec{H}_1(\ell'_o)$  in (217) are from the piecewise sinusoidal currents on the antenna. For  $V_m^s$  these fields are from the incident plane waves.

### 1.1 Computer Program Validation:

The dipole array with the nearby edge is programmed in FORTRAN using the method of moments as described previously. Instead of writing the entire code from scratch, an existing thin wire method of moments code is used to model the antenna without the edge [41]. This code can model almost any thin wire antenna and has been validated with several problems. Therefore, it is only necessary to write subroutines to include  $Z_{mn}^s$  and  $V_m^s$  of (202) and incorporate them into the program. The final program is validated by comparing the results to previously published work.

There are several antenna parameters such as gain, radiation pattern, and input impedance that may be used to validate an antenna code. While the gain and radiation pattern are not very sensitive to modeling errors, it is well known that the input impedance is very sensitive to the antenna model [35]. Therefore, this parameter is used to validate the computer code.

The input impedance is calculated by operating the antenna in the transmitting mode. In this mode the voltage used to excite the antenna is divided by the complex current at the antenna terminals. This operating condition is slightly different from the receiving mode used to determine the angles of arrival. However, it serves to adequately



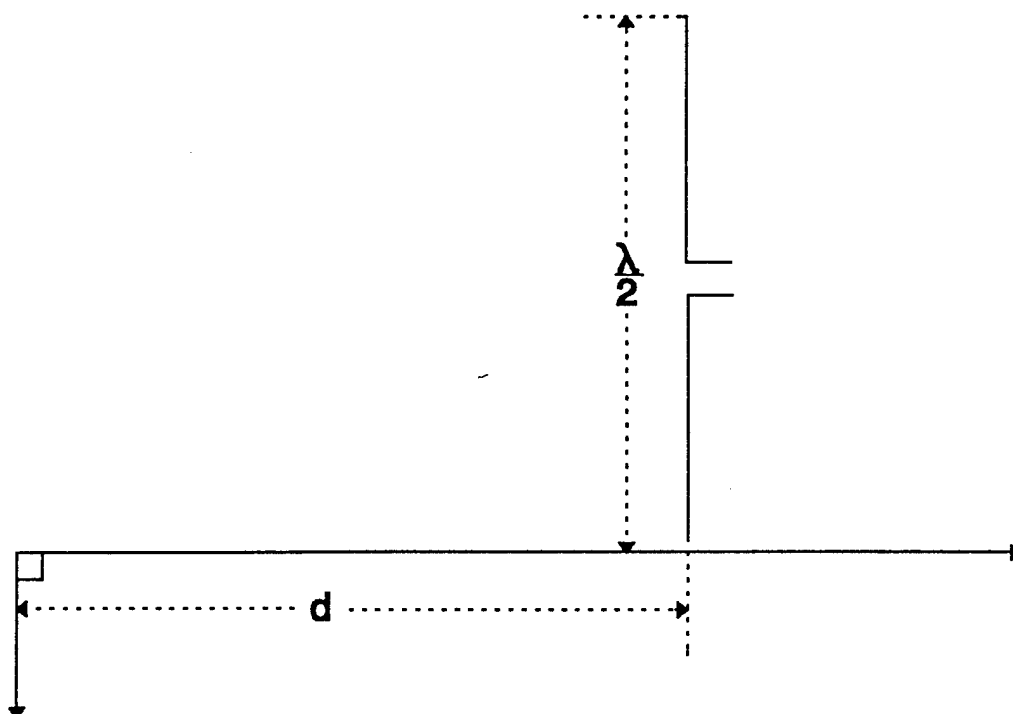


**Figure 112: Dipole with Nearby Edge**

validate the code since, from a programming point of view, it is only a slightly different problem.

To validate the computer code, the input impedance of the antenna in figure 112 is calculated. In this problem, a  $\lambda/2$  vertical dipole is placed just above a perfectly conducting surface. This surface extends to infinity in one direction but bends by  $90^\circ$  in the other direction. At the bend, the horizontal edge is 20 wavelengths long. This is very similar to the problem in [35, pp. 502-504] in which an infinitely long edge is near a monopole mounted on a perfectly conducting surface. In [35] is shown that as the edge is moved away from the monopole, the input impedance oscillates about the value of the monopole on an infinite ground plane. For this problem in figure 112, the input impedance should vary in the same manner.

Figures 113 and 114 shows the real and imaginary parts of the input impedance as a function of 'd' for the problem in figure 112. Notice that as the edge is moved away from the dipole, the impedance oscillates as expected. Notice also that the oscillations decay as the edge is moved away from the dipole. This is expected since the edge will naturally have less effect on the dipole. In the limit as 'd' approaches infinity, the input impedance is equal to the no edge case. These graphs are very similar to the impedance graphs for the monopole on a perfectly conducting surface with a nearby edge [35, p. 504].

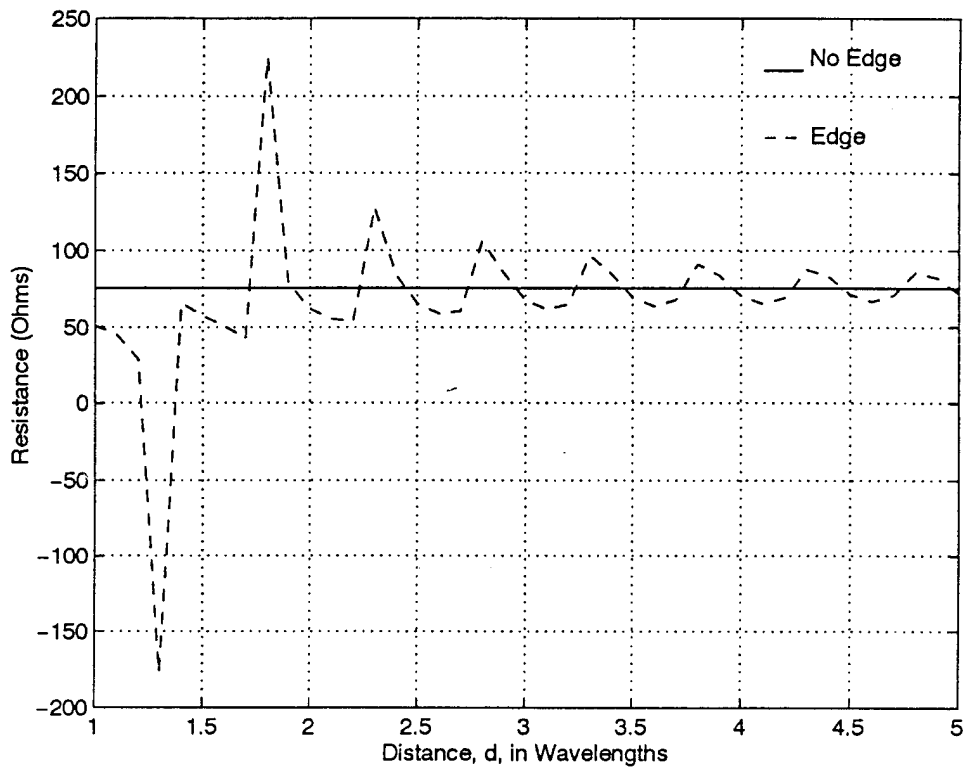


Figure 113: Real Part of Input Impedance of Dipole

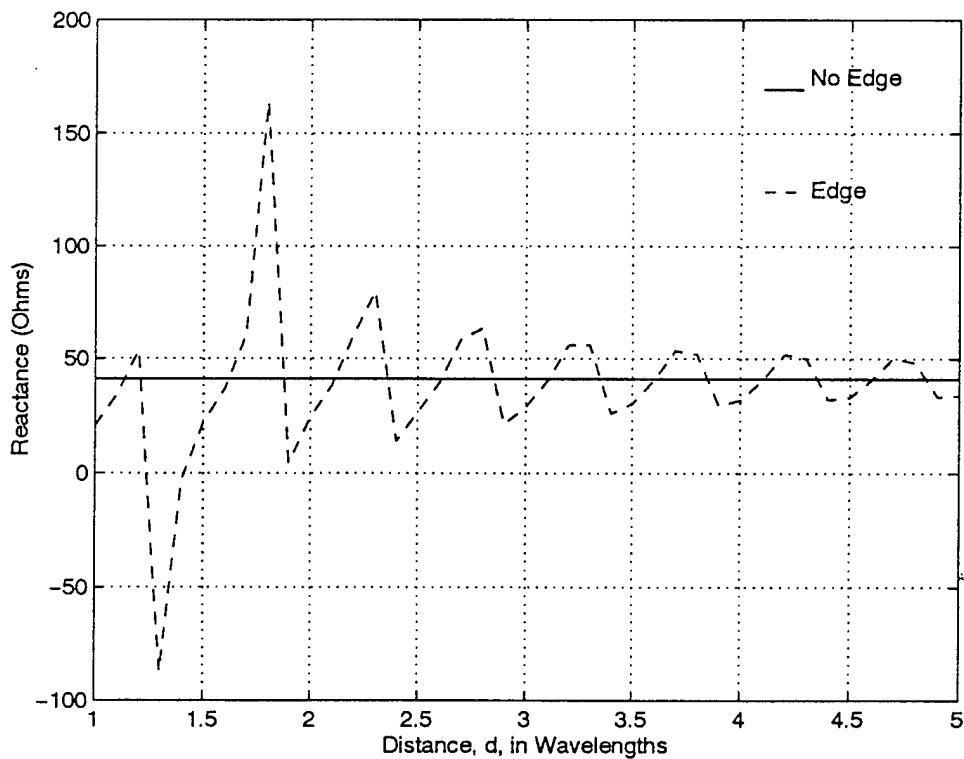


Figure 114: Imaginary Part of Input Impedance of Dipole

## REFERENCES

1. Bartlett, M. S., "Periodogram Analysis and Continuous Spectra" *Biometrika*, Vol. 37. pp. 1-16, 1950.
2. Jenkins, G., Watts, D., "Spectral Analysis and Its Applications" San Fransico, CA: Holden-Day, 1968.
3. Lang, S. W., McClellan, J. H., "Frequency Estimation with Maximum Entropy Spectral Estimators" *IEEE Trans. Acoustics, Speech, and Signal Processing*, Vol. 28 pp. 716-724, Dec. 1980.
4. McDonough, R. N., "Application of the Maximum-Likelihood Method and the Maximum-Entropy Method to Array Signal Processing" in Nonlinear Methods of Spectral Analysis Haykin, S. Ed., New York: Springer-Verlag, 1983.
5. Capon, J. "High Resolution Frequency-Wavenumber Spectrum Analysis," *Proc IEEE*, Vol. 57. pp. 1408-1418, Aug. 1969.
6. Schmidt, R. O., "Multiple Emitter Location and Signal Parameter Estimation" in *Proc. RADC Spectral Estimation Workshop*, Oct. 1979. pp. 243-258; reprinted in *IEEE Trans. on Antennas and Propagation*, Vol. AP - 34, pp. 276-280. March 1986.
7. Paulraj, A., Roy, R., Kailath, T., "Estimation of Signal Parameters via Rotational Invariance Techniques - ESPRIT" in *Proc. 19th Asilomar Conference* Pacific Grove, CA, Nov. 1985.
8. Roy, R., Paulraj, A., Kailath, "ESPRIT - a Subspace Rotation Approach to

- Estimation of Parameters of Cisoids in Noise" *IEEE Trans. Acoustics, Speech, and Signal Processing*, Vol. ASSP-34, pp. 1340-1342, Oct. 1986.
9. Roy, R. H., "ESPRIT: Estimation of Signal Parameter via Rotational Invariance Technique" Ph. D. Thesis, Stanford University, Stanford, CA, 1987.
  10. Rao, B. D., Hari, K. V. S., "Performance Analysis of Root - MUSIC" *IEEE Transactions on Acoustics, Speech, and Signal Processing*, Vol. 17. Dec. 1989. pp. 1939-1949.
  11. Srinath, H., Reddy, V. U., "Analysis of MUSIC with Sensor Gain and Phase Perturbations" *Signal Processing*, Vol 23. June 1991, pp. 245 - 256.
  12. Friedlander, B. "Sensitivity Analysis of the MUSIC Algorithm" *IEEE Transactions on Acoustics, Speech, and Signal Processing*, Vol. 38. Oct. 1990. pp. 1740-1751.
  13. Srinivas, K. R., Reddy, V. U., "Finite Data Performance of MUSIC and Minimum Norm Methods" *IEEE Transactions on Aerospace and Electronic Systems*, Vol 30. No. 1 January 1994, pp. 161 - 174.
  14. Evans, J. E., Johnson, J. R., Sun, D. F., "Application of Advanced Signal Processing Angle-of-Arrival Estimation in ATC Navigation and Surveillance Systems" MIT Lincoln Lab., Lexington, MA. Rep. 582, 1982.
  15. Shan, T. J., Wax, M., Kailath, T., "On Spatial Smoothing for Direction-of-Arrival Estimation of Coherent Signals" *IEEE Transactions on Acoustics, Speech, and Signal Processing*, Vol. ASSP - 33, pp. 806-811, 1985.
  16. Pillai, S. U., Kwon, B. H., "Forward - Backward Spatial Smoothing Techniques for Coherent Signal Identification" *IEEE Transactions on Acoustics, Speech, and*

*Signal Processing*, Vol. ASSP - 37, pp. 8 - 15, 1989.

17. Williams, R. T., Prasad, S., Mahalanabis, A. K., Sibul, L., "An Improved Spatial Smoothing technique for Bearing Estimation in Multipath Environment" *IEEE Transactions on Acoustics, Speech, and Signal Processing*, Vol. 36. pp. 1361 - 1375, 1988.
18. Du, W., Kirlin, R. L., "Improved Spatial Smoothing for DOA Estimation of Coherent Signals" *IEEE Transactions on Signal Processing*, Vol. 33. pp 806-811, 1991.
19. Friedlander, B., "Direction Finding with and Interpolated Array", in *Proc. International Conference on Acoustics, Speech, and Signal Processing (ICASSP)* 1990, Albuquerque, NM, pp. 2951-2954, 1990.
20. Friedlander, B., Weiss, A. J., "Direction Finding Using Spatial Smoothing with Interpolated Arrays" *IEEE Transactions on Aerospace and Electronic Systems* Vol. 28. No. 2, pp. 574-587, April 1992.
21. Wax, M., Sheinvald, J., "Direction Finding of Coherent Signals via Spatial Smoothing for Uniform Circular Arrays" *IEEE Transactions on Antennas and Propagation*, Vol. 42, No. 5., pp 613-620., May, 1994.
22. Gupta, I. J., and Ksienski, A. A., "Effect of Mutual Coupling on the performance of Adaptive Arrays" *IEEE Transactions on Antennas and Propagation*, 31, 5 (Sept. 1983.) pages 785-791.
23. Yeh, C. C., Leou, M. L., and Ucci, D. R., "Bearing Estimation with Mutual Coupling Present" *IEEE Transactions on Antennas and Propagation*, 37, 10 (Oct.

- 1989.) pages 1332-1335.
24. Litva, J., Zeytinoglu, M., "Application of High-Resolution Direction Finding Algorithms to Circular Arrays with Mutual Coupling Present" Final Report ( McMaster University ) Part II prepared for DREO, July, 1990.
  26. Steyskal, H., Herd, J. S., "Mutual Coupling Compensation in Small Array Antennas" *IEEE Transactions on Antennas and Propagation*. 38, 12 (Dec. 1990.) pages 1971-1975
  27. Weiss, A. J., Friedlander, B., "Direction Finding in the Presence of Mutual Coupling" In *Proc. 22nd Asilomar Conf. on Signals, Systems, and Computers*, pages 598-602, 1988.
  28. Friedlander, B., Weiss, A. J., "Direction Finding in the Presence of Mutual Coupling" *IEEE Transactions on Antennas and Propagation*. 39, 3 (March 1991.) pages 273-284.
  29. Swindlehurst, A., Kailath, T., "A Performance Analysis of Subspace-Based Methods in the Presence of Model Errors - Part 1: The MUSIC Algorithm" *IEEE Transactions on Signal Processing*. 40, 7 (July 1992) pages 1758-1774.
  30. Roller, C., Wasyliwskyj, W., "Effects of Mutual Coupling on Super-Resolution DF in Linear Arrays" In *Proc. IEEE ICASSP*, Vol. 5., pages V257-V260, San Francisco, CA, 1992.
  31. Haykin, S., Adaptive Filter Theory 2nd Ed. Prentice-Hall, Englewood Cliffs, NJ 1991.
  32. Friel, E. M., Pasala, K. M., "Wideband Bearing Estimation with Compensation for

- Mutual Coupling Effects" in *Proceedings of IEEE Antennas and Propagation / URSI Symposium*, Seattle, WA, 1994.
33. Pasala, K. M., Friel, E. M., "Mutual Coupling Effects and their Reduction in Wideband Direction of Arrival Estimation" in *IEEE Transactions on Aerospace and Electronic Systems*, Vol. 30. No. 4. October 1994, pp. 1116-1122.
  34. Thiele, G. A., Newhouse, T. H., "A Hybrid Technique for Combining Moment Methods with the Geometrical Theory of Diffraction", *Proc IEEE*, Vol. 62, pp. 1438-1447, 1974.
  35. Stutzman, W. L., Thiele, G. A., Antenna Theory and Design New York, Wiley & Sons, 1981.
  36. Pierre, M., Kaveh, M., "Experimental Performance of Calibration and Direction - Finding Algorithms" in *Proceedings of International Conference on Acoustics, Speech, and Signal Processing (ICASSP)* 1991, pp. 1365-1368.
  37. Weiss, A. J., Friedlander, B. "Eigenstructure Methods for Direction Finding with Sensor Gain and Phase Uncertainties" in *Circuits Systems Signal Proc.*, Vol. 9, No. 3, 1990.
  38. Himed, B., Weiner, D. D., "Compensation for Mutual Coupling Effects in Direction Finding" in *Proc. International Conference on Acoustics, Speech, and Signal Processing (ICASSP)* 1990, pp. 2631-2634.
  40. Richmond, J. H., "Radiation and Scattering by Thin-Wire Structures in the Complex Frequency Domain" NASA Contractor Report CR - 2396, Contract NGL 36-008-138, Hampton, Virginia. May, 1974.



41. Richmond, J. H., "Computer Program for Thin-Wire Structures in a Homogeneous Conducting Medium" NASA Contractor Report CR - 2399, June 1974.
42. Mitra, R., Computer Techniques for Electromagnetics. Hemisphere Publishing Corporation, 1987.
43. Nakano, H. Helical and Spiral Antennas - A Numerical Approach. Research Studies Press, 1987.
44. Jordan, E. C., and Balmain, K. G., Electromagnetic Waves and Radiating Systems. Prentice Hall, 1968.
45. Pillai, S. U. Array Signal Processing. Springer - Verlag, 1989.
46. Therrien, C. W., Discrete Random Signals and Statistical Signal Processing. Prentice - Hall, Englewood Cliffs, NJ, 1992.
47. Ma, M. T., Theory and Applications of Antenna Arrays, John Wiley & Sons, NY, 1974.
48. Hua, Y., Sarkar, T. K., Weiner, D. D., "An L-Shaped Array for Estimating 2-D Directions of Wave Arrival," in *IEEE Transactions on Antennas and Propagation*, Vol. 39, No. 2, February 1991, pp. 143-146.
49. Kay, S., Marple, L., "Sources and Remedies for Spectral Line Splitting in Autogressive Spectrum Analysis" in *Proceedings of the International Conference on Acoustics, Speech, and Signal Processing (ICASSP)*, pp. 151-154, 1979.
50. Balanis, C. A., Advanced Engineering Electromagnetics John Wiley & Sons, 1989.
51. Mewes, H. Personal Fax from Hinrich Mewes
52. Mewes, H. "Measurement Report"

- 53 Johnson, D. H., "The application of Spectral Estimation Methods to Bearing Estimation Problems" *Proceedings of the IEEE*, Vol. 70, No. 9, Sept. 1982, pp. 1018-1028.
- 54 Johnson D. H., Dudgeon, D. E., Array Signal Processing: Concepts and Techniques Prentic-Hall, Englewood Cliffs NJ, 1993.